Cavity quantum electrodynamics : from photonic crystals to Rydberg atoms

Edoardo Tignone

Université de Strasbourg

École Doctorale des Sciences Chimiques
ISIS (UMR 7006) et IPCMS (UMR 7504)

Thèse

présentée par Edoardo Tignone

soutenue le 1 Avril 2016

pour obtenir le grade de: **Docteur de l'Université de Strasbourg**
Discipline/Spécialité: Physique

Cavity quantum electrodynamics: From photonic crystals to Rydberg atoms

THÈSE dirigée par:
Pr. PUPILLO Guido Professeur, Université de Strasbourg

RAPPORTEURS :
Pr. GONZALEZ-FEREZ Rosario Professeur, Université de Granada
Dr. ROSCILDE Tommaso Maître de Conférences, ENS de Lyon

AUTRES MEMBRES DU JURY:
Pr. PUPILLO Guido Professeur, Université de Strasbourg
Dr. GENET Cyriaque Chargé de recherche, ISIS Strasbourg

Acknowledgments

First and foremost, I would like to thank my advisor Prof. Guido Pupillo for giving me the opportunity to carry out my research work in his Laboratory of Quantum Physics. During these three years he has been a continuous inspiration for me. I am deeply grateful to him for the long and stimulating discussions that we had; I have learnt a lot from his critical thinking and his outstanding research skills. His altruism, supportive guidance, and generosity helped me overcome several crisis situations; I have been incredibly fortunate to have an advisor like him.

Secondly, I would like to thank Dr. Claudiu Genes for his scientific guidance and brilliant mentoring. He is an amazingly smart and honest person; he gave me invaluable advise about physics and life in general.

I express my profound gratitude to Dr. Marina Litinskaya for her scientific help. She is an extremely patient teacher.

I must thank Dr. Johannes Schachenmayer for his technical advise.

A heartfelt thanks goes to my colleagues, Fabio, Rogelio, Marion, Luca, Adriano, David, Nóra, Enrique; it has been a real pleasure to meet them and share with them these three years of life. A very special thanks goes to Michael and Davide.

Finally, I would like to thank my parents and my brother Eugenio for their constant support.

Contents

Introduction

Since photons do not carry any electrical charge there is no photon-photon interaction at tree level [1]. This is the main reason why optical signals are the favorite technique for transferring information in a fast and efficient way over large distances [2]. An other important reason is that photons allow for a wider bandwidth compared to electrons [3] and thus a higher information carrying capacity [4]. However, if the linearity of light propagation through a vacuum allows for high-quality information transfer, this same immunity to crosstalk and signal-signal interference makes the photonic logic (fundamental in signal processing) very hard to implement. In order to enable light-light interaction one needs nonlinear optical processes.

Typically, when a weak light beam travels through an optical medium only linear optical processes take place, such as absorption or refraction. In order to observe a nonlinear response a sufficiently intense light beam is necessary: The associated electric field that acts on the electrons must be of the same order of magnitude as the field produced by the nucleus [2]. If this is the case, the index of refraction acquires a dependence on the amplitude of the electric field of the beam. This is different from linear optics, where the physics is taken into account by introducing an imaginary component of the index of refraction. A famous example of nonlinear response is the optical Kerr effect [5], where the light propagation depends on the local irradiance of the field itself. The need for powerful lasers explains why the first optical (classical) nonlinearities were only observed in the 1960s [6].

From then until today, the research has progressed greatly towards the implementation of optical nonlinearities at lower and lower light powers [7]. The ultimate limit for this progressive increase in resolution and accuracy is the quantum regime, where single photons interact so strongly between each other that the behavior of light pulses composed of a few photons heavily depends on the number of photons. At quantum level the nonlinear coefficients of the conventional optical materials are extremely small. However, there are several techniques to implement strong interactions between individual photons. This regime was first theoretically investigated by early works [8–10] in the 1980s. The emerging field of quantum information and computing [11] constituted an additional pressing motivation towards looking for experimental results.

The first experimental work dates back to 1995 [12] where a single atom

was placed inside an optical cavity in the strong coupling regime. This work has demonstrated the realization of nonlinear optical susceptibility at quantum level. By employing the atomic saturation, the authors of the paper managed to apply a shift ($19° \pm 3°$) to the phase of one photon. They also proposed to use this nonlinearity for a quantum-phase gate. The work presented in Ref. [12] was the first experimental step towards photonic quantum logic. After then, many advances have been made: The realization of nonlinear all-optical routers [13, 14] as well as switches [15–21] (even at ultrafast timescale [22]) and controlled-phase gates [12, 23–26] could allow for high-quality quantum information manipulation and communication through quantum networks [27].

Nonlinearities between single quanta of radiation are useful not only in quantum information science but also in fields such as quantum metrology [28] or microscopy [29]. Furthermore, photon-photon nonlinearities pave the way towards new nondestructive ways to detect [30] and sort [31, 32] photons, create deterministic single-photon sources [33] and tailor directional scattering processes [34–36]. Nonlinear optics at quantum level would enable all those applications that need creation and processing of nonclassical fields.

Nowadays there are several ways to realize strong photon-photon interactions: All of them rely on a non-photonic counterpart (an atom or an ensemble of atoms) which mediates the interaction between photons. The stronger the interaction between each photon and the non-photonic counterpart the stronger the resulting photon-photon effective interaction. The nonlinear nature of such interaction originates either from the nature of the electronic spectrum of the non-photonic element (e.g. atomic saturation or atom-atom interactions) or from its mechanical degrees of freedom; in the latter case we are in the domain of optomechanics [37, 38].

The most elementary platform to realize photon-photon nonlinearities consists in placing one atom inside a high-finesse cavity and employing atomic saturation; this procedure was used in the pioneering work [12]. In this fundamental cavity quantum electrodynamics platform, the element that mediates the interaction between two photons is an atom. The role of the cavity is to enhance the probability for a single photon to interact with the atom: Due to the cavity mirrors the photon bounces back and forth through the intracavity space several times, which enhances the probability for a photon to interact with the atom; namely, the higher the cavity finesse the higher such probability. For a two-level atom coupled to a cavity, the nonlinear nature of the interaction comes from the shape of the energy spectrum of the Jaynes-Cummings Hamiltonian [39] which naturally arises when an atom is placed inside a resonator. The Jaynes-Cummings spectrum depends on the square root of the photon number and this anharmonicity can be used to realize interesting nonlinear effects such as photon blockade [40] or a two-photon gateway [41] as well as a single-atom quantum mem-

ory [42] and quantum gates [43]. The drawback of this method is the short lifetime of the excited state of the atom [2]. However, one can use multilevel atoms with metastable states [44, 45]. This atom-cavity platform can be reproduced also in solid-state systems by fabricating microring resonators in monocrystal diamonds and coupling the cavity photons to individual nitrogen vacancies [46, 47] or by using semiconductor quantum dots [48–51].

A more complex method to realize quantum optical nonlinearities, which does not need any cavity, consists in employing the electromagnetic induced transparency technique in order to create slow photons traveling through an ensemble of atoms [45, 52]. In this case, a preferred nonlinear medium is composed of a trapped cold gas of three-level atoms in Rydberg states [31, 53–56]. Rydberg atoms are convenient because of their strong dipole moments and therefore strong mutual interactions. Additionally, the Rydberg blockade mechanism [57–59] enhances the probability for an atom-photon interaction: From the point of view of the photon, every atom behaves as a giant superatom of radius equal to the blockade radius. This effect is similar to that one described by the finesse of a resonator but unlike the cavity case, where one photon approaches many times the same atom, here one photon approaches a superatom characterized by a larger cross section, proportional to the number of atoms inside a Rydberg volume. If this number is large enough, nonlinearities happen [60–62].

In a dissipative regime, where two photons close enough to each other break the electromagnetic induce transparency condition and get absorbed by the medium, an effective photon-photon repulsion can be implemented [31]. On the contrary, in a dispersive regime one can implement an effective photon-photon attraction [56]; in this case the index of refraction of the medium depends on the photon-photon separation. Rydberg media demonstrate attraction between photons owing to the formation of bound bipolariton states [63, 64].

For an atom in a high-finesse cavity in the strong coupling regime or for a large enough Rydberg volume (when the cooperativity of the system is much larger than unit) the atom and the cavity exchange photons on a timescale much faster than any other dynamical process: From the point of view of the system atom and photon can not be anymore distinguished. These hybridize and form a bosonic quasiparticle which is called exciton-polariton or just polariton [65]. Polaritons are coherent superpositions of a cavity photon and an exciton. Owing to their mixed nature, polaritons have many fascinating properties such as a lighter effective mass than the atom and thus a steeper dispersion relation or, in other words, a larger group velocity [66] (on the other hand, dressed photons can account for mechanisms such as "slow light"). Polaritons in semiconductor microcavities show superfluidity [67] and for a sufficiently high density can condensate [65, 68–72]; in recent years, Bose-Einstein condensates of organic polaritons were realized at room temperature [73, 74]. Due to the progressive improvement in fab-

ricating semiconductor microcavities [75–79] Bose-Einstein condensates of polaritons are promising candidates for quantum simulations.

Until now we have considered nonlinearities caused by the electronic spectrum of an atom. However, optical nonlinearities can be mediated also by the phononic vibrations. This is what happens in optomechanical systems [37] where the spatial motion of a mechanical element (or an ensemble of mechanical elements) produces a shift in the resonance frequency of the surrounding resonator. A sufficiently strong optomechanical coupling can lead to quantum nonlinear optical phenomena such as photon blockade effect [80] or optical bistability at photon numbers below unity [81]. There are also theoretical proposals for realizing effective photon-photon interactions [82].

In free space a light beam can not be focused to subwavelength mode volumes. In the last years, much experimental effort has been devoted to fabricating light-matter nanointerfaces whose radiation modes can access diffraction-limited volumes such as photonic crystal waveguides [83–88], optomechanical crystals [89–92], tapered optical fibers [93–95], or conducting nanowires [96, 97]. All these platforms allow for integration of nanophotonics with atomic systems. Since the diameter of the tapered fibers must be smaller than the wavelength of the guided mode, the atoms are placed outside of the fiber and are coupled to the evanescent field. Up to now this was done for more than 1000 cold atoms [83]. An attractive alternative are the hollow-core photonic crystal fibers [98–100] where as many as 10^5 atoms [100] can be accommodated inside the micrometer core. All these platforms combined together with nano- and micro-size photonic crystal cavities [101–103] could allow for the implementation of quantum networks [13, 16, 104]. Finally, strong optical nonlinearities can be achieved also in some optical materials [105] such as graphene [106]

Even though most research works are devoted to single-photon physics, nonlinear optics can of course involve also many-body photonic systems. Because of the high capacity, fibers can present a nonlinear response [107]. From a quantum point of view researches have been performed on solitons in fibers [108, 109]. Also photon bound states in Kerr nonlinear media have been theoretically studied in 1990s [110–112] and, recently, effective two-photon bound states have experimentally been observed in Rydberg nonlinear media [56]. There are also proposals for systems of coupled cavity arrays (Jaynes-Cummings-Hubbard model) where photons can hop from one cavity to another, and each cavity contains a single emitter [66, 113–118]. Here, the nonlinearities are provided by the nodes of this photonic network due to the anharmonicity of the Jaynes-Cummings eigenenergies. The interplay between the linear propagation in the intercavity vacua and the nonlinear nodes is expected to give rise to phase transitions. Arrays of resonators can of course be combined with Rydberg atoms [119]. There are also proposals for the observation of novel collective states of light, such as crystal-like

states in optical fibers [120] and Rydberg media [121].

In this thesis we study several methods to implement strong photon-photon nonlinearities, ranging from quasiperiodic photonic crystals to Rydberg atoms inside a cavity. We also study the transport of an atomic excitation through an array of two-level emitters embedded in a cavity and show that the polaritonic modes can enhance the efficiency of the transport and help overcome the localization induced by possible disorder in atomic position and dipole orientation.

The thesis is organized as follows. Chapter 1 is devoted to an optomechanical problem. First, we analyze a high-finesse cavity surrounding a quasiperiodic stack of dielectric membranes affected by a quadratic spatial defect and we extend the results of Refs. [122, 123]; then, we use this model to simulate an optomechanical photonic crystal [89, 92]. We show that the presence of the defect greatly enhances the linear and quadratic optomechanical couplings for the array in the cavity. On the contrary, the enhancement for the crystal is only caused by the extreme localization of the light within tiny mode volumes. Sec. 1.1 reviews the transfer matrix formalism. In Sec. 1.2 we describe the optomechanical platforms. In Sec. 1.3 we perform a study of the array embedded in the cavity: In Sec. 1.3.1 we work out the transfer matrix for the quasiperiodic array of membranes up to first order in defect magnitude whereas in Secs. 1.3.2 and 1.3.3 we perform a numerical study of the optical response of the medium and the linear and quadratic optomechanical couplings, respectively. In Sec. 1.3.4 we exemplify our findings with an experimental case. In Sec. 1.4 we move to the second platform, the photonic crystal. First, in Sec. 1.4.1 we study the outer equidistant parts, then in Sec. 1.4.2 we study the crystal as a whole. In Sec. 1.4.3 we discuss the structure of the optical modes inside the crystal. Finally, Sec. 1.5 summarizes the main results.

Appendix 1.A reviews the findings of Refs. [122, 123]. Appendix 1.B contains the algebraic computations leading to the first-order transfer matrix for the quasiperiodic array. Appendix 1.C exposes the Chebyshev's identity. In Appendix 1.D some considerations about the optical response of an empty Fabry-Pérot cavity are carried out. Appendix 1.E reviews a few aspects of the band structure for an infinite one-dimensional photonic crystal. Finally, Appendix 1.F quickly reviews the Kronig-Penney model by strictly following Ref. [124].

In Chapter 2 we consider the transport of an exciton through a cavity. We show that the polaritonic modes allow for a ultrafast propagation of the exciton through the cavity and help overcome the exponential suppression induced by disorder [125]. In Sec. 2.1 we illustrate the model. Sec. 2.2 reviews the concept of polariton as well as its most basic properties. In Sec. 2.3 we consider a wave-packet scattering problem applied to our model and present both analytical (Sec. 2.3.1) and numerical (Sec. 2.3.2) results con-

cerning the transmission of the wave packet through the cavity. In Sec. 2.4 we include dissipation in the model and by employing the master equation formalism we study the steady-state current in the system under incoherent pumping from the left side of the cavity. Finally, Sec. 2.5 summarizes the main results.

In Appendix 2.A we provide a solution for the Schrödinger equation associated to the model and find the polaritonic eigenstates. In Appendix 2.B we show the analytical time-independent computations about the polaritons and the transmission of the wave packet through the cavity. In Appendix 2.C we consider some realistic parameters.

In Chapter 3 we consider photons coupled to an array of cold atoms trapped in an optical lattice inside a hollow-core photonic crystal fiber. We study photon-photon interactions mediated by hard-core repulsion between excitons. We show that, in spite of underlying repulsive interaction, photons in the scattering states demonstrate bunching, which can be controlled by tuning the interatomic separation. In Sec. 3.1 we introduce the model. In Sec. 3.2 we provide a solution for the associated Schrödinger equation and plot the wave functions for three exemplar eigenstates. In Sec. 3.3 we consider the kinematics of two bare excitons interacting via kinematic interaction. Sec. 3.4 provides a qualitative explanation for the bunching effect. Sec. 3.5 deals with the dependence of the bunching over the experimental parameters. Sec. 3.6 considers the possibility of having two-polariton bound states (bipolaritons) when the spectrum becomes gapped. Finally, Sec. 3.7 summarizes the results.

Appendix 3.A presents an analytical explanation for the bunching mechanism.

In Chapter 4 we extend the findings of Chapter 3 to Rydberg atoms. The presence of a forbidden blockade volume results in an extended kinematic interaction, which further enhances the bunching. We also study the effect of dynamical interactions on top of the hard-core repulsion. In Sec. 4.1 we introduce the model. In Sec. 4.2 we solve the associated Schrödinger equation when the center of mass of the two-excitation system is at rest. In Sec. 4.3 we provide the numerical solution to the problem and plot the two-polariton wave functions. In Sec. 4.4 we analytically solve the problem of two bare excitons interacting via an extended kinematic repulsion. Then, we add the photonic degrees of freedom and use these results to understand the kinematics of two polaritons in Sec. 4.5. Sec. 4.6 is devoted to the numerical study of bunching. In Sec. 4.7 we switch on the dynamical interaction and study its contribution; for attractive interaction we look at the bound states that form below the continuum. Sec. 4.8 is devoted to the study of the in-gap bipolaritons, which form for a kinematic or a repulsive dynamical interaction. Finally, Sec. 4.9 summarizes the main results.

In Appendix 4.A we review the basic properties of Rydberg atoms. In Appendix 4.B we solve the Schrödinger equation for a generic total wave

vector. In Appendix 4.C we calculate the dispersion relation for the simple case of two bare excitons interacting via a long-range dynamical interaction.

Chapter 1 can be found in:

E. Tignone, G. Pupillo, C. Genes,
Transmissive optomechanical platforms with engineered spatial defects,
Phys. Rev. A **90**, 053831 (2014)

Chapter 2 can be found in:

J. Schachenmayer, C. Genes, E. Tignone, G. Pupillo,
Cavity-Enhanced Transport of Excitons,
Phys. Rev. Lett. **114**, 196403 (2015)

Chapter 3 can be found in:

M. Litinskaya, E. Tignone, G. Pupillo,
Broadband photon-photon interactions mediated by cold atoms in a photonic crystal fiber,
arXiv:1512.02312 [quant-ph]
(submitted to *Scientific Reports*)

Finally, Chapter 4 contains the results of:

M. Litinskaya, E. Tignone, G. Pupillo,
Cavity polaritons with Rydberg blockade and long-range interactions,
(submitted to *Journal of Physics B: Atomic, Molecular and Optical Physics*)

1
Transmissive optomechanics with engineered spatial defects

Cavity optomechanics is the branch of physics that explores the interaction between optical and mechanical degrees of freedom in driven electromagnetic cavities [37, 126].

Micromechanical and nanomechanical motion of massive oscillators inside a cavity can be controlled at the quantum level via the cavity radiation. For instance, cooling to the motional quantum ground state of several mechanical objects has already been achieved, ranging from atoms [127] to mirrors [128] to microtoroids [129] and submicron particles [130, 131]. An example of a classical optomechanical system is illustrated in Fig. 1.1.

In an optomechanical platform the frequency of the cavity mode ω_c depends on the spatial displacement $\hat{x}$ of the mechanical oscillator [37, 38, 132]. Such a dependence can be Taylor-expanded, and for most experimental situations it suffices to keep the linear term:

$$H = \hbar(\omega_c(0) - f_c^{(1)}\hat{x})\hat{a}^\dagger\hat{a} + \hbar\Omega_m\hat{b}^\dagger\hat{b} + ... \tag{1.1}$$

Here, Ω_m is the mechanical frequency of the massive oscillator; $\hat{a}$ destroys a photon in the cavity mode whereas $\hat{b}$ destroys a phonon in the mechanical mode of the oscillator; $f_c^{(1)} = \partial\omega_c(\hat{x})/\partial\hat{x}|_{\hat{x}=0}$ is the optomechanical frequency shift per displacement. The force term $\hbar f_c^{(1)}\hat{a}^\dagger\hat{a}$ represents the radiation pressure; it derives from the momentum transfer when a single photon hits the oscillator.

In the rotating frame at the incoming laser frequency $\omega_L = \omega_c(0) + \Delta$, the displacement $\hat{x}$ can be expressed in terms of phononic operators as $\hat{x} = x_0(\hat{b} + \hat{b}^\dagger)$ with x_0 the size of the zero point fluctuations $x_0 = \sqrt{\hbar/2m_{\text{eff}}\Omega_m}$:

$$H = -\hbar\Delta\hat{a}^\dagger\hat{a} - \hbar g_0^{(1)}(\hat{b} + \hat{b}^\dagger)\hat{a}^\dagger\hat{a} + \hbar\Omega_m\hat{b}^\dagger\hat{b} + ... \tag{1.2}$$

In expansion (1.2) $g_0^{(1)} = f_c^{(1)}x_0$ is the so-called linear optomechanical coupling between a single photon and a single phonon; it measures the shift of the optical frequency of the cavity mode ω_c produced by a zero point mechanical displacement of the oscillator inside the cavity. Typically $g_0^{(1)}$ is smaller than both Ω_m and the decay rate κ of the cavity.

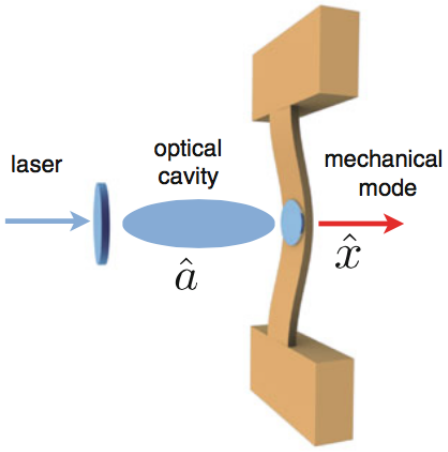

Figure 1.1: A classical optomechanical problem consists of a laser-driven Fabry-Pérot cavity whose light mode exerts a radiation pressure force $\hbar f_c^{(1)} \hat{a}^\dagger \hat{a}$ (see main text) on one of the side mirrors, which is free to vibrate. Source: Ref. [38].

Had we kept also the quadratic term in Taylor expansion (1.1), we would have had the quadratic optomechanical coupling $g_0^{(2)}$ as well. It is given by $g_0^{(2)} = f_c^{(2)} x_0^2$, where $f_c^{(2)}$ is $f_c^{(2)} = \partial^2 \omega_c(\hat{x})/\partial \hat{x}^2|_{\hat{x}=0}$.

Unlike the linear coupling, which allows for readout of the mechanical displacement $\hat{x}$ of the membrane hit by photons [133, 134], the quadratic coupling can be used for a quantum nondemolition measurement of the energy of the membrane and a high-quality obervation of its quantized nature [135, 136].

Improving both couplings is a main goal for the current generation of optomechanical experiments [80, 136–141].

Although most optomechanical studies have so far focused on platforms consisting of a single mechanical element in a Fabry-Pérot cavity setup [142–145], recent works have started to investigate multi-element approaches from both a theoretical [122, 123, 146–156] and experimental [157–161] point of view. This latter approach allows for large collective mechanical effects and is therefore a promising step towards the enhancement of both linear and quadratic optomechanical couplings.

In the limit of a one-dimensional scattering problem, an efficient analytical approach to these multi-element systems is provided by the so-called transfer matrix formalism, which is reviewed in Sec. 1.1.

Interesting experiments have been performed in this direction, by employing ensembles of N atoms either in a cloud [133] or trapped in optical lattices [162] which have indeed shown an improved linear optomechanical coupling $g_0^{(1)}$ proportional to $\sqrt{N}$.

Theoretical proposals have recently shown that $g_0^{(1)}$ can be further en-

hanced by using cavities surrounding an array of N equidistant membranes characterized by a polarizability ζ. For these systems a linear optomechanical coupling scaling as $\zeta^2 N^{3/2}$ has been predicted. The main results concerning this model are collected in Appendix 1.A.

Eventually, also quasiperiodic photonic crystals have demonstrated a remarkable increase in the strength of the linear coupling [89, 92]. In this case the increase is due to the localization of light within a small volume inside the dielectric structure and the following activation of collective vibrational modes defined by an engineered quadratic defect and localized within the same reduced volume.

Inspired by these quasiperiodic crystals, in this chapter we extend the investigations of Refs. [122, 123] to quasiperiodic arrays in the presence of engineered spatial defects in the membrane positions; we place the array inside a high-finesse optical cavity and demonstrate that indeed a tremendous enhancement in both linear and quadratic couplings is possible. We also build up a simple theoretical model for the photonic crystals themselves. For the crystal case, however, we show that a further increase of the optomechanical couplings induced by the defect can not be reached.

This chapter is organized as follows. Sec. 1.1 reviews the transfer matrix formalism. In Sec. 1.2 we introduce both of the above-mentioned optomechanical platforms: The quasiperiodic array surrounded by a cavity and the photonic crystal. In Sec. 1.3 we study the array inside the cavity. First, we find the transfer matrix for the quasiperiodic array up to first order in defect magnitude (Sec. 1.3.1 and 1.3.2), then the linear and quadratic couplings are numerically studied (Sec. 1.3.3). In Sec. 1.3.4 we exemplify our findings with an experimental case. Sec. 1.4 is instead entirely devoted to the study of the photonic crystal. We analyze the outer parts of the crystal (Sec. 1.4.1) as well as the crystal as a whole (Sec. 1.4.2) and make some general considerations about the structure of the optical modes inside it (Sec. 1.4.3). Sec. 1.5 contains the conclusions of the chapter.

Appendix 1.A presents the main results of Refs. [122, 123]. The algebraic steps to obtain the approximate transfer matrix for the quasiperiodic array are gathered in Appendix 1.B. Appendix 1.C illustrates the Chebyshev's identity. Appendix 1.D considers the optical response of an empty Fabry-Pérot cavity. Appendix 1.E reviews a few features of the band structure for an infinite one-dimensional photonic crystal. Eventually, Appendix 1.F presents the Kronig-Penney model, by following Ref. [124].

The results from this chapter have been collected in the following paper, published during the PhD:

E. Tignone, G. Pupillo, C. Genes,
Transmissive optomechanical platforms with engineered spatial defects,
Phys. Rev. A **90**, 053831 (2014)

1.1 Transfer matrix formalism

This formalism treats the one-dimensional problem of light impinguing on a mechanical element (scatterer), provided that its interaction with the electromagnetic field $E(x,t)$ is linear [122, 123, 163].

The one-dimensional Helmoltz equation for an electric field $E(x,t) = E(x)e^{i\omega t}$ which at a time $t = 0$ interacts with a scatterer at $x = 0$ is

$$\left[\partial_x^2 + \left(\frac{\omega}{c}\right)^2 \epsilon_r(x)\right] E(x) = 0. \tag{1.3}$$

The relative permettivity is $\epsilon_r(x) = \epsilon_{r0} + \delta\epsilon_r(x)$ where the first contribution ϵ_{r0} is the vacuum permettivity whereas the second one describes the dielectric scatterer:

$$\delta\epsilon_r(x) = \frac{2}{k}\zeta\delta(x). \tag{1.4}$$

In Eq.(1.4) the wavevector $k = 2\pi/\lambda$ is equal to the frequency ω divided by the speed of light in the vacuum c.

The optical element, which is treated as a beam splitter, is fully characterized by a polarizability ζ which is real and negative (in the absence of absorption). The polarizability ζ is connected to the amplitude reflectivity r of the optical element via

$$r = \frac{i\zeta}{1 - i\zeta}, \tag{1.5}$$

that is

$$R = |r|^2 = \frac{\zeta^2}{1 + \zeta^2}. \tag{1.6}$$

Here R is the intensity reflectivity.

The transfer matrix approach is a very useful tool when the electric field travels through a set of multiple elements, for instance an array of thin dielectric membranes, or mirrors, or a chain of ultracold atoms trapped in an optical lattice.

The left and right propagating waves at the left and right side of the i-th scatterer (with polarizability ζ_i) can be expressed as vectors as

$$E_i^{(\pm)} = (E_{L,i}^{\pm}, E_{R,i}^{\pm})^T \tag{1.7}$$

and the scattering of the light field is then simply described by $E_i^- = M_i(\zeta_i)E_i^+$, with

$$M_i(\zeta_i) = \begin{bmatrix} 1 + i\zeta_i & i\zeta_i \\ -i\zeta_i & 1 - i\zeta_i \end{bmatrix}. \tag{1.8}$$

Matrix (1.8) is called transfer matrix of scatterer i.

The propagation of the beam over a distance $d_{i,i+1}$ through free space between the i-th and the $i+1$-th elements is instead described by the matrix

$$F(d_{i,i+1}) = \begin{bmatrix} e^{ikd_{i,i+1}} & 0 \\ 0 & e^{-ikd_{i,i+1}} \end{bmatrix}. \tag{1.9}$$

For a sequence of membranes, the total transfer matrix is the product of the transfer matrices of the single elements.

For any one-dimensional optical system, no matter how complicated it is, the transfer matrix can always be read as

$$M = \begin{bmatrix} M_{11} & M_{12} \\ M_{21} & M_{22} \end{bmatrix} = \frac{1}{t} \begin{bmatrix} t^2 - r^2 & r \\ -r & 1 \end{bmatrix} \tag{1.10}$$

so that the complex amplitude transmissivity is $t = 1/M_{22}$ while the polarizability is $\zeta = -ir/t$ [cf. matrix (1.8)]. More details can be found in the Supplemental Material of Ref. [122].

In order to simplify the notation, from now on we will refer to intensity reflectivity and intensity transmissivity as simply reflectiviy and transmissivity (or reflection and transmission), respectively.

1.2 The optomechanical platforms

We consider N equidistant membranes arranged around the origin ($x = 0$) according to

$$x_j^0 = D\left(-\frac{1}{2} + \frac{j-1}{N-1}\right), \tag{1.11}$$

where x_j^0 is the position of the j-th membrane.

Each dielectric membrane has a polarizability ζ, and the distance between two adjacent membranes is $d = D/(N-1)$. This array of membranes behaves as a single optical discrete medium, whose overall length is D.

To mimic the quadratic defect in Refs. [89, 92] we push the membranes progressively towards the center of the ensemble, while keeping D fixed; it is pretty much like squeezing an accordion. The position x_j of element j is thus

$$x_j = x_j^0 - \frac{\alpha}{d}\left(\frac{D^2}{4} + {x_j^0}^2\right)\mathrm{sgn}(x_j^0), \tag{1.12}$$

where α is the dimensionless magnitude of the defect ($\alpha = 0$ is the equidistant configuration).

Eq. (1.12) shows that the separation between neighboring membranes decreases continuously, following a quadratic law, when proceeding from the sides of the array towards its center.

The defect α can not be arbitrarily large; there is a physical threshold above which membranes can not be pushed: Left membranes, that are being

pushed rightwards, and right membranes, that are being pushed leftwards, can not compenetrate each other. This constraint sets $\alpha = 2/[N(N-1)]$ and $\alpha = 4/[(N-3)(N+1)]$ as upper bounds in case of an even and odd number N of membranes, respectively.

The optomechanical setups that we are going to analyse in this chapter are depicted in Fig. 1.2.

The first platform includes a high-finesse Fabry-Pérot cavity (whose basic properties are reviewed in Appendix 1.D). Namely, we surround the above-mentioned array with two mirrors located at $\pm L/2$ with $L \gg D$, see Fig. 1.2a. Tuning L allows for modifications of the free spectral range $k_{FSR} = \pi/L$ of the bare optical cavity: A large L can make k_{FSR} smaller than the width of typical wave-vector window over which the optical response of the central array presents strong variations, which entails a higher sensitivity for operational procedures in k-space.

With the second platform, shown in Fig. 1.2b, we try instead to simulate a quasiperiodic photonic crystal as in Refs. [89, 92]. We position two arrays of N_m membranes with polarizability ζ_m; one is placed on the left of element 1 of the middle array and one on the right of element N. These membranes are separated from the central ensemble and from each other by a distance d_m. Unlike the previous platform, the dependence of the reflectivity R on the wave vector k of the impinging wave is not fixed. We will demonstrate in Sec. 1.4.1 that the optical response $T(k) = 1 - R(k)$ depends on d_m.

As in Refs. [122, 123], throughout this chapter we work in the so-called transmissive regime, illustrated in Appendix 1.A, where the central array is transparent to light and all N membranes are free to oscillate, independently, around their equilibrium positions.

As explained in the Introduction to this chapter, we quantify the optomechanical couplings by measuring the changes induced by these mechanical displacements (or oscillations) on the resonances of system, each resonance being identified by the corresponding wave vector $k = \omega_c/c$, where ω_c is the resonant frequency of the whole medium and c the speed of light in the vacuum. We apply the definition of $g_0^{(1)}$ and $g_0^{(2)}$, see Introduction, to the element j of the array:

$$g_j^{(1)} = c\frac{\delta k}{\delta x_j}x_0 \quad \text{and} \quad g_{j,j'}^{(2)} = c\frac{\delta^2 k}{\delta x_j \delta x_j'}x_0^2. \tag{1.13}$$

Notice that, unlike the Introduction, where a single mechanical element was considered, for a multiple set of oscillators also cross terms ($j \neq j'$) must be taken into account for the quadratic coupling. As a matter of fact, the displacement of an oscillator depends on the effect of a second distant membrane onto the cavity field.

For a single membrane in the middle of a cavity, the couplings are

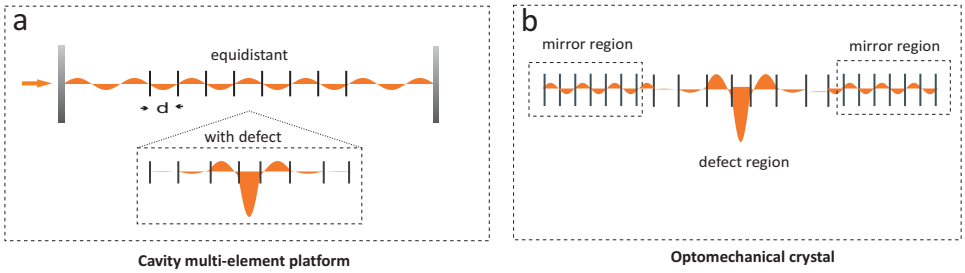

Figure 1.2: a) In an optical cavity, light propagates through an equidistant array of membranes in a transparent configuration. Localization of the cavity mode becomes possible when quadratic spacing defects are introduced (see inset). b) One-dimensional model of a quasiperiodic optomechanical crystal; the side regions effectively behave as dispersive mirrors while the central region hosts the quadratic defect.

$$g_0^{(1)} = \frac{2ck}{L}\frac{\zeta}{\sqrt{1+\zeta^2}}x_0 \quad \text{and} \quad g_0^{(2)} = \frac{2ck^2}{L}\zeta x_0^2. \tag{1.14}$$

The momentum transferred from a photon to a mechanical oscillator is enhanced by surrounding the oscillator with a couple of mirrors, since the same photon bounces back and forth several times, and hits the oscillator several times: This provides a heuristic explanation for the $1/L$ dependence in couplings (1.14).

For the rest of the chapter we will adopt the optimal value

$$g_0^{(1)} = \frac{2ck}{L}x_0 \equiv g \tag{1.15}$$

as a benchmark. It is obtained at unit reflectivity $R = 1$, that is $\zeta \gg 1$ [see Eq.(1.6)].

1.3 Array with engineered quadratic defect

In this section we perform a study of the first optomechanical platform presented in Sec. 1.2 and depicted in Fig. 1.2a. First, we analyze an array affected by a quadratic spatial defect in membrane positions; then, we put it inside a high-finesse optical cavity and study the optical response of the compound setup.

1.3.1 Transfer Matrix

We compute an analytical expression of the transfer matrix for an array with quadratic defect, see inset in Fig. 1.2a.

The transfer matrix for a membrane i with polarizability ζ_i is $M_i(\zeta_i) = \mathbb{I} + i\zeta_i(\sigma_1 + i\sigma_2)$, see also Eq. (1.8) for the matrix form. Here σ_1, σ_2 are Pauli matrices and $\mathbb{I}$ is the two-times-two identity matrix.

To mimic a typical experimental setup, all membranes are chosen to have the same polarizability ζ, that is $M_i(\zeta_i) = M(\zeta) \equiv M$ for any $i \in \{1, ..., N\}$.

In order to further simplify the notation we also dub $F_{i,i+1}$ the free-space matrix $F(d_{i,i+1})$ [see Eq. (1.9)] which describes the light propagation through the free space between membrane i and $i+1$; it can be written in a more compact form by using the Pauli matrix σ_3 as $F_{j,j+1} = e^{ik(x_{j+1}-x_j)\sigma_3}$, where x_j indicates the position of membrane j, see Eq. (1.12).

The transfer matrix for the entire array simply consists in an alternate sequence of M's and F's matrices:

$$M_{ar} = M \cdot \left(\prod_{j=1}^{N-1} F_{j,j+1} \cdot M \right). \tag{1.16}$$

The distance between neighboring membranes is $x_{j+1} - x_j = d_{j,j+1}$, and its correction to the equidistant configuration, where $d_{j,j+1} = d$ for every $j \in [1, \dots, N-1]$ (see Appendix 1.A), is

$$\mathrm{d}_{j,j+1} = \frac{d - \left(x_{j+1} - x_j\right)}{\alpha} \tag{1.17}$$

so that $d_{j,j+1} = d - \alpha \mathrm{d}_{j,j+1}$.

Since the defect is symmetric with respect to reflection about the center of the array ($x = 0$) the correction obeys $\mathrm{d}_{i,i+1} = \mathrm{d}_{N-i,N-i+1}$ for any positive integer $i \in \{1, \mathrm{Floor}[(N-1)/2]\}$.

Unfortunately, an analytical expression for matrix (1.16) valid for any defect magnitude can not be obtained. We can nevertheless consider the defect as a small perturbation $\alpha \ll 1$ to the equidistant configuration.

A Taylor expansion of $F_{j,j+1}$ around $\alpha = 0$ up to order $O(\alpha^2)$ leads to

$$F_{j,j+1} = (\mathbb{I} - ik\alpha \mathrm{d}_{j,j+1}\sigma_3) \cdot F + O(\alpha^2) \tag{1.18}$$

where matrix $F = e^{ikd\sigma_3}$ corresponds to the propagation of a plane wave with wave vector k over a free space distance d.

Inserting Eq. (1.18) in Eq. (1.16) and neglecting quadratic terms we get

$$M_{ar} = M \cdot \left(\prod_{j=1}^{N-1} (\mathbb{I} - ik\alpha \mathrm{d}_{j,j+1}\sigma_3) \cdot F \cdot M \right). \tag{1.19}$$

If we gather all linear terms in α, the transfer matrix becomes

$$M_{ar} = M_N + \alpha M_{corr} + O(\alpha^2). \tag{1.20}$$

The computational details can be found in Appendix 1.B: A key point consists in employing the Chebyshev's identity to find the N-th power of a unimodular matrix; the identity is reported in Appendix 1.C.

Matrix M_N is the transfer matrix for the equidistant configuration of the membranes ($\alpha = 0$). According to Refs. [122, 123] it has the following shape:

$$M_N = \begin{bmatrix} (1+i\chi)e^{i\mu} & i\chi \\ -i\chi & (1-i\chi)e^{-i\mu} \end{bmatrix}, \tag{1.21}$$

with an effective polarizability $\chi = \zeta U_{N-1}(a)$ and an effective phase μ satisfying

$$e^{i\mu} = \frac{1-\zeta U_{N-1}(a)}{(1-i\zeta)U_{N-1}(a) - e^{ikd}U_{N-2}(a)}. \tag{1.22}$$

Here, $a \equiv a(kd) = \cos(kd) - \zeta \sin(kd)$ and U_j stands for the Chebyshev polynomial of the second kind of degree j.

These results are shortly reviewed in Appendix 1.A; in this chapter we only provide the final expression.

The corrective term introduced by the quadratic defect, which is second term in Eq. (1.20), can be written as

$$M_{corr} = \begin{bmatrix} (1+i\xi)e^{i\nu} & i\xi \\ -i\xi & (1-i\xi)e^{-i\nu} \end{bmatrix}, \tag{1.23}$$

with first-order effective polarizability ξ given by

$$\xi = 4\zeta kb \sum_{j=1}^{[N/2]} \mathrm{d}_{j,j+1} \left(1 - \frac{\delta_{j,N/2}}{2}\right) U_{j-1}(a) U_{N-j-1}(a), \tag{1.24}$$

where $\delta_{j,N/2}$ is the Kronecker delta of j and $N/2$. The first-order effective phase ν in Eq. (1.23) is defined as

$$e^{i\nu} = \frac{(i+\xi)e^{-ikd}}{k\sum_{j=1}^{[N/2]} \mathrm{d}_{j,j+1}\left(\frac{\delta_{j,N/2}}{2} - 1\right)[C]_{22}}. \tag{1.25}$$

Function b in Eq. (1.24) is the same as a after an argument shift $kd \to kd - \pi/2$, [see Eq. (1.87)]. Matrix element $[C]_{22}$ is also provided in Appendix 1.B [Eq. (1.85)]. Inserting both Eqs. (1.21) and (1.23) in Taylor expansion (1.20), to first order in α matrix M_{ar} becomes

$$M_{ar} = \begin{bmatrix} (1+i\gamma)e^{i\lambda} & i\gamma \\ -i\gamma & (1-i\gamma)e^{-i\lambda} \end{bmatrix}, \tag{1.26}$$

with an effective polarizability and an effective phase described by

$$\begin{cases} \gamma = \chi + \alpha\xi, & (1.27) \\ e^{i\lambda} = \dfrac{1 - i(\chi + \alpha\xi)}{(1-i\chi)e^{-i\mu} + \alpha(1-i\xi)e^{-i\nu}}. & (1.28) \end{cases}$$

Notice that in the absence of defect ($\alpha = 0$) γ and λ reduce to χ and μ respectively, as it should be.

1.3.2 Numerical results

Despite expansion (1.19) being correct, the transfer matrix (1.20) is valid only for small magnitudes of the defect, on the order of $\alpha < 10^{-3}$. Unfortunately, for such tiny values of the defect the optical response of the array is almost identical to that one in the equidistant case ($\alpha = 0$). This statement is supported by Fig. 1.3(a), where the optical response for $\alpha = 9 \times 10^{-4}$ is depicted as a dashed blue curve, compared to the solid red curve which is the reflectivity for an array with $\alpha = 0$: The two lines practically overlap. In this case all $N - 1$ resonances lie within a transmissive band of width $2 \arcsin[\cos(\pi/N)/\sqrt{1+\zeta^2}]$.

In order to obtain more interesting as well as stronger deviations from the optical response of the equidistant case we need larger defects [for instance those illustrated in Figs. 1.3(b) and 1.3(c)]. For larger values of α keeping the linear terms as we did in the previous section is not enough; an exact evaluation of the transfer matrix (1.16) to any order of α is necessary.

Unfortunately, an expression for it is not an easy analytical achievement. We will therefore perform a numerical investigation, valid for any magnitude of α.

In Fig. 1.3 we consider an array of $N = 7$ membranes characterized by a polarizability $\zeta = -5$ and separated by a distance $d = 525$ nm for the equidistant configuration (depicted by the dashed blue line). From top to bottom the solid red line illustrates $\alpha = 9{\times}10^{-4}$, $\alpha = 5{\times}10^{-3}$, and $\alpha = 5{\times}10^{-2}$.

For a tiny defect, Fig. 1.3(a) shows that the reflectivity is pretty much the same as for $\alpha = 0$.

For increasing defects, we observe both a shift of the transmissive points (resonances) and a redistribution of their degeneracies. For $\alpha = 5 \times 10^{-3}$ a doubly degenerate resonance moves towards larger wave vectors $kd/\pi \sim 1.02$ in the first transmissive band gap whereas a further increase of α leads to the vanishing of all resonances but two, which merge in a doubly degenerate resonance lying in the zeroth transmissive band gap at $kd/\pi \sim 0.825$, see Fig. 1.3(c).

We now proceed to an analysis and a comparison of the linear as well as quadratic couplings with (and without) defect.

The engineered quadratic defect as implemented in the photonic crystals is particularly appropriate for enhancing both couplings [89, 92]. As a matter of fact, because of the quadratic character of the defect, the wave functions of the optical modes localized inside the array resemble Hermite polynomials and have Hermite-Gauss envelopes, similarly to what happens to the ladder of modes confined by a one-dimensional harmonic potential. The optical modes are indeed subjected to a local effective quasiharmonic

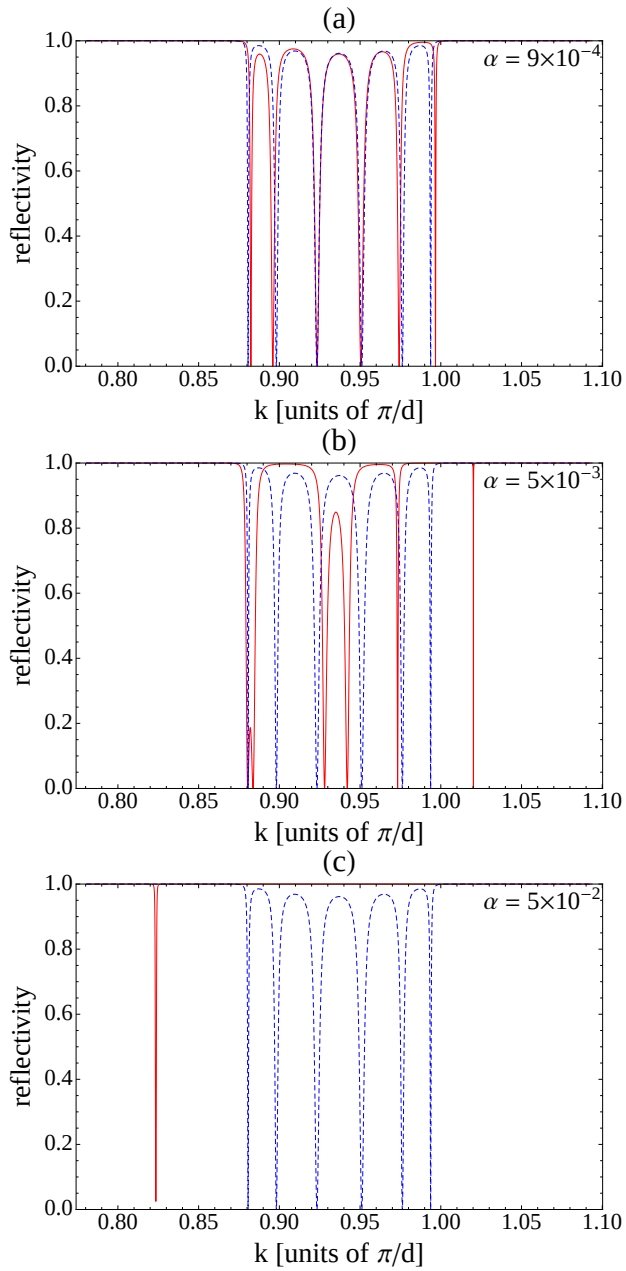

Figure 1.3: Optical response of an array of $N = 7$ membranes characterized by a polarizability $\zeta = -5$; the red continuous curves correspond to the array with defect, whereas the blue dashed curves correspond to the equidistant case. From up to down α is scanned through values 9×10^{-4}, 5×10^{-3}, and 5×10^{-2}. It is evident from panels (b) and (c) that for large magnitudes of the defect single resonances are pushed into the transmissive band gap.

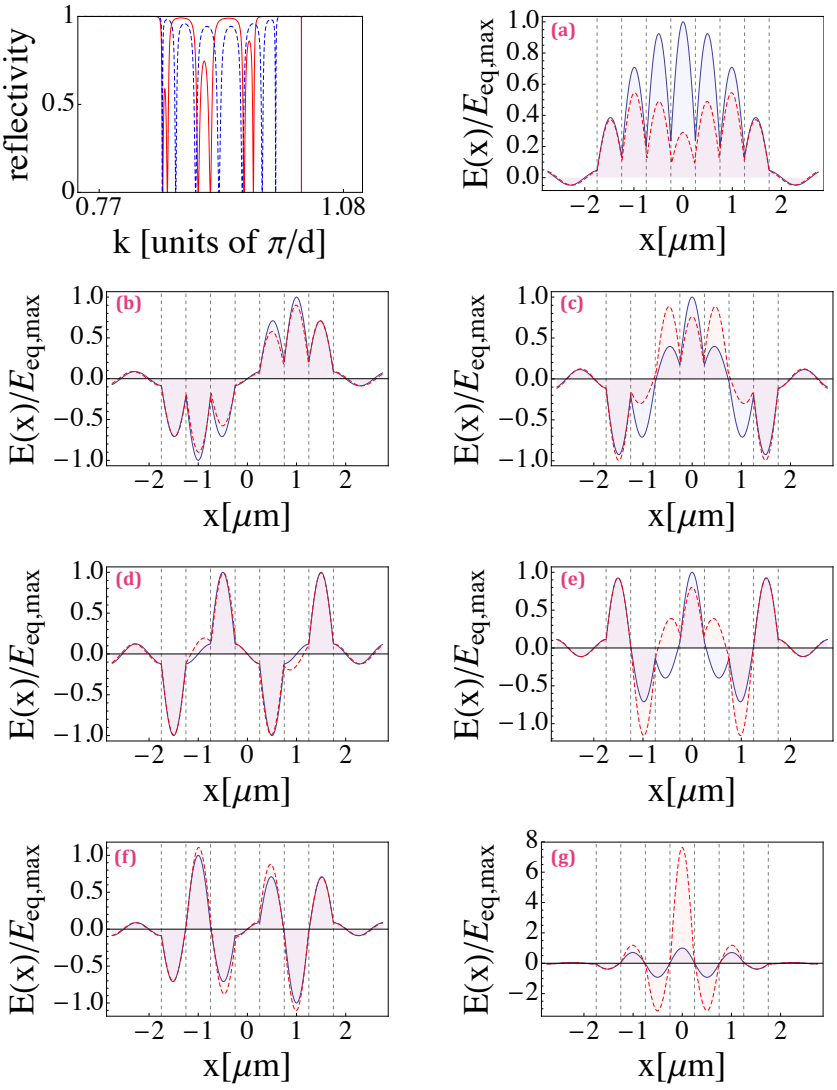

Figure 1.4: The uppermost left plot shows the dispersion relation for an array of $N = 8$ membranes with $\zeta = -4$. Both equidistant (dashed blue line) and defect (solid red line) cases with $\alpha = 3 \times 10^{-3}$ are illustrated. For each of the $N - 1$ resonances visible in the dispersion relation, we plot the electric field amplitude (normalized to the maximal value reached in the equidistant case) throughout the array. The plots are labeled in such a way that (a)-(g) correspond to the resonances in increasing order of k.

potential that closely follows the spatial defect itself and is therefore concave downwards.

Optical modes with higher energies will thus be more localized within the center of the quasiperiodic region. This is depicted in Fig. 1.4, where for a stack of $N = 8$ membranes all $N - 1$ resonances of the first transmissive

band are considered with $\alpha = 3\times10^{-3}$ (red curve) and $\alpha = 0$ (blue curve); for each membrane $\zeta = -4$. Panels (a) to (g) show the amplitude of the electric field $E(x)$ normalized with respect to the maximal value of the field itself for an equidistant array, $E_{\mathrm{eq,max}}$. Panel (g) indeed illustrates that the higher energy mode is the most localized (red curve), since it is pushed within the band gap similarly to what happens in Fig. 1.3(b).

An instructive analogy that can provide us with a heuristical comprehension of what is happening in Fig. 1.4[(b)-(g)] is the following: We can look at photons in this optomechanical platform as particles of mass m along a chain of connected one-dimensional boxes. It is known that the width W of each box defines the energetic spectrum of its inner modes as $E_n = n^2 \times \hbar\pi^2/(2mW^2)$ (in fact $k = n\pi/W$); namely, by shortening and increasing the separation between the walls of a box it is possible to tune the ladder of available energies.

In the "same" way, by shortening and increasing the separation between two neighboring membranes one can tune the ladder of available photonic intensities.

Since the linear coupling $|g_j^{(1)}|$ at membrane j depends on the local-field gradient (while the sign depends on whether the amplitude of the electric field is maximal on the left or right side of membrane j), field localization as the one shown in Fig. 1.4(g) allows for a dramatic enhancement with respect to the case $\alpha = 0$. Trapping modes in the transmissive band gaps is indeed a standard trick used by experimentalists to enhance couplings (see for instance the so-called photonic band-gap systems).

Let us now numerically look at linear and quadratic couplings.

1.3.3 The optomechanical couplings

We insert the array of Fig. 1.3 in a high-finesse optical cavity (the end mirrors have $\zeta_m = -20$ and the length of the cavity is $L = 6.3$ cm).

Looking at Fig. 1.3 we select a few notable resonances of the array without any surrounding cavity, and then look for nearby overall resonances of the compound system, in order to study the couplings for those wave vectors. We will see that the higher energy resonance in Fig. 1.3(b) at $kd/\pi \sim 1.02$ is the one that actually reaches the best coupling. According to the previous section, this is due to the fact that it lies in the band gap and is therefore localized [similarly to panel (g) of Fig. 1.4]: The normalized field amplitude at this resonance is depicted in Fig. 1.5.

The numerical results about the linear and quadratic couplings are illustrated in Fig. 1.6. Blue triangles correspond to the couplings at the blue resonance with smallest k in Fig. 1.3(a): According to Refs. [122, 123] this first transmissive point indeed maximizes the linear coupling for an equidistant array. Green dots, instead, correspond to the higher-energy resonance in presence of defect in Fig. 1.3(b) whereas red squares refer to the only sur-

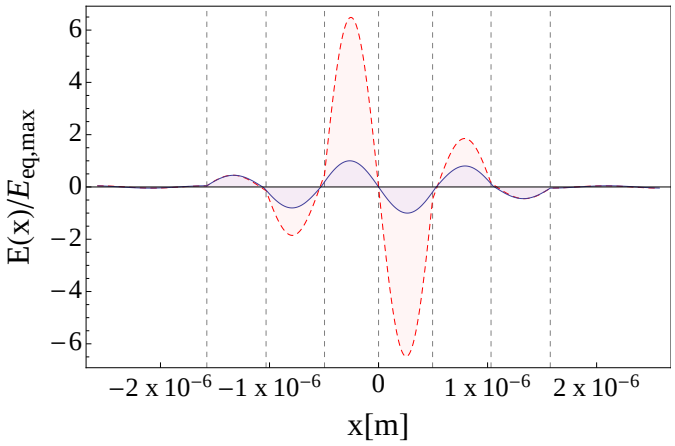

Figure 1.5: Electric field amplitude (normalized to its maximal value in the equidistant case) through the array for two cases where it is transparent to light: Without (blue solid line) and with (red dashed line) defect $\alpha = 5 \times 10^{-3}$. Although both situations show field localization, the introduction of defect dramatically enhances it.

viving degenerate resonances in Fig. 1.3(c): Since they lie in a band gap, these two last resonances allow for localization of trapped light in the middle region. That is why we have chosen them.

It is apparent from Fig. 1.6 that the defect improves both couplings by several orders of magnitude, as expected from the previous discussion.

The reference blue curve ($\alpha = 0$) shows an enhancement of 217, which is consistent with the scaling (1.67). In panel (b) the reference effective quadratic coupling is approximately 0.789×10^3 relative to the single element counterpart $g_0^{(2)}$.

Increasing a bit the defect pushes the higher energy resonance in the first energy band gap, see blue curve in Fig. 1.3(c), and improves the linear and quadratic couplings by factors of approximately 23 and 430 over the equidistant case.

A further increase of α makes all resonances vanish except two (degenerate) that are pushed in the zeroth energy band gap. Here the enhancements are 1.7 and 2.9 respectively.

Fig. 1.6 illustrates as a proof of concept that the desired enhancements in the couplings do indeed take place.

In the next subsection an experimental situation is considered, with realistic numbers, in order to demonstrate the feasibility of an experiment.

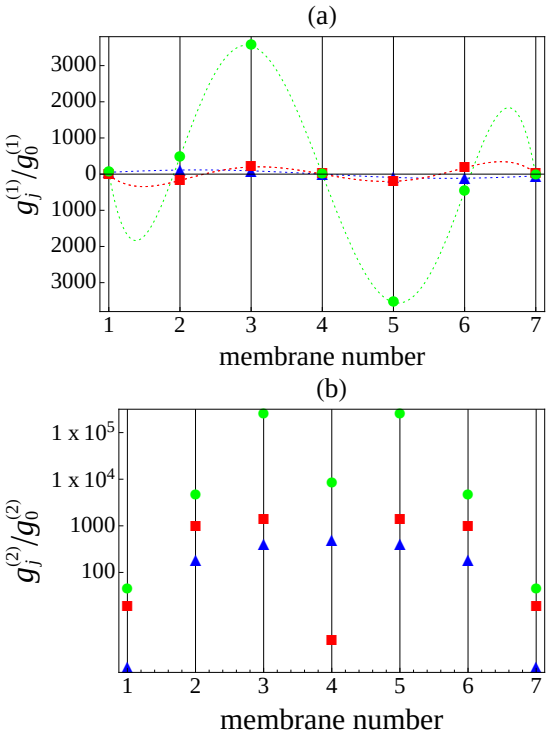

Figure 1.6: Optomechanical linear (a) and quadratic (b) coupling strengths. Here, an array of $N = 7$ membranes with $\zeta = -5$ in a cavity is considered. Separation between adjacent membranes is $d = 525$ nm. The end mirrors of the cavity have a polarizability $\zeta_m = -20$ and are separated by a distance $L = 6.3 \times 10^{-2}$ m, such that $L \gg d$. The three thin curves blue/green/red, correspond to $\alpha = 0$, and $\alpha = 5 \times 10^{-3}$ and $\alpha = 5 \times 10^{-2}$ respectively. For the numerical example considered, the introduction of the defect builds on the enhancement provided already by the access of the last transmission point by increasing $g^{(1)}/g_0^{(1)}$ by a factor of 23 and $g^{(2)}/g_0^{(2)}$ by a factor 434. Notice that we fixed $g^{(1)}/g_0^{(1)}$ for the equidistant case to the maximum value allowed, roughly equal to $\sqrt{2}/\pi\zeta^2 N^{3/2} \simeq 217$. For an even larger defect ($\alpha = 5 \times 10^{-2}$), only one resonance survives and it is moved into the zeroth energy band gap instead, with corresponding lower enhancement factors 1.73 and 2.94.

1.3.4 Experimental discussion

Let us consider an array of $N = 7$ membranes each characterized by a negative polarizability $\zeta = -5$ and a mechanical frequency $\omega_m = 2\pi \times 211$ kHz. The zero point motion of these membranes is $x_0 = 2.7$ fm.

When the immobile membranes are in the equidistant configuration and we consider the collective modes propagating along the array, according to Refs. [122, 123] the linear coupling at the first resonant point [see Eq. (1.66)

with $l = 1$] can achieve the value

$$g^{(1)}_{\mathrm{sin},1} \sim 2\pi \times 5\mathrm{kHz}.$$

This is already a great enhancement, far beyond the optimal coupling g for a single membrane placed at the center of a cavity, $g = 2\pi \times 24$ Hz [see Eq. (1.15)].

If a quadratic spatial defect is introduced, a further increase of the linear coupling is obtained. It can be as large as

$$g^{(1)} \sim 2\pi \times 117\mathrm{kHz},$$

which is a value comparable to typical mechanical resonant frequencies ω_m and optical cavity decay rate κ.

Concerning the quadratic coupling, instead, for a single membrane in the middle of a cavity it assumes very small values such as

$$g^{(2)}_0 \sim 2\pi \times 2 \times 10^{-6}\mathrm{Hz}.$$

Working in a regime where the array is completely transparent to light, the introduction of quadratic defect (which allows for field localization) can render the quadratic coupling as large as

$$g^{(1)} \sim 2\pi \times 1.4\mathrm{Hz}, \tag{1.29}$$

which is potentially observable in realistic optomechanical experiments.

Finally, we must point out that in realistic experiments several imperfections can occur and affect the performance of the array. For instance, real membranes are not infinitely thin but on the contrary they have a finite width. Also, there may be displacement problems and membranes may be misaligned with respect to cavity axis; this would eventually lead to the loss of photons, scattered outside the cavity mode, as well as absorption and other issues that are not taken into account in our simple theoretical model.

These effects are examined in detail in the Supplementary Material of Refs. [122, 123] for the case of an equidistant array. Although here we study an array with an engineered quadratic defect their analysis holds true in our case as well.

1.4 Quasiperiodic optomechanical crystal

In this section we perform a study of the second optomechanical platform presented in Sec. 1.2: An optomechanical photonic crystal.

As shown in Fig. 1.2b the crystal is modeled as a compound optomechanical medium composed of three well-defined parts: Two identical mirror regions and one defect region in between. Namely, we place a quasiperiodic array affected by a defect α in the middle of a cavity whose side mirrors

consist in two arrays of equidistant membranes. We call this cavity a "supercavity" with extended side mirrors.

To begin with, we study the empty supercavity by making use of the results of Refs. [122, 123].

1.4.1 *Supercavity*

The supercavity is not a classical cavity: Instead of two mirrors, we have to consider two arrays of N_m equidistant membranes characterized by a negative polarizability ζ_m and intermembrane distance d_m (see Fig. 1.2b). Nevertheless, the computational procedure to obtain its resonances and thus its free spectral range is the same as the one for a standard Fabry-Pérot cavity; which is why the latter is reviewed in Appendix 1.D.

The distance between the two mirror regions (the cavity length) is D.

The two mirror regions have an effective polarizability $\chi_m = \zeta_m U_{N_m-1}(a_m)$ and effective phase μ_m, see Sec. 1.3.

The transfer matrix of the supercavity is made up of a free space matrix (1.9) describing the propagation of the light inside the cavity plus two matrices (1.21) for the extended side mirrors:

$$\begin{aligned} M &= M_{N_m} \cdot F(D) \cdot M_{N_m} \\ &= \begin{bmatrix} (1+i\chi_m)e^{i\mu_m} & i\chi_m \\ -i\chi_m & (1-i\chi_m)e^{-i\mu_m} \end{bmatrix} \begin{bmatrix} e^{ikD} & 0 \\ 0 & e^{-ikD} \end{bmatrix} \begin{bmatrix} (1+i\chi_m)e^{i\mu_m} & i\chi_m \\ -i\chi_m & (1-i\chi_m)e^{-i\mu_m} \end{bmatrix}. \end{aligned} \tag{1.30}$$

As usually, the transmission is $1/|M_{22}|^2$:

$$T = \frac{1}{|e^{-i(kD+2\mu_m)}(1-i\chi_m)^2 + e^{ikD}\chi_m^2|^2}. \tag{1.31}$$

Fig. 1.7 illustrates the optical response of each side mirror (dashed blue line) of a supercavity ($N_m = 6$, $\zeta_m = -0.5$, $d_m = 768$ nm) as well as that one of the supercavity as a whole (red solid line). It shows that the reflectivity $R = 1 - T$ of the supercavity has two different kinds of resonances ($R = 0$): Those formed by the overlapping of common resonances of both side mirrors, lying thus in the transmission band, and those lying in the transmission band gaps for the single side mirrors (where they reach unity reflectivity).

The resonances of the first kind correspond to the roots of the Chebyshev polynomials of the second kind U_j ($kd/\pi \approx 0.29, 0.39, \ldots, 0.6$ etc.). Indeed, from Eq. (1.31) it is apparent that when $U_{N_m-1}(a_m) = 0$ (that is $\chi_m = 0$), T is exactly 1.

However, we are interested in the other resonance. Since they lie in the gap of the mirrors regions, the supercavity behaves as a high-finesse optical cavity, where each mirror regions has a very high polarizability ($\chi_m \gg 1$).

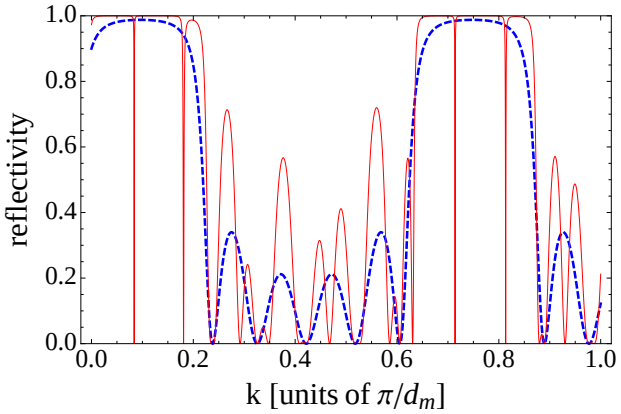

Figure 1.7: Transmission of an empty supercavity (solid red curve) and of a single extended side mirror (dashed blue curve) as a function of the momentum of the incoming plane wave. The momentum is expressed in units of $k_0 = 2\pi/\lambda$ with $\lambda = 10^{-6}$ m. Here the parameters of our cavity are $N = 6$, $\alpha = 5\times10^{-6}$, and $\zeta = -0.5$. Had we done a more realistic choice of the number of membranes, for instance N larger than 10, then we would have hardly been able to see the resonances.

A priori, these resonances should be like the Lorentzian peaks of a simple Fabry-Pérot resonator with length D, but with end mirrors having a polarizability χ_m; being their linewidth inversely proportional to χ_m^2 which is a strongly increasing function of N, these peaks become extremely sharp by increasing N_m (the dependence on ζ_m is instead quite complicated and has a sinusoidal character).

Since we want to analytically find these resonances, we shall work in a regime where the finesse F of the cavity is very high, which means $\chi_m \gg 0$:

$$F = \frac{k_{FSR}}{\kappa_k} = \frac{\pi}{D}\frac{D|\chi_m|\sqrt{1+\chi_m^2}}{\pi} = |\chi_m|\sqrt{1+\chi_m^2} \approx \chi_m^2. \tag{1.32}$$

κ_k is the linewidth of the cavity in the momenta space; according to Eq. (1.102) we have that for a simple cavity with length L and polarizability ζ of the two end mirrors

$$\kappa_k = \frac{\pi}{L|\zeta|\sqrt{1+\zeta^2}}. \tag{1.33}$$

In the high-finesse regime $1 - i\chi \approx i\chi$ because if the imaginary part of a complex number is much larger than the real one, then both the modulus and the argument of the complex number will be uneffected by the real part. Consequently

$$T = \frac{1}{\chi_m^4|1 - e^{-2i(kD+\mu_m)}|} \tag{1.34}$$

which implies that we have a resonance ($T = 1$) when

$$|1 - e^{-2i(kD+\mu_m)}| = \frac{1}{\chi_m^4} \approx 0 \tag{1.35}$$

or, in other terms, when

$$k^{(n)}D + \mu_m = n\pi \quad \text{with} \quad n \in \mathbb{Z}. \tag{1.36}$$

Let us notice that $k^{(0)} = 0$ since μ_m is exactly zero at k=0. This can be inferred from Eq. (1.22) by using the property that $a_m = 1$ at $k = 0$ and $U_j(1) = j + 1$ for any j.

Following this order, $k^{(1)}$ is the first positive resonance, $k^{(2)}$ the second positive resonance, and so forth. Of course this series covers the whole real axis but first, negative values of n mean negative $k^{(n)}$ which has no physical sense, and second, our analytical findings are valid only when $F \approx \chi^2 \gg 0$, that is inside the transmission band gaps.

After some algebraic computations, by using Eq. (1.22) we can express Eq. (1.36) as

$$\frac{U_{N_m-2}(a_m^{(n)})}{U_{N_m-1}(a_m^{(n)})} = \left[1 - i\zeta_m(1 - e^{i(k^{(n)}D-n\pi)})\right] e^{-ik^{(n)}d_m} \tag{1.37}$$

where $a_m^{(n)}$ is a_m at $k = k^{(n)}$.

Expression (1.37) can be further simplified:

$$\begin{aligned} \frac{U_{N_m-2}(a_m^{(n)})}{U_{N_m-1}(a_m^{(n)})} &= \frac{\sin((N_m - 1)\arccos(a_m^{(n)}))}{\sin(N_m \arccos(a_m^{(n)}))} \\ &= a_m^{(n)} - \sqrt{1 - a_m^{(n)2}}\cot(N_m \arccos(a_m^{(n)})). \end{aligned} \tag{1.38}$$

The cotangent of a purely-imaginary number z such that $|z| \gg 0$ satisfies $\cot z \to -i$. We can apply this property to Eqs. (1.37) and (1.38) in order to achieve

$$\tan(k^{(n)}d_m) = \zeta_m[(-1)^n \cos(k^{(n)}(d_m - D)) - 1] \tag{1.39}$$

which provides us with a simple equation for the resonances $k^{(n)}$, valid provided that

$$|\arccos(a_m^{(n)})| \ll \frac{1}{N_m} \quad \text{and} \quad |\zeta_m| > \frac{1 - \cos(kd_m)}{\sin(kd_m)}. \tag{1.40}$$

Looking at Eq. (1.36), we notice that adjacent resonances are not separated by a free spectral range π/D as we could expect for a Fabry-Pérot cavity (see Appendix 1.D), but there is an extra factor $\Delta_{(i,j)}$ which depends on the intermembrane distance d_m:

$$k^{(i)} - k^{(j)} = (i - j)\frac{\pi}{D} + \Delta_{(i,j)}, \tag{1.41}$$

with

$$\Delta_{(i,j)} = \frac{1}{iD}\log\left(\frac{1-\frac{e^{ik^{(i)}d_m}}{1-i\zeta_m}\frac{U_{N_m-2}(a_m^{(i)})}{U_{N_m-1}(a_m^{(i)})}}{1-\frac{e^{ik^{(j)}d_m}}{1-i\zeta_m}\frac{U_{N_m-2}(a_m^{(j)})}{U_{N_m-1}(a_m^{(j)})}}\right). \tag{1.42}$$

The extra factor goes to 0 at $d_m = 0$ (the argument of the logarithm reaches a unit value). This perfectly makes sense: $d_m = 0$ means that each extended mirror region collapses into a single mirror, so that the supercavity reduces to a standard cavity, where

$$k^{(i)} - k^{(j)} = (i-j)\frac{\pi}{D} \tag{1.43}$$

and the free spectral range is $k_{FSR} = \pi/D$ (cfr Appendix 1.D).

1.4.2 Array surrounded by supercavity

In the previous section, the optical response of an empty supercavity was analyzed. In this sections we place inside the supercavity an array affected by a quadratic defect, see Fig. 1.2b.

The optical response of the array was theoretically studied in Sec. 1.3.1 whereas a numerical analysis was performed in Sec. 1.3.2; see for instance Fig. 1.3.

As shown in Refs. [122, 123], within the framework of a multi-element optomechanical approach, the optimal regime to improve the optomechanical linear coupling is the transmissive regime (for a review of these results see Appendix 1.A).

In the transmissive regime the entire medium (array plus supercavity) is transparent to light, when the membranes do not move.

To reach this regime we need to tune the resonances of both the supercavity and the array in order to make them overlap and obtain an overall resonance. From this point of view the supercavity is a helpful device since its resonances are easily tunable: It is sufficient to vary the distance d_m between the single membranes, as shown in Eqs. (1.41) and (1.42).

The operational procedure to reach the transmissive regime is illustrated in Fig. 1.8: The first step consists in singling out one resonance of the array [panel (b)]; then we have to find a close resonance of the supercavity [panel (a)]; this latter resonance must lie in the band gap, and is typically much more narrow than the array resonance. Finally, by modifying d_m we tune the resonance of the supercavity so that it coincides with a resonance of the array [panel (c)].

The optomechanical crystal that we study in this section consists in a couple of extended side mirrors composed of $N_m + 1$ elements with intermembrane separation d_m, plus an array (affected by a defect α) containing $N_d = N - 2$ membranes. For simpleness' sake, we also assume $\zeta_m = \zeta$.

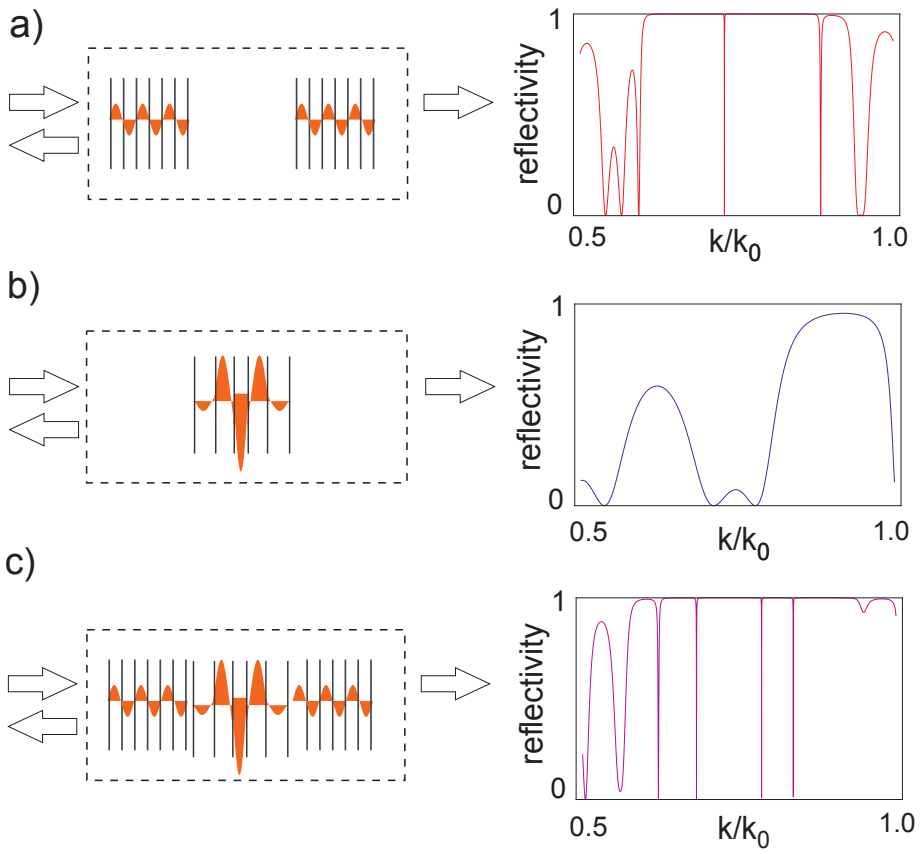

Figure 1.8: (a) Optical response of an empty supercavity as a function of the wave vector k (in units of $k_0 \equiv \pi/d$). (b) Under proper conditions, a membrane array affected by a quadratic defect can localize light. (c) The resonances of an optomechanical crystal are located close to the wave vectors for which both reflectivity plots (a) and (b) display zeros.

In the following, we chose $N_m = 20$, $N = 7$ and $\zeta = -0.5$, which corresponds to 20% reflectivity membranes. The magnitude of the quadratic defect is $\alpha = 10^{-3}$.

In Fig. 1.9 the first 8 resonant wave vectors of the supercavity are shown (dotted lines) as a function of d_m. The dashed horizontal lines, instead, represent the fixed resonances of the array.

The resonances of the supercavity are found by using Eq. (1.36) with $n \in [1, 8]$.

All dotted lines in Fig. 1.9 display irregular breaches of "fake" resonances; these transmission points correspond to the resonances which, in Fig. 1.7, lie between band gaps; these are resonances of the empty supercavity but with low finesse [let us not forget that Eq. (1.36) is true provided that the supercavity remains a high-finesse optical cavity].

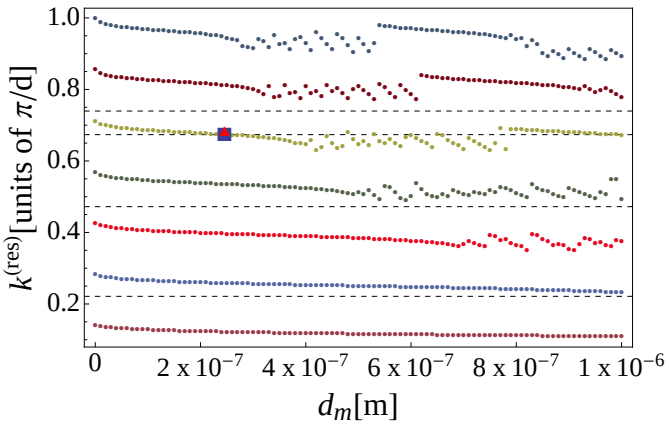

Figure 1.9: Procedure of tuning the resonances by varying d_m. The intersections of the empty supercavity resonances (dotted lines) with array resonances (dashed lines) are the common resonances. Only the first 7 resonances of the empty supercavity are plotted. Here, there is only one common resonance which is marked by a black square. The scattered plot regions indicate resonances which are located in the transmission bands (small cavity finesse); in these points the analysis is not valid. The red triangle is a true overall resonance; it is slightly shifted with respect to the common resonance because of the effective phase μ_m [see Eq. (1.22)]. The extended cavity mirrors are composed of 20 membranes whereas the array contains 7 membranes. The other parameters are $\alpha = 10^{-3}$, and $\zeta = \zeta_m = -0.5$.

Black square indicates a common resonance of the supercavity and the array whereas the red triangle marks the corresponding overall resonance of the crystal; it does not exactly coincide with the square: The slight shift is in fact introduced by the effective phase of the mirror regions μ_m [see Eq. (1.22) with $N_m \to N_m + 1$]. Nevertheless, the triangle is a good resonance, since even after the shift it is located inside the transmissive band gap, where the supercavity has a high finesse.

Using as a working point the overall resonance (red triangle in Fig. 1.9), we numerically investigated both linear and quadratic optomechanical couplings in the transmissive regime. Namely, we allowed the array membranes to vibrate around their equilibrium position while keeping the side mirrors in a frozen configuration.

The results are not as good as for the previous platform (Sec. 1.3.2): The linear coupling along the array has the sinusoidal shape characteristic of the transmissive regime, see Fig.1.6a but unfortunately we do not see a similarly large enhancement with respect to the equidistant configuration. The large values that we find are simply due to the localization of the field within a space of dimension D and do not depend on the defect α.

To exemplify this fact we consider a defective array ($\alpha = 10^{-3}$) composed of 7 membranes with $\zeta = -0.5$ with an intermembrane separation $d = 500$

nm. Let us place it in between two mirror regions consisting in 20 membranes with $\zeta_m = \zeta$: We have an optomechanical crystal made up by 47 membranes. Following the procedure depicted in Fig. 1.9, we tune the resonance by varying d_m until $d_m = 247$ nm. We reach an overall (linear) coupling of 1.98 MHz which is close to the value expected from the localization of the cavity mode within a one dimensional space of 3.5 μm [$(ck/D)x_0 = 2.9$ MHz]. Concerning the quadratic coupling, instead, the numerical estimate is 0.023 Hz whereas the analytical estimate for a cavity length of 3.5 μm is 0.025 Hz.

The lacking performance of the crystal can be explained by the cavity linewidth narrowing, an optomechanical effect that was already introduced in Refs. [122, 123]. The denominator of Eq. (1.66) can be thought of as an effective cavity optical lenght

$$D_{\text{eff}} = D - 2Nd\zeta \csc^2 \pi/N \sqrt{\sin^2 \pi/N + \zeta^2}. \tag{1.44}$$

The favorable scaling (1.67) holds true only when the ratio d/D is small or, in other words, when $D \approx D_{\text{eff}}$.

Unfortunately, this is the not case for the optomechanical crystal: For $d \ll D$ we have

$$D_{\text{eff}} = D + (2/\pi^2) d\zeta^2 N^3. \tag{1.45}$$

It approaches D as long as the quantity $(2/\pi^2)\zeta^2 N^3$ can be neglected. For the chosen parameters, the requirement is approximately $2(\zeta N/\pi)^2 < 1$; for $\zeta = -0.5$, an array composed of $N = 5$ already violates the condition.

1.4.3 Light mode structure

In this last section we briefly describe the light modes inside the cavity, induced by the presence of an engineered quadratic defect. A qualitative understanding of the localization of light within the defective region can help to design specific defect configurations with the purpose of optimizing both linear and quadratic optomechanical couplings.

For an electric field interacting with a fixed scatterer, the Helmoltz equation (1.3) can be recast in the form of a Schrödinger-type equation:

$$\left[-\frac{\hbar^2}{2m} \partial_x^2 + V(x) \right] E(x) = \mathscr{E} E(x) \tag{1.46}$$

with

$$\begin{cases} \mathscr{E} = \dfrac{\hbar^2}{2m} \left(\dfrac{\omega}{c} \right)^2, & (1.47) \\ V(x) = -\dfrac{\hbar^2}{2m} \left(\dfrac{\omega}{c} \right)^2 \delta\epsilon_r(x). & (1.48) \end{cases}$$

Here $m = \hbar^2/(2Jd^2)$ and the width of the lowest energy band is $4J$. Since the beam splitter is at the origin, see Eq. (1.4), the potential $V(x)$ vanishes at $x \neq 0$ and the electric field propagates through vacuum:

$$\left[\partial_x^2 + \left(\frac{\omega}{c}\right)^2\right] E(x) = 0. \tag{1.49}$$

For a plane wave, $E(x) = Ae^{ikx}$ (with A complex amplitude), we get the typical dispersion relation $\omega = kc$ for an electromagnetic wave traveling through vacuum.

An infinite photonic crystal can be exemplified by an infinite array of identical beam splitters, one for each membrane. We assume that membrane i is centered at position x_i. In that case $V(x)$ is the straightforward extension of potential (1.48):

$$V(x) = -\frac{\hbar^2}{m}\left(\frac{\omega}{c}\right)^2\left(\frac{\zeta}{k}\right)\sum_{i\in\mathbb{Z}}\delta(x - x_i). \tag{1.50}$$

In the absence of defect this is the analytical model for the well-known Kronig-Penney model:

$$H_0 E(\bar{x}, \bar{t}) = i\frac{dE(\bar{x}, \bar{t})}{d\bar{t}}, \tag{1.51}$$

with H_0

$$H_0 = -\partial_{\bar{x}^2} - \beta\sum_{i\in\mathbb{Z}}\delta(\bar{x} - \bar{x}_i). \tag{1.52}$$

Here $\beta = 2(\omega/c)^2(\zeta d/k)$.

In Eq. (1.52), a set of dimensionless coordinates

$$\bar{x} = \frac{x}{d} \quad \text{and} \quad \bar{t} = \frac{tJ}{h} \tag{1.53}$$

has been adopted. In Eqs. (1.53) J and h stand for the characteristic kinetic energy of the system and the Planck's constant, respectively.

Model (1.52) has an exact analytical solution [164]: It describes the formation of the band structure, similar to what has been analyzed in this chapter. The Kronig-Penney model is indeed a convenient framework to study light propagation along a one-dimensional photonic crystals. The basic idea of band structure for an infinite one-dimensional photonic crystal is briefly reviewed in Appendix 1.E while a short review of the Kronig-Penney model is available in Appendix 1.F.

From now on a well-formed band structure will be assumed.

For the purpose of looking at the dynamics in the lowest band, we follow Ref. [165] and expand the electric field $E(\bar{x}, \bar{t})$ in terms of first-band Wannier functions; Ref. [124] provides an analytical expression for them (see also Appendix 1.F).

Energy J can be, instead, extrapolated from Eq. (1.51) by employing the lowest-band Wannier functions.

If we introduce a defect α, Eq. (1.51) for the crystal assumes a potential term:

$$[H_0 + V^{(\mathrm{eff})}(\bar{x})]E(\bar{x},\bar{t}) = i\frac{dE(\bar{x},\bar{t})}{d\bar{t}}. \tag{1.54}$$

Namely, for a quadratic defect we can heuristically assume that the induced potential is $V^{(\mathrm{eff})}(\bar{x}) = \Omega\bar{x}^2$ with strength $\Omega = \alpha\beta$.

As already pointed out in Sec. 1.3.1, $V^{(\mathrm{eff})}$ is a parabola which is open downwards (inverted harmonic potential) and, as for a particle in a parabolic potential, solutions of Eq. (1.54) resemble Hermite-type polynomials.

More precisely, solutions for a particle in a parabolic potential (with positive curvature) in the discrete tight-binding limit contain Mathieu functions [165].

Following Ref. [165], for $4J/\Omega \gg 1$ we can distinguish two classes of energy eigenmodes, which are in agreement with the findings presented in this chapter.

On the one hand, for a low energy $E \lesssim 4J$, the modes are close to position eigenstates. Owing to the external harmonic trapping as well as the Bragg scattering induced by the membranes [Dirac-comb term in (1.52)] these modes are localized on either side of the potential induced by the defect.

On the other hand, in the regime $E \gtrsim 4J$ the modes are close to harmonic oscillator eigenstates and are located at the center of the (inverted) parabolic defect.

1.5 Conclusions

Recent theoretical studies [122, 123] on multi-element transmissive optomechanics show that, for an equidistant array of membranes inside a high-finesse cavity, extremely large values of linear coupling are possible; far beyond those allowed by the reflective regime.

In this chapter, motivated by these results as well as by new experiments with quasiperiodic photonic crystals [89, 92], we carried out a thorough analysis of two different optomechanical setups with the purpose of maximizing the linear and quadratic couplings.

First, we extended the theoretical investigations of Refs. [122, 123] by introducing a quadratic spatial defect in the array of membranes. We also studied the quadratic coupling and, as expected, we were able to further enhance both couplings.

Then, we tried to simulate a one-dimensional photonic crystal by inserting an array affected by quadratic defect between two equidistant arrays. Due to the typical small size of the crystal, further improvement of the couplings by employing this setup could not be achieved though.

Eventually, in the last section of this chapter, we drew an analogy between arrays of elements with an engineered quadratic defect and ultracold atoms trapped in a one-dimensional optical lattice to which we superimpose an inverted harmonic potential.

I would like to point out that the quadratic shape is not the only defect configuration allowing for the enhancement of optomechanical couplings. For instance, light modes can already be localized within a small volume by uniformly shifting the positions of a few membranes in the central region of the array (provided that the shift pushes at least one resonance into the band gap).

Introducing defects in order to trap field modes has many exciting perspectives; for example, one could think of a periodic spatial distribution of isolated defects along an array of dielectric elements. At least in principle, such superlattice of localized defects may allow for light-induced interactions between vibrational modes of membranes located around different defects.

Appendices

1.A Equidistant array in an optical cavity

In this Appendix, some results of Refs. [122, 123] are briefly reviewed.

The authors of the papers consider an equidistant array of N lossless membranes separated by a distance d and placed inside a high-finesse Fabry-Pérot cavity of length $L \gg Nd$, as shown in Fig. 1.2a. The end mirrors of the cavity have a polarizability $Z \gg 1$.

The main purpose of their work is to study the linear optomechanical coupling between the light mode of the cavity and the collective mechanical motion of the equidistant array.

By using the transfer matrix formalism, see Sec. 1.1, along with the Chebyshev's identity, see Appendix 1.C, the authors find an analytical expression for the transfer matrix M_N of the array.

Given the matrices introduced in Sec. 1.1, see Eqs. (1.8) and (1.9), the transfer matrix M_N for an equidistant array of N membranes is described by the matricial product $M(\zeta)\cdot F(d)\cdot M(\zeta)\cdot F(d)\cdots M(\zeta)$, where $M(\zeta)$ appears N times (one for each membrane).

In Refs. [122, 123], the authors adopt the trick of defining a unitary matrix M through the relation

$$\begin{aligned} &F(d/2)\cdot M(\zeta)\cdot F(d)\cdot M(\zeta)\cdot F(d)\cdots M(\zeta)\cdot F(d/2)\\ &=[F(d/2)\cdot M(\zeta)\cdot F(d)]^N\equiv M^N. \end{aligned} \tag{1.55}$$

Since M has a unitary determinant its N-th power is straightforwardly obtained thanks to Chebyshev's identity, see Appendix 1.C, and turns out to be

$$M^N=\begin{bmatrix}(1+i\chi)e^{i(kd+\mu)} & i\chi\\ -i\chi & (1-i\chi)e^{-i(kd+\mu)}\end{bmatrix}. \tag{1.56}$$

Here $\chi\equiv\zeta U_{N-1}(a)$, where $U_n(x)$ is the Chebyshev polynomial of the second kind and $a=\cos(kd)-\zeta\sin(kd)$. The phase μ instead satisfies and is defined by relation (1.22).

Matrix M^N is not exactly what we are looking for though, since it was obtained by adding on either side of M_N a matrix $F(d/2)$, as it can be seen in Eqs. (1.55).

We remove this contribution and get

$$M_N=F[\mu/(2k)]\cdot\begin{bmatrix}1+i\chi & i\chi\\ -i\chi & 1-i\chi\end{bmatrix}\cdot F[\mu/(2k)]. \tag{1.57}$$

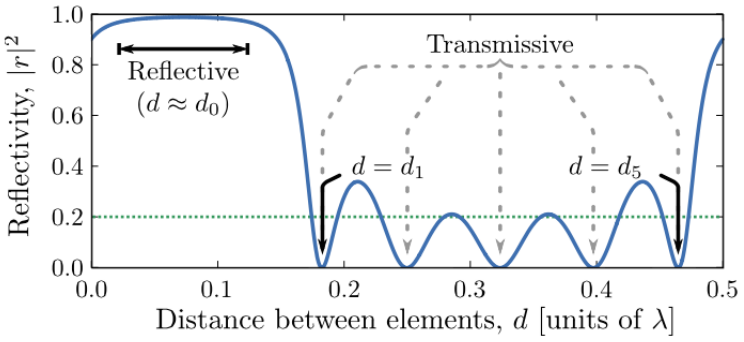

Figure 1.A.1: Dispersion relation for a stack of $N = 6$ lossless membranes. The dotted green line shows the optical response of a single element with $\zeta = -0.5$. There are $N-1 = 5$ transmissive point, with unit intensity transmissivity $T = 1-R$; the first and last resonances are marked as d_1 and d_5. An other important point is d_0: For $d \approx d_0$ the array is almost completely reflective. Source: Ref. [122].

Notice that the central matrix is the transfer matrix for a dielectric scatterer with a polarizability χ [cf. Eq. (1.8)]. It means that χ is the effective polarizability of the array as a whole discrete optical medium.

From matrix (1.57) an analytical expression for the transmission $T = 1/|M_{22}|^2$ and reflection $R = |M_{12}/M_{22}|^2$ is straightforwardly obtained.

For $N = 6$ membranes characterized by a reflectivity of 20% ($\zeta = -0.5$), Fig. 1.A.1 shows a plot of the reflectivtiy R in the first transmissive band (the optical response has a period of $\lambda/2$).

It is apparent from Fig. 1.A.1 that there are $N-1 = 5$ transmissive points, where the transmission $T = 1 - R$ reaches unity. In these points the entire array is transparent to light in the immobile configuration. It is remarkable that despite the single elements having only a reflectivity of 20% the reflectivity of their collection ranges from 0% to 99% (for $d \approx d_0$).The set of k-values between the first and last transmissive points is called transmissive band. The concept of band structure for an infinite ($N \to \infty$) one-dimensional photonic crystal is briefly reviewed in Appendix 1.E.

The equidistant array is then put inside a high-finesse optical cavity. In order to study the linear optomechanical coupling between mechanical vibrations and optical field one can work either in the reflective or in the transmissive regime:

- Reflective regime: One considers the whole array as a single completely reflective mirror and looks at the coupling of the mechanical center of mass to the light field.

- Transmissive regime: One considers the whole array as transparent to light and looks at the coupling of each membrane separately to the light field.

1.A.1 Reflective regime

The whole array is free to shift from the center. The authors of the papers consider a uniform displacement along the cavity axis, where x indicates the magnitude of the shift.

To obtain the resonances of the system (array plus cavity), they evaluate the transfer matrix as

$$M = M(Z) \cdot F(L/2 - x) \cdot M_N \cdot F(L/2 - x) \cdot M(Z) \tag{1.58}$$

where M_N is the matrix (1.57) for the equidistant array placed inside the cavity; matrices $F(x)$'s are given in Eq. (1.9) and $M(Z)$'s correspond to the end mirrors of the cavity [cf. Eq. (1.8)]. The constraint $M_{22} = 1$ must be required in order to have unit transmissivity:

$$e^{ikL} = \frac{e^{-i\mu}}{1 + i\chi}\left[i\chi\cos(2kx) \pm \sqrt{1 + \chi^2\sin^2(2kx)}\right]. \tag{1.59}$$

By using Eq. (1.59) one can find the linear optomechanical coupling of the center of mass of the array to the light field. We substitute $k \to k + \delta k$ and $x \to x + \delta x$ in Eq. (1.59). For a uniform spatial displacement neither μ nor χ change.

Around a resonance, the result is

$$L\delta k = \mp\left[2\chi\sin(2kx)/\sqrt{1 + \chi^2\sin^2(2kx)}\right]k\delta x. \tag{1.60}$$

The optical response is maximized by both $\sin(2kx) = \mp 1$ and maximal χ (that is at $d = d_0$). Under these conditions, the linear coupling is

$$g_{com} = g\sqrt{\frac{R}{N}} \tag{1.61}$$

where g is given by Eq. (1.15) and $R = \chi_0^2/(1 + \chi_0^2)$ [cf. Eq. (1.6)].

Eq. (1.61) tells us that the center-of-mass coupling is optimized for unit reflectivity $R = 1$ and that g_{com} can not be better than g.

As a consequence, if we want to enhance the linear optomechanical coupling by using a multi-element approach (getting a value larger than g), working in a reflective regime, where the entire array behaves as a single reflective mirror, is definitely not a good choice.

We will see in the next section that, instead, the transmissive regime is what we are looking for.

1.A.2 Transmissive regime

In the transmissive regime, when the N membranes are immobile the whole array is transparent to light: Each membrane interacts with and couples to the cavity field.

To reach this regime we have to work in one of the $N-1$ resonant points where $T = 1$. These points are dubbed $d_1, \dots, d_{N-1}$ (see Fig. 1.A.1 for $N = 6$) and are given by

$$d_l \equiv \frac{1}{k}\left\{\cos^{-1}\left[\cos(l\pi/N)/\sqrt{1+\zeta^2}\right] - \tan^{-1}(\zeta)\right\}. \tag{1.62}$$

Again, the array is inserted in a near resonant cavity.

Also in this case, the authors of Refs. [122, 123] use the transfer matrix formalism but unlike the previous section here they allow a single membrane, let us say the j-th membrane, to oscillate independently of the rest of the array.

We can choose as operational point any resonance d_l (the coupling will thus be l-dependent).

After some tedious computations, the authors find that the linear coupling (corresponding to the shift of the cavity resonance due to a displacement of membrane j when the array lies in the l-th transmissive point d_l) has a sinusoidal shape:

$$g_j^{(l)} \propto \sin\left(2l\pi\frac{j-\frac{1}{2}}{N}\right). \tag{1.63}$$

Namely, for the first and last transmissive points (d_1 and d_{N-1}), they get

$$\begin{aligned} g_j^{(1)} = g_j^{(N-1)} = -2\omega_c x_0 &\frac{\zeta\csc\left(\frac{\pi}{N}\right)\left[\sqrt{\sin^2\left(\frac{\pi}{N}\right)+\zeta^2}-\zeta\right]}{L - 2Nd\zeta\csc^2\left(\frac{\pi}{N}\right)\sqrt{\sin^2\left(\frac{\pi}{N}\right)+\zeta^2}} \\ &\times \sin\left(2\pi l\frac{j-\frac{1}{2}}{N}\right). \end{aligned} \tag{1.64}$$

Similar expressions hold true for the intermediate $N-3$ resonances.

In the transmissive regime all N elements are coupled to light. Under certain assumptions, it is possible to show that the dynamics of the system array plus cavity is properly described by a Hamiltonian where a single cavity mode is coupled to a single collective mechanical mode. Within this framework, the collective linear coupling strength at $d = d_l$ is

$$g_{\mathrm{sin},1}^{(l)} = \sqrt{\sum_{j=1}^{N}\left(g_j^{(l)}\right)^2}. \tag{1.65}$$

The role of the single-membrane couplings $g_j^{(l)}$'s is to select the sinusoidal profile of the collective mechanical motion coupled to light.

The analytical expression of the collective coupling is

$$g^{(l)}_{\sin,1} = g\sqrt{N}\frac{\zeta \csc(l\pi/N)\left[\sqrt{\sin^2(l\pi/N)+\zeta^2}-\zeta\right]}{L - 2Nd\zeta\csc^2(l\pi/N)\sqrt{\sin^2(l\pi/N)+\zeta^2}}. \tag{1.66}$$

For low reflectivity scatterers like atoms ($N|\zeta|/\pi \ll 1$) and comparatively large cavities ($d \ll L$), the collective coupling strength depends on $\sqrt{N}$ as $g|\zeta|\sqrt{N/2}$ [133, 162].

More importantly, instead, for $N|\zeta|/\pi \gg 1$ the collective linear coupling behaves as

$$g^{(l)}_{\sin,1} \approx \frac{\sqrt{2}}{\pi} g\zeta^2 N^{3/2}, \tag{1.67}$$

which, unlike the coupling in the reflective regime, can be order of magnitudes larger than the coupling for a single membrane in the middle of a cavity g.

Throughout Chapter 1 we operate in this transmissive regime.

1.B First-order Taylor expansion

In this Appendix it is shown how to reduce expansion (1.19) into the more compact form (1.20). We will first apply the procedure to an array composed of $N = 3$ and $N = 4$ membranes, and then extend the result to a generic number N.

1.B.1 Array of three membranes

For three membranes, Eq. (1.19) takes the simple form

$$M_{ar} = M \cdot (\mathbb{I} - ik\alpha \mathrm{d}_{1,2}\sigma_3) \cdot F \cdot M \cdot (\mathbb{I} - ik\alpha \mathrm{d}_{2,3}\sigma_3) \cdot F \cdot M \tag{1.68}$$

where, due to symmetry reasons, $\mathrm{d}_{1,2} = \mathrm{d}_{2,3}$.

Matrix (1.68) can be expaned up to order $O(\alpha^2)$ as

$$\begin{aligned} M_{ar} = M_3 - ik\alpha \mathrm{d}_{1,2}[&M \cdot \tilde{F} \cdot M \cdot F \cdot M \\ &+ M \cdot F \cdot M \cdot \tilde{F} \cdot M] \end{aligned} \tag{1.69}$$

with $\tilde{F} = F \cdot \sigma_3 = \sigma_3 \cdot F$ and $M_3 = M_{N=3}$ is the matrix for an array in its equidistant configuration ($\alpha = 0$): $M_3 = M \cdot F \cdot M \cdot F \cdot M$. Matrix M_N can be computed by following Refs. [122, 123], and is given by Eq. (1.21), see also Appendix 1.A.

We need now to estimate the terms within square brackets in Eq. (1.69). On this purpose, we first decompose $\tilde{F}$ as

$$\tilde{F} = F_{\frac{1}{2}} \cdot \tilde{F}_{\frac{1}{2}} \tag{1.70}$$

where as usually the first matrix in the product represents a monochromatic beam of wave number k that propagates over a distance $d/2$ through free space, see Eq. (1.9):

$$F_{\frac{1}{2}} = \begin{bmatrix} e^{ik\frac{d}{2}} & 0 \\ 0 & e^{-ik\frac{d}{2}} \end{bmatrix}, \tag{1.71}$$

whereas

$$\tilde{F}_{\frac{1}{2}} = F_{\frac{1}{2}} \cdot \sigma_3 = \sigma_3 \cdot F_{\frac{1}{2}}. \tag{1.72}$$

Then, we express the free-space matrix on the left side of $\tilde{F}$ as

$$F = F_{\frac{1}{2}} \cdot F_{\frac{1}{2}}, \tag{1.73}$$

and that on the right side as

$$F = \tilde{F}_{\frac{1}{2}} \cdot \tilde{F}_{\frac{1}{2}}. \tag{1.74}$$

We multiply the square brackets by the identity matrices

$$I = F_{\frac{1}{2}}^{-1} \cdot F_{\frac{1}{2}} \tag{1.75}$$

on the left side, and

$$I = \tilde{F}_{\frac{1}{2}} \cdot \tilde{F}_{\frac{1}{2}}^{-1} \tag{1.76}$$

on right side, in order to obtain the following expression:

$$M_{ar} = M_3 - ik\alpha \mathrm{d}_{1,2} F_{\frac{1}{2}}^{-1} \left[A \cdot A^{t2} + A^2 \cdot A^t \right] \tilde{F}_{\frac{1}{2}}^{-1} \tag{1.77}$$

with

$$A = F_{\frac{1}{2}} \cdot M \cdot F_{\frac{1}{2}}. \tag{1.78}$$

Notice that both matrices A and A^t are unimodular matrices.

1.B.2 Array of four membranes

For four membranes, Eq. (1.19) is

$$\begin{aligned} M_{ar} = {} & M \cdot (\mathbb{I} - ik\alpha \mathrm{d}_{1,2}\sigma_3) \cdot F \cdot M \cdot (\mathbb{I} - ik\alpha \mathrm{d}_{2,3}\sigma_3) \cdot F \\ & \cdot M \cdot (\mathbb{I} - ik\alpha \mathrm{d}_{3,4}\sigma_3) \cdot F \cdot M, \end{aligned} \tag{1.79}$$

where, again, for symmetric properties of the engineered defect, $\mathrm{d}_{1,2} = \mathrm{d}_{3,4}$.

A first-order expansion in the magnitude α of the defect leads to

$$\begin{aligned} M_{ar} = {} & M_4 - ik\alpha \mathrm{d}_{1,2}[M \cdot \tilde{F} \cdot M \cdot F \cdot M \cdot F \cdot M \\ & + M \cdot F \cdot M \cdot F \cdot M \cdot \tilde{F} \cdot M] \\ & - ik\alpha \mathrm{d}_{2,3}[M \cdot F \cdot M \cdot \tilde{F} \cdot M \cdot F \cdot M]. \end{aligned} \tag{1.80}$$

Matrix $M_4 = M_{N=4}$ represents the stack of four membranes in the absence of defect.

Following the previous section we get

$$M_{ar} = M_4 - ik\alpha F_{\frac{1}{2}}^{-1} \cdot [\mathrm{d}_{1,2}\left(A \cdot A^{t^3} + A^3 \cdot A^t\right) + \mathrm{d}_{2,3} \cdot A^2 \cdot A^{t^2}] \cdot \tilde{F}_{\frac{1}{2}}^{-1}. \tag{1.81}$$

After symmetrization of $A^2 \cdot A^{t^2}$:

$$A^2 \cdot A^{t^2} = \frac{A^2 \cdot A^{t^2} + A^2 \cdot A^{t^2}}{2}, \tag{1.82}$$

we get

$$\begin{aligned} M_{ar} = M_4 - ik\alpha \sum_{j=1}^{2} \mathrm{d}_{j,j+1} \left(1 - \frac{\delta_{j,2}}{2}\right) \\ \times F_{\frac{1}{2}}^{-1} \cdot [A^j \cdot A^{t^{4-j}} + A^{4-j} \cdot A^{t^j}] \cdot \tilde{F}_{\frac{1}{2}}^{-1}. \end{aligned} \tag{1.83}$$

1.B.3 Array of N membranes

For a stack of N membranes, the extension of Eqs. (1.77) and (1.83) yields

$$\begin{aligned} M_{ar} = M_N - ik\alpha \sum_{j=1}^{[N/2]} \mathrm{d}_{j,j+1} \left(1 - \frac{\delta_{j,\frac{N}{2}}}{2}\right) \\ \times F_{\frac{1}{2}}^{-1} \cdot [A^j \cdot A^{t^{N-j}} + A^{N-j} \cdot A^{t^j}] \cdot \tilde{F}_{\frac{1}{2}}^{-1}. \end{aligned} \tag{1.84}$$

Since both A and A^t are unimodular matrices, we can express their powers through the Chebyshev's identity, see Appendix 1.C.

After a bit of manipulations, it is possible to demonstrate that the two-times-two matrix $C = A^j \cdot A^{t^{N-j}} + A^{N-j} \cdot A^{t^j}$ is composed of the following elements:

$$\begin{aligned} [C]_{11} = [C]_{22}^* = 2\left[\mathbb{C}_{j-1}\mathbb{C}_{N-j-1} - \zeta^2 U_{j-1}(a)U_{N-j-1}(a)\right], \\ [C]_{12} = [C]_{21} = 4\zeta b U_{j-1}(a)U_{N-j-1}(a), \end{aligned} \tag{1.85}$$

where

$$\begin{cases} a(x) = \cos(x) - \zeta \sin(x), & (1.86) \\ b(x) = a(x - \pi/2) = \sin(x) + \zeta \cos(x), & (1.87) \\ \mathbb{C}_i(x) = \left(U_{i-1}(a(x)) - e^{ix}(1 + i\zeta)U_i(a(x))\right). & (1.88) \end{cases}$$

Notice that in Eqs. (1.85) we omitted the arguments in order to simplify the notation: a, b, and $\mathbb{C}_i$, stand for $a(kd)$, $b(kd)$, and $\mathbb{C}_i(kd)$, respectively.

In Eq. (1.84), matrix $F_{\frac{1}{2}}^{-1} \cdot C \cdot \tilde{F}_{\frac{1}{2}}^{-1}$ is

$$F_{\frac{1}{2}}^{-1} \cdot C \cdot \tilde{F}_{\frac{1}{2}}^{-1} = \begin{bmatrix} [C]_{11} e^{-ikd} & -[C]_{12} \\ [C]_{12} & -[C]_{11}^{*} e^{ikd} \end{bmatrix}. \tag{1.89}$$

When we insert it in Eq. (1.84) we get α-expansion (1.20).

1.C Chebyshev's identity

As stated in Ref. [166], the N-th power of a unimodular matrix can be simplified by the following matrix identity:

$$\begin{bmatrix} A & B \\ C & D \end{bmatrix}^{N} = \begin{bmatrix} AU_{N-1} - U_{N-2} & BU_{N-1} \\ CU_{N-1} & DU_{N-1} - U_{N-2} \end{bmatrix} \tag{1.90}$$

where the Chebyshev polynomials of the second kind $U_j = U_j[(A + D)/2]$ are given by:

$$U_N(x) = \frac{\sin\left[(N+1)\cos^{-1}(x)\right]}{\sin\left[\cos^{-1}(x)\right]}. \tag{1.91}$$

1.D Fabry-Pérot cavity

An empty Fabry-Pérot cavity is composed of two sufficiently good end mirrors (with polarizability $\zeta_m \gg 1$) separated by a certain distance L.

The corresponding transfer matrix is made up of a free-space matrix (1.9) for the propagation of the light inside the cavity along with two matrices (1.8) for the end mirrors:

$$\begin{aligned} M &= M(\zeta_m) \cdot F(L) \cdot M(\zeta_m) \\ &= \begin{bmatrix} 1 + i\zeta_m & i\zeta_m \\ -i\zeta_m & 1 - i\zeta_m \end{bmatrix} \begin{bmatrix} e^{ikL} & 0 \\ 0 & e^{-ikL} \end{bmatrix} \begin{bmatrix} 1 + i\zeta_m & i\zeta_m \\ -i\zeta_m & 1 - i\zeta_m \end{bmatrix}. \end{aligned} \tag{1.92}$$

According to Sec. 1.1, the transmission of the cavity is $1/|M_{22}|^2$:

$$\begin{aligned} T &= \frac{1}{|\zeta_m^2 e^{ikL} + (1 - i\zeta_m)^2 e^{-ikL}|^2} \\ &= \frac{1}{4\zeta_m^2 \left(\zeta_m^2 \sin^2(kL) - 2\zeta_m \cos(kL)\sin(kL) + 1 - \sin^2(kL) + \frac{1}{4\zeta_m^2} \right)}. \end{aligned} \tag{1.93}$$

In order to detect the cavity resonances, the denominator has to be equal to 1. Since $\zeta_m \gg 1$ we simplify the resulting expression by noticing that $1/(4\zeta_m^2) \approx 0$. We also rewrite $\cos(kL)$ as

$$\cos(kL) = \sqrt{1 - \sin^2(kL)} \tag{1.94}$$

so that $|M_{22}|^2 = 1$ reduces to

$$(\zeta_m^2 - 1)\sin^2(kL) + 1 = 2\zeta_m \sin(kL)\sqrt{1 - \sin^2(kL)}. \tag{1.95}$$

By squaring the members we get a quartic equation in terms of $\sin(kL)$, whose solution is

$$\sin^2(kL) = \frac{1}{1 + \zeta_m^2} \tag{1.96}$$

or

$$\sin(kL) = \pm\frac{1}{\sqrt{1 + \zeta_m^2}}. \tag{1.97}$$

This equation in general has two solutions in the interval $[-\pi/2, \pi/2]$:

$$kL = \pm \arcsin\left(\frac{1}{\sqrt{1 + \zeta_m^2}}\right), \tag{1.98}$$

and two solutions in the interval $[\pi/2, 3\pi/2]$:

$$kL = \pi \mp \arcsin\left(\frac{1}{\sqrt{1 + \zeta_m^2}}\right). \tag{1.99}$$

These four solutions are not unique, due to the periodicity of the sine function, and therefore we have to add a $2\pi n$-term with $n \in \mathbb{Z}$. Eventually, we should notice that not all the solutions are valid in our case, but only those for which the right member of Eq. (1.95) is positive.

As a result, in an empty cavity with sufficiently good side mirrors ($\zeta_m \gg 1$) the transmission spectrum consists of well-separated Lorentzian peaks (resonances) at momenta

$$k_n = \frac{n\pi}{L} \tag{1.100}$$

or frequencies

$$\omega_n = \frac{n\pi c}{L} \tag{1.101}$$

as well as linewidth, see [167],

$$\kappa_\nu = \frac{c}{2L|\zeta_m|\sqrt{1 + \zeta_m^2}}. \tag{1.102}$$

The distance π/L between two neighboring resonances is called free spectral range.

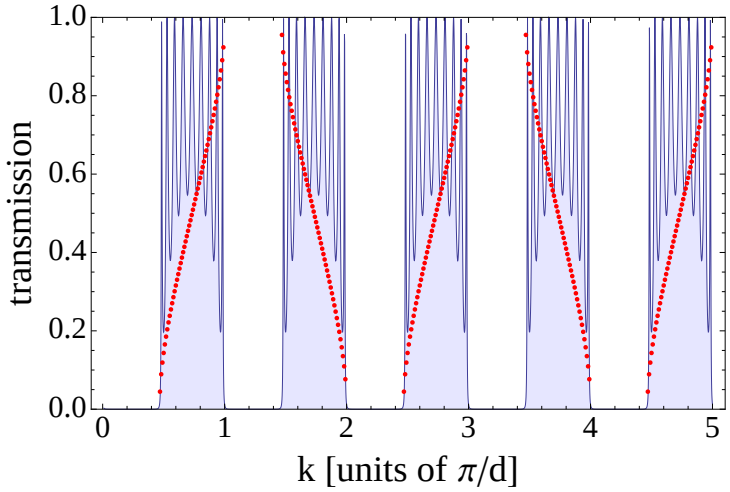

Figure 1.E.1: Optical response of an array of $N = 10$ membranes (blue solid line) in comparison with the band structure (red dotted line) of an infinite periodic photonic crystal. The polarizability of each membranes is $\zeta = -0.9$.

1.E Band Theory

An infinite array of membranes can be decomposed as a product of minimal moduli given by one membrane plus the free space up to the next membrane. The transfer matrix of each modulus is the product $M = M(\zeta)\cdot F(d)$ of a membrane with a polarizability ζ [matrix (1.8)] times a free-space matrix over a distance d [matrix (1.9)].

Matrix M is a unimodular matrix and has a real trace [168, 169]. The eigenvalues thus satisfy

$$\lambda_2 = \frac{1}{\lambda_1}. \tag{1.103}$$

If $|\lambda_1| = 1$ we can write it as

$$\lambda_1 = e^{iqd}, \tag{1.104}$$

with real quasi-momentum q. As $\lambda_2 = e^{-iqd}$, $\mathrm{Tr}\,[M \cdot F] = 2a = \lambda_1 + 1/\lambda_1 = 2\cos qd$, where a is function of kd as defined in Eq. (1.86).

It follows that

$$|\mathrm{Tr}\,[M \cdot F]| \leq 2. \tag{1.105}$$

If $|\lambda_1| \neq 1$, instead, $|\mathrm{Tr}\ [M \cdot F]| = |2a| = |\lambda_1 + \lambda_1^{-1}| = 2\cosh \kappa d > 2$ and the amplitude of the transmitted wave decreases in an exponential way as the membrane gets thicker.

Eq. (1.105) is a sufficient condition for propagating waves to exist.

Real wave vector k and Bloch wave vector q satisfy the dispersion relation

$\cos qd = a$:

$$q = \frac{1}{d}\arccos a = \frac{1}{d}\arccos\left(\cos kd - \zeta \sin kd\right). \tag{1.106}$$

For a repulsive potential ($\zeta < 0$) the top of the n-th band (with $n \in \mathbb{N}^0$) is located at $k = (n+1)\pi/d$ while the lowest band starts from a strictly positive k.

When the photonic crystal has a finite size every band turns into a so-called mini-band, which contains $N-1$ resonances (for simpleness' sake, in this chapter we refer to the mini-band as band). This can be observed in Fig. 1.E.1 where an infinite crystal band structure (red dotted line) is overlapped to the optical response of an array of $N = 10$ elements.

The band-gap width is proportional to $\exp(\zeta)$ whereas the band width to $\exp(-\zeta)$.

1.F The Kronig-Penney model

According to Sec. 1.4.3, light propagation along an infinite photonic crystal without defect is described by the following Schrödinger equation:

$$\left[-\frac{\hbar^2}{2m}\partial_x^2 + V(x)\right]E(x,t) = i\hbar\frac{dE(x,t)}{dt}. \tag{1.107}$$

The potential term $V(x)$ is provided by Eq. (1.50). As already stated, Eq. (1.107) is the Kronig-Penney model, where δ-walls are located at

$$x_j = \left(j - \frac{1}{2}\right)d \quad \text{with} \quad j \in \mathbb{Z}. \tag{1.108}$$

Following Ref. [124], Eq. (1.107) is solved by Bloch functions

$$\psi_{n,q}(x) = e^{iqx}u_{n,q}(x) \tag{1.109}$$

which in the interval $jd < x \leq (j+1)d$ change as

$$\psi_{n,q}^{(j)}(x) = e^{iqjd}\psi_{n,q}^{(0)}(x - jd). \tag{1.110}$$

Here q is the Bloch wave vector (quasimomentum). Between δ-walls the wave function obeys the Schrödinger equation in free space and only positive energies are allowed:

$$\mathscr{E} = \frac{\hbar^2 k^2}{2m} \geq 0, \tag{1.111}$$

with real wave vector $k = \omega/c$ [cf. Eqs. (1.47)] connected to q via Eq. (1.106).

For $-d/2 < x \leq d/2$

$$\begin{aligned}\psi_{n,q}^{(0)}(x) = A[&\cos(qd/2)\sin(kd/2)\cos(kx) + \\ &i\sin(qd/2)\cos(kd/2)\sin(kx)],\end{aligned} \tag{1.112}$$

where $|A|$ satisfies the renormalization constraint:

$$\int_{\text{cell}} |\psi_{n,q}(x)|^2 dx = \int_{-d/2}^{d/2} |\psi^{(0)}_{n,q}(x)|^2 dx = 1. \tag{1.113}$$

The result is

$$\frac{4}{d}|A|^{-2} = \sin(kd)^2 - \frac{\zeta}{kd}\sin(kd)(\sin(kd) - kd\cos(kd)). \tag{1.114}$$

The Wannier functions are then given by

$$w_{n,j}(x) = \frac{d}{2\pi}\int_{-\pi/d}^{\pi/d} e^{iqjd}\psi^{(0)}_{n,q}(x - jd)dq. \tag{1.115}$$

Usually, finding the convenient set of Wannier functions is not an easy task due to a "gauge freedom" in their definition [170].

Eventually, let us notice that Eqs. (1.107) and (1.50) explain why the polarizability has to be negative. For $\zeta > 0$ each mirror would behave as an infinite well (attractive δ-potential) so that Eq. (1.107) would admit, among its solutions, also bound states in the lowest energy band. A mirror can not trap photons though.

2
Cavity-enhanced transport of excitons

The capability of transporting quanta over large distances and in a very efficient way through a physical platform is a long-sought goal for experimentalists; improving the speed of the transport as well as its robustness against external perturbations is, for example, essential in quantum information theory [171–173] as well as experiments involving cold atoms and ions [54, 174–176] and organic semiconductor or solar cell physics [177–179]. A main obstacle for the effectiveness of the transport is the disorder in the system.

In the presence of disorder, in a one-dimensional chain of two-level systems the transmission of single-particle excitations is exponentially suppressed: Eigenstates are subjected to an Anderson-type localization [125] so that their transmission over a distance of N sites decays as $T \propto e^{-N}$. Here we show that the presence of an optical cavity, under certain conditions, helps overcome this exponential suppression and allows for ultrafast ballistic transmission.

In this chapter we study the transport of excitons through a chain of two-level systems surrounded by a high-finesse Fabry-Pérot cavity in the limit of strong collective light-exciton coupling. Unlike the weak coupling regime, where interaction between light and matter consists in single events of emission and absorption of photons, in the strong coupling regime light and matter can not be anymore considered as independent: The coupling of the excitons to the structured vacuum field of the cavity allows for the formation of a couple of polaritonic eigenstates. Due to their photonic fraction, polaritons are effectively endowed with a lighter mass (with respect to the bare excitons) and are thus less sensitive to the disorder in the medium. As a matter of fact, we report a dramatic enhancement in the transport efficiency which, at its worst, decays in an algebraic way $T \propto N^{-2}$. This tremendous improvement should be measurable for realistic parameters, also at room temperature [69, 73, 180–188].

As we shall see later, what couples to the vacuum field of the cavity is the symmetric superposition of the (localized) excitonic eigenstates: This highly entangled quantum state is known as collective Dicke state [189] and behaves as a uniformly delocalized exciton. Dicke states appear spontaneously in ensembles of many particles which are characterized by symmetric dynamics [190].

The results presented in this chapter, despite regarding exciton dynamics, were initially inspired by groundbreaking experiments on electronic transport through molecular semiconductors in the strong-coupling regime [180]. These experiments were performed in Strasbourg, in the group led by Prof. T. W. Ebbesen at I.S.I.S., and show that molecular materials are indeed (at least in principle) promising alternatives to standard semiconductors based on silicon [177, 191–197]: These new molecular materials are in fact less expensive and more versatile.

The theoretical model that we present can be applied to a variety of artificial systems inside a cavity, ranging from Rydberg lattice gases [198, 199], to polar molecules trapped in optical lattices [200, 201], to ions confined in a linear Paul trap [202, 203]. By employing these systems one may further extend the study to systems with multiple excitations and in higher dimensions which nowadays can not be efficiently analyzed via numerical methods [204–206]. This, in turn, may help better understand the transport in real media as well as the propagation of information in strongly correlated systems coupled to light [174, 175, 207, 208].

For large coupling [209] and reduced decoherence rate from spontaneous emission we will see that our model allows for instantaneous coherent transport of excitonic wave packets where an almost perfect efficiency ($T \propto 1$) may be reached.

This chapter is organized as follows. In Sec. 2.1 we introduce the model. In Sec. 2.2 we introduce the concept of polaritons and briefly review the basic features of these hybrid quasiparticles. In Sec. 2.3 we study a wave-packet scattering problem applied to our model and show both analytical (Sec. 2.3.1) and numerical (Sec. 2.3.2) results concerning the transmission of the wave packet through the transverse cavity. In Sec. 2.4 we include dissipation in the model; within the framework of the master equation formalism we study the steady-state current in the system under incoherent pumping from the left side of the cavity. Finally, Sec. 2.5 contains the conclusions.

In Appendix 2.A we solve the Schrödinger equation for the model and single out the polaritonic eigenstates. The solution is obtained by using both open and periodic boundary conditions. Appendix 2.B presents the analytical time-independent computations concerning the polaritons and the transmission of the wave packet through the cavity.

The results from this chapter have been collected in the following paper, published during the PhD:

J. Schachenmayer, C. Genes, E. Tignone, G. Pupillo,
Cavity-Enhanced Transport of Excitons,
Phys. Rev. Lett. **114**, 196403 (2015)

2.1 The model

We consider a one-dimensional chain composed of N two-level systems surrounded by a transverse single-mode optical cavity. Each two-level system can be mapped into a spin which can be either up ($|\uparrow\rangle$) or down ($|\downarrow\rangle$) depending on whether the two-level system is in the excited or in the ground state.

The Hamiltonian H of the system ($\hbar \equiv 1$) can be decomposed as $H = H_0 + H_{\text{cav}}$:

$$\begin{aligned} H_0 &= \sum_i \left[\omega_i \sigma_i^+ \sigma_i^- - J_i \left(\sigma_i^+ \sigma_{i+1}^- + \sigma_i^- \sigma_{i+1}^+\right)\right], \\ H_{\text{cav}} &= g \sum_i \left(\sigma_i^+ a + \sigma_i^- a^\dagger\right). \end{aligned} \tag{2.1}$$

The operators σ_i^+ and a^+ create a localized exciton on site i ($|\uparrow\rangle_i$) and a photon in the cavity mode, respectively. In the spinorial framework σ_i^+ is a raising operator. Since the atomic excitons we are dealing with have a size which is comparable to the interatomic separation, these are Frenkel excitons [210]: Extended wave functions resulting from hopping.

The first term in the Hamiltonian, H_0, corresponds to the energy of the free exciton (ω_i for an exciton located at site i) which is free to hop from one site to the next-nearest-neighboring ones at an energy cost of J_i. The site-dependent tunnelling rate is affected by disorder drawn from a normal distribution:

$$J_i = J + \delta J_i; \tag{2.2}$$

the standard deviation of such distribution is dubbed δJ. We neglect long-range contributions to the hopping since they are not large enough to suppress the disorder-induced localization [211]. Since for the system that we consider the wavelength of the dipole transition is usually much larger than the average spacing a between dipoles ($ka << 1$) we can neglect also retardation effect and inelastic interactions.

The cavity-related term H_{cav} is a typical Jaynes-Cummings Hamiltonian, with g being the single-exciton-single-photon coupling.

Here we only study the case when one excitation is present in the system: Either one exciton or one photon.

We will consider two different transport experiments: A scattering-type experiment and an incoherent-pumping experiment. In the first experiment we will look at the transmission T of an exciton wave packet traveling through the medium; in the second one instead we will look at the steady-state exciton currents propagating along the medium.

2.2 Polaritons

Let us consider the generalization of the system introduced in the previous section: N two-level systems embedded in a multimode cavity. The system is described by the Hamiltonian $H = H_0 + H_{\text{cav}}$ where the two terms are presented in Eq. (2.1). Here, however, we consider a non-flat photonic dispersion relation and we also explicitly insert the photonic creation energy:

$$\begin{aligned} H = &\sum_k \omega_p(k) a_k^+ a_k + \omega_0 \sum_j \sigma_j^+ \sigma_j^- - J \sum_j \left(\sigma_j^+ \sigma_{j+1}^- + \sigma_j^- \sigma_{j+1}^+\right) \\ &+ g \sum_j \left(\sigma_j^+ a_k e^{ikj} + \sigma_j^- a_k^+ e^{-ikj}\right). \end{aligned} \tag{2.3}$$

In Hamiltonian (2.3) there is no disorder: $\omega_i = \omega_0$ and $J_i = J$ for all sites.

In the absence of light-exciton coupling ($g = 0$), the dispersion relation $\omega_p(k) \equiv E_p(k)$ for the cavity mode and the dispersion relation $E_e(k)$ for the hopping exciton are

$$\begin{aligned} E_p(k) &= c\sqrt{k^2 + k_\perp^2}, \\ E_e(k) &= \omega_0 - 2J\cos(ak), \end{aligned} \tag{2.4}$$

where we took a unit spin-spin separation a; k and $k_\perp$ are the wave vectors along the cavity axis and along the perpendicular direction; notice that $k_\perp$ is constant. These two curves are illustrated in Fig. 2.1 (black dashed curves).

When the interaction with light is switched on ($g \neq 0$) the exciton and the photon coherently superpose and form a symmetric doublet of polaritonic modes with energies

$$\begin{aligned} E_L(k) &= \frac{1}{2}\left\{E_e(k) + E_p(k) - \sqrt{[E_e(k) - E_p(k)]^2 + 4G^2}\right\}, \\ E_U(k) &= \frac{1}{2}\left\{E_e(k) + E_p(k) + \sqrt{[E_e(k) - E_p(k)]^2 + 4G^2}\right\}, \end{aligned} \tag{2.5}$$

for the lower (L) and upper (U) polaritons, respectively. The collective coupling G is simply

$$G = g\sqrt{N}. \tag{2.6}$$

The polaritonic energies are plotted in Fig. 2.1 as red, solid curves. The magnitude of the avoided crossing at $k = 0$ is $2G$.

Notice that for the single-mode cavity (2.1) with photonic Hamiltonian $\omega_0 a^+ a$ if we neglect quadratic terms in the hopping constant J, then the polaritonic energies at $k = 0$ reduce to

$$\begin{aligned} E_L(k=0) &= \omega_0 - J - G \equiv \Omega_d, \\ E_U(k=0) &= \omega_0 - J + G \equiv \Omega_u, \end{aligned} \tag{2.7}$$

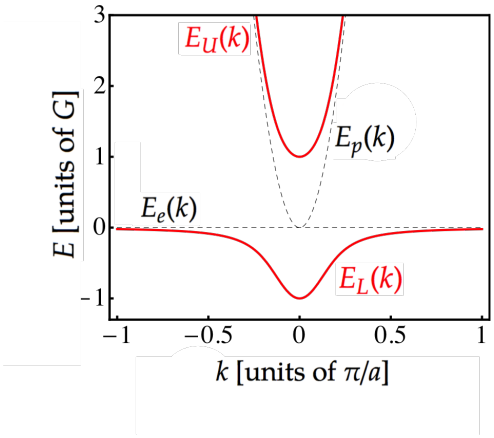

Figure 2.1: Polaritonic bands $E_L(k)$ and $E_U(k)$ compared with the free-photon and bare-exciton bands, $E_p(k)$ and $E_e(k)$ respectively; a is the spin-spin separation; G the collective light-matter coupling

and the polaritonic creation operators for the upper and the lower modes are given by

$$u^+ = \frac{a^+ + \sigma_0^+}{\sqrt{2}} \quad \text{and} \quad d^+ = \frac{a^+ - \sigma_0^+}{\sqrt{2}} \tag{2.8}$$

where

$$\sigma_0^\pm = \sum_{i=1}^{N} \frac{\sigma_i^\pm}{\sqrt{N}} \tag{2.9}$$

are the Fourier transforms $\sigma_k^\pm$ at $k = 0$ [see Eq. (2.50)]. They create and annihilate, respectively, a collective Dicke state. Results (2.7) and (2.9) are reviewed in Appendix 2.A

2.3 Wave-packet scattering

As shown in Fig. 2.2, via the Hamiltonian term H_0 in (2.1) we add M two-level systems to the left and to the right of the cavity, so that the total number of spins is $\mathcal{N} = N + 2M$.

For simplicity we consider a unit spin-spin separation. We neglect any site dependence of the on-site energy and define $\omega_i = \omega_0$ inside the cavity ($i = M+1, \dots, M+N$) while $\omega_i = \omega$ outside of the cavity. The detuning is $\Delta = \omega - \omega_0$. Moreover, in order to simulate an impedance-like mechanism, we introduce a different hopping constant $J_i = J'$ to hop in ($i = M$) and out ($i = M+N$) of the cavity.

In this scattering experiment, at an initial time $t = 0$ we consider a wave packet of excitons

$$|\psi(t=0)\rangle \propto \sum_{j=1}^{\mathcal{N}} e^{-iq_0 j} e^{-(j-j_0)^2/(4\delta^2)} |j\rangle \tag{2.10}$$

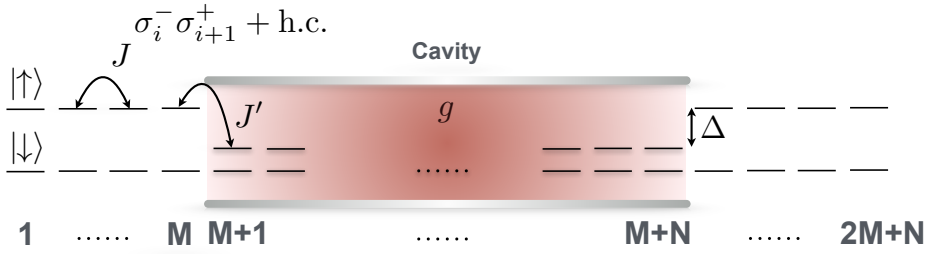

Figure 2.2: A chain of N two-level systems is embedded in a cavity and coupled to M sites to the left of the cavity and M sites to the right. An excitonic wave packet enters the cavity and propagates through it, from left to right; g is the exciton-photon coupling; J is the exciton hopping constant and is identical everywhere except the first and last site inside the cavity where $J = J'$ to allow for impedance effects.

with width δ (which corresponds to the standard deviation of the Gaussian envelope).

The wave packet is initially centered at site j_0, so that the initial distance from the (left) end mirror of the cavity is $\delta_x = M - j_0$.

In Eq. (2.10), $|j\rangle$ stands for a single excitation at site j:

$$|j\rangle \equiv |\uparrow\rangle_j \bigotimes_{i\neq j} |\downarrow\rangle_i \,. \tag{2.11}$$

We inject this wave packet from the left by kicking it with an initial quasi-momentum q_0. To provide a realistic example, we take $\delta_x = 20$, $\delta = 5$ and $q_0 = \pi/2$ [which entails a group velocity $v_g = 2J\sin(q_0) = 2J$; unit interspin distance a].

We want to check how large is the portion of wave packet that, under the right choice of parameters, can be transported almost instantaneously to the other side of the cavity upon scattering (cf. Fig. 2.3).

2.3.1 *Analytical results*

In the absence of coupling to light ($g = 0$), the wave packet propagates through the cavity via ordinary hopping: If it was centered about the left side mirror of the cavity, the wave packet would thus reach the right side mirror after a time N/v_g with $v_g = 2J$. We also have to take into account the initial displacement δ_x of the wave packet with respect to the cavity as well as its finite width δ; in this case the (long) time required to overcome the cavity is

$$t_l J = \delta_x + 2\delta + N/2. \tag{2.12}$$

In this section we want to show that, by switching the coupling g on, we can employ the collective polariton mode to make the wave packet hop N sites almost immediately.

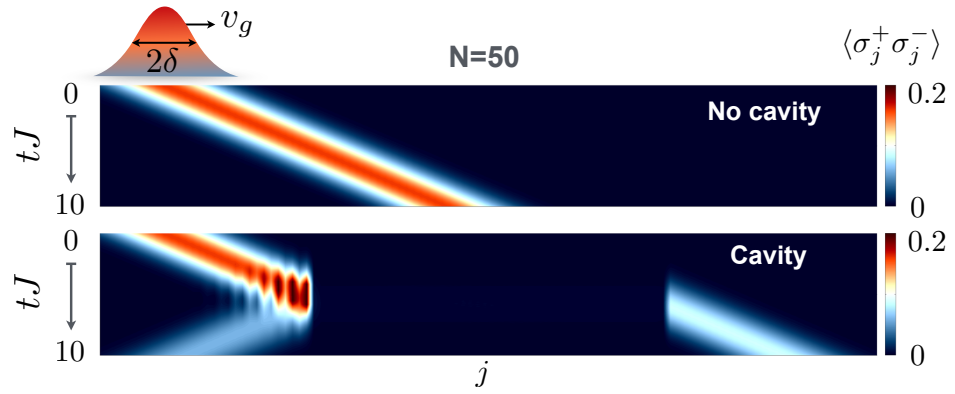

Figure 2.3: For $N = 50, M = 20, v_g = 2J, \delta = 3, \Delta = 69J, J' = 10J, g = 10J$, a large wave-packet fraction can be nearly instantaneously transferred to the right end of the cavity, on a timescale which is much smaller than the one required by ordinary site-by-site hopping $t \ll N/v_g$.

For large values of the coupling, the timescale t_c for an atomic excitation to couple in and out of the polariton mode can be very small, since

$$t_c \propto \sqrt{N}/g. \tag{2.13}$$

The transmission of the wave packet to the right side of the cavity can then take place on a ultrashort timescale $t_s \ll t_l$:

$$t_s J = \delta_x + 2\delta \tag{2.14}$$

which is dominated by the time required for the whole wave packet to enter the cavity plus the time to get completely out of it.

From a dynamical point of view, this problem can be dealt with as if it was an elastic-scattering process through the cavity, characterized therefore by a Bloch momentum q and a transmission function $T_q = |t_q|^2$ which establishes all the transmission properties of the medium [212–215] (the transmissivity t_q is the coefficient contained in the corresponding Lippmann-Schwinger scattering equation [216]). Following Ref. [214], we find an analytical expression for T_q (see Appendix 2.B):

$$t_q = -2i\frac{\beta}{1 + 2i\beta} \tag{2.15}$$

with

$$\beta = \frac{1}{2NJ\sin(q)} \sum_n \frac{|J'|^2}{\omega - 2J\cos(q) - \Omega_n}. \tag{2.16}$$

In Eq. (2.16), Ω_n indicates the n-th eigenvalue of the reduced Hamiltonian for the N sites which are coupled to the cavity mode, see Appendix 2.A.

The transmission T_q is obtained by inserting Eq. (2.16) in Eq. (2.15).

There are three resonant regions where perfect transmission ($T_q = 1$) can be reached:

- $\Delta \sim 0$: The transmission takes place via ordinary hopping. The width of this energy window (which contains $N-1$ resonances) is approximately $4J$, as expected from the kinematics of a bare exciton. Four hopping rates is indeed the typical bandwidth in the case of bare excitons allowed for hopping in a one-dimensional tight-binding model.
- $\Delta \sim -J - G$: At this energy, the resonance with the lower polariton is fully established. The transmission of the wave packet is then mediated by the collective lower polariton mode. The resonance has a Lorentzian shape, whose full width at half maximum depends on the number of spins embedded in the cavity, as $w = J'^2/(N|v_g|)$.
- $\Delta \sim -J + G$: The same as the previous point, but for the upper polariton.

Notice that the overall number of resonances (where ballistic scattering occurs) is $N+1$, which corresponds, as it should, to the initial number of degrees of freedom: N spins plus one photon.

The condition

$$g\sqrt{N} > \max[w, 4J, \kappa] \tag{2.17}$$

defines the strong coupling regime, where the three above-mentioned regions (lower polariton, hopping "band", upper polariton) are well separated in energy from each other. This regime corresponds to the region in momentum space where the photonic and excitonic energies are near resonance. Here the polaritonic energies are qualitatively different from the free-case ones. Far from this region, however, we enter the weak-coupling regime, where the lower and upper polaritons behave as free exciton and photon, respectively:

$$E_L(k) \approx E_e(k) \quad \text{and} \quad E_U(k) \approx E_p(k). \tag{2.18}$$

This is apparent in Fig. 2.1 where solid and dashed lines start overlapping.

In the following we concentrate on the strong-coupling regime, where close to a polaritonic resonance T_q is

$$T_q = \frac{1}{1 + \frac{N^2 J^2 \sin^2(q)}{J'^4}[\omega - 2J\cos(q) - \Omega_{u,d}]^2} \tag{2.19}$$

where pedices u, d indicate the upper and lower polaritons respectively.

The details concerning Eq. (2.19) are collected in Appendix 2.B.

2.3.2 *Numerical results*

We performed a numerical study of the time-dependent wave-packet scattering via exact diagonalization. We adopt as figure of merit the following time-dependent transmission:

$$T_{t'} = \sum_{j>M+N} \langle \sigma_j^+ \sigma_j^- \rangle_{t'}. \tag{2.20}$$

At a given time t', $T_{t'}$ measures the total number of excitations that have successfully passed through the cavity.

In this section we demonstrate that a large ultrafast transmission T_{t_s} [where t_s is given by Eq. (2.14)] is in fact possible if the exciton propagates as a dressed exciton via the polaritonic mode. This can happen provided that two conditions are fulfilled:

- The energy of the incoming wave packet $|\psi(t)\rangle$ has to be on resonance with the chosen polariton.
- Since the polariton peaks are characterized by a full width at half maximum w [see Eq.(2.102)], in order to pass through the cavity the wave packet has to fit into the energy window w. It means that in real space the wave packet has to be sufficiently large, on the order of N (the length of the cavity in units of spin-spin separation).

In order to fulfill the second condition we notice that w depend on J'; by properly tuning J' we can ensure that w does not depend on N anymore:

$$J' \propto \tilde{J}_N \equiv (2\ln 2)^{1/4} J \sqrt{\frac{N}{2\delta}} \tag{2.21}$$

Plot 2.4(a) illustrates $T_{t'}$ for different detunings. The red continuous curve describes the dynamics on a short timescale ($t' = t_s$) whereas the black dotted one on a long timescale ($t' = t_l$). We consider $N = 100$ two-level systems inside the cavity, each of them independently coupled to light via $g = 50J$. We also choose $J' = 4\tilde{J}_N$.

We detect the two polariton peaks, which as expected allow for unit transmission on the ultrafast timescale t_s. Their positions and widths follow the analytical time-independent result of the previous section (see also Appendix 2.B), depicted as a blue solid curve. The transmission T_{t_l} on a long timescale shows an additional peak at $\Delta \sim 0$. This central band, which actually contains $N - 1$ resonances, corresponds to regular hopping of the exciton through the cavity; here $T_{t_l} < 1$ (because of the backscattering at the cavity entrance owing to the impedance-like effect, $J' > J$). The red curve does not display this central small peak because t_s is a too short time for an uncoupled exciton to hop through the entire cavity.

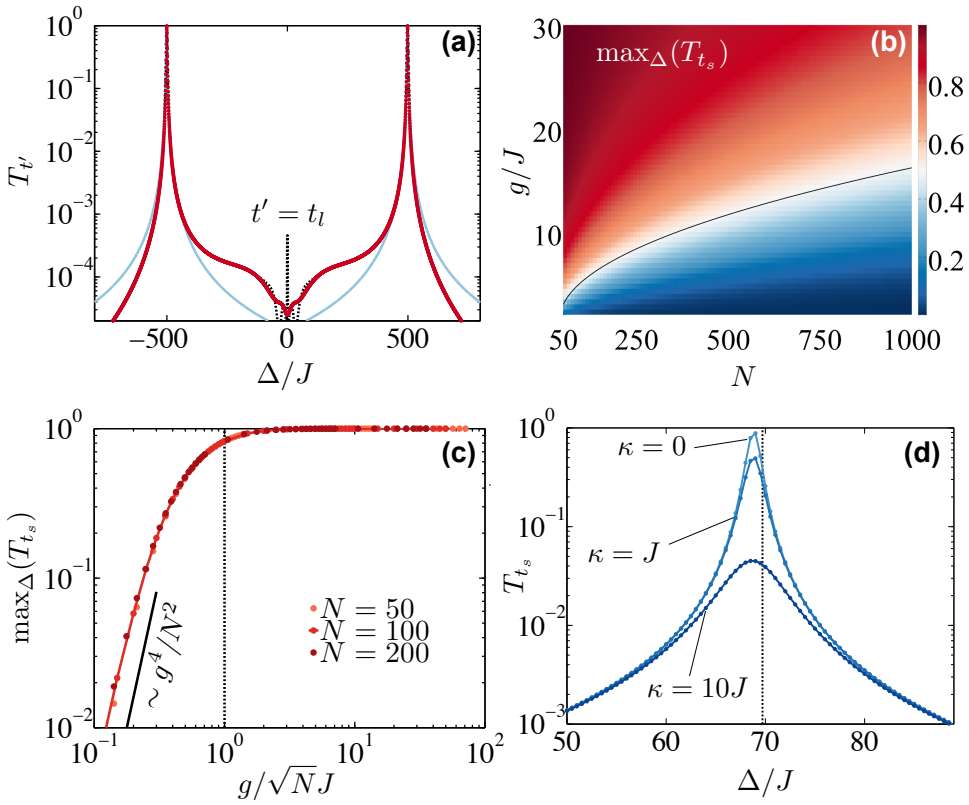

Figure 2.4: Transmission T_{t_s} within a ultrafast timescale t_s for a wave packet with $\delta = 5$, $\delta_x = 20$, $v_g = 2J$, and $J' = 4\tilde{J}_N$. Panel (a) compares the transmission on a long timescale T_{t_l} (dotted black curve) with the transmission on a ultrafast timescale T_{t_s} (solid red curve). We consider $N = 100$ sites inside the cavity, each of them coupled to light via $g = 50J$: Since we are in the strong collective coupling regime ($G = 500J$) the two polariton peaks are well resolved in momentum space; numerical computations agree with the analytical estimate of Sec. 2.3.1 (blue solid curve). T_{t_l} presents an additional peak at $\Delta \sim 0$, which corresponds to the propagation via regular hopping. Panel (b) illustrates how $\max_\Delta(T_{t_s})$ changes by varying g and N. For $g \propto \sqrt{N}$ (solid line) ultrafast transmission remains constant. Panel (c) shows the transition at $g \sim \sqrt{N}J$ (dotted vertical line) between inelastic- and elastic-scattering regime: For $N = 50, 100, 200$, optimal transmission $\max_\Delta(T_{t_s})$ is plotted as function of $g/\sqrt{N}$ in units of J. For small coupling values, $T_{t_s} \sim g^4/N^2$ (black solid segment). Panel (d) shows the impact of finite cavity decay κ on the resonance peaks; the other parameters are $N = M = 50$ and $g = 10J$.

Usually, for small values of g the scattering process on a ultrashort timescale t_s becomes inelastic since the exciton starts losing its photon-like properties, and $T_{t_s} < 1$. Despite this, as shown in Fig. 2.4(b), a large portion of the wave packet succeeds in passing through the whole cavity and reaches the M spins on its right. Fig. 2.4(b) illustrates the best possible T_{t_s} for a detuning Δ chosen in proximity of the upper polariton energy when both g and N are varied: Along the black solid curve $g \sim \sqrt{N}J$ the transmission T_{t_s} acquires a large constant value even for small couplings, which does not depend on the number of spins in the cavity.

The coupling $g = \sqrt{N}J$ traces the border between the inelastic and elastic-scattering regimes; indeed, beyond such value the exciton couples in and out the polariton mode in a timescale t_c which can be neglected compared to the other timescales, see Eq. (2.13). Fig. 2.4(c) shows T_{t_s} as a function of $g/\sqrt{N}J$ for $N = 50$, 100, or 200 spins in the cavity. We notice that the transmission follows a universal behavior, which is independent on N. As expected, for $g \ll \sqrt{N}J$ and within a ultrafast timescale t_s, the exciton wave packet has not enough time to completely reach the other side of the cavity, and T_{t_s} reaches finite but small values. By increasing g the fraction of wave packet which succeeds in passing trough the cavity increases, and $T_{t_s} \sim 80\%$ for $g = \sqrt{N}J$. Eventually, in the elastic regime $g \gg \sqrt{N}J$ we reach a ballistic transmission $T_{t_s} \sim 100\%$ over arbitrarily long arrays of spins.

Fig. 2.4(c) also shows that in this inelastic-scattering regime with a strong collective coupling (2.17) the transmission behaves as $T_{t_s} \sim g^4/N^2$: The transmission decreases only algebraically with the number of spins N. This results may have a positive impact when disorder is introduced in the system. As we shall see at the end of this section, the algebraic dependence will contribute to overcome the typical exponential suppression induced by the disorder.

Up to now we considered a perfect medium in a perfect cavity. However, a realistic cavity is characterized by a nonzero cavity decay rate $\kappa \neq 0$. A realistic resonator implies the leakage of exciton (and photon) population which, in turn, implies both a decrease of T_{t_s} and a broadening of the full width at half maximum of the Lorentzian transmission. Fig. 2.4(d) shows that, nevertheless, a large wave-packet fraction can be still transferred within a ultrafast timescale t_s for $\kappa \sim J$, which is a typical decay rate for experiments that employ polar molecules.

For $\kappa \gg 1$ the dynamics of the system can be described by an all-to-all flipping mechanism:

$$H_{eff} \approx \frac{2g^2}{\kappa} \sum_{i,j} \sigma_i^- \sigma_j^+ . \tag{2.22}$$

Hamiltonian (2.22) is obtained via an adiabatic elimination of the photonic mode; it allows for ultrafast transmission too. This situation can be exper-

imentally reproduced with trapped ions, which even without a cavity can display long-range interactions (see Appendix 2.C).

In the artificial media that we have analyzed so far there is no disorder. Realistic systems are of course not perfect; for instance, in organic semiconductors disorder affects both the spatial distribution and dipole orientation of molecules [site-dependent hopping (2.2)]. Moreover, the coupling strength of a single molecule to light is usually a fraction of the hopping energy scale ($g \sim 0.1J$).

Fig. 2.5(a) illustrates the results for the same system as in Fig. 2.4 with a fixed detuning $\Delta = g\sqrt{N} - J$, on resonance with the energy of the upper polariton; a disorder in the hopping is introduced, characterized by a standard deviation $\delta J = 0.2$ [see Eq. (2.2)]. In the absence of a cavity the transmission T_{t_l} within a long timescale t_l is exponentially suppressed, in agreement with Anderson-type localization [125]. The result is then a vanishing transmission for a large number of sites. For instance, for $N \gtrsim 400$ we get $T_{t_l} < 10^{-6}$. However, the introduction of a cavity and a nonzero coupling g can importantly modify the nature of the localized eigenstates of the system [217, 218]: Even weak couplings as $g = 0.05J$, $0.1J$, or $0.2J$ can lift the exponential suppression of the transmission so that a small but significant part of the wave packet can be transferred beyond the cavity, even for a very large number of site as $N = 10^4$. In the strong collective coupling regime (right of vertical lines) we notice that the universal algebraic behavior $T_{t'} \sim 1/N^2$ survives the disorder. Finally, notice that the presence of a small coupling has a remarkable effect also in the weak collective coupling regime (left of vertical lines): A constant transmission is possible (even though small), which is orders of magnitudes larger than the transmission without a cavity. These parameters are relevant, for example, for current experiments with organic semiconductors, where molecules have a typical dipole moment $d = e\times 0.75$ nm and a spacing $x = 3$ nm ($\delta x = 0.2$ nm), which entail a tunnelling rate $J = d^2/(4\pi\epsilon_0 x^3) \approx 0.03$ eV. Since for $N = 10^5$ molecules a Rabi splitting $\Omega_R \approx 1$ eV can be obtained, the coupling to light is indeed $g \approx 0.0016 \approx 0.05J$. Moreover, $\omega = 2\text{eV} \approx 70J$.

All the above-mentioned results keep being true also at higher dimensions d. On the one hand it is true that, for $d > 1$, relative improvement of T_{t_l} over the $g = 0$ case can get smaller and smaller as d increases, since it becomes easier for the wave packet to overcome an impurity along the path (whereas for $d = 1$ it can not be avoided). On the other hand, however, according to the Lieb-Robinson bound [172], a finite T_{t_s} without a cavity is impossible also for two or three dimensions whereas the cavity mode (and thus the polaritonic mechanism that we are presenting in this chapter) takes place in any dimension d. Since Anderson localization takes place also in two and three dimensions (below the mobility edge [219]), we still expect an exponential enhancement.

2.4 Incoherent pumping

In this case the dynamics of our model is studied via the master equation formalism. Within this framework, the time evolution of the density matrix ρ of the system follows

$$\dot{\rho} = -i[H, \rho] + \sum_{\alpha} \mathscr{L}_{\alpha}(\rho) \tag{2.23}$$

and all dissipative processes are taken into account by the terms

$$\mathscr{L}_{\alpha}(\rho) \equiv -\{L_{\alpha}^{\dagger} L_{\alpha}, \rho\} + 2L_{\alpha}\rho L_{\alpha}^{\dagger} \tag{2.24}$$

with L_{α} being the Lindblad operators.

We consider a variety of dissipative channels: Since the cavity is not perfect but photons can actually leak out, we account for the cavity decay by means of the operator $L_{\kappa} \equiv \kappa a/2$ with κ being the decay rate; we also include spontaneous emission from each two-level system via $L_{\text{sp.em.},i} \equiv \gamma_{\text{sp.em.}}\sigma_i^-/2$ (due for instance to radiative decay) as well as dephasing via $L_{\text{deph},i} \equiv \gamma_{\text{deph}}\sigma_i^+\sigma_i^-/2$. The latter is caused, for example, by the finite temperature which makes the system vibrate and induces fluctuations in level-spacing.

In this experiment, unlike the scattering-type one of Sec. 2.3, we do not couple external arrays to the cavity; we instead consider N spins inside a cavity and incoherently pump excitons to the leftmost site ($i = 1$) and remove them from the rightmost one ($i = N$). Within the master equation formalism these two operations can be taken into account by including two additional dissipative terms with Lindblad operators

$$L_P \equiv \sqrt{\frac{\gamma_P}{2}}\sigma_1^+ \tag{2.25}$$

for the incoherent exciton pumping, and

$$L_{\text{out}} \equiv \sqrt{\frac{\gamma_{\text{out}}}{2}}\sigma_N^- \tag{2.26}$$

for the exciton removal.

We are interested in the output current

$$\begin{aligned} I_{\text{out}} &= \text{tr}[n_e \mathscr{L}_{\text{out}}(\rho)] \\ &= \text{tr}[\sigma_N^+\sigma_N^- \mathscr{L}_{\text{out}}(\rho)] \end{aligned} \tag{2.27}$$

in the steady state.

In analogy to Ref. [220], since we are considering a steady state, $d\langle n_e\rangle/dt = 0$, that is

$$\frac{d}{dt}\text{tr}[n_e\rho] = \text{tr}[n_e\dot{\rho}] = 0. \tag{2.28}$$

By replacing $\dot{\rho}$ according to the master equation (2.23), one obtains

$$\begin{aligned} I_{\text{out}} = \; & \text{tr}[n_e \mathscr{L}_P(\rho)] + \text{tr}[n_e \mathscr{L}_{\text{out}}(\rho)] + \text{tr}[n_e \mathscr{L}_{\text{sp.em.}}(\rho)] \\ & + \text{tr}[n_e \mathscr{L}_{\text{deph}}(\rho)] - i\text{tr}[n_e[H, \rho]]. \end{aligned} \tag{2.29}$$

In the next section we analyze the dynamics of the system with both $\gamma_P > 0$ and $\gamma_{\text{out}} > 0$ in order to show how the steady-state current I_{out} behaves. As we shall see, I_{out} is tremendously enhanced via the coupling to the cavity mode.

2.4.1 *Numerical results*

Here we consider a spontaneous emission rate $\gamma_{\text{sp.em.}} = 0.04J$ as well as a dephasing rate $\gamma_{\text{deph}} = 0.9J$. The pump rate γ_P operates as a "voltage" for the exciton current: Fig. 2.5(b) depicts I_{out} as a function of γ_P. Contrary to previous studies on excitons traveling through multimode cavities [221], the plot shows that even realistically small exciton-light couplings ($g = 0.05J$, $0.1J$, $0.2J$) dramatically enhances I_{out} over the cavity-free current.

In agreement with the previous study on the wave-packet scattering, Fig. 2.5(c) illustrates that in the absence of a cavity I_{out} is suppressed in an exponential way as the number N of sites is increased; this is of course caused by the various dissipation channels as well as by the disorder. If a cavity is added, however, even for small values of g which can barely guarantee the strong collective coupling regime (as $g = 0.05, 0.1, 0.2J$), the exponential decrease is traded for an algebraic one, $g \propto 1/N^2$, exactly as for the ultrafast transmission T_{t_s} in the previous section.

Finally, in Fig. 2.5(d) the steady-state current I_{out} is plotted as a function of g for different rates κ of the cavity decay. We can see that I_{out} undergoes a sudden enhancement as g becomes larger than e specific value which is indicated by vertical lines; this values indicates the coupling beyond which G exceeds all other energy scales and we enter the strong collective coupling regime. Clearly, the larger is κ the larger has to be the threshold coupling in order to compensate a more effective exciton loss from the cavity (see $\kappa = 10$ in the plot).

2.5 Conclusions

In this chapter, we demonstrated that the presence of an optical cavity enhances in a tremendous way the transport of excitons along a chain of two-level systems. We studied this transport problem through two different approaches.

In Sec. 2.3 we dealt with a wave-packet scattering experiment where a wave packet, starting from a spin chain on the left side of the cavity, enters the cavity and propagates through it until reaching the other side. Our

figure of merit was the time-dependent transmission $T_{t'}$, which measures the overall number of excitations that reach the right side of the cavity. We have numerically shown that a ballistic transmission on a ultrafast timescale is possible via the polaritonic modes, which is much faster than the usual transmission via regular hopping. We also provided an analytical expression for the time-independent transmission close to the polaritonic resonances (either lower or upper) in the strong coupling regime, that is when they are well resolved.

In Sec. 2.4 we introduced several dissipative channels in our problem (cavity decay, disorder in hopping, spontaneous emission, dephasing) and we looked at the steady-state current under an incoherent pumping process where an exciton is injected on the leftmost site of the cavity. Everything is carried out numerically, within the framework of the master equation formalism. The results, also in this case, show that the current is incredibly enhanced by the coupling of the exciton to light ($g > 0$). More importantly, we demonstrated that in the strong collective coupling regime the current only decays algebraically with the number of sites as $1/N^2$ instead of showing the exponential suppression typical of Anderson-type localization [125].

The findings collected in this chapter are relevant for organic semiconductors at room temperature, which being affected by disorder can not efficiently conduct; the presence of a transverse cavity may indeed increase their conduction properties by several orders of magnitude. Of course, also the performances of artificial media are strongly ameliorated; for instance, systems made up of Rydberg atoms, cold ions at sub-mK temperatures, or polar molecules, would certainly benefit from our discoveries. While parameters for the organic media are reported in the main text, examples of parameters concerning these last systems can be found in Appendix 2.C.

This work has many exciting perspectives. It paves the way towards new studies on strong coupling. For instance, one could extend the problem to multiple excitations which can interact with each other, and try to understand whether the strong coupling regime can induce a propagation on ultrashort timescales of both classical and quantum correlations [207, 208, 222].

From a numerical point of view, at least in one dimension, an answer might be provided by an adjusted density matrix renormalization group algorithm [204–206]. Higher dimensionalities are tougher; in order to conduct a proper investigation at $d > 1$ one should abandon the idea of using a numerical approach and try instead to simulate the problem by employing experimental setups [223].

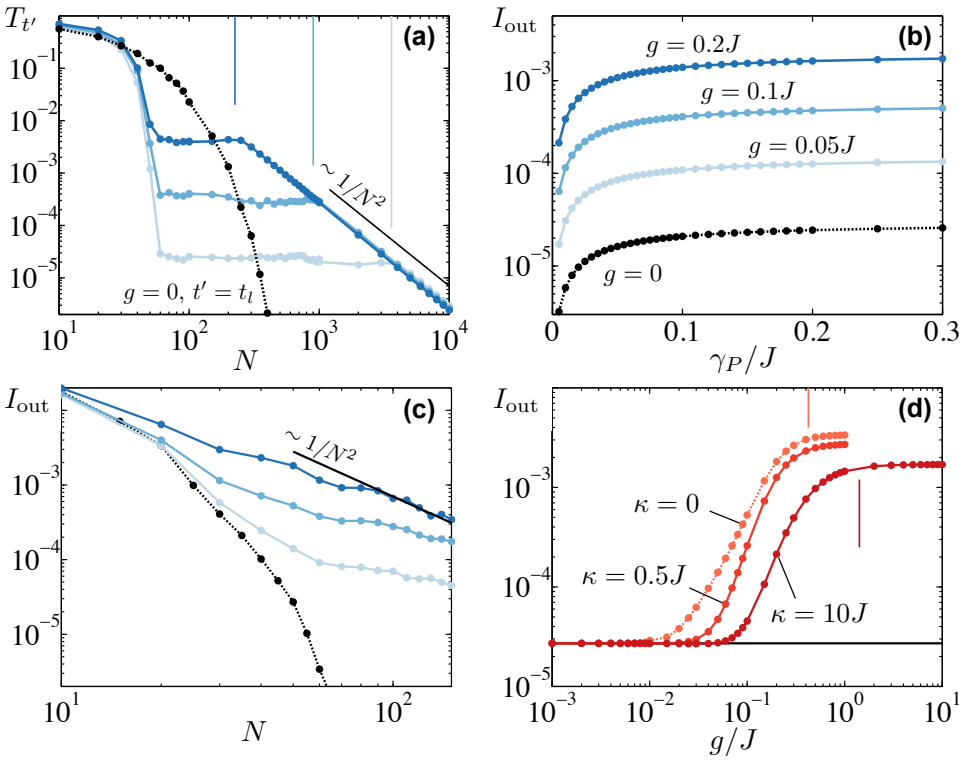

Figure 2.5: In panels (a), (b), and (c) the blue solid lines indicate realistic values of coupling $g = 0.05J, 0.1J, 0.2J$ (the darker the blue the larger the value). Panel (a) presents both transmissions T_{t_s} and T_{t_l} as function of N. As in Fig. 2.4(a), we tune the wave-packet energy on resonance with the energy of upper polariton; we show an average over 200 disorder realization in J_i, characterized by the same standard deviation $\delta J = 0.2J$. The black dotted curve corresponds to T_{t_l} in the absence of a cavity; for $g > 0$ we only plot the ultrafast transmission T_{t_s}. It is again apparent the exponential decay of T_{t_l} with N. On the contrary, T_{t_s} gets a constant value in the weak coupling regime and then decays algebraically as $1/N^2$ (see black solid segment) for couplings above $G = 3J$ (vertical lines). Panels (b), (c), and (d) illustrate the response of the system under incoherent pumping in presence of spontaneous emission ($\gamma_{\text{sp.em.}} = 0.04J$), dephasing ($\gamma_{\text{deph}} = 0.9J$), and disorder ($\delta_J = 0.2J$), where a single disorder realization is taken into account. In panel (b) the steady-state current I_{out} is depicted for 50 sites inside the cavity and in presence of dissipation. The incoherent pumping rate is $\gamma_P = 0.5J$ whereas $\gamma_{\text{out}} = 2J$. The presence of a cavity ($g > 0$) induces a large increase in the current. In plot (c) the exponential Anderson-type localization ($g = 0$) is overcome thanks to the coupling to light: In the weak coupling regime the decay is subexponential, while in the strong coupling regime I_{out} decays algebraically; it is illustrated by the black solid segment. In panel (d) the current I_{out} is plotted against g for $N = 50$ sites and a few different values of cavity decay κ. Vertical lines indicate the thresholds of the strong coupling regime: $g\sqrt{N} = 3J$ and $g\sqrt{N} = 10J$, respectively.

Appendices

2.A Schrödinger equation

In this Appendix we look for the $N+1$ eigenvalues Ω_n of the Hamiltonian (2.1) where we explicitly introduce the photonic energy ω_0:

$$\begin{aligned} H = \omega_0 a^+ a + \omega_0 \sum_{i=1}^{N} \sigma_i^+ \sigma_i^- - J \sum_{i=1}^{N-1} \left(\sigma_i^+ \sigma_{i+1}^- + \sigma_i^- \sigma_{i+1}^+ \right) \\ + \sum_{i=1}^{N} g \left(\sigma_i^+ a + \sigma_i^- a^\dagger \right). \end{aligned} \tag{2.30}$$

We will see how polaritons naturally arise from the Schrödinger equation $H|n\rangle = \Omega_n |n\rangle$; we will use two different approaches (open boundary conditions and periodic boundary conditions) and reach the same results.

Eventually, we will see how polaritonic eigenstates are modified after introduction of disorder in the coupling g.

2.A.1 Open boundary conditions

We forget about the cavity (it will come back later).

Open boundary conditions means that we are considering a chain of N sites with finite length $L = N - 1$ (in units of lattice constant) while on the left of site 1 and on the right of site N there is the vacuum; the state has to be strictly zero there.

To solve this problem we adopt a trick: We add a zeroth site on the left of the first site and a $(N+1)$-th site on the right of the N-th site and change the boundary conditions in such a way that the wave function vanishes at sites 0 and $N+1$. This is, in principle, the setup of a chain with length $L = N+1$ and periodic boundary conditions with the further boundary condition that at the zeroth site the wave function vanishes. Without the additional boundary condition the energy eigenstates have the typical Fourier-type form

$$\sigma_{\mathrm{f},q}^\dagger = \frac{1}{\sqrt{N+1}} \sum_{j=1}^{N} e^{iqj} \sigma_j^+. \tag{2.31}$$

According to the additional boundary condition we need that $\sigma_{j=0} \sigma_{\mathrm{f},q}^\dagger = 0$, which is not satisfied by the Fourier-type operators.

The following linear combination, however, does satisfy such requirement:

$$\sigma_k^\dagger = \frac{1}{\sqrt{2i}}(\sigma_{f,q(k)}^\dagger - \sigma_{f,q(k)}^\dagger) = \sqrt{\frac{2}{N+1}} \sum_{j=1}^{N} \sin\left(\frac{\pi}{N+1} kj\right) \sigma_j^\dagger \tag{2.32}$$

and limits q to the set of values $\{\pi/(N+1)k\}$ with $1 \leq k < (N+1)$. The inverse transformation is

$$\sigma_j^\dagger = \sqrt{\frac{2}{N+1}} \sum_{k=1}^{N} \sin\left(\frac{\pi}{N+1} kj\right) \sigma_k^\dagger. \tag{2.33}$$

Eqs. (2.32) and (2.33) imply $|k\rangle = \sum_{j=1}^{N} \alpha_k^j |j\rangle$ and $|j\rangle = \sum_{k=1}^{N} \alpha_k^j |k\rangle$, with

$$\alpha_k^j = \sqrt{\frac{2}{N+1}} \sin\left(\frac{\pi}{N+1} kj\right). \tag{2.34}$$

These coefficients satisfy

$$\sum_{j=1}^{N} \alpha_k^j \alpha_{k'}^j = \delta_{k,k'} \quad \text{and} \quad \sum_{k=1}^{N} \alpha_k^j \alpha_k^{j'} = \delta_{j,j'}. \tag{2.35}$$

Let us now come back to our problem, where the chain is surrounded by a high-finesse optical cavity. All the above considerations justify the choice

$$|n\rangle = \sum_{j=1}^{N} \alpha_k^j |j0\rangle + \beta |01\rangle \tag{2.36}$$

for the single-excitation subspace ansatz; α_k^j is the probability amplitude for an exciton at the j-th two-level system whereas β is the probability amplitude for a cavity photon. As we shall see, the exciton amplitudes take into account the lenght of the cavity.

By solving $H_{MM}|n\rangle = \Omega_n |n\rangle$, the projection on the photonic state turns out to be

$$\beta = \frac{g}{\Omega_n - \omega_0} \sum_{j=1}^{N} \alpha_k^j \tag{2.37}$$

whereas that one on the exciton at site j (that is $|j0\rangle$) is:

$$\omega_0 \alpha_k^j - J(\alpha_k^{j-1} + \alpha_k^{j+1}) + g\beta = \Omega_n \alpha_k^j. \tag{2.38}$$

By employing definition (2.34) of α_k^j we get

$$\alpha_k^{j-1} + \alpha_k^{j+1} = 2\alpha_k^j \cos\left(\frac{\pi}{N+1} k\right). \tag{2.39}$$

As a consequence, the photonic projection reduces to

$$\omega_k \alpha_k^j + g\beta = \Omega_n \alpha_k^j, \tag{2.40}$$

where

$$\omega_k = \omega_0 - 2J\cos\left(\frac{\pi}{N+1}k\right). \tag{2.41}$$

Inserting the value of β:

$$\alpha_k^j = \frac{g^2}{\Omega_n - \omega_0} \frac{\sum_{i=1}^N \alpha_k^i}{\Omega_n - \omega_k}. \tag{2.42}$$

Then, by multiplying both members by α_k^j, taking the sum over k, and using the fact that $\sum_{p=1}^N |\alpha_p^j|^2 = 1$, we obtain

$$\frac{g^2}{\Omega_n - \omega_0} \sum_{k=1}^N \frac{\alpha_k^j \sum_{i=1}^N \alpha_k^i}{\Omega_n - \omega_k} = 1 \tag{2.43}$$

and a further sum of both members over j leads to

$$\frac{g^2}{N(\Omega_n - \omega_0)} \sum_{k=1}^N \frac{\left(\sum_{i=1}^N \alpha_k^i\right)^2}{\Omega_n - \omega_k} = 1. \tag{2.44}$$

To achieve analytical expressions for the polaritonic resonances without using the numerically exact formula (2.44) we notice that Eq. (2.40), after insertion of the β-value, reduces to:

$$\omega_k \alpha_k^j + \frac{g^2 \sum_{i=0}^N \alpha_k^i}{\Omega_n - \omega_0} = \Omega_n \alpha_k^j. \tag{2.45}$$

By summing over j and eliminating the common factor $\sum_{i=0}^N \alpha_k^i$, one obtains

$$\omega_k + \frac{g^2 N}{\Omega_n - \omega_0} = \Omega_n. \tag{2.46}$$

Since in the above formulas we used sums over photonic probabilities over all sites, it should presumably give us the polaritonic energies and, indeed, by inserting $k = 0$ we obtain

$$\begin{aligned} \Omega_d &= \omega_0 - J - \sqrt{J^2 + g^2 N}, \\ \Omega_u &= \omega_0 - J + \sqrt{J^2 + g^2 N}, \end{aligned} \tag{2.47}$$

which are the polaritonic resonances. We can neglect the quadratic term in J and obtain Eqs. (2.7).

We choosed $k = 0$ because it entail a vanishing group velocity; we could also have chosen $k = N + 1$.

For completeness' sake, let us finally see how Eq. (2.44) changes in the presence of random hopping:

$$\begin{aligned} H = \omega_0 a^+ a + \omega_0 \sum_{i=1}^{N} \sigma_i^+ \sigma_i^- - \sum_{i=1}^{N-1} J_i \left(\sigma_i^+ \sigma_{i+1}^- + \sigma_i^- \sigma_{i+1}^+ \right) \\ + g \sum_i \left(\sigma_i^+ a + \sigma_i^- a^\dagger \right). \end{aligned} \tag{2.48}$$

If we had assumed $J_i = J + \delta J_i$ with δJ_i small enough to leave the sinusoidal nature of the exciton modes unchanged, the relation (2.44) would have had a further term:

$$\frac{g^2}{N(\Omega_n - \omega_0)} \sum_{k=1}^{N} \frac{\left(\sum_{i=1}^{N} \alpha_k^i \right)^2}{\Omega_n - \omega_k} = 1 + 2 \sum_{k=1}^{N-1} \sum_{j=1}^{N-1} \frac{\delta J_j \alpha_k^j \alpha_k^{j+1}}{N(\Omega_n - \omega_k)}. \tag{2.49}$$

Indeed, if $\delta J_i = C$ was a constant we could gather it as a common factor, remaining thus with the sum $\sum_{j=1}^{N-1} \alpha_k^j \alpha_k^{j+1}$ which is 0.

2.A.2 *Periodic boundary conditions*

The solution in this section is in principle exact as $N \to \infty$. The Fourier transforms of the excitonic operators are

$$\begin{aligned} \sigma_k^+ &= \frac{1}{\sqrt{N-1}} \sum_{j=0}^{N-1} \sigma_j^+ e^{-i \frac{2\pi k}{N} j}, \\ \sigma_k^- &= \frac{1}{\sqrt{N-1}} \sum_{j=0}^{N-1} \sigma_j^- e^{+i \frac{2\pi k}{N} j}. \end{aligned} \tag{2.50}$$

It can be easily demonstrated that

$$\omega_0 \sum_{i=1}^{N} \sigma_i^+ \sigma_i^- - J \sum_{i=1}^{N-1} \left(\sigma_i^+ \sigma_{i+1}^- + \sigma_i^- \sigma_{i+1}^+ \right) = \sum_{k=0}^{N-1} \omega_k \sigma_k^+ \sigma_k^- \tag{2.51}$$

with

$$\omega_k = \omega_0 - 2J \cos\left(\frac{2\pi}{N} k \right). \tag{2.52}$$

We can then rewrite

$$\begin{aligned} \sum_{k=0}^{N-1} \omega_k \sigma_k^+ \sigma_k^- &= \sum_{k=1}^{N-1} \omega_k \sigma_k^+ \sigma_k^- + (\omega_0 - 2J) \sigma_{k=0}^+ \sigma_{k=0}^- \\ &\equiv \sum_{k=1}^{N-1} \omega_k \sigma_k^+ \sigma_k^- + (\omega_0 - 2J) \sigma_0^+ \sigma_0^-. \end{aligned} \tag{2.53}$$

The operators $\sigma_0^{\pm}$ [cf. Eq. (2.50)] create and destroy a collective Dicke state:

$$\sigma_0^{\pm} = \frac{1}{\sqrt{N}} \sum_{i=1}^{N} \sigma_i^{\pm}. \tag{2.54}$$

The Jaynes-Cummings term in (2.30) transforms according to

$$\begin{aligned} g \sum_{i=0}^{N} \left(\sigma_i^{+} a + \sigma_i^{-} a^{\dagger} \right) &= g\sqrt{N} (\sigma_{k=0}^{+} a + \sigma_{k=0}^{-} a^{+}) \\ &\equiv G(\sigma_0^{+} a + \sigma_0^{-} a^{+}). \end{aligned} \tag{2.55}$$

The photonic energy $\omega_0 a^{+} a$, instead, does not change. Collecting all terms, Hamiltonian (2.30) becomes

$$H = \omega_0 a^{+} a + (\omega_0 - 2J)\sigma_0^{+}\sigma_0^{-} + G(\sigma_0^{+} a + \sigma_0^{-} a^{+}) + \sum_{k=1}^{N-1} \omega_k \sigma_k^{+} \sigma_k^{-}. \tag{2.56}$$

Introducing the polaritonic operators (2.8), Hamiltonian (2.56) can be recast in the form:

$$H_{MM} = u^{\dagger} u(\omega_0 - J + g\sqrt{N}) + d^{\dagger} d(\omega_0 - J - g\sqrt{N}) + J(d^{\dagger} u + u^{\dagger} d) + \sum_{k=1}^{N-1} \omega_k \sigma_k^{\dagger} \sigma_k^{-}, \tag{2.57}$$

where the nondiagonal term can be neglected since J is small compared to the other energy scales.

The Hamiltonian can be rewritten in a short form as

$$H_{MM} = \Omega_u \left| u \right\rangle \left\langle u \right| + \Omega_d \left| d \right\rangle \left\langle d \right| + \sum_{k=1}^{N-1} \Omega_k \left| k \right\rangle \left\langle k \right|, \tag{2.58}$$

where

$$\begin{aligned} \Omega_{u,d} &= \omega_0 - J \pm g\sqrt{N}, \\ \Omega_k &= \omega_0 - 2J \cos\left(\frac{2\pi}{N} k \right). \end{aligned} \tag{2.59}$$

This, again, demonstrates Eqs. (2.7).

2.A.3 *Random coupling*

For the Hamiltonian (2.30) with a site-dependent coupling g_j,

$$\begin{aligned} H = \omega_0 a^{\dagger} a + \omega_0 \sum_{j1}^{N} \sigma_j^{\dagger} \sigma_j^{-} - J \sum_{j=1}^{N-1} (\sigma_{j+1}^{\dagger} \sigma_j^{-} + \sigma_j^{\dagger} \sigma_{j+1}^{-}) \\ + \sum_{j=1}^{N} g_j (a^{\dagger} \sigma_j^{-} + a \sigma_j^{\dagger}), \end{aligned} \tag{2.60}$$

one solves the Schrödinger equation in the single excitation subspace. Following Sec. 2.A.1 one obtains a nonlinear equation for the eigenvalues Ω_n:

$$\frac{1}{N(\Omega_n-\omega_0)}\sum_{k=1}^{N}\frac{\left(\sum_{i=1}^{N} g_i\alpha_k^i\right)^2}{\Omega_n-\omega_k}=1, \tag{2.61}$$

where α_k^j are given by (2.34). One of the steps to obtain this expression was the projection onto the single-exciton subspace:

$$\omega_k\alpha_k^i+\frac{g_i\sum_{j=0}^{N} g_j\alpha_k^j}{\Omega_n-\omega_0}=\Omega_n\alpha_k^i. \tag{2.62}$$

From Eq. (2.62) one obtains an estimate for the polaritonic resonances by just multiplying all terms by g_i and then summing over i:

$$\omega_k+\frac{\sum_{i=0}^{N} g_i^2}{\Omega_n-\omega_0}=\Omega_n. \tag{2.63}$$

As a consequence, in fact, for a site-dependent coupling g_i, the two polaritonic resonances are located at:

$$\Omega_{u,d}=\omega_0-J\pm\sqrt{J^2+\sum_{i=0}^{N} g_i^2} \tag{2.64}$$

or, neglecting the quadratic term in J,

$$\Omega_{u,d}=\omega_0-J\pm\tilde{G} \tag{2.65}$$

with a collective photon-exciton coupling $\tilde{G}=\sqrt{\sum_{i=0}^{N} g_i^2}$.

2.B Transmission

In this Appendix we demonstrate that the transmission for the system studied in Sec. 2.3 close to the polaritonic peaks is indeed given by Eq. (2.19).

2.B.1 General form

In order to calculate the transmission T_q we follow Ref. [214]. We write the Hamiltonian for the N spins embedded in the cavity (central region of Fig. 2.2) in its eigenbasis,

$$H_C=\sum\Omega_n\Pi_n^{\dagger}\Pi_n, \tag{2.66}$$

with eigenvalues Ω_n and projectors $\Pi_n=|\text{vac}\rangle\langle n|$, which annihilate an excitation in the eigenstates $\{|n\rangle\}$; the vacumm state $|\text{vac}\rangle$ corresponds to the absence of excitons and photons inside the cavity.

The Hamiltonian $H = H_0 + H_{cav}$ of the system conserves the number of excitations [see Eqs. (2.1)]:

$$\left[H, \sum_{i=1}^{\mathscr{N}} \sigma_i^+ \sigma_i^- + \sum_n \Pi_n^+ \Pi_n\right] = 0. \tag{2.67}$$

Therefore we can write the following ansatz for a general one-excitation eigenstate of H:

$$|\psi_q\rangle = \left[\sum_{j_L=1}^{M} C_{j_L,q}^{(L)} \sigma_{j_L}^+ + \sum_{j_R=M+N+1}^{\mathscr{N}} C_{j_R,q}^{(R)} \sigma_{j_R}^+ + \sum_n p_q^n \Pi_n^+\right] |\text{vac}\rangle \tag{2.68}$$

which depends on the quasimomentum q. The first and second terms represent an exciton hopping through the array on the left and right side of the cavity, respectively, whereas the third term describes a generic single excitation inside the cavity. In Eq. (2.68) $\mathscr{N} = 2M + N$ is the total number of sites (cf. Sec. 2.3).

The Hamiltonian H of the system in Fig. 2.2 can be decomposed as

$$H = \sum_{\alpha=L,R} \left[H_\alpha + H_{\text{int},\alpha}\right] + H_C. \tag{2.69}$$

where the pedices L, R and C refer to the left, right, central regions of the system, namely

$$\begin{aligned} H_L &= \omega \sum_{j_L=1}^{M} \sigma_{j_L}^+ \sigma_{j_L}^- - J \sum_{j_L=1}^{M-1} \left(\sigma_{j_L+1}^+ \sigma_{j_L}^- + \sigma_{j_L+1}^- \sigma_{j_L}^+\right), \\ H_R &= \omega \sum_{j_R=M+N+1}^{2M+N} \sigma_{j_R}^+ \sigma_{j_R}^- - J \sum_{j_R=M+N+1}^{2M+N-1} \left(\sigma_{j_R+1}^+ \sigma_{j_R}^- + \sigma_{j_R+1}^- \sigma_{j_R}^+\right) \end{aligned} \tag{2.70}$$

and

$$\begin{aligned} H_{\text{int},L} &= -J' \left(\sigma_{M+1}^+ \sigma_M^- + \sigma_{M+1}^- \sigma_M^+\right), \\ H_{\text{int},R} &= -J' \left(\sigma_{M+N+1}^+ \sigma_{M+N}^- + \sigma_{M+N+1}^- \sigma_{M+N}^+\right). \end{aligned} \tag{2.71}$$

$H_{\text{int},L}$ and $H_{\text{int},R}$ describe the interaction with the cavity as the exciton enters and comes out from it.

The Fourier transforms of the excitonic creation operators ($\alpha = L, R$),

$$\begin{aligned} \sigma_{j_\alpha}^+ &= \frac{1}{\sqrt{M}} \sum_{k=0}^{M-1} e^{-i\frac{2\pi k}{M} j_\alpha} \sigma_{k_\alpha}^+, \\ \sigma_{j_\alpha}^- &= \frac{1}{\sqrt{M}} \sum_{k=0}^{M-1} e^{i\frac{2\pi k}{M} j_\alpha} \sigma_{k_\alpha}^-, \end{aligned} \tag{2.72}$$

allow us to rewrite H_L and H_R as

$$H_\alpha = \sum_{k=0}^{M-1} \omega_{k_\alpha} \sigma^+_{k_\alpha} \sigma^-_{k_\alpha} \tag{2.73}$$

where $k_\alpha \in K_M \equiv \left\{0, \frac{2\pi}{M}, \dots, \frac{2\pi(M-1)}{M}\right\}$ and $\omega_{k_L} = \omega_{k_R} \equiv \omega_k$:

$$\omega_k = \omega - 2J \cos\left(\frac{2\pi}{M} k\right). \tag{2.74}$$

In position space:

$$\begin{aligned} H_L &= \sum_{j_L, i_L = 1}^{M} f^{(L)}_{i_L, j_L}(\omega_0, J) \left|j_L\right\rangle \left\langle i_L\right|, \\ H_R &= \sum_{j_R, i_R = M+N+1}^{2M+N} f^{(R)}_{i_R, j_R}(\omega_0, J) \left|j_R\right\rangle \left\langle i_R\right|, \end{aligned} \tag{2.75}$$

with

$$f^{(\alpha)}_{i_\alpha, j_\alpha}(\omega_0, J) = \sum_{k=0}^{M-1} \frac{\omega_k}{M} e^{i \frac{2\pi}{M} k (i_\alpha - j_\alpha)}. \tag{2.76}$$

In order to find a general expression for T_q we have to solve the Schrödinger equation for Hamiltonian (2.69) in the single-excitation subspace:

$$H \left|\psi_q\right\rangle = E_q \left|\psi_q\right\rangle; \tag{2.77}$$

we adopt ansatz (2.68).

The Schrödinger equation (2.77) leads to a set of three equations. More precisely, the projections on the left and right regions give

$$\sum_{i_L=1}^{M} C^{(L)}_{i_L, q} f^{(L)}_{i_L, j_L}(\omega_0, J) + \delta_{j_L, M} \sum_n p^n_q J'^*_{n,L} - E_q C^{(L)}_{j_L, q} = 0 \tag{2.78}$$

for every $j_L \in \{1, \dots, M\}$, and

$$\sum_{i_R=M+N+1}^{2M+N} C^{(L)}_{i_R, q} f^{(R)}_{i_R, j_R}(\omega_0, J) + \delta_{j_R, M+N+1} \sum_n p^n_q J'^*_{n,R} - E_q C^{(R)}_{j_R, q} = 0 \tag{2.79}$$

for every $j_R \in \{M+N+1, \dots, \mathcal{N}\}$. Quantities $J'_{n,L}$ and $J'_{n,R}$ involve excitation amplitudes for the two outermost two-level systems inside the cavity: $J'_{n,L} = -J' \left\langle n\right| \sigma^+_{M+1} \left|\text{vac}\right\rangle$, $J'_{n,R} = -J' \left\langle n\right| \sigma^+_{M+N} \left|\text{vac}\right\rangle$. The equation relative to the cavity system, valid for every $\left|n\right\rangle$, instead, is

$$C^{(L)}_{M,q} J'_{n,L} + C^{(R)}_{M+N+1,q} J'_{n,R} + p^n_q (\Omega_n - E_q) = 0. \tag{2.80}$$

We assume the following probability amplitudes:

$$\begin{aligned} C^{(L)}_{j_L,q} &= \frac{2-\delta_{j_L,M}}{2}\left(e^{-iq(j_L-M)} + r_q e^{iq(j_L-M)}\right), \\ C^{(R)}_{j_R,q} &= \frac{2-\delta_{j_R,M+N+1}}{2} t_q e^{iq(j_R-(M+N+1))}. \end{aligned} \tag{2.81}$$

The delta factors take into account the fact that we are not dealing with a side-coupled cavity but with a direct-coupled cavity [224].

From Eqs. (2.80) and (2.81), it follows that the probabilistic weight for the eigenstate $|n\rangle$ is, up to an arbitrary phase,

$$p^n_q = \frac{(1+r_q)J'_{n,L} + t_q J'_{n,R}}{2(E_q - \Omega_n)}. \tag{2.82}$$

To find the transmission and reflection coefficients we employ Eqs. (2.78) and (2.79). Let us consider, for instance, Eq. (2.78). After some algebraic computation, and by using using the following properties:

$$\begin{aligned} \sum_{i_L=1}^{M} e^{i\frac{2\pi}{M} i_L\left(k-\frac{Mq}{2\pi}\right)} &= M\delta_{k,\frac{Mq}{2\pi}}, \\ \sum_{i_L=1}^{M} e^{i\frac{2\pi}{M} i_L\left(k+\frac{Mq}{2\pi}\right)} &= M\delta_{k,-\frac{Mq}{2\pi}}, \end{aligned} \tag{2.83}$$

one gets, for $j_L < M$,

$$\begin{aligned} &\sum_{k=0}^{M-1} \omega_k \left(\delta_{k,\frac{Mq}{2\pi}} e^{-iq(j_L-M)} + r_q \delta_{k,-\frac{Mq}{2\pi}} e^{iq(j_L-M)}\right) \\ &+ \sum_n p^n_q J'_{n,L} - E_q\left(e^{-iq(j_L-M)} + r_q e^{iq(j_L-M)}\right) = 0. \end{aligned} \tag{2.84}$$

At low momenta ($M \gg 1$) $\omega_k = \omega - 2J + v_k k$ where v_k is the group velocity and satisfies $v_{-x} = -v_x$:

$$v_k = \frac{M}{2\pi}\frac{\partial \omega_k}{\partial k} = -2J\sin\left(\frac{2\pi k}{M}\right). \tag{2.85}$$

By using the low-energy effective field theory [224], the diagonal term of the Hamiltonian in momentum space can be expressed as:

$$\sum_{k\in K_M} \omega_k \sigma^+_k \sigma^-_k = \int_{-\infty}^{+\infty} \phi^+(x)\left(\omega - 2J - i v_k \frac{\partial}{\partial x}\right)\phi(x), \tag{2.86}$$

where $\phi(x) \equiv \int_{-\infty}^{+\infty} dk e^{ikx} \sigma_k^-$ satisfies the commutation relation $\left[\phi(x), \phi(x')^+\right] = \delta(x - x')$. In the continuum limit, Lippman-Schwinger states (2.81) for a direct-coupled cavity can be written as:

$$\begin{aligned} C_q^{(L)}(x_L) &= e^{iq\left(x_L - \frac{M}{2}\right)}[\theta(-x_L) + r_q \theta(x_L)], \\ C_q^{(R)}(x_R) &= e^{iq\left(x_R - \frac{M}{2}\right)} t_q \theta(x_R), \end{aligned} \tag{2.87}$$

where x_L and x_R run both from $-\infty$ to $+\infty$. Strictly speaking, these formulae imply a prefactor $e^{ikM/2}$ in Eq. (2.82); it is irrelevant though since it disappears in all physical results.

Notice that in Eq. (2.84) the delta functions change ω_k in

$$\omega_{\frac{Mq}{2\pi}} = \omega_{-\frac{Mq}{2\pi}} = \omega - 2J\cos(q) \equiv \omega_q \tag{2.88}$$

which does not depend on the cavity length M anymore. The corresponding group velocity of the wave packet is $v_q = -2J\sin(q)$.

Using Eqs. (2.86) and (2.87) then

$$\left(\omega - 2J - iv_q \frac{\partial}{\partial x_L}\right) C_q^{(L)}(x_L) = E_q C_q^{(L)}(x_L) - iv_q e^{iq\left(x_L - \frac{M}{2}\right)}[-\delta(-x_L) + r_q \delta(x_L)]. \tag{2.89}$$

where everything is a function of q and does not depend on the number M of two-level systems.

The term proportional to $E_q = \omega - 2J - iv_q q$ eliminates with the same term, but with opposite sign, that is the third term of the time-independent equation for the left branch [Eq. (2.78)], so that Eq. (2.78) in continuum space, after eliminating all deltas through an overall integration [$x_L \in (-\infty, +\infty)$], reduces to:

$$2iJ\sin(q)(-1 + r_q) + \sum_n p_q^n J'^*_{n,L} = 0. \tag{2.90}$$

Similarly, the equation for the transmission (2.79) reduces to:

$$2iJ\sin(q)t_q + \sum_n p_q^n J'^*_{n,R} = 0. \tag{2.91}$$

Inserting expression (2.82) for the p_q^n's, Eqs. (2.90) and (2.91) lead to

$$t_q = \frac{-2i\beta}{\Gamma_L \Gamma_R + |\beta|^2}, \tag{2.92}$$

and

$$r_q = \frac{\Gamma_L^* \Gamma_R - |\beta|^2}{\Gamma_L \Gamma_R + |\beta|^2}, \tag{2.93}$$

where, after taking into account that our variables do not run from $-\infty$ to ∞ but actually travel back and forth through the same path,

$$\Gamma_\alpha = 1 - \frac{i}{J\sin(q)} \sum_n \frac{\left|J'_{n,\alpha}\right|^2}{\omega - 2J\cos(q) - \Omega_n}, \tag{2.94}$$

and

$$\beta = -\frac{1}{J\sin(q)} \sum_n \frac{J'_{n,L} J'^*_{n,R}}{\omega - 2J\cos(q) - \Omega_n}. \tag{2.95}$$

Now we have to find the eigenvalues Ω_n and the quantities $J'_{n,L}$ and $J'_{n,R}$; for this purpose we have to solve the Schrödinger equation $H_C |n\rangle = \Omega_n |n\rangle$, where H_C is

$$H_C = \omega_0 a^+ a + \omega_0 \sum_{j=M+1}^{M+N} \sigma_j^+ \sigma_j^- - J \sum_{j=M+1}^{M+N-1} (\sigma_{j+1}^+ \sigma_j^- + \sigma_j^+ \sigma_{j+1}^-) + g \sum_{j=M+1}^{M+N} (a^+ \sigma_j^- + a \sigma_j^+). \tag{2.96}$$

Such Schrödinger equation was already solved in Appendix 2.A.

2.B.2 *Transmission close to polaritonic peaks*

Let us now imagine that the energy of the wave packet coming from the left is nearly resonant with one of the polariton states, $\omega_q \approx \Omega_{u,d}$. By using the results in Sec. 2.A.2 we can check that

$$\begin{aligned} J'_{u,L} &= -J' \langle u | \sigma_{M+1}^+ |\text{vac}\rangle = -\frac{J'}{\sqrt{2N}}, \\ J'_{d,L} &= -J' \langle d | \sigma_{M+1}^+ |\text{vac}\rangle = +\frac{J'}{\sqrt{2N}}, \end{aligned} \tag{2.97}$$

for every $k \in \{1, \dots, M\}$. Similarly,

$$\begin{aligned} J'_{u,R} &= -J' \langle u | \sigma_{M+N}^+ |\text{vac}\rangle = -\frac{J'}{\sqrt{2N}}, \\ J'_{d,R} &= -J' \langle d | \sigma_{M+N}^+ |\text{vac}\rangle = +\frac{J'}{\sqrt{2N}}. \end{aligned} \tag{2.98}$$

In the eigenbasis $\{|d\rangle, |u\rangle, K_N = \{|2\pi/N\rangle, \dots, |2\pi(N-1)/N\rangle\}\}$ then, close to one polaritonic resonance, expression (2.95) reduces to

$$\beta = \frac{|J'|^2}{N|v_q|} \frac{1}{\left(\omega_q - \Omega_{u,d}\right)} \tag{2.99}$$

whereas $\Gamma_L = \Gamma_R \equiv \Gamma$ becomes

$$\Gamma = 1 + i\beta. \tag{2.100}$$

Consequently the transmission is

$$T_q = \frac{w}{w + [\Delta + J[1 - 2\cos(q)] \mp G]^2} \tag{2.101}$$

where $\Delta = \omega - \omega_0$, which is exactly Eq. (2.19); w is the full width at half maximum of the resonance:

$$w = -\frac{|J'|^2}{NJ\sin(q)}. \tag{2.102}$$

Finally, let us notice that the resonance $T_q = 1$ occurs for an energy of incoming exciton wave packet equal to

$$\omega_{u,d} = \omega_0 - J[1 - 2\cos(q)] \pm g\sqrt{N}. \tag{2.103}$$

2.C Realistic parameters

We report some realistic numbers for artificially engineered media.

2.C.1 Cold Ions

For ions trapped in a linear Paul trap a hopping rate $J \approx 400\,\text{Hz}$ is within reach [175]. In this case, however, the hopping is mediated by mechanical degrees of freedom of the ion crystal; we have thus to take into account also long-range contributions to it. Usually the decay exponents range from $\alpha = 0.1$, which corresponds to fully established all-to-all interactions, to $\alpha = 2$. For all-to-all interactions there is no need of a cavity or a photonic mode to mediate the interaction. However, if we consider a cavity with $\kappa \sim$ MHz, then $g \sim 10\,\text{MHz}$ can be achieved [225]: A very strong collective coupling G can thus be engineered even for a lossy cavity ($\kappa \gg J$).

2.C.2 Rydberg atoms

We consider a Rydberg lattice gas [199], where the two spin states are the states $|nS\rangle$ and $|n'P\rangle$, respectively. An example, for ^{87}Rb atoms, are the states $|60S_{1/2}\rangle$ and $|59P_{3/2}\rangle$ with a transition energy $\omega_0 \approx 18.5\,\text{GHz}$ [199]. The transition dipole moment ($d \sim n^2$) for such transition is of the order of $d = 2000\,ea_0$. According to Ref. [209], microwave high-finesse cavities (Q-factor $= 3 \times 10^8$, $\kappa \approx 1\,\text{kHz}$) can be engineered for resonant transition frequencies of 51 GHz with $d \approx 1000\,ea_0$ and $g \sim d\sqrt{\omega_0} \approx 300\,\text{kHz}$. For an interatomic separation $x \approx 20\,\mu\text{m}$, the tunneling rate (in the nearest neighbor approximation) is $J \approx 80\,\text{kHz}$ [226], which means that the regime $g \gg J \gg \kappa$ can be reached. Finally, also the spontaneous emission rate is negligible, since the lifetime of the Rydberg states can be as large as tens of milliseconds.

2.C.3 *Polar molecules*

We consider polar molecules where rotational states can be mapped on spin states ($\omega_0 \sim 2\,\mathrm{GHz}$). These molecules trapped in an optical lattice can be inserted into a microwave optical cavity. In these systems $J \approx 50\,\mathrm{Hz}$ is experimentally achievable [200, 201] and it is thus easy to obtain a strong coupling to light $g \gg J$. The drawback of having such a small hopping rate, however, is that in order to have a negligible cavity decay rate ($\kappa \ll J$) an extremely good cavity is required. For $Q = 10^8$, for instance, $\kappa = 125\,\mathrm{Hz} \gg J$ The states are long-lived and allow to study coherent dynamics over a timescale $\sim 0.1\,\mathrm{s}$ [200].

3
Broadband two-photon interactions mediated by cold atoms in a photonic crystal fiber

In classical electrodynamics light does not interact with light and in quantum electrodynamics photons do not directly couple to each other. In order to describe photon-photon interactions higher-order processes must be taken into account, which are very unlikely to happen: The Feynman diagram for the two-photon scattering is a box diagram (the photon-photon interaction is mediated by a virtual fermion-antifermion couple) with cross section $\sigma(\gamma\gamma \to \gamma\gamma) \propto \alpha^4$ where γ indicates a photon and the fine-structure constant is $\alpha = 1/137$ [1].

Making photons strongly interact with each other is a long sought-after goal in physics [2, 227]. Several fields would benefit from interacting photons, ranging from many-body physics [66, 120, 121] to quantum information [19–23, 98, 228–230] and metrology [231–233]. Several techniques are nowadays available to induce interactions between photons. It is for instance possible to induce photonic nonlinearities via the coupling of photons to saturable atomic or molecular single two-level emitters by surrounding them with an optical cavity [26, 234]. An other way is employing the anharmonicity of the spectrum of the Jaynes-Cummings Hamiltonian as a function of number of photons [235, 236]; the photon blockade is based on this effect [40]. Moreover, such anharmonicity is the main reason why arrays of coupled resonators with emitters are interesting systems [115, 119]. A third possible approach consists in dressing the photons with atoms and employing the atomic dipolar or van der Waals interaction between the latters. In this case, in order to realize the nonlinear medium, Rydberg atoms under condition of electromagnetically induced transparency are preferred [31, 53–56] because of the strong dipole moment carried by Rydberg atoms. Recent experimental results with Rydberg media [31, 56] have shown attraction between photons caused by formation of narrow bound states of two polaritons [63, 64] with frequencies of the order of MHz.

In this chapter we propose to observe photon-photon interactions in a one-dimensional chain of two-level atoms trapped in an optical lattice (in a Mott insulator state) inside a hollow-core photonic crystal fiber, see Fig. 3.1. A similar setup is for instance adopted in Ref. [99] where strontium atoms are used. We will, however, choose Rb atoms and we will not take losses

through the fiber walls into account. Alternative systems are array of cold atoms along nanophotonic waveguides [93, 95, 237–241].

In the strong coupling regime [cf. Eq. (2.17)] light and atoms in the fiber exchange excitations so fast that photons and excitons can not be considered independently: Due to their strong coupling a doublet of lower and upper polaritons naturally arises in the system, as illustrated in Fig. 3.3 (for a review on polariton see Sec. 2.2).

Unlike systems that employ Rydberg gases here we do not need any explicit dynamical interaction between atomic excitations. We only need the very basic fact that each two-level system is saturable, meaning that each atom can accommodate only one excitation at the time; this exclusion property is called kinematic interaction [210]; it is usually a very weak effect in solids. Since the excitons, despite being bosons, exclude each other on a same site (on-site replusion), we will refer to them as hard-core bosons. Here we show that for cold atoms the kinematic interaction is instead a non negligible effect and causes bunching in the photonic component of the two-polariton states, which occurs in the continuum of unbound two-polariton states and can be realistically observed within a broad GHz frequency range. The ultimate explanation for these correlations is the mismatch of the quantization volumes for excitonic and photonic states. We expect this bunching to be particularly robust against decoherence. Photonic crystal fibers are commonly used [98–100, 242–246] but our scheme may be engineered also in different ways. There are indeed many theoretical proposals for coupling light modes to ordered one-dimensional ensembles of quantum emitters [93, 95, 237–241, 247–253] and even solid-state realizations can be implemented, for example by introducing silicium vacancies in photonic crystals [254, 255].

This chapter is organized as follows. In Sec. 3.1 we describe the model. In Sec. 3.2 we solve the Schrödinger equation and plot the wave functions for three exemplar eigenstates. In Sec. 3.3 we solve the problem of two bare excitons which interact via kinematic interaction. In Sec. 3.4 we explain in a qualitative way the bunching effect. Sec. 3.5 is devoted to the dependence of the bunching effect over the various experimental parameters. Sec. 3.6 analyzes the possibility of having true bound states when the spectrum is gapped. Finally, in Sec. 3.7 we sum up the main results.

In Appendix 3.A we provide an analytical explanation for the bunching.

The results from this chapter have been collected in the following paper, submitted (not yet published) during the PhD:

M. Litinskaya, E. Tignone, G. Pupillo,
Broadband photon-photon interactions mediated by cold atoms in a photonic crystal fiber,
(Submitted to *Scientific Reports*)

3.1 The model

The model that we propose is depicted in Fig. 3.1. We consider an ordered array of N atoms separated by a lattice spacing a and placed inside a photonic crystal fiber; the transition frequency for each atom is E_0 whereas the hopping constant is $t \propto d^2/a^3$ with d being the transition dipole moment. We consider nearest-neighbor hopping only. The Hamiltonian describing the dynamics of such system is [cf. Eq. (2.3)]:

$$\begin{aligned} H = {} & E_0 \sum_s P_s^\dagger P_s + t \sum_s \left(P_s^\dagger P_{s+1} + P_s^\dagger P_{s-1} \right) + \sum_{q_\nu} E_p(q_\nu) b^\dagger(q_\nu) b(q_\nu) \\ & + g \sum_{s,q_\nu} \left[P_s^\dagger b(q_\nu) e^{iqs} + P_s b^\dagger(q_\nu) e^{-iq_\nu s} \right]. \end{aligned} \tag{3.1}$$

Operators $P_s^\dagger$ and $b^\dagger(q_\nu)$ create, respectively, an atomic excitation at site s and a cavity photon characterized by a wave vector q_ν along the cavity axis. According to Eq. (2.4), the photonic dispersion relation is

$$E_p(q_\nu) = c\sqrt{q_\nu^2 + q_\perp^2} \tag{3.2}$$

with

$$q_\nu = \frac{2\pi\nu}{Na} \tag{3.3}$$

and ν integer. As usually c is the speed of light whereas $q_\perp$ is the transverse momentum of the photon. If we consider the lowest-energy mode of a perfect open cylindrical cavity, $q_\perp$ is the smallest-valued quantity that satisfies

$$J_0(q_\perp R) = 0 \tag{3.4}$$

where J_0 is the zeroth Bessel function of the first kind and R is the radius of the cavity [256]. We have to consider J_0 since it is the only Bessel function of the first kind that does not vanish in correspondence of the cavity axis, where the array of atoms lies.

The light-matter coupling is

$$g = d\sqrt{\frac{2\pi E_0}{V}} \tag{3.5}$$

with $V = \pi R^2 Na$ being the the volume of the cylindric hollow core.

3.2 Solution

The atomic part of the Hamiltonian (3.1) can be automatically diagonalized by taking the Fourier transform

$$P(q_\nu) = \frac{1}{\sqrt{N}} \sum_n P_n e^{-iq_\nu n}, \tag{3.6}$$

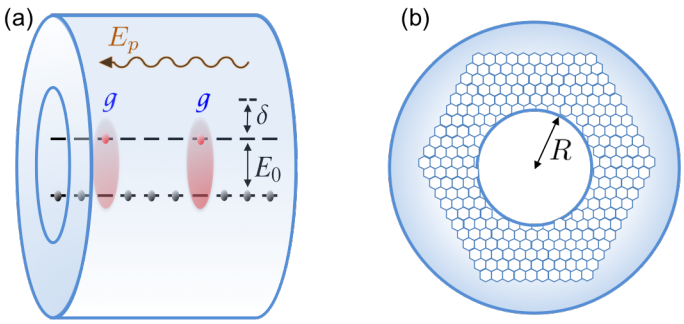

Figure 3.1: (a) Longitudinal sketch of an ensemble of two-level atoms inside a photonic crystal fiber; g is the light-emitter coupling; E_p is the guided mode of the cavity while E_0 is the energy of the atomic transition; $\delta = E_p(0) - E_0$ is the detuning. (b) Transversal section of the photonic crystal fiber; R is the radius of the hollow core.

which leads to the following dispersion relation for bare excitons:

$$E_e(q_\nu) = E_0 + 2t \cos a q_\nu. \tag{3.7}$$

Notice that Eq. (3.7) is analogous to the second equation in (2.4). The effect of the hopping is much weaker than the effects originating from the formation of polaritons; as a consequence, the hopping term could be easily dropped. This is apparent in Fig. 3.3, where the excitonic dispersion relation (lower dashed line) is practically constant and equal to E_0. This is visible also in the inset of Fig. 3.2, where the lower-lower polariton branch (blue curve) looks flat compared to the others.

Since we are interested in the two-particle dynamics, we have to solve the Schrödinger equation in the two-particle subspace where the most general ansatz for a wave function is

$$|\Psi\rangle = \sum_{nm} \left\{ \frac{A_{nm}}{\sqrt{2}} |b_n b_m\rangle + B_{nm} |b_n P_m\rangle + \frac{C_{nm}}{\sqrt{2}} |P_n P_m\rangle \right\} \tag{3.8}$$

with

$$b_n = \frac{1}{\sqrt{N}} \sum_{q_\nu} b(q_\nu) e^{i q_\nu n}. \tag{3.9}$$

In Eq. (3.8) the coefficients A_{nm}, B_{nm} and C_{nm} are the probability amplitudes for having two photons, one photon and one exciton, or two excitons at sites n, m respectively.

Since photons are identical bosons, and so are excitons, their amplitudes are symmetric ($A_{nm} = A_{mn}$, $C_{nm} = C_{mn}$). Additionally, the C-coefficients have to satisfy the hard-core repulsion condition

$$C_{nn} = 0, \tag{3.10}$$

which comes from the saturability of the two-level systems.

A photon and an exciton are instead distinguishable particles, therefore B-coefficients do not have a particular symmetry. B_{nm} can be decomposed into its symmetric (S) and antisymmetric (A) components as $B_{nm} = B^S_{nm} + B^A_{nm}$.

The Schrödinger equation obtained by letting the Hamiltonian operator (3.1) act on the wave function (3.8) can be rearranged as a set of equations for A-, B- and C-coefficients:

$$\begin{aligned}
EA_{nm} &= \sum_s \left(E_p(n-s)A_{sm} + E_p(m-s)A_{sm}\right) + \sqrt{2}GB^S_{nm}, \\
EB^S_{nm} &= E_0 B^S_{nm} + \frac{1}{2}\left[\sum_s E_p(n-s)\left(B^S_{sm} + B^A_{sm}\right) + E_p(m-s)\left(B^S_{sn} + B^A_{sn}\right)\right] \\
&\quad + \sqrt{2}G(A_{nm} + C_{nm}) + \frac{t}{2}\left[B^S_{n,m-1} + B^A_{n,m-1} + B^S_{n,m+1} + B^A_{n,m+1}\right] \\
&\quad + \frac{t}{2}\left[B^S_{n-1,m} - B^A_{n-1,m} + B^S_{n+1,m} - B^A_{n+1,m}\right], \\
EB^A_{nm} &= E_0 B^A_{nm} + \frac{1}{2}\left[\sum_s E_p(n-s)\left(B^S_{sm} + B^A_{sm}\right) - E_p(m-s)\left(B^S_{sn} + B^A_{sn}\right)\right] \\
&\quad + \frac{t}{2}\left[B^S_{n,m-1} + B^A_{n,m-1} + B^S_{n,m+1} + B^A_{n,m+1}\right] \\
&\quad - \frac{t}{2}\left[B^S_{n-1,m} - B^A_{n-1,m} + B^S_{n+1,m} - B^A_{n+1,m}\right], \\
EC_{nm} &= 2E_0 C_{nm} - D(n-m)C_{nm} + \left[t(C_{nm-1} + C_{nm+1} + C_{n+1m} + C_{n-1m}) + \sqrt{2}GB^S_{nm}\right] \\
&\quad \times (1 - \delta_{nm}).
\end{aligned} \tag{3.11}$$

We move in the Fourier space by using the relation

$$C_{nm} = \frac{1}{N}\sum_{k_1,k_2} C(k_1,k_2)e^{i(nk_1+mk_2)} \tag{3.12}$$

for C-coefficients. A similar expression is valid for B- and A- coefficients.

We define the total and relative wave vectors:

$$K_{\nu'} = q_{\nu_1} + q_{\nu_2} \quad \text{and} \quad k_\nu = \frac{q_{\nu_1} - q_{\nu_2}}{2}. \tag{3.13}$$

Since we are working in a lattice geometry (i.e. translational invariant) $K_{\nu'}$ is a good quantum number. Here we analyze in details the case $K_{\nu'} = 0$ whereas the case $K_{\nu'} \neq 0$, which is qualitatively similar, is shortly discussed.

For $K_{\nu'} = 0$, $q_{\nu_2} = -q_{\nu_1}$, and

$$k_\nu = \frac{2\pi\nu}{Na} \tag{3.14}$$

with an index

$$\nu = -\frac{N}{2} + 1, ..., \frac{N}{2} \tag{3.15}$$

The integer index ν runs over the Brillouin zone as usual because $K/2 = 0$ is a legal lattice momentum, see Ref. [257] for major details. By using several times the property

$$\sum_{n=-N/2+1}^{N/2} e^{ikn} = N\delta_{k,0} \tag{3.16}$$

we get:

$$\begin{aligned} E_\rho A_\rho(k_\nu) &= 2E_p(k_\nu)A_\rho(k_\nu) + G\sqrt{2}B_\rho(k_\nu), \\ E_\rho B_\rho(k_\nu) &= [E_e(k_\nu) + E_p(k_\nu)]B_\rho(k_\nu) + G\sqrt{2}[A_\rho(k_\nu) + C_\rho(k_\nu)], \\ E_\rho C_\rho(k_\nu) &= 2E_e(k_\nu)C_\rho(k_\nu) + G\sqrt{2}B_\rho(k_\nu) + S_\rho, \end{aligned} \tag{3.17}$$

The index ρ labels the two-polariton state and the term

$$S_\rho = -\frac{G\sqrt{2}}{N}\sum_{q_\nu} B_\rho(q_\nu) - \frac{4t}{N}\sum_{q_\nu} C_\rho(q_\nu)\cos aq_\nu \tag{3.18}$$

accounts for scattering between polaritons induced by the kinematic interaction. For $K_{\nu'} = 0$, $B = B^S$ and $B^A = 0$. The collective coupling G between the Dicke state and the cavity mode is $G = g\sqrt{N}$ [cf. (2.6)]. Qualitatively, it is clear that if $S(k)$ is less than the typical level spacing $2\pi/Na$, the interaction is ineffective. This is true for small-k region, where the density of states is low. The role of the scattering increases with the increase of density of states, that is at larger k, where the polariton states acquire more excitonic character.

If $S_\rho = 0$ the problem described by the system (3.17) reduces to two polaritons inside the hollow core of a photonic crystal fiber which do not interact with each other; in this case the dispersion relation is just

$$[E - 2E_L(k_\nu)][E - E_L(k_\nu) - E_U(k_\nu)][E - 2E_U(k_\nu)] \equiv \Delta(E, k_\nu) = 0 \tag{3.19}$$

with $E_L(k_\nu)$ and $E_U(k_\nu)$ being the energies of the polaritons, see Eqs. (2.7). The dispersion plot is analogous to Fig. 2.1 but with two polaritons instead of one. In other words we have four polaritonic curves corresponding to all possible combinations:

- $E_{LL}(k_\nu) = E_L(k_\nu) + E_L(k_\nu)$ (blue curve in Fig. 3.2);
- $E_{LU}(k_\nu) = E_{UL}(k_\nu) = E_L(k_\nu) + E_U(k_\nu)$ (green curve in Fig. 3.2);
- $E_{UU}(k_\nu) = E_U(k_\nu) + E_U(k_\nu)$ (red curve in Fig. 3.2).

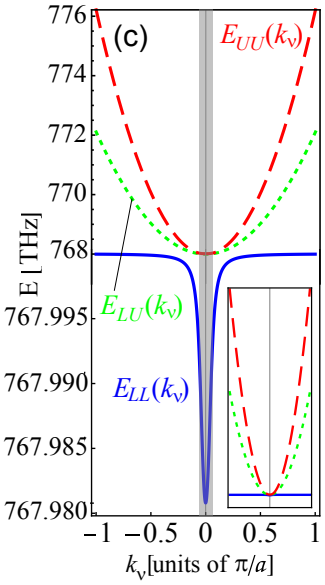

Figure 3.2: Band structure in the presence of two excitations. $E_{LL}(k_\nu)$, $E_{LU}(k_\nu) = E_{UL}(k_\nu)$, $E_{UU}(k_\nu)$ are the energy bands of two lower, one lower and one upper, and two upper polaritons; a is the lattice constant. The shaded region corresponds to the strong coupling region $k_\nu < k_{SC}$, see Eq. (3.20). The lower polariton is plotted on a different energy scale; the inset, instead, shows all polariton bands plotted on the same scale.

The lower-upper ($LU-$) and upper-lower ($UL-$) curves are degenerate.

We define the characteristic wave vector

$$k_{SC} = 2\frac{\sqrt{E_0 G}}{c\hbar} \tag{3.20}$$

which satisfies the relation $E_L(k_{SC}) = E_0$ where the lower band $E_L(k_\nu)$ is approximated by a parabola.

Figure 3.2 illustrates the first Brillouin zone, which is divided into two distinguished regions: For $k_\nu < k_{SC}$ (grey area around $k_\nu = 0$) the matter and light are strongly coupled; this is the strong coupling region. Outside of the grey region ($k_\nu > k_{SC}$), we enter the weak coupling regime where the polariton components practically behave as free excitons and photons, see Eq. (2.18). This is very clear also in Fig. 3.3 and Fig. 2.1, where one excitation is considered: At large momenta the lower and upper polaritonic energies (solid curves) strictly follow the energies of an uncoupled exciton and photon (dashed curves), respectively.

If $S_\rho \neq 0$ (the case we are interested in) the hard-core repulsion between excitons is turned on; now the two polaritons effectively interact via their excitonic fractions and the solutions of equations (3.1) are wave packets of free-polariton states. We will prove that the correlations between pho-

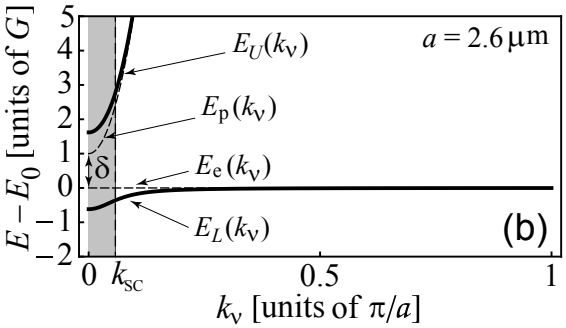

Figure 3.3: Band structure in the presence of a single excitation [cf. Fig. (2.1)]; only the positive half of the Brillouin zone is depicted. $E_L(k)$ and $E_U(k)$ are the energy bands of the lower and upper polaritons, respectively; $E_p(k)$ and $E_e(k)$ are the energies of a free photon and a free exciton; a is the lattice constant. We consider a positive detuning $\delta = E_p(0) - E_0$. The shaded region corresponds to the strong coupling region $k_\nu < k_{SC}$.

tons are induced by constructive interference among several components of these wave packets. Since the atomic dressing of the photons (and thus the effective interaction between the photons themselves) increases for larger coupling, this interference effect is more visible at momenta $k_\nu \lesssim k_{SC}$ when a strong coupling is reached.

3.2.1 *Analytical solution*

For $S_\rho \neq 0$, system (3.17) has an analytical solution. The Fourier transform of the constraint $C_{nn} = 0$ is, see Eq. (3.12):

$$\sum_{\nu=-N/2+1}^{N/2} C(k_\nu) \equiv 0. \tag{3.21}$$

By employing relation (3.21), we rewrite Eqs. (3.17) as a set of three independent equations of the form

$$\begin{aligned}
A_\rho(k_\nu)\Delta(E_\rho,k_\nu) &= \frac{1}{N}\sum_{k_{\nu'}} A_\rho(k'_\nu)\Delta(E_\rho,k'_\nu),\\
\frac{B_\rho(k_\nu)\Delta(E_\rho,k_\nu)}{(E_\rho - 2E_p(k_\nu))} &= \frac{1}{N}\sum_{k_{\nu'}} \frac{B_\rho(k'_\nu)\Delta(E_\rho,k'_\nu)}{(E_\rho - 2E_p(k'_\nu))},\\
\frac{C_\rho(k_\nu)\Delta(E_\rho,k_\nu)}{\phi(E_\rho,k_\nu)} &= \frac{1}{N}\sum_{k_{\nu'}} \frac{C_\rho(k'_\nu)\Delta(E_\rho,k'_\nu)}{\phi(E_\rho,k'_\nu)},
\end{aligned} \tag{3.22}$$

where $\Delta(E_\rho,k_\nu)$ is defined in Eq. (3.19) while

$$\phi(E,k_\nu) = [E - 2E_p(k_\nu)][E - E_p(k_\nu) - E_e(k_\nu)] - 2G^2. \tag{3.23}$$

Eqs. (3.22) are of the form

$$x_\rho(k_\nu) = \frac{1}{N}\sum_{k_{\nu'}} x_\rho(k_{\nu'}). \tag{3.24}$$

Each of them is solved by $x_\rho(k_\nu) = const(\rho)$. More precisely, we get

$$A_\rho(k_\nu) = \frac{2G^2 c_\rho}{\Delta(E_\rho, k_\nu)}, \quad B_\rho(k_\nu) = \frac{[G\sqrt{2}(E_\rho - 2E_p(k_\nu))c_\rho]}{\Delta(E_\rho, k_\nu)}, \quad C_\rho(k_\nu) = \frac{\phi(E_\rho k_\nu)c_\rho}{\Delta(E_\rho, k_\nu)}, \tag{3.25}$$

with the normalization constant c_ρ being

$$c_\rho = \left(\sum_{k_\nu}[\phi^2(E_\rho, k_\nu) + 2G^2(E_\rho - 2E_p)^2 + 4G^4]/\Delta^2(E_\rho, k_\nu)\right)^{-1/2}. \tag{3.26}$$

3.2.2 *Numerical results*

Figure 3.4 illustrates the real-space Fourier transform of the amplitudes (3.25) for three different eigenstates belonging to the two-polariton spectrum. We consider three eigenstates located in the lower-lower (*LL*-) branch; their energies are singled out by arrows in Fig. 3.5. The states are labelled by indices ρ_1, ρ_2, and ρ_3 for increasing energies. The corresponding exemplar plots in Fig. 3.4 illustrate how the three components (A, B and C) of the wave function modify according to the region of the Brillouin zone.

For small ρ [$E_\rho \lesssim 2E_L(k_{SC})$] the exciton-light coupling prevails over the kinematic interaction. In this region the two-polariton *LL*-band almost overlaps with the bare photonic dispersion relation [cf. Figs. 3.3 and 2.1 for one excitation]; it means that the polaritons are mostly photonic. Since the dispersion curve is steep the group velocity is high and the photonic fraction of the two-polariton state does not have "time" to feel the weak kinematic interaction induced by the small excitonic fraction. In this regime the three components, A, B, and C behave as monochromatic free wave states (see upper panel in Fig. 3.4) except for the condition $C(n) = 0$ at interexcitonic separation of $n = 0$ sites. Each eigenstate is approximately described by a single wave vector k_ν belonging to the set (3.14). In particular, the excitonic fraction behaves as:

$$C_\nu(n) \propto (1 - \delta_{n0}) \cos ank_\nu. \tag{3.27}$$

For larger energies, that is larger values of ρ, both $B(n)$ and $C(n)$ display modulated oscillations, whose amplitude increases at larger interparticle separations. On the contrary the photon-photon amplitude $A(n)$ starts showing a pronounced peak at $n = 0$ (see middle plot in Fig. 3.4), proving a bunching feature.

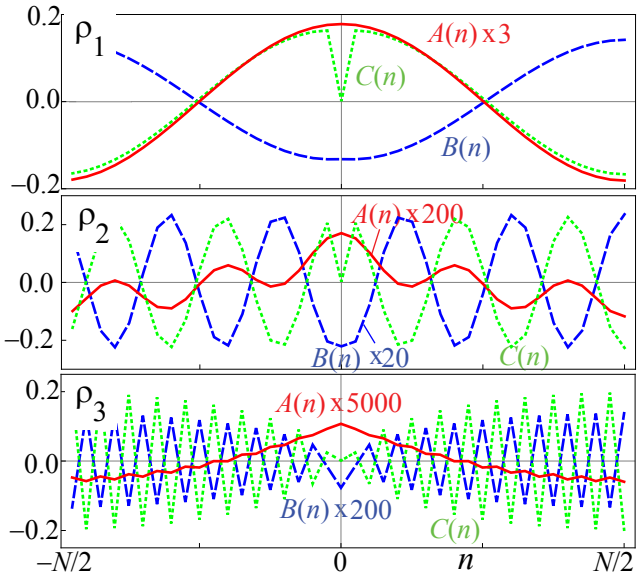

Figure 3.4: Photon-photon, exciton-photon, and exciton-exciton amplitudes $A(n) - \langle A(n)\rangle$ (solid red line), $B(n) - \langle B(n)\rangle$ (dashed blue line), $C(n) - \langle C(n)\rangle$ (dotted green line) as a function of the interparticle separation n. Here, the notation $\langle X(n)\rangle = \sum_n X(n)/N$ ($X = A, B, C$) is the average over all sites. Scaling factors are shown in the plots; $N = 40$; $a = 5.3$ μm. From top to bottom, panels refer to the points ρ_1, ρ_2, ρ_3 of Fig. 3.5.

Eventually, by further increasing the energies [$E_\rho \gtrsim 2E_L(k_{SC})$], the two-polariton LL-band almost overlaps with the bare excitonic dispersion relation [cf. Figs. 3.3 and 2.1 for one excitation]; here the two polaritons are mostly excitons. The bunching effect is further enhanced, since it is due to the kinematic interaction; however, as shown by the lower panel in Fig. 3.4, in term of amplitudes it looks like it actually becomes smaller: It is due to the fact that at larger energies the photonic fraction gets smaller and smaller, see Fig. 3.6. In other words there is a stronger bunching effect but a smaller photonic fraction which is available for it. For $E_\rho \gtrsim 2E_L(k_{SC})$ the polaritons effectively behave as two bare excitons interacting via kinematic interaction. In this case, as we shall see in the next section, the set $\{k_\nu\}$ does no properly describe the system anymore.

In order to better understand the effect of the kinematic interaction, and the reasons why it induces bunching in the photonic component, we have to study the case of two bare excitons.

3.3 Kinematics of two bare excitons

We consider two excitons uncoupled to light ($G \equiv 0$) accommodated on a one-dimensional lattice by sites n_1 and n_2 and separated by a distance

$n = |n_1 - n_2|$. These excitons interact kinematically by repelling each other away from the same site. The Schrödinger equation of the system is

$$EC^{(ex)}_{n_1 n_2} = 2E_0 C^{(ex)}_{n_1 n_2} + (1 - \delta_{n_1 n_2}) \sum_s \left(t_{n_1 s} C^{(ex)}_{s n_2} + t_{n_2 s} C^{(ex)}_{n_1 s} \right) \tag{3.28}$$

with t_{ij} being the long-range hopping constant.

Let us choose the index μ to label the eigenstates of Eq. (3.28). Since excitons are hard-core bosons, their compound amplitude obeys

$$C^{(ex)}_{nn} = 0. \tag{3.29}$$

By means of property (3.29) and moving in the framework of a nearest neighbor approximation for the hopping ($t_{ii+1} = t$), Eq. (3.28) can be straightforwardly expressed in following the form:

$$E^{(ex)}_\mu C^{(ex)}_\mu(n) = (1 - \delta_{n0}) \Big\{ 2E_0 C^{(ex)}_\mu(n) + 2t[C^{(ex)}_\mu(n+1) + C^{(ex)}_\mu(n-1)] \Big\}. \tag{3.30}$$

The normalized solutions of Eq. (3.30) are

$$C^{(ex)}_\mu(n) \equiv g_n(\mu) = \frac{\sqrt{2}(1 - \delta_{n0})}{\sqrt{N}} \sin |n| \kappa_\mu \tag{3.31}$$

with wave vectors κ_μ with

$$\kappa_\mu = \frac{2\pi\mu}{Na}, \tag{3.32}$$

and

$$\mu = \left[-\frac{(N-1)}{2}, \frac{(N-1)}{2} \right]. \tag{3.33}$$

Notice that since the index μ is half-integer the wave vectors of the set $\{\kappa_\mu\}$ lie exactly between the wave vectors belonging to the set $\{\kappa_\nu\}$ in Eq. (3.14).

The functions (3.31) constitute an orthonormal basis in both position and momentum spaces:

$$\begin{aligned} \textstyle\sum_n g_n(\mu_1) g_n(\mu_2) &= \delta_{|\mu_1|,|\mu_2|} \\ \textstyle\sum_\mu g_{n_1}(\mu) g_{n_2}(\mu) &= (1 - \delta_{n_1 0}) \delta_{|n_1|,|n_2|}. \end{aligned} \tag{3.34}$$

Also the spectrum of Eq. (3.30) is described by the wave vectors κ_μ:

$$E^{(ex)}_\mu = 2E_0 + 4t \cos a\kappa_\mu. \tag{3.35}$$

The fact that the elements of $\{\kappa_\mu\}$ are in-between those of $\{\kappa_\nu\}$ is of crucial importance; it entails the fact that amplitudes $C^{(ex)}_\mu(k_\nu)$ do not have poles

but rather a boosted contribution from the wave vectors $k_\nu \approx \kappa_\mu$. This is apparent from the denominator of the Fourier transform of Eq. (3.31):

$$C_\mu^{(ex)}(k) = \frac{\sin a\kappa_\mu + (-1)^\mu \sin ak_\nu \sin(ak_\nu N/2)}{\cos ak_\nu - \cos a\kappa_\mu}. \tag{3.36}$$

We see how the hard-core repulsion, despite being weak, can not be neglected at all since it modifies the nature of the excitonic modes in a non-perturbative way.

3.4 Discussion

As we have seen in the previous sections, at large ρ the problem of two effectively free excitons interacting via kinematic interaction is described by a wave vector set $\{\kappa_\mu\}$ with an half-integer index μ [see Eqs. (3.32) and (3.33)] whereas when the coupling of excitons to light gets sufficiently stronger than the kinematic interaction, we can describe the physics via a wave vector set $\{k_\nu\}$ with an integer index ν [see Eqs. (3.14) and (3.15)].

In other terms, the quantum number ρ which labels the two-polariton states is subjected (while increasing) to a gradual transition from ν-numbers to μ-numbers. In the basis $\{k_\nu\}$ this smooth passage represents the formation of wave packets.

The energy of the two-polariton state is well approximated by

$$E_\rho = 2E_L(k_{\text{eff}}(\rho)), \tag{3.37}$$

with

$$k_{\text{eff}}(\rho) = \frac{2\pi\rho_*}{Na}, \qquad \rho_* = (\rho - 1)\frac{N/2 - 1/2}{N/2 - 1}. \tag{3.38}$$

The effective wave vector k_{eff} and its label ρ_* properly describe the adiabatic passage from set $\{k_\nu\}$ to set $\{\kappa_\mu\}$: At small ρ, in fact, $k_{\text{eff}}(\rho) \approx k_\nu$ while, at large ρ, $k_{\text{eff}}(\rho) \approx \kappa_\mu$. This can be seen in Fig. 3.5 where the exact numerical results for the energies (cyan dots) are well reproduced by the following analytical expression:

$$E_\rho = 2E_L(k_{\text{eff}}(\rho)). \tag{3.39}$$

The presence of $\Delta(E_\rho, k_\nu)$ at the denominator of amplitudes (3.25) suggests that $A_\rho(k_\nu)$ displays a peak-like feature at $k_\nu \sim \pm k_{\text{eff}}(\rho)$ [see Eq. (3.19)]; these components, however, control the overall envelope of $A_\rho(k_\nu)$ only for $k_{\text{eff}}(\rho) < k_{SC}$. On the contrary, inside the weak coupling regime $k_{\text{eff}}(\rho) > k_{SC}$, the upper-upper ($UU$-) band dominates the general shape of the wave packet:

$$\frac{1}{\Delta(E_\rho, k_\nu)} \propto \frac{1}{E_U^2(k_\nu)} \approx \frac{1}{E_p^2(k_\nu)}. \tag{3.40}$$

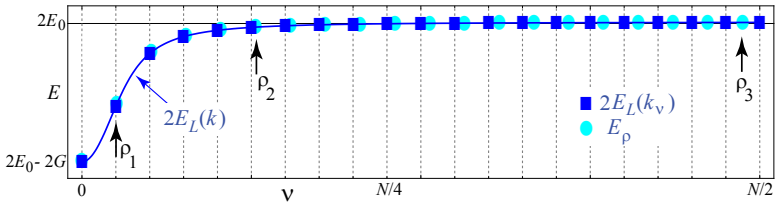

Figure 3.5: *LL*-band for two polaritons. Blue squares indicate the eingenenergies $2E_L(k_\nu)$ for two polariton that do not interact. The numerically exact energies are instead depicted as cyan dots and are indicated at the positions that correspond to $k_{\text{eff}}(\rho)$.

This resonant term decays extremely fast (see inset in Fig. 3.2); as a consequence, it suppresses the contributions $A_\rho(k_\nu \sim k_{\text{eff}}(\rho))$ to the wave packet which comes from the monochromatic waves with wave vectors $k_{\text{eff}}(\rho)$. We can conclude that for larger ρ only k_ν states which lie in the strong coupling regime $k_\nu \lesssim k_{SC}$ affect and effectively contribute to amplitudes $A_\rho(k_\nu)$ while higher-k_ν states are off resonance. When ρ is sufficiently large, amplitudes $A(k)$ show a pronounced cusp-like feature around $k_\nu = 0$. This bunching feature in momentum space is mapped into a bunching feature in real space too, as shown in the central and lower panels of Fig. 3.4. Let us finally point out that even for a polychromatic exciting source we will see bunching, which can not be averaged out since $A_\rho(n)$ displays bunching (i.e. maximum at $n = 0$) for all ρ such that $k_{\text{eff}}(\rho) \gtrsim k_{SC}$.

This is of course a qualitative explanation. These reasonings are better quantified in Appendix 3.A where we provide an explanation of the mechanism underlying the bunching phenomenon and demonstrate how the bunching arises from interference among different $A(k_\nu)$-components.

3.5 Control of photon-photon correlations

The platform that we propose (Fig. 3.1) can be realized by employing ultracold rubidium or strontium atoms in a Mott insulator state where each lattice site accommodates one atom: An example of such system is available in Ref. [99] where strontium atoms are placed inside the hollow core of a kagome-lattice photonic crystal.

We consider the $D_2(5^2S_{1/2} \rightarrow 5^2P_{3/2})$ transition of rubidium atoms at $E_0 = 384$ THz; the transition dipole is then $d = 4.22$ a.u. and we choose the radius of the fiber in such a way that the lowest cavity mode $E_p(0) = ck_\perp$ perfectly hits the atomic transition:

$$ck_\perp = E_0. \tag{3.41}$$

Since $k_\perp$ is defined by the condition $J_0(k_\perp R) = 0$ [cf. Eq.(3.4)] and the first

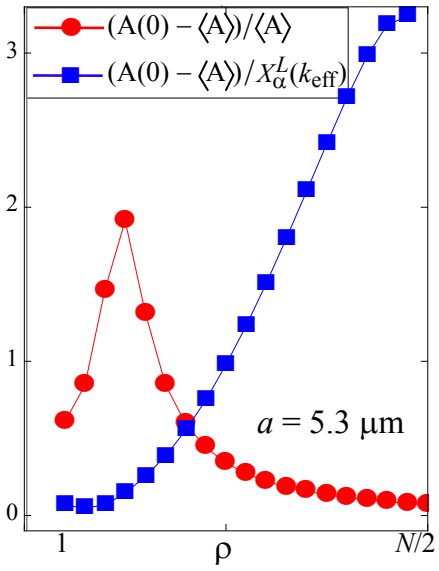

Figure 3.6: Strenght of the bunching in absolute value (red circles) or scaled by the photonic component of the corresponding eigenstate (blue squares) as a function of ρ.

zero of $J_0(x)$ is 2.4048, relation (3.41) becomes

$$c\frac{2.4048}{R} = E_0 \tag{3.42}$$

which results in a radius $R = 0.299$ μm.

In order to study the photon-photon correlations, we use the following figure of merit for bunching:

$$\begin{aligned} \Delta A_\rho &= \frac{|A_\rho(n=0)| - \langle A_\rho\rangle}{\langle A_\rho\rangle} \quad \text{if} \quad |A_\rho(n=0)| - \langle A_\rho\rangle > 0, \\ \Delta A_\rho &= 0 \quad \text{otherwise.} \end{aligned} \tag{3.43}$$

with

$$\langle A_\rho\rangle = \sum_n \frac{|A_\rho(n)|}{N}. \tag{3.44}$$

In Fig. 3.6 we plot ΔA_ρ as a function of ρ (red circles). At large energies ΔA displays an apparent decrease, which is due to a decrease of the photonic component in the two-polariton state. This can be proved by plotting ΔA_ρ divided by the photonic fraction $X^L_\alpha(k_{\rm eff}(\rho))$ in the two-polariton state when there is no kinematic interaction. This is shown by blue squares in Fig. 3.6 where the ratio monotonically increases. An analytical form for $X^L_\alpha(k_{\rm eff}(\rho))$ is given by Eq. (3.54).

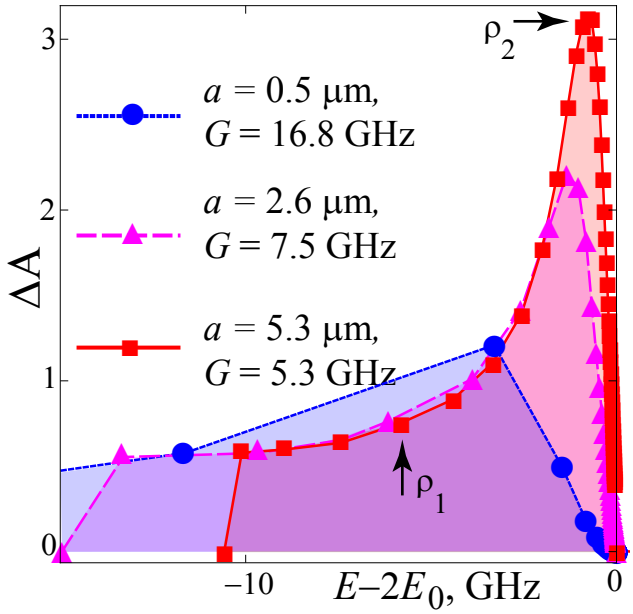

Figure 3.7: For $a = 532$ nm, 2.66 μm, and 5.32 μm, the real space amplitude $|\Delta A(n = 0)|$ is plotted versus the energy of the states belonging to the *LL*-band. Here, $N = 100$ atoms are considered.

In Fig. 3.7 we show the bunching strength $\Delta A(E_\rho)$ for several values of the lattice constant: $a = 532$ nm, $a = 2.66$ μm, and $a = 5.32$ μm. We see that ΔA_ρ increases as a increases. This may be a bit counterintuitive, since larger a entails a lower atomic density; however, as stated in Appendix 3.A [see Eq. (3.69) and discussion below] the optimal condition for bunching is having large photonic and excitonic fractions at the same time, which happens in the strong coupling regime only. Since the strong coupling region is of the order of k_{SC} [which is given by Eq. (3.20)] the best situation is when k_{SC} can be compared to the size of the Brillouin zone π/a:

$$\frac{ak_{SC}}{\pi} \approx 1. \tag{3.45}$$

Since $ak_{SC}/\pi \propto a^{3/4}$ it is clear that the larger a the better is. Unlike natural solids, where a is of the order of 5$\AA$ and electronic transitions are of the order of ~ 2 eV ($ak_{SC}/\pi \sim 2a\sqrt{w_0 G}/\pi c\hbar \sim 10^{-4}$), in cold-atom systems an extremely flat dispersion relation can be easily obtained, which in turn implies a pronounced bunching in a continous band with GHz width, see Fig. 3.7.

An other heuristic argumentation to explain why a larger a improves the bunching is the following: If we want the kinematic interaction to be effective, we need term (3.18) to be larger than the energy spacing between neighboring eigenstate, which according to Eq.(3.14) is $2\pi/Na$ and thus gets smaller as a increases.

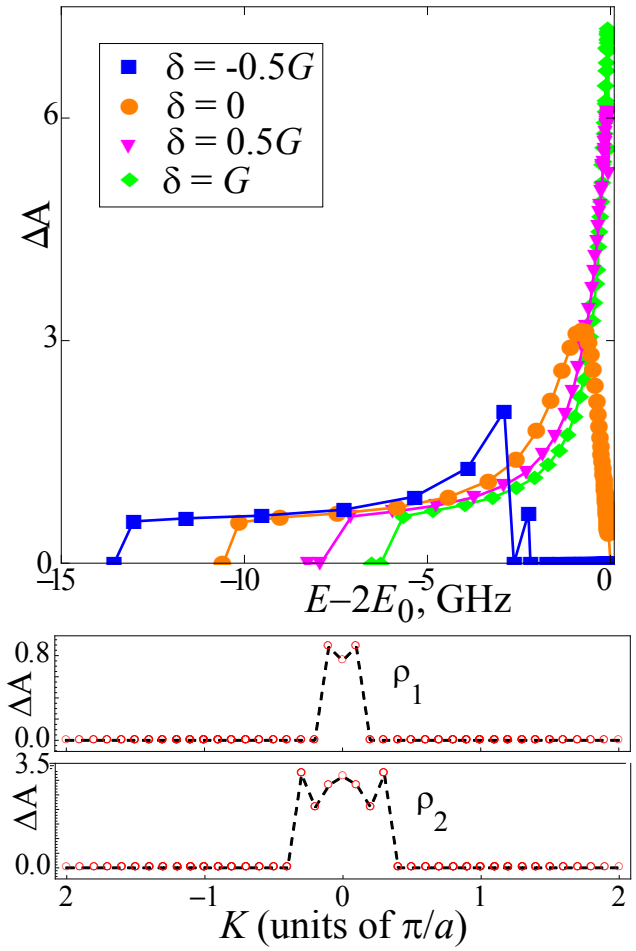

Figure 3.8: For $\delta = -G/2$, 0, $G/2$, and G, in the upper panel the bunching strength is plotted versus the energy of the states in the LL-band. Below, for the states indicated by ρ_1 (upper panel) and ρ_2 (lower panel) in Fig. 3.7, the plots show the figure of merit for bunching ΔA as a function of the total wave vector $K_{\nu'}$.

In Fig. 3.8 (upper panel) we plot ΔA as a function of energy for different detunings $\delta = E_p(0) - E_0$. Large negative detunings imply wider frequency windows for bunching, since the corresponding LL-bands $E_{LL}(k_{\text{eff}}(\rho))$ get wider. The central and lower panels, instead, demonstrate that the bunching is still present for nonvanishing center-of-mass momenta $K_{\nu'} \neq 0$. This is extremely important since can be observed in the experiments.

3.6 Gap states

When the energy $E_p(0)$ of the lowest cavity mode is greater than the energy E_0 of the atomic transition ($\delta > 0$) a gap immediately opens in the polaritonic spectrum. For a vanishing detuning $\delta = 0$ and a small lattice constant a there

is no gap since the LL-band at the border of the Brillouin zone $E_{LL}(\pi/a)$ is equal to LU-band for a vanishing wave vector $E_{LU}(0) = E_L(0) + E_U(0) = 2E_0$ [cf. Eq. (2.5)]:

$$E_{LL}(\pi/a) = E_{LU}(0) \tag{3.46}$$

This can be seen in Fig. 3.2.

If instead a is large enough to fulfill condition (3.45) the LL-band never overlaps the bare exciton band and a small gap opens, even at zero detuning:

$$\Delta_{LU} = E_{LU}(k_\nu = 0) - E_{LL}(k_\nu = \pi/a) > 0. \tag{3.47}$$

Here, bound states of two polaritons form inside the gap region, at the bottom of the LU-band. Their wave function has a well-defined shape: While the exciton-exciton (C) amplitude obeys the hard-core constraint and reaches its maximum for $|n| = 1$, photon-photon (A) and exciton-photon (B) amplitudes are peaked around $n = 0$ as it can be seen in Fig. 3.9. For moderate interatomic distance a, this state merges with the LU-band; however, as a becomes larger ($a \sim 25$ μm) it separates from the band and enters the gap. The larger is a, the deeper it will penetrate into the gap, which entails a larger bunching effect. An example is provideed by Fig. 3.9 for a low atomic density ($a = 50.3$ μm).

Given the repulsive nature of the kinematic interaction, it may seem counterintuitive the presence of bound states in the system. This gap bipolariton is analogous to the kinematic exciton-exciton bound state that overlaps with the continuum states in organic crystals with two molecules in a unit cell [258]; unlike there, however, the bipolariton bound state lies in the gap and is thus robust against decoherent process such as coupling to phononic modes or disorder.

Eventually, let us notice that by further lowering the atomic density the excitons start interacting with photons belonging to higher Brillouin zones. In other words, an exciton characterized by k_ν couples to photons with k_ν, but also $k_\nu \pm 2\pi/a$, $k_\nu \pm 4\pi/a$, and so on and so forth.

We have numerically checked that for our choice of parameters we enter this regime for $a \gtrsim 50$ μm.

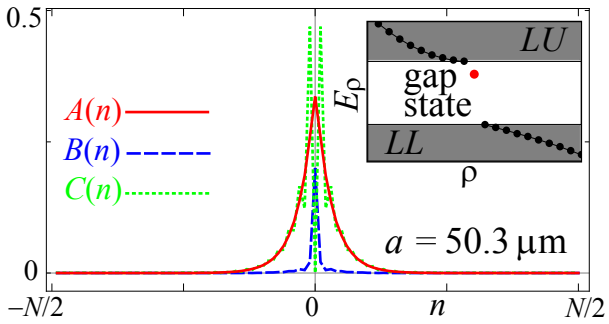

Figure 3.9: Wave function of a polariton-polariton bound state lying within the gap (see inset) for an interatomic separation $a = 50.3$ μm.

3.7 Conclusions

In this chapter we studied the two-photon correlations in a one-dimensional system, where an ordered chain of two-level cold atoms is confined in an optical lattice inside a hollow-core photonic crystal fiber. This system is for instance implemented in Ref. [99] with strontium atoms; here, we considered instead realistic parameters for the D_2 transition or rubidium atoms.

The correlations that we observed suggest an attraction between photons, which tend to bunch in the continuuum; such effect occurs over a frequency range of several GHz. This is an improvement over the typical correlations observed for example in nonlinear Rydberg media under electromagnetically induced transparency where the frequency range is of the order of MHz.

We also proved both analytically and numerically that this bunching effect can be easily manipulated by tuning the spacing a of the confining optical lattice.

Our findings hold true as long as the Rabi splitting $2G$ between the lower and upper polaritons is much larger than the sum of the excitonic and photonic broadenings, which is true for a high-finesse cavity and if the atomic Mott insulator state is accurately realized. Provided that these conditions are satisfied, the scheme that we propose can be possibly implemented in alternative ways other than one-dimensional fibers, such as nanophotonic waveguides [93, 95, 120, 237–241, 259, 260] and metallic nanowires [96].

Finally, in the last section of this chapter we showed that for a low enough atomic density, a gap opens in the two-polariton spectrum and despite the underlying repulsive interaction, bipolaritonic bound state arise. In this chapter we did not consider dynamical interactions. Dipole forces could introduce additional kinds of bound states, both in the gap or below the polaritonic LL-band (see chapter 4) analogously to what happens in Refs. [261, 262] for atoms in an optical lattice or in Ref. [263] for a Jaynes-Cummings-Hubbard model.

As we shall see in the next chapter, the same phenomenon of photonic bunching takes place when considering a linear chain of Rydberg atoms inside a one-dimensional resonator. Since two excited Rydberg atoms have to stay away from each other by a distance which can not be shorter than twice the Rydberg radius (this phenomenon is called Rydberg blockade), the mismatch between the quantization volumes induced by the presence of the kinematic interaction is much larger. Moreover, unlike low-excited atoms, Rydberg atoms show nonnegligible long-range interactions; these dipole-dipole or van der Waals dynamics makes the nonlinear physics of the system even wealthier.

Appendices

3.A Formation of wave packets

In the Schrödinger equation obtained by letting the Hamiltonian (3.1) act on the wave function (3.8) we can distinguish two subsystems, depending on whether there is kinematic interaction or not. In the subsystem composed of two photons or one photon and one exciton there is no hard-core repulsion and the physics is properly described by wave vectors k_ν [see Eqs. (3.14) and (3.15)]. In the presence of kinematic interaction, however, that is in the subsystem composed of two-exciton states, the physics is better described by wave vectors κ_μ [see Eqs. (3.32) and (3.33)]. The collective light-matter coupling G mixes these two sets of quantum numbers ($\{k_\nu\}$ and $\{\kappa_\mu\}$) so that wave packets form in the wave vector basis $\{k_\nu\}$.

Lowest-energy states are almost photon-like, meaning that there the coupling to light prevails over the kinematic interaction; in that case, as shown in Sec. 3.4, the two-polariton states are well described by wave vectors $\{k_\nu\}$. At largest energies however, when polaritons resemble bare excitons, the two-polariton states are better characterized by wave vectors $\{\kappa_\mu\}$. The shift from ν- to μ-quantum numbers is continuous.

In this Appendix we quantify this gradual transition by proving that the bunching is indeed caused by the intermixing of the two sets of ν- and μ-quantum numbers. We also demonstrate that the bunching feature is optimal when both the excitonic and photonic fractions are significantly present: On the one hand, the excitonic fraction is required due to its kinematic interaction, which is the necessary mechanism for the bunching itself; on the other hand, the photonic fraction must be large too, in order to make the bunching visible.

We define the operators $\alpha_n^\dagger$, $\beta_n^\dagger$ and $\gamma_n^\dagger$, which create, respectively, two photons, one photon and one exciton, and two excitons with an interparticle separation n.

In terms of these three operators the two-particle wave function can be written as

$$|\Psi\rangle = \sum_s \Big[A(s)\,|\alpha_s\rangle + B(s)\,|\beta_s\rangle + C(s)\,|\gamma_s\rangle \Big] \tag{3.48}$$

while the Hamiltonian

$$\tilde{H}_{\text{eff}} = \tilde{H}_{AB} + \tilde{H}_C^{(KI)} + \tilde{H}_{AB-C}^{(KI)} \tag{3.49}$$

is the sum of three terms:

$$\begin{aligned}\tilde{H}_{AB} &= \sum_{n,m}\left[2E_p(n-m)\alpha_n^\dagger\alpha_m + \left(E_p(n-m)+E_e(n-m)\right)\beta_n^\dagger\beta_m\right] \\ &\quad + G\sqrt{2}\sum_n\left[\alpha_n^\dagger\beta_n + \beta_n^\dagger\alpha_n\right], \\ \tilde{H}_C^{(KI)} &= \sum_{n,m}(1-\delta_{n0})2E_e(n-m)\gamma_n^\dagger\gamma_m, \\ \tilde{H}_{AB-C}^{(KI)} &= G\sqrt{2}\sum_n(1-\delta_{n0})\left[\gamma_n^\dagger\beta_n + \beta_n^\dagger\gamma_n\right].\end{aligned} \tag{3.50}$$

The Hamiltonian $\tilde{H}_{AB-C}^{(KI)}$ couples the noninteracting (AB) and the interacting (C) subsystems.

The corresponding Schrödinger equation is analogous to Eqs. (3.11).

The Hamiltonian $\tilde{H}_{AB}$ is diagonal in the following operatorial basis:

$$\xi_{i\nu}^\dagger = X_\alpha^{i\nu}\alpha_\nu^\dagger + X_\beta^{i\nu}\beta_\nu^\dagger, \tag{3.51}$$

as

$$\tilde{H}_{AB} = \sum_{i,\nu} E_{pi\nu}\xi_{i\nu}^\dagger\xi_{i\nu} \tag{3.52}$$

with $i = (U, L)$ being the polariton index; ν runs in the interval (3.15) and

$$E_{p,(i=U,L)\nu} = E_{p\nu} + \frac{E_{e\nu} + E_{p\nu} \pm \sqrt{(E_{e\nu}-E_{p\nu})^2 + 8G^2}}{2} \tag{3.53}$$

where $E_{p\nu} \equiv E_p(k_\nu)$. Energies $E_{p,(i=U,L)\nu}$ are made up by the energy of one photon plus the energy of one exciton-polariton whose coupling rate is $\sqrt{2}G$. This could have been predicted by studying Eqs. (3.17) in the absence of exciton-exciton amplitudes, $C \equiv 0$.

In Eq. (3.51)

$$X_\alpha^{i\nu} = \sqrt{\frac{\left(E_{p,i\nu} - E_{p\nu} - E_{e\nu}\right)^2}{2G^2 + \left(E_{p,i\nu} - E_{p\nu} - E_{e\nu}\right)^2}}, \qquad X_\beta^{i\nu} = \sqrt{\frac{2G^2}{2G^2 + \left(E_{p,i\nu} - E_{p\nu} - E_{e\nu}\right)^2}}. \tag{3.54}$$

The Hamiltonian $\tilde{H}_C^{(KI)}$ of the interacting subsystem can be instead diagonalized as

$$\tilde{H}_C^{(KI)} = \sum_\mu E_\mu^{(ex)}\chi_\mu^\dagger\chi_\mu. \tag{3.55}$$

The spectrum $E_\mu^{(ex)}$ was introduced in Eq. (3.35); the operators are

$$\chi_\mu^\dagger = \sum_{s=-N/2+1}^{N/2} g_s(\mu)\gamma_s^\dagger \tag{3.56}$$

where the orthonormal g-functions are defined in Eq. (3.31).

Finally, the coupling operator $\tilde{H}_{AB-C}$ can be expressed by employing both ξ- and χ-operators as

$$\tilde{H}^{(KI)}_{AB-C} = \frac{G}{N}\sum_{i\nu\mu}\Lambda_{\nu\mu}X^{i\nu}_{\beta}\left(\chi^{\dagger}_{\mu}\xi_{i\nu}+\xi^{\dagger}_{i\nu}\chi_{\mu}\right) \tag{3.57}$$

with $\Lambda_{\nu\mu}$ being

$$\Lambda_{\nu\mu} = \frac{1}{2}\left[\cot\frac{\pi(\nu+|\mu|)}{N} - \cot\frac{\pi(\nu-|\mu|)}{N}\right]. \tag{3.58}$$

These coefficients are ultimately responsible for coupling the wave vectors k_ν and κ_μ and inducing the interference phenomena that lead to photon-photon bunching.

We define the wave function

$$|\Psi\rangle = \sum_{i\nu} p_{i\nu}\,|\xi_{i\nu}\rangle + \sum_{\mu} e_{\mu}\,|\chi_{\mu}\rangle\,; \tag{3.59}$$

by applying $\tilde{H}_{\text{eff}}$ on it, we get

$$\left(E-E_{p,i\nu}\right)p_{i\nu} = \frac{GX^{i\nu}_{\beta}}{N}\sum_{\mu}\Lambda_{\nu\mu}e_{\mu}, \qquad \left(E-E_{\mu}\right)e_{\mu} = \frac{G}{N}\sum_{i\nu}X^{i\nu}_{\beta}\Lambda_{\nu\mu}p_{i\nu}. \tag{3.60}$$

In the equation for p-amplitudes we replace e-amplitudes by their values obtained from the second equation in (3.60). If we neglect the hopping ($t = 0$) we end up with the following self-consistent equation:

$$\left(E-E_{p,i\nu}\right)p_{i\nu} = \frac{G^2X^{i\nu}_{\beta}}{2N(E-2E_0)}\sum_{i'\nu'}F_{\nu\nu'}X^{i'\nu'}_{\beta}\,p_{i'\nu'} \tag{3.61}$$

where

$$F_{\nu\nu'} = N\left(\delta_{\nu,\nu'}+\delta_{\nu,-\nu'}\right) - \frac{2}{N}. \tag{3.62}$$

The kernel function $F_{\nu\nu'}$ represents two well-distinguished processes: The δ-terms describe elastic-scattering phenomena; the $2/N$ term is instead responsible for the development of wave packets.

The real-space amplitude $A(n)$ for having two photons at a distance of n sites from each other is

$$A(n) = \langle\alpha_n|\,\Psi\rangle = \frac{1}{\sqrt{N}}\sum_{i\nu}p_{i\nu}X^{i\nu}_{\alpha}e^{-\frac{2\pi i\nu n}{N}}. \tag{3.63}$$

The exponential weight decays fast and suppresses the amplitude when n is large. On the contrary for $n = 0$ the phase vanishes and the amplitude for

two photons being accommodated by the same site results from a collective superposition of p-amplitudes:

$$A(0) = \frac{1}{N} \sum_{i\nu} p_{i\nu} X_\alpha^{i\nu}. \tag{3.64}$$

By means of Eqs. (3.60) we obtain

$$A_\rho(0) = \frac{G}{N\sqrt{N}} \sum_{i\nu} \frac{X_\alpha^{i\nu} X_\beta^{i\nu}}{(E_\rho - E_{p,i\nu})} \sum_\mu \Lambda_{\nu\mu} e_\mu. \tag{3.65}$$

A first important point in Eq. (3.65) is the resonant term $1/(E_\rho - E_{p,i\nu})$; owing to the mismatch between the wave vectors $\{k_\nu\}$ and $\{k_\mu\}$ this term will never diverge; the energy E_ρ indeed always lies in-between neighboring eigenenergies of the ideal-case spectrum. The absence of real energetic poles avoids the issue of having an imaginary part in the energy, and consequently a decay in time. Nevertheless, the term $1/(E_\rho - E_{p,i\nu})$ contains precious information concerning the bunching: Even though it has no real poles (which is a good thing) it has quasipoles as soon as E_ρ gets resonant with the band $E_{p,i\nu}$; this gives us information to predict whether a certain eigenstate at a certain energy will display bunching or not. It also follows that for

$$E_\rho < \min\left\{E_{p,i\nu}\right\} = E_{p,L,\nu=0} \tag{3.66}$$

the photons do not bunch and display a free behavior. We conclude that even though the eigenstates of the noninteracting subsystem with spectrum $E_{p,i\nu}$ are not real excitations (single polaritons) of the system, they are important since they are virtual states through which the two excitons communicate with each other. Indeed, as it can be deduced from the denominator $E_\rho - E_{p,i\nu}$ of Eq. (3.65), the nonphysical energies $E_{p,i\nu}$ act as channels for virtual scattering.

From the representations (3.8) and (3.48) of the wave function $|\Psi\rangle$ we get the relation

$$C(s) = \langle \gamma_s | \Psi \rangle = \sum_\mu e_\mu g_s(\mu) \tag{3.67}$$

which, in turn, leads to

$$2e_\mu = \sum_s g_s(\mu) C(s). \tag{3.68}$$

At large energies (and quantum numbers ρ) the two-polariton states behave as two-exciton states so that we can approximate amplitudes $C(s)$ in Eq. (3.68) with amplitudes (3.31). In order to take into account the presence of a nonvanishing photon-exciton and exciton-exciton components we introduce a normalization coefficient X_γ^ρ. The orthogonality properties (3.34) of g-functions eventually lead to

$$A_\rho(0) \approx \frac{G X_\gamma^\rho}{N^{\frac{3}{2}}} \sum_{i=L,U} \sum_\nu \frac{X_\alpha^{i\nu} X_\beta^{i\nu}}{(E_\rho - E_{p,i\nu})} \Lambda_{\nu\mu}. \tag{3.69}$$

From Eq. (3.69) we see how exciton-exciton amplitude X_α^{iv} and photon-photon amplitude X_β^{iv} have to be both large if we want the corresponding state to contribute in a relevant way to $A(0)$. This condition, which can be approximately written as

$$|X_\alpha^{iv}| \approx |X_\beta^{iv}|, \tag{3.70}$$

is satisfied only in the strong coupling region.

Since a larger lattice constant a implies a smoother transition between photonic-like and excitonic-like parts of the LL-band, it also entails a larger strong coupling region over the Brillouin zone. This is why a large a is favorable for a large bunching. This also explains why in natural solids, where interparticle separation is of the order of 1 $\mathring{A}$, the kinematic interaction does not play an important role as it does in the atomic systems.

4
Cavity polaritons with Rydberg blockade and long-range interactions

In this final chapter we extend the results of the previous chapter to Rydberg atoms [60, 264]. We propose to implement strong interactions between single photons of a cavity coupled to an ordered array of Rydberg atoms. Here, we consider a one-dimensional chain of Rydberg atoms trapped in an optical lattice in the Mott insulator state inside a hollow-core photonic crystal fiber, as shown in Fig. 4.1. Other possible realizations are arrays of atoms trapped outside of a nanophotonic waveguide and coupled to the evanescent light field [93, 95, 237–241].

Contrary to works that employ the electromagnetic induced transparency technique in gaseous systems [31, 53–56] where Rydberg atoms are modelled as three-level emitters, here we model them as two-level systems. One-photon scheme in excitations of Rydberg states via ultraviolet lasers is nowadays within reach [265–268] and adopted in several theoretical proposals [269, 270]. Rydberg atoms dynamically interact via long-range dipole-dipole or van der Waals forces, which ultimately entail the so-called Rydberg blockade effect [57–62]. If a low-excited atom can not accommodate two excitons (usual kinematic interaction), the blockade effect greatly enhances such excluded volume leading to a superatom whose radius is equal to the blockade radius r_B. These superatoms effectively behaving as extended two-level systems, the accommodated excitons interact via an extended (repulsive) kinematic interaction. In other words, propagating excitons behave as hard-core bosons whose hard core has a one-dimensional volume equal to $2r_B$. As we shall see later, such large excluded volume leads to a more visible bunching feature with respect to the case of low-excited atoms, meaning that the deviation of the wave functions from the plane-wave-like behavior is more pronounced. Furthermore, Rydberg atoms also allow for the observation of antibunching in the photonic component of the two-polariton wave function associated to the lowest energy eigenstates.

This chapter is organized as follows. In Sec. 4.1 we introduce the model. In Sec. 4.2 we solve the associated Schrödinger equation when the center of mass of the two-excitation system is at rest. In Sec. 4.3 we numerically solve the problem and plot the wave functions for three exemplar eigenstates. In Sec. 4.4 we solve the problem of two bare excitons interacting via

the extended kinematic interaction. Then, we use these results to study the kinematics of two polaritons in Sec. 4.5. Sec. 4.6 is devoted to the numerical study of bunching. In Sec. 4.7 we turn on the dynamical interaction and study its contributions; for an attractive interaction we look at the bound states that form below the continuum. Sec. 4.8 is devoted to the study of the in-gap bipolariton states, which form for a kinematic or repulsive dynamical interaction. Finally, Sec. 4.9 summarizes the conclusions.

In Appendix 4.A we review the basic properties of Rydberg atoms. In Appendix 4.B we provide an analytical solution for a generic total wave vector. In Appendix 4.C we work out the dispersion relation for the simple case of two excitons that interact only dynamically.

The results from this chapter have been collected in the following paper, submitted (not yet published) during the PhD:

M. Litinskaya, E. Tignone, G. Pupillo,
Cavity polaritons with Rydberg blockade and long-range interactions,
(submitted to *Journal of Physics B: Atomic, Molecular and Optical Physics*)

4.1 The model

The model that we propose is illustrated in Fig. 4.1. We consider an ordered array of N Rydberg atoms separated by a lattice spacing a and placed inside a hollow-core photonic crystal fiber; the transition frequency for each atom is E_0 whereas the hopping constant is $t \propto d^2/a^3$ with d being the transition dipole moment. We consider nearest-neighbor hopping only. $D(n-m)$ accounts for long-range (dipole-dipole or van der Waals) interaction between atomic excitations located at sites n and m. The Hamiltonian describing the dynamics of such system is [cf. Eqs. (2.3) and (3.1)]:

$$\begin{aligned} H = {} & E_0 \sum_s P_s^\dagger P_s + t \sum_s \left(P_s^\dagger P_{s+1} + P_s^\dagger P_{s-1} \right) \\ & + \frac{1}{2} \sum_{s,p} D(s-p) P_s^\dagger P_p^\dagger P_s P_p + \sum_{q_\nu} E_p(q_\nu) b^\dagger(q_\nu) b(q_\nu) \\ & + \sum_{q_\nu} E_p(q_\nu) b^\dagger(q_\nu) b(q_\nu) + g \sum_{s,q_\nu} \left(P_s^\dagger b(q_\nu) e^{i q_\nu s} + P_s b^\dagger(q_\nu) e^{-i q_\nu s} \right). \end{aligned} \tag{4.1}$$

Operators $P_s^\dagger$ and $b^\dagger(q_\nu)$ create, respectively, an atomic excitation at site s and a cavity photon characterized by a wave vector q_ν along the cavity axis. As usually, the photonic dispersion relation is

$$E_p(q_\nu) = c\sqrt{q_\nu^2 + q_\perp^2} \tag{4.2}$$

with

$$q_\nu = \frac{2\pi\nu}{Na} \tag{4.3}$$

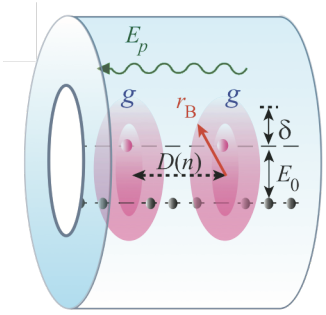

Figure 4.1: Sketch of the ensemble of two-level Rydberg atoms inside the hollow core of a photonic crystal fiber; the blockade radius is r_B; g is the light-emitter coupling, E_p is the photonic field in the cavity while E_0 is the energy of the atomic transition; $\delta = E_p(0) - E_0$ is the detuning. D(n) is the dynamical interaction, which depends on the exciton-exciton separation.

and ν an integer; c indicates the speed of light through a vacuum whereas $q_\perp$ is the transverse momentum of the photon and satisfies condition (3.4) with R being the radius of the fiber core.

The light-matter coupling strength is

$$g = d\sqrt{\frac{2\pi E_0}{V}} \tag{4.4}$$

with $V = \pi R^2 Na$ being the the volume of the cylindric core.

4.2 Analytical solution

As in Chapter 3, we will refer to the lower-lower, lower-upper, and upper-upper polaritonic bands, as *LL*-, *LU*-, and *UU*-band, respectively. The effect of the hopping is negligible compared to that arising from the strong intracavity light-matter coupling. Indeed, in Fig. 4.2 the curvature of the dispersion relation for a bare exciton (lower dashed line) is barely visible, $E_e(k_\nu) \approx E_0$.

Since we are considering two excitations, following the previous chapter [see Eq. (3.8)] we can restrict our wave function to a two-particle subspace:

$$|\Psi\rangle = \sum_{nm} \left\{ \frac{A_{nm}}{\sqrt{2}} |b_n^\dagger b_m^\dagger\rangle + B_{nm} |b_n^\dagger P_m^\dagger\rangle + \frac{C_{nm}}{\sqrt{2}} |P_n^\dagger P_m^\dagger\rangle \right\}, \tag{4.5}$$

where, because of indistinguishability, both photon-photon and exciton-exciton amplitudes are symmetric ($A_{nm} = A_{mn}$, $C_{nm} = C_{mn}$). Contrary, since a photon and an exciton are distinguishable quanta, B-coefficients do not have a particular symmetry. We decompose B_{nm} into their symmetric (S) and antisymmetric (A) components, $B_{nm} = B^S_{nm} + B^A_{nm}$.

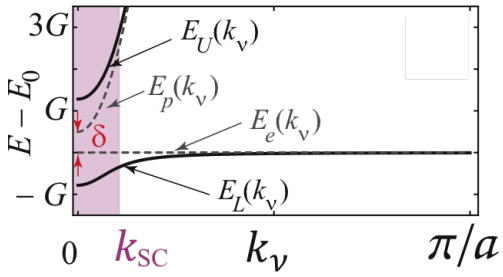

Figure 4.2: Band structure in the presence of an individual excitation (cf. Fig. 2.1); only the positive half of the Brillouin zone is depicted. $E_L(k)$ and $E_U(k)$ indicate the energy bands of the lower and upper polaritons, respectively; $E_p(k)$ and $E_e(k)$ are the energies of a free photon and a free exciton; a is the lattice constant. We take a positive detuning $\delta = E_p(0) - E_0$. The shaded pink area corresponds to the strong coupling region $k_\nu < k_{SC}$ where k_{SC} is defined in Eq. (3.20).

Beyond the usual kinematic interaction between atomic excitations, originating from atomic saturability [271] (see Chapter 3), here we have to take into account the Rydberg blockade effect: The presence of an atomic excitation shifts, via its dynamical interaction D, the energy levels of neighboring atoms out of resonance [58, 59, 272]; this effect is described in Appendix 4.A. In order to describe the blockade mechanism we introduce a blockade radius r_B and assume that interexciton separations less than $2(r_B/a) + 1$ lattice sites are forbidden. The radius r_B can greatly exceed the lattice spacing a. Notice that for $r_B = 0$ this problem reduces to the ordinary kinematic interaction described in the previous chapter, which only accounts for atomic saturability of the two-level emitters.

In order to describe this extended kinematic repulsion we remove the two-exciton states $|P_n P_m\rangle$ with $|n - m| \leq 2(r_B/a) + 1$ from the total basis set. We consider the Schrödinger equation obtained by applying Hamiltonian (4.1) to wave function (4.5) and multiply the terms proportional to $|P_n P_m\rangle$ by $(1 - \theta(n - m))$ with the θ-function defined by:

$$\begin{aligned} \theta(x) &= 0 \quad \text{if} \quad |x| \leq r_B/a, \\ \theta(x) &= 1 \quad \text{otherwise.} \end{aligned} \tag{4.6}$$

Consequently, the amplitudes C_{nm} associated to forbidden states where two atomic excitations lie inside the same blockade sphere [$|n-m| \leq 2(r_B/a)+1$] are not defined. For convenience we choose:

$$\theta(n - m)C_{nm} = 0. \tag{4.7}$$

Notice that $\theta(n - m)$ reduces to δ_{nm} for low-excited atoms, so that constraint (4.7) reduces to condition (3.10)

We solve the symmetrized Schrödinger equation and Fourier transform the solution. Afterwards, we follow the typical procedure for taking advan-

tage of the translational invariance of the overall system and we define the total and relative wave vectors:

$$K_{\nu'} = q_{\nu_1} + q_{\nu_2} \quad \text{and} \quad k_\nu = \frac{q_{\nu_1} - q_{\nu_2}}{2}, \tag{4.8}$$

in terms of which we rewrite the solution.

According the Noether's theorem [273] the total wave vector $K_{\nu'}$ for two bare atomic excitations is a good quantum number, so that each eigenstate is labeled by a certain $K_{\nu'}$. Here we deal with the simpler case $K_{\nu'} = 0$ and briefly extend the results to the $K_{\nu'} \neq 0$ case. The solution for $K_{\nu'} \neq 0$ is reported in Appendix 4.B.

For $K_{\nu'} = 0$ only the symmetric component of the mixed amplitudes survives, $B = B^S$. Since $q_{\nu_2} = -q_{\nu_1}$ we get

$$k_\nu = \frac{2\pi\nu}{Na} \tag{4.9}$$

with an index ν covering the usual domain within the first Brillouin zone [257]:

$$\nu = -\frac{N}{2} + 1, ..., \frac{N}{2}. \tag{4.10}$$

For a vanishing total wave vector ($K_{\nu'} = 0$), we straightforwardly obtain that $A-$, $B-$, and C-amplitudes satisfy a set of equations analogous to Eqs. (3.17) in presence of Rydberg atoms. Again, pedix ρ labels the two-polariton states:

$$\begin{aligned}
E_\rho A_\rho(k_\nu) &= 2E_p(k_\nu)A_\rho(k_\nu) + G\sqrt{2}B_\rho(k_\nu), \\
E_\rho B_\rho(k_\nu) &= \left[E_p(k_\nu) + E_e(k_\nu)\right]B_\rho(k_\nu) + G\sqrt{2}[A_\rho(k_\nu) + C_\rho(k_\nu)], \\
E_\rho C_\rho(k_\nu) &= 2E_e(k_\nu)C_\rho(k_\nu) + G\sqrt{2}B_\rho(k_\nu) + S_\rho(k_\nu).
\end{aligned} \tag{4.11}$$

In the exciton-exciton equation, the term $S_\rho(k_\nu)$ describes scattering processes between polaritons, induced by both dynamical and kinematic interactions:

$$\begin{aligned}
S_\rho(k_\nu) = \frac{1}{N}\sum_{q_\nu}\Big\{&D(k_\nu - q_\nu)C_\rho(q_\nu) - \theta(k_\nu - q_\nu)G\sqrt{2}B_\rho(q_\nu) \\
&- \theta(k_\nu - q_\nu)\, 4t\cos aq_\nu\, C_\rho(q_\nu)\Big\}.
\end{aligned} \tag{4.12}$$

The excitonic energy is $E_e(k_\nu) = E_0 + 2t\cos ak_\nu$ whereas $G = g\sqrt{N}$ is as usually the collective coupling between the Dicke state and the cavity mode [see Eq. (2.6)].

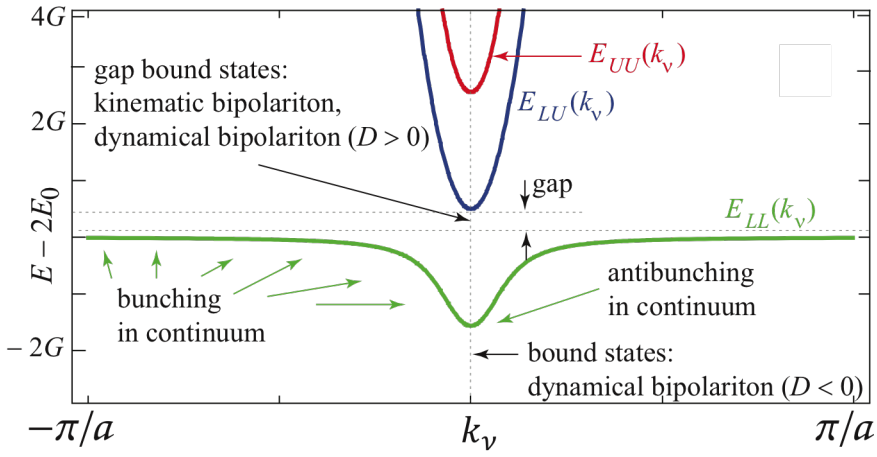

Figure 4.3: Band structure in the two-excitation case. $E_{LL}(k_\nu) = 2E_L(k_\nu)$, $E_{LU}(k_\nu) = E_{UL}(k_\nu) = E_L(k_\nu) + E_U(k_\nu)$, $E_{UU}(k_\nu) = 2E_U(k_\nu)$; a is the lattice constant. The figure summarizes the main results from this chapter.

If the polaritons do not interact with each other, Eqs. (4.11) reduce to the simple form

$$X(k_\nu)\Delta(E, k_\nu) = 0, \tag{4.13}$$

with X staying for A, B or C, and

$$\Delta(E, k_\nu) = [E - 2E_L(k_\nu)][E - E_L(k_\nu) - E_U(k_\nu)][E - 2E_U(k_\nu)]. \tag{4.14}$$

In the dispersion relation (4.14) $E_L(k_\nu)$ and $E_U(k_\nu)$ are the energies of the free lower and upper polaritons respectively, see Eqs. (2.5). These are shown in Fig. 4.2. The two-particle eigenenergies [the roots of $\Delta(E, k_\nu)$] are the possible combinations of the kind $E_{L,U}(k_\nu) + E_{L,U}(k_\nu)$ (see Fig.4.3).

Now, we turn on the interaction between polaritons, $S(k) \neq 0$; in this case, a good solution to system (4.11) is given by Eqs. (3.25) with $\theta(k)$ instead of c_ρ.

In the previous chapter it was shown that in the absence of dynamical interaction ($D = 0$) and for low-excited atoms ($r_B = 0$) the actual spectrum was described by a set of wave vectors (3.32) which were gradually shifted with respect to the ideal wave vectors (3.14): The deviation was accumulated with the increase of the polariton-polariton label ρ, as depicted in Fig. 3.5. This cumulative displacement leaded to the exclusion of the state associated to two atomic excitations located at the same site, as expressed in condition (3.10), which ultimately entailed the fact that in the original wave vector set (3.14) the eigenstates looked like wave packets, whose mutual interference caused a bunching pattern.

In the rest of the chapter we fully generalize this model to Rydberg atoms. We demonstrate that the bunching is greatly enhanced for large blockade radii. Then, we will shortly discuss the effect of a long-range dynamical interaction on photonic correlations.

4.3 Numerical solution

Let us study the effect of the blockade mechanism. For the moment we neglect the dynamical interaction, $D = 0$. In Fig. 4.4, for $r_B = 0$ (left column) and $10a$ (right column), we plot the real-space Fourier transform and the amplitudes that solve Eqs. (4.11) plus the condition $\sum_q \theta(k-q)C(q) \equiv 0$; we center the amplitudes about their average values $\langle X(n)\rangle = \sum_n X(n)/N$ ($X = A$,B, or C). A well-defined behavior can be observed; for lowest-energy eigenstates (upper plots) lying at the bottom of the LL-band (small ρ), all three amplitudes oscillate as:

$$X_\rho \propto \cos(2\pi\nu/Na) \tag{4.15}$$

except for interatomic separations within a blockade sphere ($|n| < 2(r_B/a) + 1$), where C-amplitudes vanish because of the kinematic interaction. The photons, which are coupled to the excitons, tend to follow the exciton-exciton repulsion and effectively repel each other. This antibunching is particularly visible for large r_B [panel (b)] where a clear depletion in the photonic A-amplitude occurs in correspondence of the Rydberg blockade sphere. For larger energies the behavior of the photonic component drastically changes and photons show bunching (although the excitons keep repelling each other), see panel (c). As expected, also in this case a large r_B enhances the deformation [panel (d)]. A further increase of ρ [panels (e) and (f)] leads to an apparent decrease of the bunching cusp; this effect is due to the fact that when we exceed the strong coupling regime the total wave function becomes more and more excitonic. In other words, the photonic fraction gets smaller and smaller. It was shown in the previous chapter that in fact the strength of the bunching mechanism increases as ρ increases, see blue squares in Fig. 3.6. For even larger ρ, associated to eigenstates belonging to the LU- and UU-band (not shown in the figure), the bunching is in principle still observable since the polaritons are mainly photonic (see Fig. 4.2 for the single-particle case). Yet one has to verify that such states can be experimentally excited.

In Chapter 3 we have shown that for the usual kinematic interaction, the bunching feature derives from a mismatch between two quantization volumes: The volume for the noninteracting subsystem and the volume for the exciton-exciton subsystem, where the state $C(n = 0)$ was excluded. Here we want to generalize that argumentation. We will first solve the Schrödinger equation for two bare excitons.

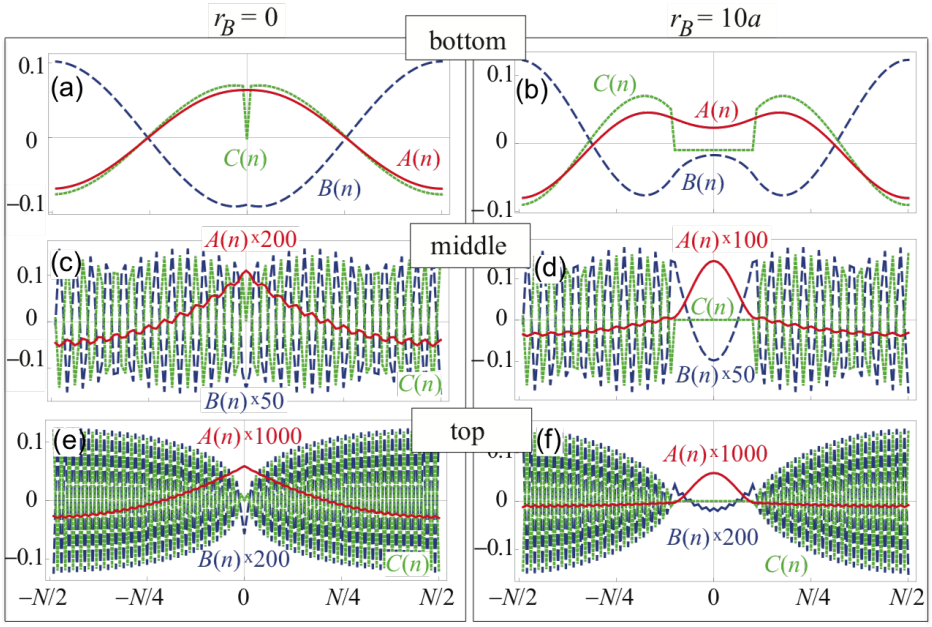

Figure 4.4: Amplitudes $C(n) - \langle C(n)\rangle$ (green dotted line), $B(n) - \langle B(n)\rangle$ (blue dashed line), and $A(n) - \langle A(n)\rangle$ (red solid line) for $r_B = 0$ (left column) and $r_B = 10a$ (right column); we consider $N = 100$ atoms loaded in the fiber. First row represents a low-energy state belonging to the bottom of the polaritonic *LL*-band; second and third rows instead depict a state singled out from the middle and the top of the band. The collective matter-light coupling is $G = 15\,GHz$; $a = 2.66\,\mu$m. Panel (b) demonstrates photon-photon antibunching; second and third rows show bunching.

4.4 Kinematics of two bare excitons

As in Sec. 3.3 we consider two excitons uncoupled to light ($G \equiv 0$) accommodated on a one-dimensional lattice by sites n_1 and n_2 and separated by a distance $n = |n_1 - n_2|$. These excitons interact kinematically and behave like hard-core spheres of radius r_B.

The Schrödinger equation of the system is

$$EC^{(ex)}_{n_1n_2} = 2E_0C^{(ex)}_{n_1n_2} + (1-\theta_{n_1n_2})\sum_s \left(t_{n_1s}C^{(ex)}_{sn_2} + t_{n_2s}C^{(ex)}_{n_1s}\right). \tag{4.16}$$

This equation is the same as Eq. (3.28) with $\theta_{n_1n_2}$ instead of $\delta_{n_1n_2}$. Here $\theta_{n_1n_2}$ is the discretized version of $\theta(x)$, see Eq. (4.6):

$$\begin{aligned} &\theta_{n_1n_2} = 0 \quad \text{if} \quad |n_1 - n_2| \le r_B/a, \\ &\theta_{n_1n_2} = 1 \quad \text{otherwise.} \end{aligned} \tag{4.17}$$

As in the previous chapter, we define $n = |n_1 - n_2|$. We call μ the label that indicates the eigenstates of this equation. By means of the hard-core

condition

$$\theta(n_1 - n_2)C^{(ex)}_{n_1 n_2} = 0, \tag{4.18}$$

and working within the framework of the the nearest neighbor approximation we can write

$$\begin{aligned} E^{(ex)}_\mu C^{(ex)}_\mu(n) = (1-\theta(n))\Big\{ & 2E_0 C^{(ex)}_\mu(n) \\ & + 2t[C^{(ex)}_\mu(n+1) + C^{(ex)}_\mu(n-1)]\Big\}. \end{aligned} \tag{4.19}$$

Eq. (4.19) is solved by the following normalized amplitudes:

$$C^{(ex)}_\mu(n) \equiv g_n(\mu) = \frac{\sqrt{2}(1-\theta(n))}{\sqrt{N-2(r_B/a)}} \sin\kappa_\mu[|n| - (r_B/a)], \tag{4.20}$$

where

$$\kappa_\mu = \frac{2\pi|\mu|}{Na - 2r_B}, \quad \mu = -\frac{(N-1)}{2} + \frac{r_B}{a}, ..., \frac{(N-1)}{2} - \frac{r_B}{a}, \tag{4.21}$$

and the basis elements $g_n(\mu)$ compose an orthonormal set in position as well as wave vector space:

$$\begin{aligned} \textstyle\sum_n g_n(\mu_1)g_n(\mu_2) &= \delta_{|\mu_1|,|\mu_2|} \\ \textstyle\sum_\mu g_{n_1}(\mu)g_{n_2}(\mu) &= (1-\theta(n_1))\delta_{|n_1|,|n_2|}. \end{aligned} \tag{4.22}$$

Unlike the solution for low-excited atoms there is a θ-factor instead of a δ-factor [cf. (3.31) and (3.34)]. Eventually, the eigenspectrum is described by

$$E^{(ex)}_\mu = 2E_0 + 4t\ \cos a\kappa_\mu. \tag{4.23}$$

We conclude that the kinematics of bare excitons that interact via an extended kinematic interaction is fully described by a wave vector set $\{\kappa_\mu\}$ (4.21) which mismatches the wave vector set $\{k_\nu\}$ (4.9) associated to non-interacting polaritons. This new set has two characteristic features. First, the normalization depends on the blockade sphere [as $N - 2(r_B/a)$] and not simply on the number N of atoms. Second, exactly as for the low-excited atoms in Chapter 3, $\{\kappa_\mu\}$ has a half-integer index so that its elements lie in-between neighboring wave vectors k_ν. As we shall see, this behavior will influence the two-Rydberg-polariton kinematics exactly as it did for low-excited atoms [cf. Fig. 3.5 and panel (b) in Fig. 4.5].

This mismatch implies that amplitudes $C^{(ex)}_\mu(k_\nu)$ do not have zeros, but rather magnified contributions from wave vectors $k_\nu \approx \kappa_\mu$. This is apparent after Fourier transforming Eq. (4.20):

$$C^{(ex)}_\mu(k_\nu) = \frac{\sin a\kappa_\mu \cos(k_\nu r_B) + (-1)^\mu \sin ak_\nu \sin(ak_\nu N/2)}{\cos ak - \cos a\kappa_\mu}. \tag{4.24}$$

Now that we have discussed the bare-excitonic case and shown that the effect of the extended kinematic interaction is not perturbative, we can add a cavity. In the next section we will see how the extended kinematic interaction affects the polariton kinematics.

4.5 Kinematics of two polaritons

We insert the one-dimensional array of two-level Rydberg atoms in a cavity. We want to study the effects of the blockade volume on the two-polariton kinematics. As in Appendix 3.A, we notice that in the Schrödinger equation associated to this system [Hamiltonian (4.1) acting on wave function (4.5), with $D = 0$] we can distinguish two subsystems, depending on whether there is an extended kinematic interaction or not. In the subsystem describing two photons or one photon and one exciton there is no blockade volume repulsion and the kinematics is correctly described by wave vectors k_ν [see Eq. (4.9) and (4.10)]. In the presence of an extended kinematic interaction, however, that is in the subsystem composed of two-exciton states, as we have seen in the previous section the physics is better accounted for by wave vectors κ_μ (4.21). The collective light-matter coupling G mixes these two sets of quantum numbers ($\{k_\nu\}$ and $\{\kappa_\mu\}$) so that wave packets form in the wave vector basis $\{k_\nu\}$.

In order to provide some analytics, we introduce the operators $\alpha_n^\dagger$, $\beta_n^\dagger$ and $\gamma_n^\dagger$. These create a couple of photons, one exciton and one photon, and a couple of excitons with interparticle separation of n sites. Then

$$|\Psi\rangle = \sum_s \Big[A(s)\,|\alpha_s\rangle + B(s)\,|\beta_s\rangle + C(s)\,|\gamma_s\rangle\Big] \tag{4.25}$$

whereas the Hamiltonian $\tilde{H}_{\text{eff}} = \tilde{H}_{AB} + \tilde{H}_C^{(KI)} + \tilde{H}_{AB-C}^{(KI)}$ corresponds to Hamiltonian (3.50) with a θ-factor instead of a δ-factor:

$$\begin{aligned}
\tilde{H}_{AB} &= \sum_{n,m}\Big[2E_p(n-m)\alpha_n^\dagger\alpha_m + \Big(E_p(n-m) + E_e(n-m)\Big)\beta_n^\dagger\beta_m\Big] \\
&\quad + G\sqrt{2}\sum_n\Big[\alpha_n^\dagger\beta_n + \beta_n^\dagger\alpha_n\Big], \\
\tilde{H}_C^{(KI)} &= \sum_{n,m}[1-\theta(n)]2E_e(n-m)\gamma_n^\dagger\gamma_m, \\
\tilde{H}_{AB-C}^{(KI)} &= G\sqrt{2}\sum_n[1-\theta(n)]\Big[\gamma_n^\dagger\beta_n + \beta_n^\dagger\gamma_n\Big],
\end{aligned} \tag{4.26}$$

with $\tilde{H}_{AB-C}^{(KI)}$ representing the coupling between the interacting (C) and non-interacting (AB) subsystems. By applying Hamiltonian (4.26) on wave function (4.25) we get the Fourier transform of (4.11).

Following Appendix 3.A we diagonalize the Hamiltonian terms H_{AB} and $H_C^{(KI)}$, see (3.52) and (3.55) where now basis functions $g_s(\mu)$ take into

account the extended blockade volume and are given by Eq. (4.20). The coupling operator $\tilde{H}_{AB-C}$ can be expressed by employing both ξ- and χ-operators as

$$\tilde{H}^{(KI)}_{AB-C} = \frac{G}{\sqrt{N(N-2(r_B/a))}} \sum_{i\nu\mu} \Lambda_{\nu\mu} X^{i\nu}_{\beta} \left(\chi^{\dagger}_{\mu} \xi_{i\nu} + \xi^{\dagger}_{i\nu} \chi_{\mu} \right). \tag{4.27}$$

As you can notice, unlike the case of low-excited atoms, here the normalization constant takes into account the excluded Rydberg sphere via the number of sites effectively available, $(N - 2(r_B/a))$, instead of the total number of sites N, as in Eq. (3.57). Also the coupling coefficients, responsible for mixing the wave vector sets $\{k_\nu\}$ and $\{\kappa_\mu\}$, unlike coefficients (3.58) display a dependence on the Rydberg radius:

$$\Lambda_{\nu\mu} = \frac{\cos\left(\frac{\pi\nu(2r_B+a)}{Na} + \frac{\pi|\mu|a}{Na-2r_B}\right)}{2\sin\left(\frac{\pi\nu}{N} + \frac{\pi|\mu|a}{Na-2r_B}\right)} - \frac{\cos\left(\frac{\pi\nu(2r_B+a)}{Na} - \frac{\pi|\mu|a}{Na-2r_B}\right)}{2\sin\left(\frac{\pi\nu}{N} - \frac{\pi|\mu|a}{Na-2r_B}\right)}. \tag{4.28}$$

By using the convenient ansatz (3.59) and letting $\tilde{H}_{\text{eff}}$ act on it, we get Eqs. (3.60) with the renormalized volume:

$$\begin{aligned} \left(E - E_{p,i\nu}\right) p_{i\nu} &= \frac{G X^{i\nu}_{\beta}}{\sqrt{N(N-2(r_B/a))}} \sum_{\mu} \Lambda_{\nu\mu} e_{\mu}, \\ \left(E - E^{(ex)}_{\mu}\right) e_{\mu} &= \frac{G}{\sqrt{N(N-2(r_B/a))}} \sum_{i\nu} X^{i\nu}_{\beta} \Lambda_{\nu\mu} p_{i\nu}. \end{aligned} \tag{4.29}$$

We can eliminate the excitonic amplitudes e_μ from system (4.29) and get Eq. (3.61) with

$$F_{\nu\nu'} = N\left(\delta_{\nu,\nu'} + \delta_{\nu,-\nu'}\right) - \theta\left[\frac{2\pi}{N}(\nu - \nu')\right] - \theta\left[\frac{2\pi}{N}(\nu + \nu')\right]. \tag{4.30}$$

This is different from the case of low-excited atoms (3.62): The θ-terms describe the effect of the Rydberg sphere and describe the scattering processes through the interacting system (C) which mix different wave vectors and effectively lead to wave packet of the ν-states. Panel (c) in Fig. 4.5 shows that a larger Rydberg blockade radius enhances this intermixing.

With the increase of the energy along the LL-band the photonic fraction of the states becomes weaker and weaker until far away from the strong coupling region, where the nature of the states becomes purely excitonic. This trend is illustrated in Fig. 4.5(a), where the two-photon, exciton-photon, and two-exciton amplitudes associated to states belonging to the LL-band are plotted in the positive half of the first Brillouin zone.

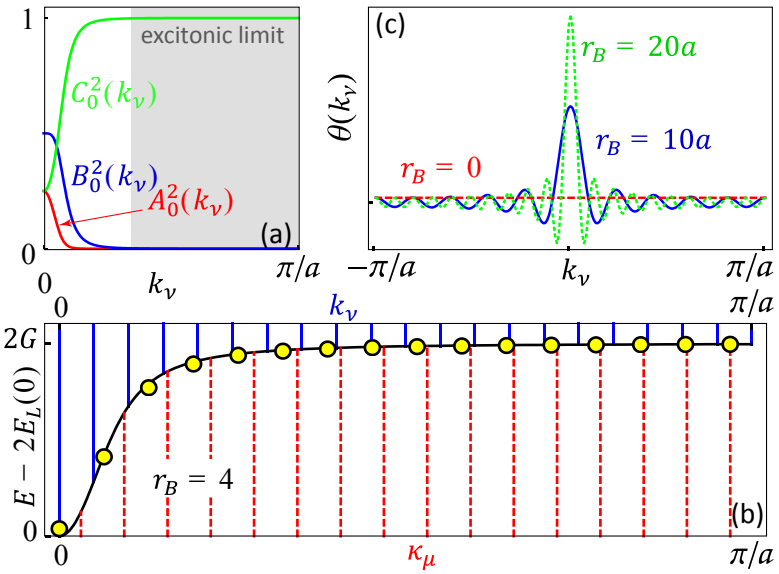

Figure 4.5: In panel (a) the photon-photon $[A_0(k_\nu)^2$; red], photon-exciton $[B_0(k_\nu)^2$; blue], and exciton-exciton $[A_0(k_\nu)^2$; green] amplitudes are plotted for the states in the polaritonic *LL*-band; the grey shaded area $k_\nu > k_{SC}$ is outside of the strong coupling region, where the photonic fraction gradually drops until it completely disappears in the excitonic limit. $G = 15\ GHz$; $a = 2.66\ \mu$m; $N = 40$. Panel (b) shows $\theta(k_\nu)$ for several values of Rydberg radii, $r_B = 0,\ 10a,\ 20a$. In panel (c) for $r_B = 4a$ exact two-polariton eigenenergies are depicted as yellow circles; solid blue vertical lines indicate the elements of $\{k_\nu\}$ whereas dashed red vertical lines are the elements of $\{\kappa_\mu\}$.

Similarly to relations (3.38), the gradual crossover between ν- and μ-states can be described by an effective wave vector

$$k_{\,\mathrm{eff}}(\rho) = \frac{Na - 2r_B - a}{Na - 2r_B}\,\frac{\pi(\rho - 1)}{Na/2 - r_B - a} \tag{4.31}$$

where the quantum number ρ ranges from 1 up to $N/2 - r_B/a$ for the *LL*-band: For the minimal value $\rho = 1$ of the argument, $k_{\,\mathrm{eff}}(\rho = 1)$ vanishes, as for free states; for the maximal value $\rho = N/2 - r_B/a$, instead, it reaches the value

$$k_{\,\mathrm{eff}}(\rho = N/2 - r_B/a) = \pi\frac{Na - 2r_B - a}{Na - 2r_B} \tag{4.32}$$

as for bare excitons. The numerically calculated energies are shown for $r_B = 4a$ by yellow circles in panel (c). Indeed, as the energy increases they move from the wave vectors k_ν (blue solid grid lines) to the wave vectors κ_μ (red dashed grid lines).

4.6 Photon-photon bunching

By following the steps shown in the previous chapter we directly obtain the amplitude for having two photons located at the same site. Unsurprisingly, it is the same as that for low-excited atoms (3.65) apart from the renormalized volume that takes into account the Rydberg blockade:

$$A_\rho(0) = \frac{G}{N\sqrt{N-2(r_B/a)}} \sum_{i\nu} \frac{X_\alpha^{i\nu} X_\beta^{i\nu}}{(E_\rho - E_{p,i\nu})} \sum_\mu \Lambda_{\nu\mu} e_\mu. \tag{4.33}$$

As discussed below Eq. (3.65), due to the mismatch between quantum numbers $A_\rho(0)$ does not have real poles but quasipoles. We can further simplify Eq. (4.33) by following the steps used to get Eq. (3.69) in order to reduce Eq. (4.33) to

$$A_\rho(0) \approx \frac{G X_\gamma^\rho}{\sqrt{2N(N-2(r_B/a))}} \sum_{i=L,U} \sum_\nu \frac{X_\alpha^{i\nu} X_\beta^{i\nu}}{(E_\rho - E_{p,i\nu})} \Lambda_{\nu,\rho-\frac{1}{2}}. \tag{4.34}$$

As in Chapter 3, X_γ^ρ is a normalization coefficient that takes into account the nonvanishing photon-photon and photon-exciton fractions of the wave packet.

From Eq. (4.34) it is apparent that also for Rydberg atoms condition (3.70) is fundamental for an efficient bunching and whatever makes the dispersion relation flatter increases the bunching because spreads the strong coupling region over the Brillouin zone. This is why larger lattice constants a lead to better bunching.

In order to quantify bunching we use the figure of merit (3.43). In panel (a) of Fig. 4.6 the bunching ΔA_ρ is plotted for the states in the LL-band and for three different values of the blockade radius $r_B = 0$, $r_B = 3a$, and $r_B = 10a$. We consider a positive detuning $\delta = 0.1G$, which explains the presence of a gap (grey area) between the LL-band and the LU-band (not shown). Empty markers indicate states featuring antibunching. We see that a larger Rydberg radius r_B enhances the bunching, which can be observed in a frequency window of the order of the collective light-matter coupling G ($\approx GHz$).

It has been know for years [274] that bound states can form for repulsive interactions in a gapped spectrum of noninteracting particles. Due to its repulsive nature, the extended kinematic interaction implies, other than an increase in bunching, the creation of an in-gap state. In the previous chapter we analyzed the formation of this two-polariton state in presence of an usual kinematic interaction (Fig. 3.9). This repulsively bound pair is indicated by the highest-energy state shown in Fig. 4.6(a): For $r_B = 0$ it corresponds to the lowest energy state of the LU-band (it is a quasibound state), for $r_B = 3a$ it is pulled down in the middle of the gap, and for $r_B = 10a$ it starts merging with the LL-band. This process is illustrated with a higher resolution in

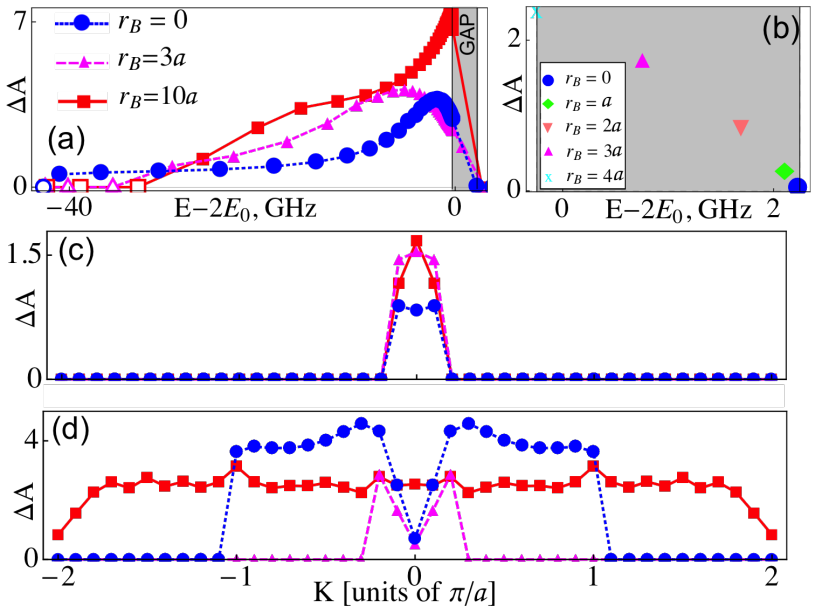

Figure 4.6: Panel (a) depicts the figure of merit for bunching ΔA [see Eq. (3.43)] for states belonging to the *LL*-band for $r_B = 0$, $r_B = 3a$, and $r_B = 10a$. A larger Rydberg radius induces a bunching increase and leads to formation of an in-gap bound state. This is visible in panel (b) which shows for several Rydberg radii how the lowest-energy state of the *LU*-band for $r_B = 0$ [rightmost circle in panel (a)] gradually moves through the gap towards the *LL*-band as r_B increases. This in-gap bound pair of polaritons gets more and more bounded as r_B increases. Panels (c) and (d) show ΔA as a function of the total wave vector $K_{\nu'}$ for a state located at the bottom and top of the *LL*-band, respectively; bunching survives also for finite values. Parameters are $a = 2.66$ μm, $G = 22$ GHz, $\delta = 0.1G$, and $N = 100$.

Fig. 4.6(b) where more Rydberg radii are considered; a magnification of the gap shows a gradual displacement of the bipolariton energy towards the *LL*-band as well as an increase in bunching. This kinematic bipolariton is a true bound state and is particularly robust against decoherence, as explained below Fig. 3.9. The larger the two-exciton repulsion (i.e. r_B), the larger the binding energy of the bipolariton; we will discuss this point again in Sec. 4.8.

Up to now we have dealt with $K_{\nu'} = 0$. For practical realizations, however, it is fundamental the survival of this phenomenon at values $K_{\nu'} \neq 0$. Panels (c) and (d) of Fig. 4.6 show that the bunching survives also for finite total wave vectors; panel (c) considers a state situated at the bottom of the *LL*-band (low energies) whereas panel (c) illustrates a high-energy state located at the very top of the band, right below the gap. In panel (c) it is visible how large r_B produces larger correlations.

The effects of the lattice spacing a were already studied in the previous chapter for usual kinematic interaction (Fig. 3.7) as well as those of detuning δ, see upper panel in Fig. 3.8. Those results hold true also for extended

kinematic interaction.

4.7 Dynamical interaction and bound states

Let us now discuss the role of the dynamical interaction ($D \neq 0$) on the top of the extended kinematic interaction. We find that dynamical interactions do not spoil bunching, which can be understood by looking at the Fourier transform of the scattering term (4.12). If we neglect the hopping ($G \gg t$), as long as

$$D(n)C(n) \ll G\sqrt{2}\theta(n)B(n) \tag{4.35}$$

the dynamical contribution to the two-polariton scattering is greatly exceeded by the term responsible for bunching. Inside a Rydberg sphere, condition (4.35) is definitely true since the photonic amplitude gets its maximal value. As a consequence, in the absence of gap ($\delta = 0$) the dynamical interaction is relevant only for attractive interaction; for negative values of D bound two-polariton states (bipolaritons) can arise below the LL-band.

Before studying the bipolaritons let us look at the their simpler photon-free version, the biexcitons; an instructive analysis is carried out in Appendix 4.C. The dispersion relation for two bare excitons located at sites n and m that interact only dynamically (without kinematic interaction and hopping) is

$$(E - 2E_0)C_{nm} = D_{nm}C_{nm}. \tag{4.36}$$

Eq. (4.36) provides us with a simple but enlightening reference picture of biexcitonic spectrum, whose levels split off the continuum. There are as many split levels from $2E_0$ as the number of interacting neighbors that are considered in the specific model; these levels can be distinguished from each other according to the broadening that affects the system. If we label our states via the interparticle distance $|n-m|$, for a long-range dipole-dipole interaction the $|n-m|$-th eigenstate is split by $D/|n-m|^3$ with D being D_{nm} at $|n-m| = 1$. For a van der Waals interaction, instead, the split is equal to $D/|n-m|^6$. More details are collected in Appendix 4.C.

Similarly to what is done in Appendix 4.C, bipolaritons can be found by means of the $K_{\nu'} \neq 0$ version of Eqs. (4.11), that is Eqs. (4.62). Provided that $t \ll G$ Eqs. (4.62) allow to substitute A- and B- amplitudes, reaching an integral equation which involves solely the two-exciton component of the wave functions:

$$C_{K_{\nu'}}(k_\nu) = \frac{1 + \phi_{K_{\nu'}}(E, k_\nu)}{N(E - 2E_0)} \sum_{q_\nu} D(k_\nu - q_\nu) C_{K_{\nu'}}(q_\nu) \tag{4.37}$$

with

$$\phi_{K_{\nu'}}(E, k_\nu) = 2G^2 \frac{E - E_{pp}(K_{\nu'}, k_\nu)}{\Delta_{K_{\nu'}}(k_\nu)} \tag{4.38}$$

and E_{pp} defined in Eq. (4.61).

In the framework of the nearest neighbor approximation the dynamical interaction simplifies as

$$D(k_\nu - q_\nu) = 2D\cos a(k_\nu - q_\nu) = 2D[\cos ak_\nu \cos aq_\nu + \sin ak_\nu \sin aq_\nu] \quad (4.39)$$

which, once inserted in Eqs. (4.37), allows to work out a closed-form analytical expression for its eigenstates. Conjecture (4.39) is a standard assumption for usual hard-core bosons ($r_B = 0$) interacting via dipole-dipole interaction; it is not sufficient for extended hard-core bosons ($r_B \gg 1$) where we should rather consider the long-range nature of the interaction. Nevertheless, we can employ approximation (4.39) toghether with the intuition deriving from relation (4.36), where the long-range character of the interaction is taken into account, to predict that the addition of a further neighbor in the interaction will entail the splitting of one more state from the continuum of unbound states.

Similarly to Appendix 4.C we define

$$\alpha_{K_\nu'} = \sum_{q_\nu} C_{K_\nu'}(q_\nu)\cos aq_\nu \quad (4.40)$$

and

$$\beta_{K_\nu'} = \sum_{q_\nu} C_{K_\nu'}(q_\nu)\sin aq_\nu. \quad (4.41)$$

Then, Eq. (4.37) splints into two parts:

$$\begin{aligned}
(E-2E_0)\alpha_{K_\nu'} &= \frac{2D}{N}\Bigg\{\alpha_{K_\nu'}\sum_{K_\nu'}[1+\phi_{K_\nu'}(E,k_\nu)]\cos^2 ak_\nu \\
&\quad + \beta_{K_\nu'}\sum_{K_\nu'}[1+\phi_{K_\nu'}(E,k_\nu)]\sin ak_\nu\cos ak_\nu\Bigg\}, \\
(E-2E_0)\beta_{K_\nu'} &= \frac{2D}{N}\Bigg\{\alpha_{K_\nu'}\sum_{K_\nu'}[1+\phi_{K_\nu'}(E,k_\nu)]\sin ak_\nu\cos ak_\nu \\
&\quad + \beta_{K_\nu'}\sum_{K_\nu'}[1+\phi_{K_\nu'}(E,k_\nu)]\sin^2 ak_\nu\Bigg\}.
\end{aligned} \quad (4.42)$$

System (4.42) has a unique nontrivial solution provided that the deter-

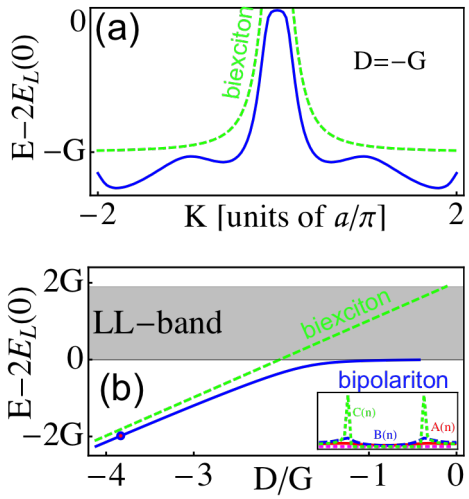

Figure 4.7: Panel (a) illustrates as a blue solid line the bipolariton energy $E_{bP}(K_{\nu'})$ as a function of the total wave vector $K_{\nu'}$ in the first Brillouin zone. The green dashed line describes the biexcitonic energy. Panel (b) shows how the bipolariton energy $E_{bP}(K_{\nu'})$ splits off the continuum as $|D|$ gets comparable to G and, finally, how it asymptotically tends to the energy of a bare biexciton. The inset illustrates the shape of the bipolariton wave function for the eigenstate corresponding to the circled energy at $D = -2G$. Parameters are $a = 2.66\ \mu$m, $G = 22$ GHz, $\delta = 0.1G$, and $N = 100$.

minant of the matrix composed of the coefficients is not zero:

$$\left(E - 2E_0 - D\left[1 + \frac{2}{N}\sum_{k_\nu}\phi_{K_{\nu'}}(E, k_\nu)\sin^2 ak_\nu\right]\right)\times$$

$$\times\left(E - 2E_0 - D\left[1 + \frac{2}{N}\sum_{k_\nu}\phi_{K_{\nu'}}(k_\nu)\cos^2 ak_\nu\right]\right) = \tag{4.43}$$

$$= \left(\frac{2D}{N}\sum_{k_\nu}\phi_{K_{\nu'}}(k_\nu)\sin ak_\nu\cos ak_\nu\right)^2.$$

The two terms within brackets on the left-hand side are reminiscent of the biexcitonic dispersion (4.36) where the interaction term is now renormalized by light-matter coupling. The first of them, however, corresponds to an unphysical state, where the two-exciton amplitude (C) is asymmetric. We only keep the contribution from second term, which leads to a real symmetric solution $E_{bP}(K_{\nu'})$ corresponding to a bipolariton lying below the LL-band continuum. The dependence of $E_{bP}(K_{\nu'})$ on $K_{\nu'}$ is plotted in panel (a) of Fig. 4.7 as a blue solid line and compared to the biexciton (green dashed line). A negative value $D = -G$ is taken.

When the center of mass of the two-polariton system is at rest ($K_{\nu'} = 0$) the eigenequation (4.43) simplifies:

$$E = 2E_0 + D\left[1 + \frac{4G^2}{N}\sum_{k_\nu}\frac{E - 2E_p(k_\nu)}{\Delta(E, k_\nu)}\cos^2 ak_\nu\right]. \tag{4.44}$$

For negative values of D this equation describes the creation of a bound bipolariton state below the continuum. As shown in panel (b) of Fig. 4.7, the eigenenergy of the bipolariton state and its separation from the LL-band substantially depend on the competition between D and G. For the same parameters used in panel (a), we see that as $D \approx -1.5G$ the bipolariton (blue solid line) splits off the continuuum (grey region). As the strength $|D|$ of the dynamical interaction increases and dominates over the light-matter coupling, the bipolariton level asymptotically tends to the biexciton energy, $E_{bE}^{(1)} = 2E_0 - |D|$ (green dashed line). The wave function of this split bound state is mainly excitonic, and presents two symmetric peaks separated by the forbidden volume $2r_B + a$, as shown in the inset of panel (b).

The three plots in Fig. 4.8 show the figure of merit ΔA for bunching for continuum polariton-polariton states in presence of different interactions (and strengths) on top of the hard-core kinematic repulsion; only the LL-band is shown. Plotted data are the result of exact numerical simulations, where the long-range nature of the interaction is taken into account. Namely, we consider two different types of interactions: A "nearest neighbor" approximation, whose strength vanishes for interatomic distances larger than $2r_B + a$, and the long-range van der Waals potential. These two interactions are implemented in the code as

$$\begin{aligned} D_{nm}^{(NNA)} &= D\delta(|n-m|a - 2r_B - a), \\ D_{nm}^{(VdW)} &= D\theta(n-m)\left[\tfrac{2(r_B/a)+1}{n-m}\right]^6. \end{aligned} \tag{4.45}$$

The θ-function is defined in Eqs. (4.6); the role of the weight $(2(r_B/a)+1)^6$ is allowing for a better match between the two potentials: Both are equal to D at $|n-m| = 2(r_B/a) + 1$.

Looking at the upper plot in Fig. 4.8 we can distinguish two different cases: $0 < -D < 1.5G$ and $-D > 1.5G$. In the first case of weak attractive interaction, a single bipolariton state splits from the continuum (black-border triangle), as shown in the upper panel of Fig. 4.8. For stronger dynamical attraction $-D > 1.5G$ this effect is magnified and the bipolariton reaches lower energies (black-border square). For a positive Rydberg radius $r_B = 3a$ this bunching is destroyed (central plot) since photons follow the excitons which must stay far apart, keeping an interparticle distance $2r_B + a$. A large blockade radius thus suppresses the bunching in the lowest-energy split

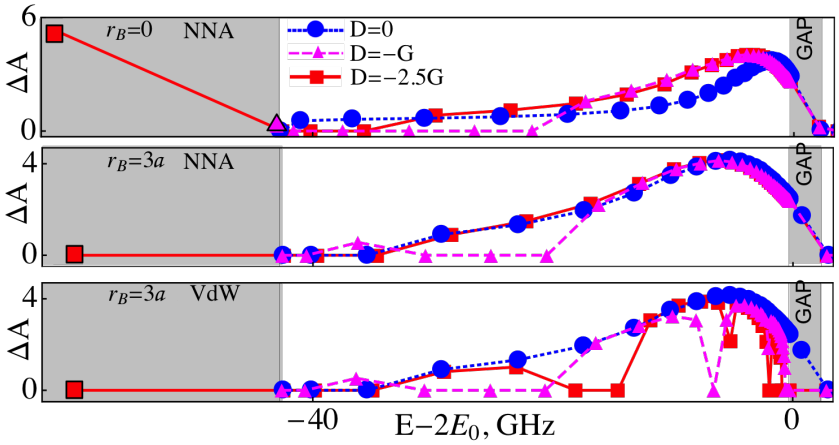

Figure 4.8: Panels show the figure of merit for bunching ΔA for the two-polariton eigenenergies in the LL-band. Upper and middle panels consider the nearest neighbor approximation potential (NNA) for an usual ($r_B = 0$, upper plot) and extended ($r_B = 3a$, middle plot) kinematic interaction; the potential is simulated by the first line in Eqs. (4.45). Lower panel illustrates the situation for $r_B = 3a$ in presence of a van der Waals (VdW) potential, defined in the second line of Eqs. (4.45). Parameters are $a = 2.66$ μm, $G = 22$ GHz, $\delta = 0.1G$, and $N = 100$.

state. Finally, the van der Waals potential (lower plot) slightly modifies the situation, yet the significant physics does not change; the case $r_B = 0$ with van der Waals interaction is not shown in Fig. 4.8 since it does not display significative differences with respect to the nearest neighbor case. Unfortunately we did not have enough time to perform an accurate study of the disordered pattern induced by the van der Waals potential.

4.8 Gap states

So far we studied the effect of an attractive dynamical interaction. However, as already noticed in Sec. 4.7 [panels (a) and (b) of Fig. 4.7], provided that the two-polariton spectrum is gapped ($\delta > 0$), repulsive interaction leads to formation of in-gap bipolaritons [274]. The same state formation was observed in Sec. 3.6 for an usual kinematic interaction ($r_B = 0$), see Fig. 3.9.

The in-gap dynamical bound state is associated to the solution of the dispersion relation (4.44) for $D > 0$. For simplicity we restrict to the case $K_{\nu'} = 0$, which can be done without any loss of generality. Panel (a) of Fig. 4.9 shows the eigenenergy $E_{bP}(K_{\nu'} = 0)$ of the in-gap bipolariton as the ratio D over G is tuned. The detuning is $\delta = 0.5G$. We consider the nearest neighbor approximation for the potential ($r_B = 0$), see Eq. (4.43),

$$E - 2E_0 - D\left[1 + \frac{2}{N}\sum_{k_\nu} \phi_{K_{\nu'}}(k_\nu)\cos^2 a k_\nu\right] = 0 \tag{4.46}$$

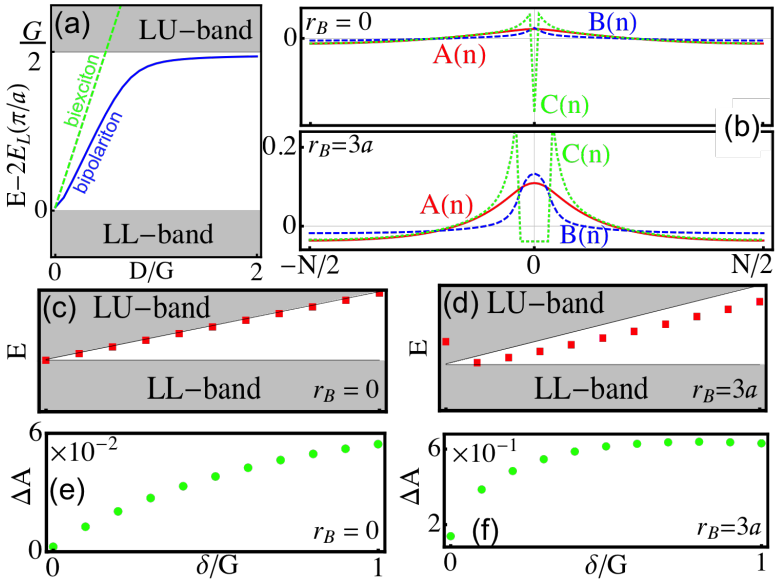

Figure 4.9: (a) $D > 0$; position of the bipolariton level $E_{bP}(K_{\nu'} = 0)$ in the gap (blue solid line) compared the biexciton level (green dashed line). The grey shaded areas indicate the *LL*-band and the *LU*-band. Plots in panel (b) show the wave functions of the bipolariton for $r_B = 0$ (upper plot) and $r_B = 3a$ (lower plot). Other relevant parameters are $D = 0$, $\delta = 0.1$. The two states correspond respectively to the blue circle and pink up-pointing triangle in panel (b) of Fig. 4.6. Panels (c) and (d) display the position of the bipolariton for $r_B = 0$ and $r_B = 3$ as the detuning is varied from 0 up to G. Panels (e) and (f), for the same points as panels (c) and (d), show that the figure of merit ΔA for bunching gets enhanced by larger detunings.

where long-range contributions are indeed negligible. Notice that the right-hand side of Eq. (4.46) is 0 only because $K_{\nu'} = 0$. For $D \gg G$ the bipolariton asymptotically tends to overlap the continuum, which ultimatively switches the bunching off.

The excitons in the bipolariton wave function try to stay close to each other, as much as they can be within the framework of the kinematic interaction: They keep a distance equal to $2r_B + a$, see panel (b) of Fig. 4.9 where we only consider extended kinematic interaction ($D = 0$). The same behavior holds true if we turn on the dynamical counterpart ($D \neq 0$), as shown in Fig. 4.10 for van der Waals potential with strength $D = 0.5G$. The photons instead bunch, this tendency being more pronounced for larger Rydberg radii [lower plot in panel (b) of Fig. 4.9, $r_B = 3a$]. The states in the upper ($r_B = 0$) and lower ($r_B = 3a$) plots of panel (b) are indicated as a blue dot and a pink up-pointing triangle respectively in panel (b) of Fig. 4.6.

The dynamical strength D is a powerful control knob to tune the position of the bound state in the gap, and consequently the enhancement of the associated bunching. Alternatively, one can think of keeping D fixed while

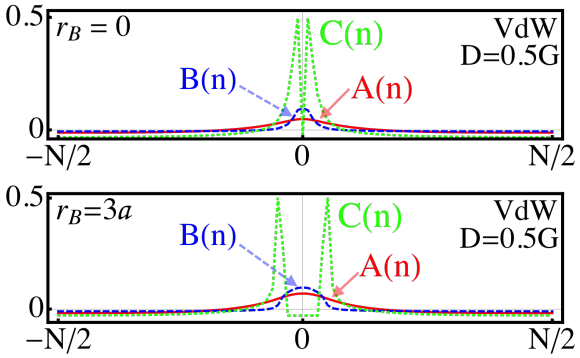

Figure 4.10: Wave function of an in-gap bipolariton bound state for a repulsive van der Waals dynamical interaction ($D = 0.5G$) with $r_B = 0$ (upper panel) and $3a$ (lower panel).

changing the detuning δ of the system. Panels (c) and (d) of Fig. 4.9 show the position of the bipolariton eigenenergy for $r_B = 0$ and $r_B = 3a$ as the detuning is varied from 0 up to G. For the usual kinematic interaction the state is always stuck to the continuum of the LU-band [see also rightmost blue circle in panels (a) and (b) of Fig. 4.6, where $\delta = 0.1G$]. For a larger Rydberg radius ($r_B = 3a$), as soon as a gap opens ($\delta \neq 0$) the bipolariton enters the gap. For larger values of detuning then it penetrates more and more the gap [see also in-gap pink up-pointing triangle in panels (a) and (b) of Fig. 4.6, where $\delta = 0.1G$]. Eventually, panels (e) and (f) show, for the same points of the upper plots, how the bunching increases by increasing the detuning δ.

4.9 Conclusions

In this chapter we extended the results of Chapter 3 to Rydberg atoms. We studied the two-photon correlations for cavity photons coupled to a one-dimensional ordered array of Rydberg atoms. The optical nonlinearities are caused by both dynamical and (extended) kinematic interactions. We found that a large Rydberg radius greatly enhances the nonlinear response of the system. We observed a two-photon bunching within a GHz frequency window as well as narrow bipolariton states that split from the continuum owing to the (attractive) dynamical interaction. Moreover, if the two-polariton spectrum is gapped a repulsive dynamical interaction leads to formation of in-gap bound states. The same kind of in-gap pairs can be produced also by the kinematic interaction provided that the Rydberg radius is sufficiently large.

This model is valid as far as all broadenings present in the system are dominated by the collective light-matter coupling G: A clean preparation of the Mott insulator state in the one-dimensional lattice is fundamental to

avoid both collisional and Doppler broadenings; we also need a very low leakage rate of photons out of the fiber. The model is based on the assumption that the guided mode of the fiber is resonantly coupled to the atomic transition, see Eq. (4.2):

$$E_0 \approx E_p(0) = ck_\perp, \tag{4.47}$$

which can be obtained using a narrow fiber radius R; for the lowest fiber mode, the resonance condition requires R to be of the order of a micron fraction. A second requirement for the model to hold, is that such resonance must be isolated or, in other words, energetically resolved. The separation between different atomic levels must be larger than G, which does not allow for a too large principal quantum number n. According to Eq. (4.54), a large n entails too close atomic levels, so that a single cavity photon couples to a set of excitonic resonances and the physics may slightly change. Contrary, large n is needed for a large blockade radius ($r_B \gg a$), where we heuristically define

$$r_B = \left(\frac{C_6}{2G}\right)^{1/6} a \tag{4.48}$$

as the distance below which the energy levels of a nonexcited atom sitting in the vicinity of an excited atom will experience the shift $\sim 2G$, and therefore will be removed from the energy interval useful for interactions with photons. Due to the large scale of G, condition (4.48) may suggest that it is not so easy to reach large Rydberg radii.

It would be very fascinating to observe these phenomena in different systems such as solids. As diffusely explained in the previous chapter, the quality of bunching is strictly related to the size of the strong coupling region $k < k_{SC}$: The larger the size the better the coupling. Therefore, natural semiconductors are not promising candidates for the implementation of photonic bunching. However, recent experiments [275] where Rydberg Wannier-Mott excitons up to a principal quantum number $n = 20$ have recently been detected in dicopper oxide let us hope that extended kinematic interaction ($r_B \gg a$) in solids may one day be within reach.

Appendices

4.A Rydberg atoms

In this appendix the main properties of Rydberg atoms are reviewed; more details can be found in Ref. [60]. Rydberg atoms are excited atoms characterized by a very large principal quantum number n [264]. Let us consider an electron (charge $-e$) which orbits a nucleus of positive charge $+Ze$. The centripetal force is

$$F_c = \frac{mv^2}{r} \tag{4.49}$$

whereas the Coulomb potential is

$$F_p = \frac{Ze^2}{4\pi\epsilon_0 r^2}. \tag{4.50}$$

In Eq. (4.50) ϵ_0 indicates the vacuum permettivity. Inserting in the equality between forces (4.49) and (4.50) a quantized angular momentum ($mvr = n\hbar$, with m being the electron mass) we obtain

$$r = \frac{a_0 n^2}{Z} \tag{4.51}$$

where $a_0 = 4\pi\epsilon_0\hbar^2/(em^2)$ is the Bohr radius. From the energy conservation one obtains that the binding energy that keeps the valence electron attached to the core is

$$E_b = -\frac{Ry}{n^2} \tag{4.52}$$

where the Rydberg constant is

$$Ry = \frac{Z^2 e^4 m}{16\pi^2\epsilon_0^2\hbar^2}. \tag{4.53}$$

The binding energy (4.52) is valid for hydrogen-like systems such as alkali atoms with a high angular momentum $l > 3$. For $l \leq 3$, the valence electron can get closer to the core and penetrates the intermediate closed electron shells, leading to polarisation of the core. Moreover, since the valence electron is closer, the nucleus feels a stronger potential. Both these effects, polarisation and stronger potential, contribute to an overall increase of the

binding energy and formula (4.52) has to be slightly modified by introducing a quantum defect δ_{nl}

$$E_b = -\frac{Ry}{(n-\delta_{nl})^2}. \tag{4.54}$$

This expression takes into account the effects coming from low angular momenta $l \leq 3$. We dub this effective quantum number $n^* = n - \delta_{nl}$.

Other than the dependence $E_b \propto n^{-2}$, the radius R of the orbit scales as $r \propto n^2$ which automatically leads to the same dependence for the (huge) dipole moment $d \propto n^2$. As a consequence, Rydberg atoms feel and react in an exaggerated way to very weak external fields, and dipole-dipole interaction between Rydberg atoms can be observed on μm distances. Other remarkable properties are the radiative timescale $\tau \propto n^{-3}$, which renders Rydberg atoms long-lived states, and the energy gap between neighboring n states, $\Delta \propto n^{-3}$.

For a short interatomic separation, Rydberg atoms interact via a dipole-dipole force:

$$V(R) = \pm\frac{C_3}{R^3} \propto n^{*4} \tag{4.55}$$

whereas when the atoms are far away from each other the interaction is a van der Waals force:

$$V(R) = -\frac{C_6}{R^6} \propto n^{*11}. \tag{4.56}$$

The transition between these two regimes takes place for a separation $R_{vdw} \propto n^{*7/3}$ known as van der Waals radius.

An important property of Rydberg atoms is the dipole blockade. Let us consider two Rydberg atoms in their ground states $|g\rangle$. We excite them to their Rydberg states $|r\rangle$ with Rabi frequency $\Omega = E_{|r\rangle} - E_{|g\rangle}$ ($\hbar \equiv 1$). If the atoms are far enough, the state $|rr\rangle$ where both atoms are in the excited state is populated at a rate Ω.

As the atoms approach each other, the van der Waals interaction (4.56) acts as a pure energy shift over $E_{|rr\rangle}$ and pulls the energy out of resonance with the excitation laser, see Fig. 4.A.1. As a consequence, the system can no longer be excited in the doubly excited state $|rr\rangle$.

In a realistic system the state $|rr\rangle$ has a natural finite linewidth Γ_r. Additionally, we have to take into account its power-broadened width Ω. The dipole blockade takes place at an interatomic distance such that

$$V(R) > \hbar \times \max(\Omega, \Gamma_r). \tag{4.57}$$

Since for large n^* the lifetime $\tau \propto 1/\Gamma_r$ of Rydberg states is typically long, we can assume $\Omega \gg \Gamma_r$ so that we enter the dipole blockade regime as soon as

$$V(R) = \hbar\Omega. \tag{4.58}$$

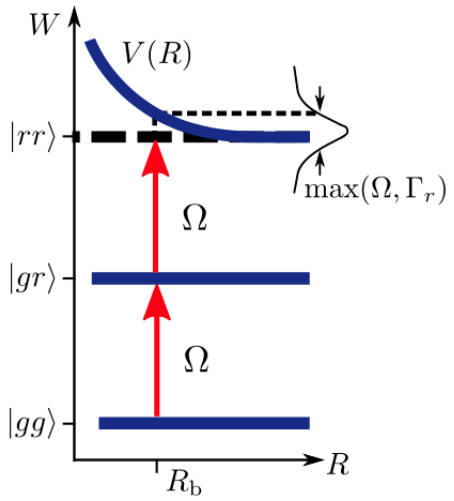

Figure 4.A.1: Interactions between Rydberg dipoles induces a shift by an amount $V(R)$, bringing the energy of the state $|rr\rangle$ out of resonance with the source. If the detuning is larger than $\max(\Omega, \Gamma_r)$ the atoms can not be excited together. Source: Ref. [60].

If we insert the explicit form of the van der Waals potential (4.56) in condition (4.58), we obtain

$$R_b = \sqrt[6]{\frac{C_6}{\Omega}} \tag{4.59}$$

which is called blockade radius. If we have an ensemble of Rydberg atoms, we can imagine every excited state as surrounded by a hard sphere of radius R_b. Two excitations within the same sphere are forbidden; in other words, the minimal separation between two excited Rydberg atoms is $2R_b$ (or in the lattice analog $2R_b + a$ with a being the lattice spacing). In Chapter 4 we refer to the Rydberg radius as r_B.

4.B Generic total wave vector

We let the Hamiltonian (4.1) act on the wave function (4.5). In order to eliminate the basis elements $|P_n P_m\rangle$ associated to two excitons within the same blockade sphere, we multiply the corresponding amplitudes by $(1-\theta(n-m))$ with the θ-function $\theta(x)$ defined in conditions (4.6). After symmetrization

of the resulting equations, we obtain:

$$\begin{aligned}
EA_{nm} &= \sum_s [E_p(n-s)A_{sm} + E_p(m-s)A_{ns}] + G\sqrt{2}B^S_{nm},\\
EB^S_{nm} &= E_0 B^S_{nm} + \frac{1}{2}\sum_s [E_p(n-s)(B^S_{sm} + B^A_{sm}) + E_p(m-s)(B^S_{sn} + B^A_{sn})]\\
&\quad + G\sqrt{2}(A_{nm} + C_{nm}) + \frac{t}{2}\Big[(B^S_{nm-1} + B^A_{nm-1} + B^S_{nm+1} + B^A_{nm+1})\\
&\quad + (B^S_{n-1m} - B^A_{n-1m} + B^S_{n+1m} - B^A_{n+1m})\Big],\\
EB^A_{nm} &= E_0 B^A_{nm} + \frac{1}{2}\sum_s [E_p(n-s)(B^S_{sm} + B^A_{sm}) - E_p(m-s)(B^S_{sn} + B^A_{sn})]\\
&\quad + G\sqrt{2}(A_{nm} + C_{nm}) + \frac{t}{2}\Big[(B^S_{nm-1} + B^A_{nm-1} + B^S_{nm+1} + B^A_{nm+1})\\
&\quad - (B^S_{n-1m} - B^A_{n-1m} + B^S_{n+1m} - B^A_{n+1m})\Big],\\
EC_{nm} &= 2E_0 C_{nm} + (1-\theta(n-m))G\sqrt{2}B^S_{nm} + D(n-m)C_{nm}\\
&\quad + t(C_{nm-1} + C_{nm+1} + C_{n+1m} + C_{n-1m})(1-\theta(n-m)).
\end{aligned} \tag{4.60}$$

Eqs. (4.11) correspond to the Fourier transform of Eqs. (4.60) after the introduction of the total and relative wave vectors (4.8). We express the amplitudes as $A(k_1,k_2) \to A_{K_{\nu'}}(k_\nu)$, etc., and introduce the following two-particle energies:

$$E_{ij}(k_\nu) = E_i(K_{\nu'}/2 + k_\nu) + E_j(K_{\nu'}/2 - k_\nu) \equiv E_i(q_{\nu_1}) + E_j(q_{\nu_2}), \qquad i,j \in e,p. \tag{4.61}$$

Each eigenstate is characterized by certain $K_{\nu'}$ and for a generic propagation of the center of mass B^A does not necessarily vanish. In the k-space we finally get:

$$\begin{aligned}
EA_{K_{\nu'}}(k_\nu) &= E^{K_{\nu'}}_{pp}(k_\nu)A_{K_{\nu'}}(k_\nu) + G\sqrt{2}B^S_{K_{\nu'}}(k_\nu),\\
EB^S_{K_{\nu'}}(k_\nu) &= \frac{1}{2}[E^{K_{\nu'}}_{pe}(k_\nu) + E^{K_{\nu'}}_{pe}(-k_\nu)]B^S_{K_{\nu'}}(k_\nu) + \frac{1}{2}[E^{K_{\nu'}}_{pe}(k_\nu) - E^{K_{\nu'}}_{pe}(-k_\nu)]B^A_{K_{\nu'}}(k_\nu)\\
&\quad + G\sqrt{2}(A_{K_{\nu'}}(k_\nu) + C_{K_{\nu'}}(k_\nu)),\\
EB^A_{K_{\nu'\nu'}}(k_\nu) &= \frac{1}{2}[E^{K_{\nu'}}_{pe}(k_\nu) + E^{K_{\nu'}}_{pe}(-k_\nu)]B^A_{K_{\nu'}}(k_\nu) + \frac{1}{2}[E^{K_{\nu'}}_{pe}(k_\nu) - E^{K_{\nu'}}_{pe}(-k_\nu)]B^S_{K_{\nu'}}(k_\nu),\\
EC_{K_{\nu'}}(k_\nu) &= 2E^{K_{\nu'}}_{ee}(k_\nu)C_{K_{\nu'}}(k_\nu) + G\sqrt{2}B^S_{K_{\nu'}}(k_\nu) - \frac{G\sqrt{2}}{N}\sum_{q_\nu}\theta(k_\nu - q_\nu)B^S_{K_{\nu'}}(q_\nu)\\
&\quad - \frac{4t}{N}\sum_{q_\nu}\theta(k_\nu - q_\nu)C^S_{K_{\nu'}}(q_\nu)\cos\frac{aK_{\nu'}}{2}\cos aq_\nu + \frac{1}{N}\sum_{q_\nu}D(k_\nu - q_\nu)C_{K_{\nu'}}(q_\nu).
\end{aligned} \tag{4.62}$$

The term proportional to D in the fourth equation accounts for the dynamical interaction between excitons whereas the terms proportional to the θ-function account for the extended kinematic interaction. For $K_{\nu'} = 0$ Eqs. (4.62) reduce to Eqs. (4.11).

4.C Biexcitons

To get some intuition, let us look at the two-particle eigenstates of Hamiltonian

$$H = E_0 \sum_s P_s^\dagger P_s + \frac{1}{2} \sum_{s,p} D(s-p) P_s^\dagger P_p^\dagger P_s P_p. \tag{4.63}$$

We use the two-particle wave function in the site representation, $|\Psi_{ee}\rangle = \sum_{n,m} C_{nm} P_n^\dagger P_m^\dagger |0\rangle$, and find the dispersion equation in the form:

$$(E - 2E_0) C_{nm} = D_{nm} C_{nm}. \tag{4.64}$$

Both C_{nm} and $D_{nm} = D(n-m)$ depend on the relative distance between the excitations, $r = |n-m|$, and this is the quantum number which characterizes the eigenstates (except for $r = 0$). The r-th eigenfunction describes two atomic excitations separated by a distance r. The corresponding eigenstate is split from $E = 2E_0$ by the energy D/r^n with D being D_{nm} at $|n-m| = 1$. If the interaction is attractive, then $D < 0$, and the state with the smallest separation between the excitations has the lowest energy; for repulsive interaction, instead, it has the highest energy. If we account only for the interactions between a finite number of neighbors, then the number of split bands is equal to the number of neighbors we consider as interacting. For instance, in the nearest neighbor approximation we have a single biexcitonic band. Other states (with the separations $r = 2, 3, 4...$) are degenerate. We can form any linear combination of their wave functions, so that they can be considered as extended. For next- and next-next-neighbor interaction we will find two biexcitonic bands, and so on. Accounting for all interactions will remove all the degeneracies. However, in practice it is important to consider only those bands that are split by an energy larger than the excitonic linewidth. Finally, adding the kinematic interaction on top of it will modify this picture to some extent, but most likely not qualitatively.

Now let us look at the solutions in the wave-vector representation. Fourier-transforming Eq. (4.64) yields:

$$(E - 2E_0) C(k_1, k_2) = \frac{1}{N} \sum_q D(q) C(k_1 - q, k_2 + q), \tag{4.65}$$

with the Fourier transforms defined as

$$\begin{aligned} D(q) &= \sum_n D_n e^{-iqn}, & D_n &= \frac{1}{N} \sum_q D(q) e^{iqn}, \\ C(k_1, k_2) &= \frac{1}{N} \sum_{n,m} C_{nm} e^{-i(k_1 n + k_2 m)}, & C_{nm} &= \frac{1}{N} \sum_{k_1, k_2} C(k_1, k_2) e^{i(k_1 n + k_2 m)}. \end{aligned} \tag{4.66}$$

We introduce the total wave vector, $K = k_1 + k_2$, and the wave vector of relative motion, $k = (k_1 - k_2)/2$, and rewrite (4.65) as

$$(E - 2E_0)C_K(k) = \frac{1}{N}\sum_q D(k-q)C_K(q). \tag{4.67}$$

This system of equations has an analytical solution as the dependences of the interaction potential $D(k-q)$ on k and q can be separated. In the nearest-neighbor approximation, $D(k-q) = 2D\cos a(k-q) = 2D[\cos ak \cos aq + \sin ak \sin aq]$. Introducing

$$\alpha_K = \sum_q C_K(q)\cos aq, \qquad \beta_K = \sum_q C_K(q)\sin aq, \tag{4.68}$$

we get by multiplying (4.67) by $\cos ak$ and $\sin ak$ and summing over k:

$$\begin{aligned}(E - 2E_0)\alpha_K &= \frac{2D}{N}\left\{\alpha_K \sum_k \cos^2 ak + \beta_K \sum_k \sin ak \cos ak\right\},\\ (E - 2E_0)\beta_K &= \frac{2D}{N}\left\{\alpha_K \sum_k \sin ak \cos ak + \beta_K \sum_k \sin^2 ak\right\}.\end{aligned} \tag{4.69}$$

As $\sum_k \cos^2 ak = \sum_k \sin^2 ak = N/2$, $\sum_k \sin ak \cos ak = 0$, these two equations decouple and give the same result for the biexciton: $E = 2E_0 + D$. Similarly, we can include next-next-neighbor interaction, and get two biexcitonic bands, and so on and so forth.

Résumé en Français

Les photons n'ayant pas de charge électrique, il n'y a pas d'interaction photon-photon [1]. Pour cette raison, les signaux optiques sont préférés pour le transfert des données de façon efficace à longue distance [2]. La propagation linéaire de la lumière dans le vide empêche les interférences et corrélations croisées entre signaux optiques, et empêche donc l'implémentation de portes logiques photoniques ce qui est indispensable pour le traitement du signal. Pour activer les interactions entre photons, des processus optiques non linéaires sont necéssaires.

Typiquement, lorsqu'un faisceau lumineux très faible se propage dans un matériau, les processus optiques linéaires comme l'absorption ou la réfraction dominent. Dans l'optique linéaire, il suffit de considérer un index de réfraction avec une composante imaginaire. Pour observer une réponse non linéaire, un faisceau suffisamment intense est nécessaire : le champ électrique associé doit être comparable à celui qui est produit par les noyaux atomiques [2]. Dans ce cas, l'index de réfraction dépend de l'amplitude du champ électrique. Un exemple célèbre de réponse non linéaire est l'effet Kerr optique [5], où la propagation de la lumière dépend de l'éclairement énergétique local du champ électrique. La nécessité d'utiliser des lasers puissants est la raison pour laquelle les non linéarités optiques ont été observés pour la première fois dans les années 1960 [6].

À partir de là, la recherche a beaucoup progressé vers la réalisation de non linéarités optiques avec des lasers de plus en plus faibles [7], jusqu'au régime quantique, où un seul photon peut modifier la propagation de la lumière. Dans le régime quantique, les coefficients non linéaires sont typiquement très faibles. Il existe toutefois plusieurs techniques pour réaliser des intéractions fortes entre photons. Les premières études théoriques remontent aux années 1980, et l'émergence du calcul quantique [11] a accéléré encore d'avantage les réalisations expérimentales.

Le premiére expérience remonte à 1995 [12]. Avec un seul atome dans une cavité Fabry-Pérot de haute finesse, une susceptibilité optique non linéaire au niveau du photon unique a été demontré. L'expérience presentée en [12] est la premiére expérience vers la réalisation de portes logiques photoniques. Depuis cette expérience, de nombreux résultats ont été obtenu : La réalisation de routers non linéaires à fonctionnement entièrement optique [13, 14], ainsi que des interrupteurs [15–22] et portes quantique à phase controllée [12, 23–26]. Tout cela permet une manipulation de l'information

quantique de haute précision et ouvre la voie vers la réalisation de réseaux quantiques [27].

Les non linéarités entre quanta de lumière ne sont pas utiles qu'à l'information quantique, mais aussi à la métrologie [28] et la miscroscopie quantique [29]. En outre, les non linéarités photon-photon ouvrent la voie vers de nouvelles techniques non destructive pour mesurer [30] et manipuler les photons [31, 32]. On peut aussi réaliser des sources déterministes de photons uniques [33]. En général, les processus optiques non linéares sont indispensables à toutes les applications qui exigent la création et la manipulation de champs électromagnétiques non classiques.

Actuellement, il existe beaucoup de méthodes pour réaliser des interactions fortes photon-photon. Tous ces méthodes s'appuient sur une composante non photonique (un atome ou un ensemble d'atomes) jouant le rôle de médiateur entre les deux photons. La nature non linéaire de l'intéraction peut naître soit du spectre électronique de la composante non photonique (grâce à sa structure anharmonique), soit de ses degrés de liberté méchaniques ; dans le deuxième cas, il s'agit du domaine de la physique optoméchanique [37, 38].

Le dispositif le plus simple pour réaliser des non linéarités photon-photon consiste à mettre un atome dans une cavité Fabry-Pérot de haute finesse, et utiliser la saturabilité énergétique atomique. Cette procédure a été utilisée par Turchette Q. A. et al. [12]. Dans cette expérience d'électrodynamique quantique en cavité, l'élément jouant le rôle de médiateur entre photons est un atome. La cavité sert à améliorer la probabilité d'intéraction photon-atome, car le photon pouvant rebondir plusieurs fois entre les miroirs de la cavité, il peut à chaque passage intéragir avec l'atome. Par conséquent, plus la finesse de la cavité est grande, plus la probabilité d'intéraction sera élevée. Pour un atome à deux niveaux énergétiques couplé à la cavité, la non linéarité de l'intéraction à pour origine le spectre de l'opérateur hamiltonien de Jaynes-Cummings [39]. Le spectre de Jaynes-Cummings varie comme la racine carrée du nombre de photons, et cette anharmonicité peut être utilisée pour réaliser des effets non linéaires comme le blocage photonique [40], les portes logiques quantiques [41, 43], et la mémoire quantique pour enregistrer un photon avec un atome unique [42]. Le désavantage de cette procédure est la durée de vie très courte de l'état excité atomique [2]. Pour résoudre ce problème, on peut utiliser des atomes à plusieurs niveaux énergétiques métastables [44, 45]. Ce dispositif atome-cavité est aussi réalisable avec des systèmes à l'état solide. On citera par exemple les points quantiques semiconducteurs [48–51].

Une méthode plus complexe pour réaliser des non linéarités optiques sans aucune cavité consiste à employer la technique de transparence induite électromagnétiquement pour ralentir les photons qui se propagent dans un ensemble d'atomes [45, 52]. Typiquement, on considère des atomes froids à trois niveaux énergétiques dans des états de Rydberg [31, 53–56]. Les

atomes de Rydberg possèdent un fort moment dipolaire ce qui induit de fortes intéractions entre atomes. De plus, le mécanisme de blocage de Rydberg [57–59] améliore la probabilité d'interaction atome-photon car, du point de vue du photon, chaque atome de Rydberg se comporte comme un atome géant caractérisé par un rayon appelé "rayon de Rydberg". Cet effet ressemble à l'effet de la finesse d'une cavité mais contrairement à la cavité (dans laquelle un photon s'approche de l'atome plusieurs fois), ici un photon s'approche d'un "super-atome" avec une section efficace qui varie comme le nombre d'atomes dans le volume de Rydberg. Si le nombre d'atomes est suffisamment grand, des non linéarités optiques peuvent apparaître [60–62].

Dans un régime dissipatif, où deux photons proches brisent la condition de transparence induite électromagnétiquement et sont absorbés par l'ensemble d'atomes, une repulsion effective entre photons peut être réalisée [31]. Au contraire, dans un régime dispersif, une attraction effective a été récemment realisée [56]. Dans ce cas, l'indice de réfraction dépend de la distance séparant les photons. L'attraction photon-photon est causée par la formation d'états liés de deux polaritons [63, 64].

Pour un atome dans une cavité de haute finesse, un fort couplage atome-photon ou un grand volume de Rydberg (et donc une grande cooperativité), l'atome et la cavité échangent des photons plus rapidement que tous les autres processus dynamiques. Du point de vue du système, l'atome et le photon ne sont plus distinguables. Atomes et photons s'hybrident et forment une quasiparticule bosonique appellée polariton excitonique ou simplement polariton [65]. En raison de leur nature mixte, les polaritons ont des propriétés intéressantes, comme une masse effective plus légère que la masse atomique et donc une relation de dispersion plus raide (i.e. une large vitesse de groupe [66]). Les polaritons de microcavité peuvent devenir superfluide [67], et peuvent condenser lorsque la densité est suffisament élevée [65, 68–72]. Récemment, des condensats de Bose-Einstein ont été realisé avec des polaritons organiques à température ambiante [73, 74]. Grâce aux progrès techniques réalisés dans la fabrication de microcavités semiconductrices [75–79], les condensats de Bose-Einstein polaritoniques sont devenus des candidats prometteurs pour la simulation quantique.

Jusqu'à maintenant, nous avons considéré les non linéarités causées par le spectre atomique. Toutefois, les non linéarités optiques peuvent être produites en utilisant des vibrations phononiques, comme dans les systèmes optomécaniques [37]. Un fort couplage phonon-photon peut causer des phénomènes optiques non linéaires comme par example le "blocage" photonique [80] ou la bistabilité optique au niveau quantique [81]. Il y a aussi de nombreuses propositions théoriques pour réaliser des interactions effectives photon-photon [82].

Dans le vide, la diffraction limite la focalisation de la lumière à des volumes égaux ou supérieurs à la longueur d'onde cubique. Au cours des

dernières années, la recherche a beaucoup progressé vers la fabrication de nano-interfaces lumière-matière pour permettre la focalisation de la lumière en dessous de volumes interdits par la diffraction. On citera par example les guides d'ondes à cristaux photoniques [83–88], les cristaux optomécaniques [89–92], les fibres optiques [93–95], ou encore les nano-fils conducteurs [96, 97]. Les fibres optiques ayant un diamètre inférieur à la longueur d'onde du mode optique guidé, les atomes sont placés à l'exterieur de la fibre et couplés au champ électromagnétique évanescent [83]. On peut également placer les atomes à l'intérieur d'une fibre à cristaux photoniques [98–100]. Tous ces dispositifs, lorsqu'ils sont associés à des nanocavités ou microcavités à cristaux photoniques [101–103], ouvrent la voie vers la réalisation de reseaux quantiques [13, 16, 104]. Enfin, de fortes non linéarités optiques peuvent être réalisées dans des matériaux comme le graphène [106].

La plupart des chercheurs étudient la physique des photons uniques. Néanmoins, les non linéarités optiques peuvent également être intéressantes dans des systèmes à plusieurs photons. Il existe de nombreuses études s'intéressant à un ensemble de cavités couplées (modéle de Jaynes-Cummings-Hubbard) où les photons sautent d'une cavité à une autre, chaque cavité contenant un atome à deux niveaux énérgetiques [66, 113–118]. Dans ce cas, les non linéarités sont causées par l'anharmonicité du spectre de Jaynes-Cummings. L'intéraction entre la propagation linéaire de la lumière dans le vide et la non linearité dans les cavités est responsable de transitions de phase. Les ensembles de cavités peuvent être aussi combinés avec des atomes de Rydberg [119]. Il existe aussi des propositions visant à observer de nouvelles phase collectives de la lumière, comme les phases cristallines dans les fibres optiques [120], ou dans des ensembles d'atomes de Rydberg [121].

Dans cette thèse, je présente tous les projets de recherche menés à bien pendant mon doctorat, dont deux déjà publiés dans des journaux scientifiques et deux encore en cours de publication. En particulier, la thèse est divisée en quatre chapitres, avec un chapitre dédié à chaque projet.

Dans ces quatre projets, je m'intéresse à l'optique quantique, plus particulièrement à l'électrodynamique quantique à l'intérieur d'un résonateur : une cavité Fabry-Pérot à un seul mode optique dans les deux premiers projets, ainsi qu'une fibre à cristaux photoniques supportant plusieurs modes dans les deux derniers projets.

Dans le premier chapitre de cette thèse, je présente mes résultats de recherche sur les cristaux photoniques et l'amélioration du couplage entre les degrés de liberté optiques et mécaniques [276]. Les cristaux photoniques sont des structures périodiques construites à partir de matériaux diélectriques qui modifie la propagation des photons de la même façon qu'un potentiel périodique dans un cristal semi-conducteur modifie la propagation des électrons. Il apparaît des gap d'énergie dans lesquels aucun mode photonique ne peut se propager [89, 92]. Nous étudions alors la possibil-

ité d'améliorer le couplage optoméchanique photon-phonon entre le mode de résonance d'une cavité Fabry-Pérot de haute finesse et les vibrations mécaniques des éléments diélectriques à l'intérieur de la cavité [37, 38]. Il a été récemment démontré qu'un ensemble périodique de membranes diélectriques placé à l'intérieur d'une cavité peut augmenter le couplage optoméchanique linéaire qui devient beaucoup plus grand que la valeur attendue dans le cas d'un seul élément réfléchissant placé entre les deux miroirs de la cavité [122, 123]. Pour obtenir ce résultat remarquable, il faut toutefois opérer dans un régime très particulier, où l'ensemble des membranes (lorsqu'elles sont immobiles) est transparent à la lumière; ce régime est appelé régime transmissif. Dans le cadre de notre projet de recherche, nous généralisons ces résultats en introduisant un défaut quadratique dans la disposition des membranes. En régime transmissif, nous étudions donc une structure quasipériodique de membranes et cherchons à augmenter encore plus les couplages linéaires et quadratiques.

Nous considérons notamment deux dispositifs. Le premier dispositif [voir Fig. 1.2(a)] est une cavité Fabry-Pérot de haute finesse contenant une structure quasipériodique d'éléments diélectriques. Le second dispositif [voir Fig. 1.2(b)] consiste en un modèle très simple avec lequel on cherche à simuler un cristal photonique quasipériodique. Ici, les deux miroirs de la cavité du premier dispositif sont remplacés par deux ensembles périodiques de membranes. Dans le premier cas, nous montrons numériquement (et toujours en travaillant dans un régime d'optoméchanique transmissif) que l'introduction du défaut spatial induit un régime de localisation de la lumière autour de la région quadratique, c'est à dire au milieu de la cavité. A son tour, cette localisation est responsable d'une augmentation du couplage photon-phonon. De plus, on montre que le couplage photon-phonon quadratique est également augmenté [122, 123].

Concernant le deuxième dispositif, on détecte aussi une augmentation des couplages linéaires et quadratiques, mais dans ce cas, cette augmentation n'est pas dûe aux défauts quadratiques introduits au milieu du cristal, mais plutôt au fait que la longueur effective de la cavité est beaucoup plus grande que sa longueur réelle [122, 123].

Dans le deuxième chapitre de cette thèse, nous présentons nos résultats de recherche sur le transport d'excitons à travers une cavité visant à augmenter l'efficacité du transport [277]. Ce projet à été inspiré par des expériences pionnières menées dans le groupe du Professeur Thomas Ebbesen sur des semi-conducteurs organiques à l'Institut de Science et d'Ingénierie Supramoléculaires de Strasbourg [180]. Le modèle que l'on étudie ici est une chaîne unidimensionnelle d'atomes froids comprenant chacun deux niveaux énergétiques : un atome peut être dans son état excité ou dans son état fondamental. De ce point de vue, chaque atome est assimilable à un spin 1/2. Le modèle est illustré sur la Fig. 2.2. Autour de cette chaîne d'atomes, on place alors une cavité transversale. Si un atome est excité, il

peut donc émettre un photon dans la cavité puis se désexciter, ou vice-versa : un atome dans son état fondamental peut absorber un photon et être promu dans son état excité. Ce modèle peut être réalisé en laboratoire en utilisant par exemple des atomes de Rydberg dans une microcavité. Lorsqu'ils sont excités par un laser, ces atomes s'organisent spontanément dans un réseau en raison de leur interactions mutuelles [198, 199]. Ce modèle peut également être réalisé en utilisant des molécules polaires dans un réseau optique de microcavité [200, 201], ou encore des ions froids dans un piége de Paul linéaire [202, 203].

Lorsque l'exciton n'est pas couplé au vide électromagnétique dans la cavité, il se propage alors le long de la chaîne en sautant d'un site à l'autre. Autrement dit, dans le formalisme spinoriel, le spin est annihilé sur un site et recrée sur un des sites premiers voisins. Ce processus de transport site-par-site prend un certain temps, surtout si l'exciton doit traverser un très grand nombre d'atomes. De plus, si l'on introduit du désordre dans le système, ce dernier tend à supprimer le transport de façon exponentielle, comme dans le processus de localisation d'Anderson [125]. L'objectif de recherche présenté dans ce chapitre est de rendre ce processus plus rapide et efficace. Grâce au couplage entre exciton et photon, ces deux quanta s'hybrident et forment deux branches de polariton à l'intérieur de la cavité [181, 182]. Ces quasiparticules, en tant que superpositions cohérentes de photons et d'excitons, ont une masse effective très faible. Grâce à leur fraction photonique non nulle, les polaritons possèdent en outre une vitesse de groupe supérieure à celle d'un exciton non couplé, et sont aussi moins sensibles au désordre et aux processus dissipatifs pouvant affecter les matériaux réels.

Dans ce chapitre, nous simulons numériquement deux expériences. Dans la première expérience, on étudie analytiquement et numériquement la transmission d'un paquet d'onde excitonique. Dans la seconde, on injecte de façon incohérente une excitation à l'intérieur de la cavité, et l'on mesure le courant excitonique dans un état stationnaire. Dans cette seconde simulation, nous utilisons le formalisme de l'équation maîtresse [278]. Dans ces deux expériences, nous avons observé qu'à résonance avec un des deux modes de polariton, on peut transmettre l'exciton via le mode polaritonique dans un temps très court. En outre, le désordre n'affecte la propagation excitonique que de façon algébrique (loi de puissance) et non pas exponentielle. Ce résultat est très important : il suggère en effet que l'utilisation de modes polaritoniques pourrait permettre d'augmenter la conductivité des semi-conducteurs organiques, et ainsi avoir des applications intéressantes dans l'industrie.

Dans le troisième chapitre de cette thèse, nous présentons nos résultats de recherche sur la réalisation d'interactions entre photons grâce à la médiation d'atomes ultrafroids piégés dans un réseaux optique unidimensionnelle et placés à l'intérieur d'une fibre à cristaux photoniques [279].

Il est bien connu que les photons n'interagissent pas directement entre eux. Malgré cela, il existe plusieurs façons de concevoir des non linéarités photoniques. On peut par exemple exploiter l'anharmonicité du spectre de l'Hamiltonien de Jaines-Cummings lorsque l'on considère des excitations multiples [115]. On peut aussi exploiter les interactions dipolaires entre atomes, en utilisant typiquement des atomes de Rydberg à trois niveaux sous conditions de transparence induite électromagnétiquement [31, 54–56]. Ici, nous proposons aux expérimentateurs une méthode plus simple pour réaliser des interactions entre photons: faire interagir les photons par l'intermédiaire d'atomes en utilisant la saturabilité énergétique de ces derniers.

Chaque atome est décrit comme un système à deux niveaux énergétiques : l'état excité et l'état fondamental, et interagit avec la cavité par échange d'une excitation. Chaque atome est aussi un système saturable au sens où il ne peut pas accueillir plus d'un exciton. On dit alors que les excitons agissent comme des bosons de "coeur-dur", ce qui permet d'inclure le principe d'exclusion de Pauli: on ne peut pas avoir deux excitons sur le même site. Cette interaction est de nature cinématique et non pas dynamique.

Dans notre problème (voir Fig. 3.1), on considère notamment deux excitons dans la fibre optique et, comme dans le chapitre précédent, chaque exciton se couple à la lumière pour former un couple de polaritons. Etant donné que l'on considère deux excitons, on a donc quatre polaritons dans la fibre. Ces polaritons interagissent entre eux en raison de leur fraction excitonique non nulle. Dans un régime de couplage collective fort, les photons interagissent indirectement entre eux puisqu'ils sont "collées" aux excitons et sont par conséquent forcés à suivre leur interaction.

En particulier, nous avons détecté un régime dans lequel on peut réaliser le "bunching" photon-photon: les deux photons sont enclins à rester ensemble, c'est à dire localisés sur le même site de la chaîne d'atomes.

Dans le case où le spectre d'excitation soit gappé, l'interaction cinématique permet la formation d'états liés dans le gap.

Dans le quatrième et dernière chapitre de cette thèse, nous étendons les résultats du chapitre précédent aux atomes de Rydberg.

Dans ce modèle, les atomes de Rydberg dans la fibre à cristaux photoniques ont deux niveaux énergétiques. Les excitons qui se propagent sont aussi considérés comme des bosons de coeur-dur mais à la différence des atomes normaux, le rayon d'exclusion appelé "rayon de Rydberg" couvre en général plusieurs unités de distance atomique. A cause de l'extension du rayon de Rydberg, la tendance des photons à rester unis est encore plus évidente et marquée.

Les atomes de Rydberg interagissent aussi dynamiquement par une interaction à longue portée; dans le cas où cette interaction soit attractive on peut observer la formation d'états liés même si le spectre d'excitation n'est

pas gappé.

Bibliography

[1] V. P. Berestetskii, L. P. Pitaevskii, and E. M. Lifshitz, *Quantum Electrodynamics, Second Edition: Volume 4 (Course of Theoretical Physics)* (Butterworth-Heinemann; 2 edition, 2005).

[2] D. E. Chang, V. Vuletic, and M. D. Lukin, Quantum nonlinear optics [mdash] photon by photon, Nat Photon **8**, 685 (2014).

[3] J. Whitaker, *The Electronics Handbook, Second Edition*, Electrical Engineering Handbook (CRC Press, 2005).

[4] A. Jerri, The Shannon sampling theorem — Its various extensions and applications: A tutorial review, Proceedings of the IEEE .

[5] G. New, *Introduction to Nonlinear Optics* (Cambridge University Press, 2011).

[6] P. A. Franken and J. F. Ward, Optical Harmonics and Nonlinear Phenomena, Rev. Mod. Phys. **35**, 23 (1963).

[7] R. L. Byer, Quasi-Phasematched Nonlinear Interactions and Devices, Journal of Nonlinear Optical Physics and Materials **6**, 549 (1997).

[8] G. J. Milburn, Quantum optical Fredkin gate, Phys. Rev. Lett. **62**, 2124 (1989).

[9] N. Imoto, H. A. Haus, and Y. Yamamoto, Quantum nondemolition measurement of the photon number via the optical Kerr effect, Phys. Rev. A **32**, 2287 (1985).

[10] S. E. Harris, J. E. Field, and A. Imamoğlu, Nonlinear optical processes using electromagnetically induced transparency, Phys. Rev. Lett. **64**, 1107 (1990).

[11] T. D. Ladd, F. Jelezko, R. Laflamme, Y. Nakamura, C. Monroe, and J. L. O'Brien, Quantum computers, Nature **464**, 45 (2010).

[12] Q. A. Turchette, C. J. Hood, W. Lange, H. Mabuchi, and H. J. Kimble, Measurement of Conditional Phase Shifts for Quantum Logic, Phys. Rev. Lett. **75**, 4710 (1995).

[13] D. O'Shea, C. Junge, J. Volz, and A. Rauschenbeutel, Fiber-Optical Switch Controlled by a Single Atom, Phys. Rev. Lett. **111**, 193601 (2013).

[14] I. Shomroni, S. Rosenblum, Y. Lovsky, O. Bechler, G. Guendelman, and B. Dayan, All-optical routing of single photons by a one-atom switch controlled by a single photon, Science **345**, 903 (2014), http://www.sciencemag.org/content/345/6199/903.full.pdf .

[15] D. A. B. Miller, Are optical transistors the logical next step?, Nat Photon **4**, 3 (2010).

[16] D. E. Chang, A. S. Sorensen, E. A. Demler, and M. D. Lukin, A single-photon transistor using nanoscale surface plasmons, Nat Phys **3**, 807 (2007).

[17] J. Hwang, M. Pototschnig, R. Lettow, G. Zumofen, A. Renn, S. Gotzinger, and V. Sandoghdar, A single-molecule optical transistor, Nature **460**, 76 (2009).

[18] W. Chen, K. M. Beck, R. Bücker, M. Gullans, M. D. Lukin, H. Tanji-Suzuki, and V. Vuletic, All-Optical Switch and Transistor Gated by One Stored Photon, Science **341**, 768 (2013), http://www.sciencemag.org/content/341/6147/768.full.pdf .

[19] H. Gorniaczyk, C. Tresp, J. Schmidt, H. Fedder, and S. Hofferberth, Single-Photon Transistor Mediated by Interstate Rydberg Interactions, Phys. Rev. Lett. **113**, 053601 (2014).

[20] D. Tiarks, S. Baur, K. Schneider, S. Dürr, and G. Rempe, Single-Photon Transistor Using a Förster Resonance, Phys. Rev. Lett. **113**, 053602 (2014).

[21] S. Baur, D. Tiarks, G. Rempe, and S. Dürr, Single-Photon Switch Based on Rydberg Blockade, Phys. Rev. Lett. **112**, 073901 (2014).

[22] T. Volz, A. Reinhard, M. Winger, A. Badolato, K. J. Hennessy, E. L. Hu, and A. Imamoğlu, Ultrafast all-optical switching by single photons, Nat Photon **6**, 605 (2012).

[23] T. G. Tiecke, J. D. Thompson, N. P. de Leon, L. R. Liu, V. Vuletic, and M. D. Lukin, Nanophotonic quantum phase switch with a single atom, Nature **508**, 241 (2014).

[24] J. L. O'Brien, G. J. Pryde, A. G. White, T. C. Ralph, and D. Branning, Demonstration of an all-optical quantum controlled-NOT gate, Nature **426**, 264 (2003).

[25] Y. M. Hao, G. W. Lin, K. Xia, X. M. Lin, Y. P. Niu, and S. Q. Gong, Quantum controlled-phase-flip gate between a flying optical photon and a Rydberg atomic ensemble, Scientific Reports **5**, 10005 EP (2015).

[26] J. Volz, M. Scheucher, C. Junge, and A. Rauschenbeutel, Nonlinear π phase shift for single fibre-guided photons interacting with a single resonator-enhanced atom, Nat Photon **8**, 965 (2014).

[27] H. J. Kimble, The quantum internet, Nature **453**, 1023 (2008).

[28] V. Giovannetti, S. Lloyd, and L. Maccone, Advances in quantum metrology, Nat Photon **5**, 222 (2011).

[29] A. Muthukrishnan, M. O. Scully, and M. S. Zubairy, Quantum microscopy using photon correlations, Journal of Optics B: Quantum and Semiclassical Optics **6**, S575 (2004).

[30] A. Reiserer, S. Ritter, and G. Rempe, Nondestructive Detection of an Optical Photon, Science **342**, 1349 (2013), http://www.sciencemag.org/content/342/6164/1349.full.pdf .

[31] T. Peyronel, O. Firstenberg, Q.-Y. Liang, S. Hofferberth, A. V. Gorshkov, T. Pohl, M. D. Lukin, and V. Vuletic, Quantum nonlinear optics with single photons enabled by strongly interacting atoms, Nature **488**, 57 (2012).

[32] G. Nikoghosyan and M. Fleischhauer, Photon-Number Selective Group Delay in Cavity Induced Transparency, Phys. Rev. Lett. **105**, 013601 (2010).

[33] Y. O. Dudin and A. Kuzmich, Strongly Interacting Rydberg Excitations of a Cold Atomic Gas, Science **336**, 887 (2012), http://www.sciencemag.org/content/336/6083/887.full.pdf .

[34] J. Petersen, J. Volz, and A. Rauschenbeutel, Chiral nanophotonic waveguide interface based on spin-orbit interaction of light, Science **346**, 67 (2014), http://www.sciencemag.org/content/346/6205/67.full.pdf .

[35] M. Neugebauer, T. Bauer, P. Banzer, and G. Leuchs, Polarization Tailored Light Driven Directional Optical Nanobeacon, Nano Letters **14**, 2546 (2014), pMID: 24724814, http://dx.doi.org/10.1021/nl5003526 .

[36] F. J. Rodríguez-Fortuño, I. Barber-Sanz, D. Puerto, A. Griol, and A. Martínez, Resolving Light Handedness with an on-Chip Silicon Microdisk, ACS Photonics **1**, 762 (2014), http://dx.doi.org/10.1021/ph500084b .

[37] M. Aspelmeyer, T. J. Kippenberg, and F. Marquardt, Cavity optomechanics, Rev. Mod. Phys. **86**, 1391 (2014).

[38] A. Clerk and F. Marquardt, Basic Theory of Cavity Optomechanics, in *Cavity Optomechanics*, Quantum Science and Technology, edited by M. Aspelmeyer, T. J. Kippenberg, and F. Marquardt (Springer Berlin Heidelberg, 2014) pp. 5–23.

[39] E. Jaynes and F. Cummings, Comparison of quantum and semiclassical radiation theories with application to the beam maser, Proceedings of the IEEE **51**, 89 (1963).

[40] K. M. Birnbaum, A. Boca, R. Miller, A. D. Boozer, T. E. Northup, and H. J. Kimble, Photon blockade in an optical cavity with one trapped atom, Nature **436**, 87 (2005).

[41] A. Kubanek, A. Ourjoumtsev, I. Schuster, M. Koch, P. W. H. Pinkse, K. Murr, and G. Rempe, Two-Photon Gateway in One-Atom Cavity Quantum Electrodynamics, Phys. Rev. Lett. **101**, 203602 (2008).

[42] H. P. Specht, C. Nolleke, A. Reiserer, M. Uphoff, E. Figueroa, S. Ritter, and G. Rempe, A single-atom quantum memory, Nature **473**, 190 (2011).

[43] A. Reiserer, N. Kalb, G. Rempe, and S. Ritter, A quantum gate between a flying optical photon and a single trapped atom, Nature **508**, 237 (2014).

[44] J. I. Cirac, P. Zoller, H. J. Kimble, and H. Mabuchi, Quantum State Transfer and Entanglement Distribution among Distant Nodes in a Quantum Network, Phys. Rev. Lett. **78**, 3221 (1997).

[45] M. Fleischhauer, A. Imamoğlu, and J. P. Marangos, Electromagnetically induced transparency: Optics in coherent media, Rev. Mod. Phys. **77**, 633 (2005).

[46] B. J. M. Hausmann, B. Shields, Q. Quan, P. Maletinsky, M. McCutcheon, J. T. Choy, T. M. Babinec, A. Kubanek, A. Yacoby, M. D. Lukin, and M. Lončar, Integrated Diamond Networks for Quantum Nanophotonics, Nano Letters **12**, 1578 (2012), pMID: 22339606, http://dx.doi.org/10.1021/nl204449n .

[47] A. Faraon, P. E. Barclay, C. Santori, K.-M. C. Fu, and R. G. Beausoleil, Resonant enhancement of the zero-phonon emission from a colour centre in a diamond cavity, Nat Photon **5**, 301 (2011).

[48] P. Michler, A. Kiraz, C. Becher, W. V. Schoenfeld, P. M. Petroff, L. Zhang, E. Hu, and A. Imamoğlu, A Quantum Dot Single-Photon Turnstile Device, Science **290**, 2282 (2000), http://www.sciencemag.org/content/290/5500/2282.full.pdf .

[49] A. Laucht, F. Hofbauer, N. Hauke, J. Angele, S. Stobbe, M. Kaniber, G. Böhm, P. Lodahl, M.-C. Amann, and J. J. Finley, Electrical control of spontaneous emission and strong coupling for a single quantum dot, New Journal of Physics **11**, 023034 (2009).

[50] M. Pelton, C. Santori, J. Vučković, B. Zhang, G. S. Solomon, J. Plant, and Y. Yamamoto, Efficient Source of Single Photons: A Single Quantum Dot in a Micropost Microcavity, Phys. Rev. Lett. **89**, 233602 (2002).

[51] I. Fushman, D. Englund, A. Faraon, N. Stoltz, P. Petroff, and J. Vučković, Controlled Phase Shifts with a Single Quantum Dot, Science **320**, 769 (2008), http://www.sciencemag.org/content/320/5877/769.full.pdf .

[52] K. Hammerer, A. S. Sørensen, and E. S. Polzik, Quantum interface between light and atomic ensembles, Rev. Mod. Phys. **82**, 1041 (2010).

[53] D. Maxwell, D. J. Szwer, D. Paredes-Barato, H. Busche, J. D. Pritchard, A. Gauguet, K. J. Weatherill, M. P. A. Jones, and C. S. Adams, Storage and Control of Optical Photons Using Rydberg Polaritons, Phys. Rev. Lett. **110**, 103001 (2013).

[54] G. Günter, H. Schempp, M. Robert-de Saint-Vincent, V. Gavryusev, S. Helmrich, C. S. Hofmann, S. Whitlock, and M. Weidemüller, Observing the Dynamics of Dipole-Mediated Energy Transport by Interaction-Enhanced Imaging, Science **342**, 954 (2013), http://www.sciencemag.org/content/342/6161/954.full.pdf .

[55] A. V. Gorshkov, J. Otterbach, M. Fleischhauer, T. Pohl, and M. D. Lukin, Photon-Photon Interactions via Rydberg Blockade, Phys. Rev. Lett. **107**, 133602 (2011).

[56] O. Firstenberg, T. Peyronel, Q.-Y. Liang, A. V. Gorshkov, M. D. Lukin, and V. Vuletic, Attractive photons in a quantum nonlinear medium, Nature **502**, 71 (2013).

[57] A. Gaetan, Y. Miroshnychenko, T. Wilk, A. Chotia, M. Viteau, D. Comparat, P. Pillet, A. Browaeys, and P. Grangier, Observation of collective excitation of two individual atoms in the Rydberg blockade regime, Nat Phys **5**, 115 (2009).

[58] M. D. Lukin, M. Fleischhauer, R. Cote, L. M. Duan, D. Jaksch, J. I. Cirac, and P. Zoller, Dipole Blockade and Quantum Information Processing in Mesoscopic Atomic Ensembles, Phys. Rev. Lett. **87**, 037901 (2001).

[59] E. Urban, T. A. Johnson, T. Henage, L. Isenhower, D. D. Yavuz, T. G. Walker, and M. Saffman, Observation of Rydberg blockade between two atoms, Nat Phys **5**, 110 (2009).

[60] J. D. Pritchard, *Cooperative optical non-linearity in a blockaded Rydberg ensemble*, edited by S. (Online), Springer theses. (Springer, 2012).

[61] J. D. Pritchard, D. Maxwell, A. Gauguet, K. J. Weatherill, M. P. A. Jones, and C. S. Adams, Cooperative Atom-Light Interaction in a Blockaded Rydberg Ensemble, Phys. Rev. Lett. **105**, 193603 (2010).

[62] J. D. Pritchard, K. J. Weatherill, and C. S. Adams, Nonlinear optics using cold Rydberg atoms, in *Annual Review of Cold Atoms and Molecules*, Quantum Science and Technology, edited by K. W. Madison, Y. Wang, A. M. Rey, and K. Bongs (Springer Berlin Heidelberg, 2013) pp. 301–350.

[63] P. Bienias, S. Choi, O. Firstenberg, M. F. Maghrebi, M. Gullans, M. D. Lukin, A. V. Gorshkov, and H. P. Büchler, Scattering resonances and bound states for strongly interacting Rydberg polaritons, Phys. Rev. A **90**, 053804 (2014).

[64] M. F. Maghrebi, M. J. Gullans, P. Bienias, S. Choi, I. Martin, O. Firstenberg, M. D. Lukin, H. P. Büchler, and A. V. Gorshkov, Coulomb Bound States of Strongly Interacting Photons, Phys. Rev. Lett. **115**, 123601 (2015).

[65] T. Byrnes, N. Y. Kim, and Y. Yamamoto, Exciton-polariton condensates, Nat Phys **10**, 803 (2014).

[66] I. Carusotto and C. Ciuti, Quantum fluids of light, Rev. Mod. Phys. **85**, 299 (2013).

[67] A. Amo, J. Lefrere, S. Pigeon, C. Adrados, C. Ciuti, I. Carusotto, R. Houdre, E. Giacobino, and A. Bramati, Superfluidity of polaritons in semiconductor microcavities, Nat Phys **5**, 805 (2009).

[68] J. Kasprzak, M. Richard, S. Kundermann, A. Baas, P. Jeambrun, J. M. J. Keeling, F. M. Marchetti, M. H. Szymanska, R. Andre, J. L. Staehli, V. Savona, P. B. Littlewood, B. Deveaud, and L. S. Dang, Bose-Einstein condensation of exciton polaritons, Nature **443**, 409 (2006).

[69] R. Balili, V. Hartwell, D. Snoke, L. Pfeiffer, and K. West, Bose-Einstein Condensation of Microcavity Polaritons in a Trap, Science **316**, 1007 (2007), http://www.sciencemag.org/content/316/5827/1007.full.pdf .

[70] J. M. Ménard, C. Poellmann, M. Porer, U. Leierseder, E. Galopin, A. Lemaître, A. Amo, J. Bloch, and R. Huber, Revealing the dark side of a bright exciton–polariton condensate, Nat Commun **5** (2014).

[71] H. Deng, H. Haug, and Y. Yamamoto, Exciton-polariton Bose-Einstein condensation, Rev. Mod. Phys. **82**, 1489 (2010).

[72] B. Deveaud, Exciton-Polariton Bose-Einstein Condensates, Annual Review of Condensed Matter Physics **6**, 155 (2015).

[73] J. D. Plumhof, T. Stöferle, L. Mai, U. Scherf, and R. F. Mahrt, Room-temperature Bose–Einstein condensation of cavity exciton–polaritons in a polymer, Nat Mater **13**, 247 (2014).

[74] K. S. Daskalakis, S. A. Maier, R. Murray, and S. Kéna-Cohen, Nonlinear interactions in an organic polariton condensate, Nat Mater **13**, 271 (2014).

[75] E. Wertz, L. Ferrier, D. D. Solnyshkov, R. Johne, D. Sanvitto, A. Lemaitre, I. Sagnes, R. Grousson, A. V. Kavokin, P. Senellart, G. Malpuech, and J. Bloch, Spontaneous formation and optical manipulation of extended polariton condensates, Nat Phys **6**, 860 (2010).

[76] D. Tanese, E. Gurevich, F. Baboux, T. Jacqmin, A. Lemaître, E. Galopin, I. Sagnes, A. Amo, J. Bloch, and E. Akkermans, Fractal Energy Spectrum of a Polariton Gas in a Fibonacci Quasiperiodic Potential, Phys. Rev. Lett. **112**, 146404 (2014).

[77] T. Jacqmin, I. Carusotto, I. Sagnes, M. Abbarchi, D. D. Solnyshkov, G. Malpuech, E. Galopin, A. Lemaître, J. Bloch, and A. Amo, Direct Observation of Dirac Cones and a Flatband in a Honeycomb Lattice for Polaritons, Phys. Rev. Lett. **112**, 116402 (2014).

[78] F. Baboux, L. Ge, T. Jacqmin, M. Biondi, A. Lemaître, L. Le Gratiet, I. Sagnes, S. Schmidt, H. E. Türeci, A. Amo, and J. Bloch, Bosonic Condensation and Disorder-Induced Localization in a Flat Band, ArXiv e-prints (2015), arXiv:1505.05652 [cond-mat.mes-hall] .

[79] B. Besga, C. Vaneph, J. Reichel, J. Estève, A. Reinhard, J. Miguel-Sánchez, A. m. c. Imamoğlu, and T. Volz, Polariton Boxes in a Tunable Fiber Cavity, Phys. Rev. Applied **3**, 014008 (2015).

[80] P. Rabl, Photon Blockade Effect in Optomechanical Systems, Phys. Rev. Lett. **107**, 063601 (2011).

[81] S. Gupta, K. L. Moore, K. W. Murch, and D. M. Stamper-Kurn, Cavity Nonlinear Optics at Low Photon Numbers from Collective Atomic Motion, Phys. Rev. Lett. **99**, 213601 (2007).

[82] H.-K. Li, X.-X. Ren, Y.-C. Liu, and Y.-F. Xiao, Photon-photon interactions in a largely detuned optomechanical cavity, Phys. Rev. A **88**, 053850 (2013).

[83] A. Goban, C. L. Hung, S. P. Yu, J. D. Hood, J. A. Muniz, J. H. Lee, M. J. Martin, A. C. McClung, K. S. Choi, D. E. Chang, O. Painter, and H. J. Kimble, Atom–light interactions in photonic crystals, Nat Commun **5** (2014).

[84] S. Pleasants, Photonic-crystal waveguides: Trapping single atoms, Nat Photon **8**, 427 (2014).

[85] Y. A. Vlasov, M. O'Boyle, H. F. Hamann, and S. J. McNab, Active control of slow light on a chip with photonic crystal waveguides, Nature **438**, 65 (2005).

[86] S. Ek, P. Lunnemann, Y. Chen, E. Semenova, K. Yvind, and J. Mork, Slow-light-enhanced gain in active photonic crystal waveguides, Nat Commun **5** (2014).

[87] T. Baba, Slow light in photonic crystals, Nat Photon **2**, 465 (2008).

[88] K. Ishizaki, M. Koumura, K. Suzuki, K. Gondaira, and S. Noda, Realization of three-dimensional guiding of photons in photonic crystals, Nat Photon **7**, 133 (2013).

[89] M. Eichenfield, J. Chan, R. M. Camacho, K. J. Vahala, and O. Painter, Optomechanical crystals, Nature **462**, 78 (2009).

[90] J. Gomis-Bresco, D. Navarro-Urrios, M. Oudich, S. El-Jallal, A. Griol, D. Puerto, E. Chavez, Y. Pennec, B. Djafari-Rouhani, F. Alzina, A. Martínez, and C. M. S. Torres, A one-dimensional optomechanical crystal with a complete phononic band gap, Nat Commun **5** (2014).

[91] M. Eichenfield, R. Camacho, J. Chan, K. J. Vahala, and O. Painter, A picogram- and nanometre-scale photonic-crystal optomechanical cavity, Nature **459**, 550 (2009).

[92] J. Chan, M. Eichenfield, R. Camacho, and O. Painter, Optical and mechanical design of a "zipper" photonic crystaloptomechanical cavity, Opt. Express **17**, 3802 (2009).

[93] E. Vetsch, D. Reitz, G. Sagué, R. Schmidt, S. T. Dawkins, and A. Rauschenbeutel, Optical Interface Created by Laser-Cooled Atoms Trapped in the Evanescent Field Surrounding an Optical Nanofiber, Phys. Rev. Lett. **104**, 203603 (2010).

[94] G. Sagué, E. Vetsch, W. Alt, D. Meschede, and A. Rauschenbeutel, Cold-Atom Physics Using Ultrathin Optical Fibers: Light-Induced Dipole Forces and Surface Interactions, Phys. Rev. Lett. **99**, 163602 (2007).

[95] K. P. Nayak, P. N. Melentiev, M. Morinaga, F. L. Kien, V. I. Balykin, and K. Hakuta, Optical nanofiber as an efficient tool for manipulating and probing atomic fluorescence, Opt. Express **15**, 5431 (2007).

[96] A. V. Akimov, A. Mukherjee, C. L. Yu, D. E. Chang, A. S. Zibrov, P. R. Hemmer, H. Park, and M. D. Lukin, Generation of single optical plasmons in metallic nanowires coupled to quantum dots, Nature **450**, 402 (2007).

[97] R. Kolesov, B. Grotz, G. Balasubramanian, R. J. Stohr, A. A. L. Nicolet, P. R. Hemmer, F. Jelezko, and J. Wrachtrup, Wave-particle duality of single surface plasmon polaritons, Nat Phys **5**, 470 (2009).

[98] M. R. Sprague, P. S. Michelberger, T. F. M. Champion, D. G. England, J. Nunn, X. M. Jin, W. S. Kolthammer, A. Abdolvand, P. S. J. Russell, and I. A. Walmsley, Broadband single-photon-level memory in a hollow-core photonic crystal fibre, Nat Photon **8**, 287 (2014).

[99] S. Okaba, T. Takano, F. Benabid, T. Bradley, L. Vincetti, Z. Maizelis, V. Yampol'skii, F. Nori, and H. Katori, Lamb-Dicke spectroscopy of atoms in a hollow-core photonic crystal fibre, Nat Commun **5** (2014).

[100] G. Epple, K. S. Kleinbach, T. G. Euser, N. Y. Joly, T. Pfau, P. S. J. Russell, and R. Löw, Rydberg atoms in hollow-core photonic crystal fibres, Nat Commun **5** (2014).

[101] J. D. Thompson, T. G. Tiecke, N. P. de Leon, J. Feist, A. V. Akimov, M. Gullans, A. S. Zibrov, V. Vuletic, and M. D. Lukin, Coupling a Single Trapped Atom to a Nanoscale Optical Cavity, Science **340**, 1202 (2013), http://www.sciencemag.org/content/340/6137/1202.full.pdf .

[102] T.-R. Lin, C.-H. Lin, and J.-C. Hsu, Strong Optomechanical Interaction in Hybrid Plasmonic-Photonic Crystal Nanocavities with Surface Acoustic Waves, Scientific Reports **5**, 13782 EP (2015).

[103] J. Chan, A. H. Safavi-Naeini, J. T. Hill, S. Meenehan, and O. Painter, Optimized optomechanical crystal cavity with acoustic radiation shield, Applied Physics Letters **101**, 081115 (2012), http://dx.doi.org/10.1063/1.4747726.

[104] S. Ritter, C. Nolleke, C. Hahn, A. Reiserer, A. Neuzner, M. Uphoff, M. Mucke, E. Figueroa, J. Bochmann, and G. Rempe, An elementary quantum network of single atoms in optical cavities, Nature **484**, 195 (2012).

[105] U. Gubler and C. Bosshard, Optical materials: A new twist for nonlinear optics, Nat Mater **1**, 209 (2002).

[106] M. Gullans, D. E. Chang, F. H. L. Koppens, F. J. G. de Abajo, and M. D. Lukin, Single-Photon Nonlinear Optics with Graphene Plasmons, Phys. Rev. Lett. **111**, 247401 (2013).

[107] G. Agrawal, *Nonlinear Fiber Optics* (Academinc, 2012).

[108] Y. Lai and H. A. Haus, Quantum theory of solitons in optical fibers. I. Time-dependent Hartree approximation, Phys. Rev. A **40**, 844 (1989).

[109] P. D. Drummond, R. M. Shelby, S. R. Friberg, and Y. Yamamoto, Quantum solitons in optical fibres, Nature **365**, 307 (1993).

[110] R. Y. Chiao, I. H. Deutsch, and J. C. Garrison, Two-photon bound state in self-focusing media, Phys. Rev. Lett. **67**, 1399 (1991).

[111] I. H. Deutsch, R. Y. Chiao, and J. C. Garrison, Two-photon bound states: The diphoton bullet in dispersive self-focusing media, Phys. Rev. A **47**, 3330 (1993).

[112] K. V. Kheruntsyan and P. D. Drummond, Three-dimensional quantum solitons with parametric coupling, Phys. Rev. A **58**, 2488 (1998).

[113] M. J. Hartmann, F. G. S. L. Brandao, and M. B. Plenio, Strongly interacting polaritons in coupled arrays of cavities, Nat Phys **2**, 849 (2006).

[114] S.-L. Su, X.-Q. Shao, H.-F. Wang, and S. Zhang, Preparation of three-dimensional entanglement for distant atoms in coupled cavities via atomic spontaneous emission and cavity decay, Scientific Reports **4**, 7566 EP (2014).

[115] C.-z. Zhu, S. Endo, P. Naidon, and P. Zhang, Scattering and Bound States of two Polaritons in an Array of Coupled Cavities, Few-Body Systems **54**, 1921 (2013).

[116] A. D. Greentree, C. Tahan, J. H. Cole, and L. C. L. Hollenberg, Quantum phase transitions of light, Nat Phys **2**, 856 (2006).

[117] D. G. Angelakis, M. F. Santos, and S. Bose, Photon-blockade-induced Mott transitions and *XY* spin models in coupled cavity arrays, Phys. Rev. A **76**, 031805 (2007).

[118] F. Badshah, S. Qamar, and M. Paternostro, Dynamics of interacting Dicke model in a coupled-cavity array, Phys. Rev. A **90**, 033813 (2014).

[119] Y. Zhang, J. Fan, J. Q. Liang, J. Ma, G. Chen, S. Jia, and F. Nori, Photon Devil's staircase: photon long-range repulsive interaction in lattices of coupled resonators with Rydberg atoms, Scientific Reports **5**, 11510 EP (2015).

[120] D. E. Chang, V. Gritsev, G. Morigi, V. Vuletic, M. D. Lukin, and E. A. Demler, Crystallization of strongly interacting photons in a nonlinear optical fibre, Nat Phys **4**, 884 (2008).

[121] J. Otterbach, M. Moos, D. Muth, and M. Fleischhauer, Wigner Crystallization of Single Photons in Cold Rydberg Ensembles, Phys. Rev. Lett. **111**, 113001 (2013).

[122] A. Xuereb, C. Genes, and A. Dantan, Strong Coupling and Long-Range Collective Interactions in Optomechanical Arrays, Phys. Rev. Lett. **109**, 223601 (2012).

[123] A. Xuereb, C. Genes, and A. Dantan, Collectively enhanced optomechanical coupling in periodic arrays of scatterers, Phys. Rev. A **88**, 053803 (2013).

[124] F. B. Pedersen, G. T. Einevoll, and P. C. Hemmer, Wannier functions for the Kronig-Penney model, Phys. Rev. B **44**, 5470 (1991).

[125] P. W. Anderson, Absence of Diffusion in Certain Random Lattices, Phys. Rev. **109**, 1492 (1958).

[126] P. Meystre, A short walk through quantum optomechanics, Annalen der Physik **525**, 215 (2013).

[127] P. Maunz, T. Puppe, I. Schuster, N. Syassen, P. W. H. Pinkse, and G. Rempe, Cavity cooling of a single atom, Nature **428**, 50 (2004).

[128] S. Groblacher, K. Hammerer, M. R. Vanner, and M. Aspelmeyer, Observation of strong coupling between a micromechanical resonator and an optical cavity field, Nature **460**, 724 (2009).

[129] E. Verhagen, S. Deleglise, S. Weis, A. Schliesser, and T. J. Kippenberg, Quantum-coherent coupling of a mechanical oscillator to an optical cavity mode, Nature **482**, 63 (2012).

[130] N. Kiesel, F. Blaser, U. Delić, D. Grass, R. Kaltenbaek, and M. Aspelmeyer, Cavity cooling of an optically levitated submicron particle, Proceedings of the National Academy of Sciences of the United States of America **110**, 14180 (2013).

[131] P. Asenbaum, S. Kuhn, S. Nimmrichter, U. Sezer, and M. Arndt, Cavity cooling of free silicon nanoparticles in high vacuum, Nat Commun **4** (2013).

[132] C. K. Law, Interaction between a moving mirror and radiation pressure: A Hamiltonian formulation, Phys. Rev. A **51**, 2537 (1995).

[133] N. Brahms, T. Botter, S. Schreppler, D. W. C. Brooks, and D. M. Stamper-Kurn, Optical Detection of the Quantization of Collective Atomic Motion, Phys. Rev. Lett. **108**, 133601 (2012).

[134] A. H. Safavi-Naeini, J. Chan, J. T. Hill, T. P. M. Alegre, A. Krause, and O. Painter, Observation of Quantum Motion of a Nanomechanical Resonator, Phys. Rev. Lett. **108**, 033602 (2012).

[135] J. C. Sankey, C. Yang, B. M. Zwickl, A. M. Jayich, and J. G. E. Harris, Strong and tunable nonlinear optomechanical coupling in a low-loss system, Nat Phys **6**, 707 (2010).

[136] U. Akram, N. Kiesel, M. Aspelmeyer, and G. J. Milburn, Single-photon opto-mechanics in the strong coupling regime, New Journal of Physics **12**, 083030 (2010).

[137] A. Nunnenkamp, K. Børkje, and S. M. Girvin, Single-Photon Optomechanics, Phys. Rev. Lett. **107**, 063602 (2011).

[138] A. Nunnenkamp, K. Børkje, and S. M. Girvin, Cooling in the single-photon strong-coupling regime of cavity optomechanics, Phys. Rev. A **85**, 051803 (2012).

[139] J. Qian, A. A. Clerk, K. Hammerer, and F. Marquardt, Quantum Signatures of the Optomechanical Instability, Phys. Rev. Lett. **109**, 253601 (2012).

[140] M. Ludwig, A. H. Safavi-Naeini, O. Painter, and F. Marquardt, Enhanced Quantum Nonlinearities in a Two-Mode Optomechanical System, Phys. Rev. Lett. **109**, 063601 (2012).

[141] A. Kronwald, M. Ludwig, and F. Marquardt, Full photon statistics of a light beam transmitted through an optomechanical system, Phys. Rev. A **87**, 013847 (2013).

[142] M. Karuza, C. Molinelli, M. Galassi, C. Biancofiore, R. Natali, P. Tombesi, G. D. Giuseppe, and D. Vitali, Optomechanical sideband cooling of a thin membrane within a cavity, New Journal of Physics **14**, 095015 (2012).

[143] M. Karuza, C. Biancofiore, M. Bawaj, C. Molinelli, M. Galassi, R. Natali, P. Tombesi, G. Di Giuseppe, and D. Vitali, Optomechanically induced transparency in a membrane-in-the-middle setup at room temperature, Phys. Rev. A **88**, 013804 (2013).

[144] A. M. Jayich, J. C. Sankey, B. M. Zwickl, C. Yang, J. D. Thompson, S. M. Girvin, A. A. Clerk, F. Marquardt, and J. G. E. Harris, Dispersive optomechanics: a membrane inside a cavity, New Journal of Physics **10**, 095008 (2008).

[145] D. Lee, M. Underwood, D. Mason, A. B. Shkarin, S. W. Hoch, and J. G. E. Harris, Multimode optomechanical dynamics in a cavity with avoided crossings, Nat Commun **6** (2015).

[146] K. Stannigel, P. Komar, S. J. M. Habraken, S. D. Bennett, M. D. Lukin, P. Zoller, and P. Rabl, Optomechanical Quantum Information Processing with Photons and Phonons, Phys. Rev. Lett. **109**, 013603 (2012).

[147] J. Eisert, M. B. Plenio, S. Bose, and J. Hartley, Towards Quantum Entanglement in Nanoelectromechanical Devices, Phys. Rev. Lett. **93**, 190402 (2004).

[148] M. Bhattacharya, H. Uys, and P. Meystre, Optomechanical trapping and cooling of partially reflective mirrors, Phys. Rev. A **77**, 033819 (2008).

[149] M. J. Hartmann and M. B. Plenio, Steady State Entanglement in the Mechanical Vibrations of Two Dielectric Membranes, Phys. Rev. Lett. **101**, 200503 (2008).

[150] M. Ludwig, K. Hammerer, and F. Marquardt, Entanglement of mechanical oscillators coupled to a nonequilibrium environment, Phys. Rev. A **82**, 012333 (2010).

[151] J. M. Dobrindt and T. J. Kippenberg, Theoretical Analysis of Mechanical Displacement Measurement Using a Multiple Cavity Mode Transducer, Phys. Rev. Lett. **104**, 033901 (2010).

[152] K. Stannigel, P. Rabl, A. S. Sørensen, P. Zoller, and M. D. Lukin, Optomechanical Transducers for Long-Distance Quantum Communication, Phys. Rev. Lett. **105**, 220501 (2010).

[153] G. Heinrich, M. Ludwig, J. Qian, B. Kubala, and F. Marquardt, Collective Dynamics in Optomechanical Arrays, Phys. Rev. Lett. **107**, 043603 (2011).

[154] D. E. Chang, A. H. Safavi-Naeini, M. Hafezi, and O. Painter, Slowing and stopping light using an optomechanical crystal array, New Journal of Physics **13**, 023003 (2011).

[155] H. Seok, L. F. Buchmann, S. Singh, and P. Meystre, Optically mediated nonlinear quantum optomechanics, Phys. Rev. A **86**, 063829 (2012).

[156] S. Chesi, Y.-D. Wang, and J. Twamley, Diabolical points in multi-scatterer optomechanical systems, Scientific Reports **5**, 7816 EP (2015).

[157] Q. Lin, J. Rosenberg, D. Chang, R. Camacho, M. Eichenfield, K. J. Vahala, and O. Painter, Coherent mixing of mechanical excitations in nano-optomechanical structures, Nat Photon **4**, 236 (2010).

[158] I. Mahboob, E. Flurin, K. Nishiguchi, A. Fujiwara, and H. Yamaguchi, Interconnect-free parallel logic circuits in a single mechanical resonator, Nat Commun **2**, 198 (2011).

[159] I. Mahboob, K. Nishiguchi, H. Okamoto, and H. Yamaguchi, Phonon-cavity electromechanics, Nat Phys **8**, 387 (2012).

[160] F. Massel, T. T. Heikkila, J. M. Pirkkalainen, S. U. Cho, H. Saloniemi, P. J. Hakonen, and M. A. Sillanpaa, Microwave amplification with nanomechanical resonators, Nature **480**, 351 (2011).

[161] K. Zhang, P. Meystre, and W. Zhang, Role Reversal in a Bose-Condensed Optomechanical System, Phys. Rev. Lett. **108**, 240405 (2012).

[162] S. Camerer, M. Korppi, A. Jöckel, D. Hunger, T. W. Hänsch, and P. Treutlein, Realization of an Optomechanical Interface Between Ultracold Atoms and a Membrane, Phys. Rev. Lett. **107**, 223001 (2011).

[163] I. H. Deutsch, R. J. C. Spreeuw, S. L. Rolston, and W. D. Phillips, Photonic band gaps in optical lattices, Phys. Rev. A **52**, 1394 (1995).

[164] O. L. Berman and R. Y. Kezerashvili, Graphene-based one-dimensional photonic crystal, Journal of Physics: Condensed Matter **24**, 015305 (2012).

[165] A. M. Rey, G. Pupillo, C. W. Clark, and C. J. Williams, Ultracold atoms confined in an optical lattice plus parabolic potential: A closed-form approach, Phys. Rev. A **72**, 033616 (2005).

[166] P. Yeh, *Optical Waves in Layered Media* (Wiley, 2005).

[167] C. Genes, A. Xuereb, G. Pupillo, and A. Dantan, Enhanced optomechanical readout using optical coalescence, Phys. Rev. A **88**, 033855 (2013).

[168] M. P. and Soukoulis C. M., Wave Propagation: From Electrons to Photonic Crystals and Left-Handed Materials, in *Wave Propagation: From Electrons to Photonic Crystals and Left-Handed Materials* (Princeton University Press, 2008).

[169] J. D. Joannopoulos, S. G. Johnson, J. N. Winn, and R. D. Meade, *Photonic Crystals: Molding the Flow of Light. second edition*, edited by P. U. Press (2008).

[170] N. Marzari, A. A. Mostofi, J. R. Yates, I. Souza, and D. Vanderbilt, Maximally localized Wannier functions: Theory and applications, Rev. Mod. Phys. **84**, 1419 (2012).

[171] S. Bose, Quantum communication through spin chain dynamics: an introductory overview, Contemporary Physics **48**, 13 (2007), http://dx.doi.org/10.1080/00107510701342313 .

[172] E. Lieb and D. Robinson, The finite group velocity of quantum spin systems, Communications in Mathematical Physics **28**, 251 (1972).

[173] B. Nachtergaele, Y. Ogata, and R. Sims, Propagation of Correlations in Quantum Lattice Systems, Journal of Statistical Physics **124**, 1 (2006).

[174] P. Jurcevic, B. P. Lanyon, P. Hauke, C. Hempel, P. Zoller, R. Blatt, and C. F. Roos, Quasiparticle engineering and entanglement propagation in a quantum many-body system, Nature **511**, 202 (2014).

[175] P. Richerme, Z.-X. Gong, A. Lee, C. Senko, J. Smith, M. Foss-Feig, S. Michalakis, A. V. Gorshkov, and C. Monroe, Non-local propagation of correlations in quantum systems with long-range interactions, Nature **511**, 198 (2014).

[176] M. Cheneau, P. Barmettler, D. Poletti, M. Endres, P. Schausz, T. Fukuhara, C. Gross, I. Bloch, C. Kollath, and S. Kuhr, Light-cone-like spreading of correlations in a quantum many-body system, Nature **481**, 484 (2012).

[177] S. R. Forrest, The path to ubiquitous and low-cost organic electronic appliances on plastic, Nature **428**, 911 (2004).

[178] G. D. Scholes and G. Rumbles, Excitons in nanoscale systems, Nat Mater **5**, 683 (2006).

[179] S. M. Menke, W. A. Luhman, and R. J. Holmes, Tailored exciton diffusion in organic photovoltaic cells for enhanced power conversion efficiency, Nat Mater **12**, 152 (2013).

[180] E. Orgiu, J. George, J. A. Hutchison, E. Devaux, J. F. Dayen, B. Doudin, F. Stellacci, C. Genet, J. Schachenmayer, C. Genes, G. Pupillo, P. Samori, and T. W. Ebbesen, Conductivity in organic semiconductors hybridized with the vacuum field, Nat Mater **14**, 1123 (2015).

[181] D. G. Lidzey, D. D. C. Bradley, M. S. Skolnick, T. Virgili, S. Walker, and D. M. Whittaker, Strong exciton-photon coupling in an organic semiconductor microcavity, Nature **395**, 53 (1998).

[182] D. G. Lidzey, D. D. C. Bradley, T. Virgili, A. Armitage, M. S. Skolnick, and S. Walker, Room Temperature Polariton Emission from Strongly Coupled Organic Semiconductor Microcavities, Phys. Rev. Lett. **82**, 3316 (1999).

[183] R. J. Holmes and S. R. Forrest, Strong Exciton-Photon Coupling and Exciton Hybridization in a Thermally Evaporated Polycrystalline Film of an Organic Small Molecule, Phys. Rev. Lett. **93**, 186404 (2004).

[184] D. M. Coles, P. Michetti, C. Clark, W. C. Tsoi, A. M. Adawi, J.-S. Kim, and D. G. Lidzey, Vibrationally Assisted Polariton-Relaxation Processes in Strongly Coupled Organic-Semiconductor Microcavities, Advanced Functional Materials **21**, 3691 (2011).

[185] T. Schwartz, J. A. Hutchison, C. Genet, and T. W. Ebbesen, Reversible Switching of Ultrastrong Light-Molecule Coupling, Phys. Rev. Lett. **106**, 196405 (2011).

[186] S. Kéna-Cohen, S. A. Maier, and D. D. C. Bradley, Ultrastrongly Coupled Exciton–Polaritons in Metal-Clad Organic Semiconductor Microcavities, Advanced Optical Materials **1**, 827 (2013).

[187] E. Wertz, A. Amo, D. D. Solnyshkov, L. Ferrier, T. C. H. Liew, D. Sanvitto, P. Senellart, I. Sagnes, A. Lemaître, A. V. Kavokin, G. Malpuech, and J. Bloch, Propagation and Amplification Dynamics of 1D Polariton Condensates, Phys. Rev. Lett. **109**, 216404 (2012).

[188] M. Alloing, M. Beian, M. Lewenstein, D. Fuster, Y. González, L. González, R. Combescot, M. Combescot, and F. Dubin, Evidence for a Bose-Einstein condensate of excitons, EPL (Europhysics Letters) **107**, 10012 (2014).

[189] R. H. Dicke, Coherence in Spontaneous Radiation Processes, Phys. Rev. **93**, 99 (1954).

[190] B. M. Garraway, The Dicke model in quantum optics: Dicke model revisited, Philosophical Transactions of the Royal Society of London Series A **369**, 1137 (2011).

[191] H. Shirakawa, E. J. Louis, A. G. MacDiarmid, C. K. Chiang, and A. J. Heeger, Synthesis of electrically conducting organic polymers: halogen derivatives of polyacetylene, (CH), J. Chem. Soc., Chem. Commun. , 578 (1977).

[192] C. W. Tang and S. A. VanSlyke, Organic electroluminescent diodes, Applied Physics Letters **51** (1987).

[193] J. H. Burroughes, D. D. C. Bradley, A. R. Brown, R. N. Marks, K. Mackay, R. H. Friend, P. L. Burns, and A. B. Holmes, Light-emitting diodes based on conjugated polymers, Nature **347**, 539 (1990).

[194] C. Kim, P. E. Burrows, and S. R. Forrest, Micropatterning of Organic Electronic Devices by Cold-Welding, Science **288**, 831 (2000), http://www.sciencemag.org/content/288/5467/831.full.pdf .

[195] A. Kahn, N. Koch, and W. Gao, Electronic structure and electrical properties of interfaces between metals and π-conjugated molecular films, Journal of Polymer Science Part B: Polymer Physics **41**, 2529 (2003).

[196] H. Sirringhaus, M. Bird, and N. Zhao, Charge Transport Physics of Conjugated Polymer Field-Effect Transistors, Advanced Materials **22**, 3893 (2010).

[197] A. C. Arias, J. D. MacKenzie, I. McCulloch, J. Rivnay, and A. Salleo, Materials and Applications for Large Area Electronics: Solution-Based Approaches, Chemical Reviews **110**, 3 (2010), pMID: 20070114, http://dx.doi.org/10.1021/cr900150b .

[198] R. Löw, H. Weimer, J. Nipper, J. B. Balewski, B. Butscher, H. P. Büchler, and T. Pfau, An experimental and theoretical guide to strongly interacting Rydberg gases, Journal of Physics B: Atomic, Molecular and Optical Physics **45**, 113001 (2012).

[199] S. Bettelli, D. Maxwell, T. Fernholz, C. S. Adams, I. Lesanovsky, and C. Ates, Exciton dynamics in emergent Rydberg lattices, Phys. Rev. A **88**, 043436 (2013).

[200] B. Yan, S. A. Moses, B. Gadway, J. P. Covey, K. R. A. Hazzard, A. M. Rey, D. S. Jin, and J. Ye, Observation of dipolar spin-exchange interactions with lattice-confined polar molecules, Nature **501**, 521 (2013).

[201] K. R. A. Hazzard, B. Gadway, M. Foss-Feig, B. Yan, S. A. Moses, J. P. Covey, N. Y. Yao, M. D. Lukin, J. Ye, D. S. Jin, and A. M. Rey, Many-Body Dynamics of Dipolar Molecules in an Optical Lattice, Phys. Rev. Lett. **113**, 195302 (2014).

[202] D. Porras and J. I. Cirac, Effective Quantum Spin Systems with Trapped Ions, Phys. Rev. Lett. **92**, 207901 (2004).

[203] A. Friedenauer, H. Schmitz, J. T. Glueckert, D. Porras, and T. Schaetz, Simulating a quantum magnet with trapped ions, Nat Phys **4**, 757 (2008).

[204] G. Vidal, Efficient Simulation of One-Dimensional Quantum Many-Body Systems, Phys. Rev. Lett. **93**, 040502 (2004).

[205] S. R. White and A. E. Feiguin, Real-Time Evolution Using the Density Matrix Renormalization Group, Phys. Rev. Lett. **93**, 076401 (2004).

[206] A. J. Daley, C. Kollath, U. Schollwöck, and G. Vidal, Time-dependent density-matrix renormalization-group using adaptive effective Hilbert spaces, Journal of Statistical Mechanics: Theory and Experiment **2004**, P04005 (2004).

[207] Z.-X. Gong, M. Foss-Feig, S. Michalakis, and A. V. Gorshkov, Persistence of Locality in Systems with Power-Law Interactions, Phys. Rev. Lett. **113**, 030602 (2014).

[208] J. Schachenmayer, B. P. Lanyon, C. F. Roos, and A. J. Daley, Entanglement Growth in Quench Dynamics with Variable Range Interactions, Phys. Rev. X **3**, 031015 (2013).

[209] J. M. Raimond, M. Brune, and S. Haroche, Manipulating quantum entanglement with atoms and photons in a cavity, Rev. Mod. Phys. **73**, 565 (2001).

[210] V. M. Agranovich, *Excitations in organic solids* (Oxford University Press, 2008).

[211] A. Rodríguez, V. A. Malyshev, G. Sierra, M. A. Martín-Delgado, J. Rodríguez-Laguna, and F. Domínguez-Adame, Anderson Transition in Low-Dimensional Disordered Systems Driven by Long-Range Nonrandom Hopping, Phys. Rev. Lett. **90**, 027404 (2003).

[212] R. Landauer, Spatial Variation of Currents and Fields Due to Localized Scatterers in Metallic Conduction, IBM Journal of Research and Development **1**, 223 (2010).

[213] M. Büttiker, Y. Imry, R. Landauer, and S. Pinhas, Generalized many-channel conductance formula with application to small rings, Phys. Rev. B **31**, 6207 (1985).

[214] M. Biondi, S. Schmidt, G. Blatter, and H. E. Türeci, Self-protected polariton states in photonic quantum metamaterials, Phys. Rev. A **89**, 025801 (2014).

[215] P. Longo, P. Schmitteckert, and K. Busch, Few-Photon Transport in Low-Dimensional Systems: Interaction-Induced Radiation Trapping, Phys. Rev. Lett. **104**, 023602 (2010).

[216] D. Ryndyk, R. Gutiérrez, B. Song, and G. Cuniberti, Green Function Techniques in the Treatment of Quantum Transport at the Molecular Scale, in *Energy Transfer Dynamics in Biomaterial Systems*, Springer Series in Chemical Physics, Vol. 93, edited by I. Burghardt, V. May, D. A. Micha, and E. R. Bittner (Springer Berlin Heidelberg, 2009) pp. 213–335.

[217] A. Biella, F. Borgonovi, R. Kaiser, and G. L. Celardo, Subradiant hybrid states in the open 3D Anderson-Dicke model, EPL (Europhysics Letters) **103**, 57009 (2013).

[218] G. Celardo, A. Biella, L. Kaplan, and F. Borgonovi, Interplay of superradiance and disorder in the Anderson Model, Fortschritte der Physik **61**, 250 (2013).

[219] E. Abrahams, P. W. Anderson, D. C. Licciardello, and T. V. Ramakrishnan, Scaling Theory of Localization: Absence of Quantum Diffusion in Two Dimensions, Phys. Rev. Lett. **42**, 673 (1979).

[220] D. Manzano, M. Tiersch, A. Asadian, and H. J. Briegel, Quantum transport efficiency and Fourier's law, Phys. Rev. E **86**, 061118 (2012).

[221] V. M. Agranovich and Y. N. Gartstein, Nature and dynamics of low-energy exciton polaritons in semiconductor microcavities, Phys. Rev. B **75**, 075302 (2007).

[222] M. Litinskaya, Exciton polariton kinematic interaction in crystalline organic microcavities, Phys. Rev. B **77**, 155325 (2008).

[223] R. Feynman, Simulating physics with computers, International Journal of Theoretical Physics **21**, 467 (1982).

[224] J.-T. Shen and S. Fan, Theory of single-photon transport in a single-mode waveguide. I. Coupling to a cavity containing a two-level atom, Phys. Rev. A **79**, 023837 (2009).

[225] A. Stute, B. Casabone, P. Schindler, T. Monz, P. O. Schmidt, B. Brandstatter, T. E. Northup, and R. Blatt, Tunable ion-photon entanglement in an optical cavity, Nature **485**, 482 (2012).

[226] F. Robicheaux, J. V. Hernández, T. Topçu, and L. D. Noordam, Simulation of coherent interactions between Rydberg atoms, Phys. Rev. A **70**, 042703 (2004).

[227] T. Guerreiro, A. Martin, B. Sanguinetti, J. S. Pelc, C. Langrock, M. M. Fejer, N. Gisin, H. Zbinden, N. Sangouard, and R. T. Thew, Nonlinear Interaction between Single Photons, Phys. Rev. Lett. **113**, 173601 (2014).

[228] J. Claudon, J. Bleuse, N. S. Malik, M. Bazin, P. Jaffrennou, N. Gregersen, C. Sauvan, P. Lalanne, and J.-M. Gerard, A highly efficient single-photon source based on a quantum dot in a photonic nanowire, Nat Photon **4**, 174 (2010).

[229] M. Gräfe, R. Heilmann, A. Perez-Leija, R. Keil, F. Dreisow, M. Heinrich, H. Moya-Cessa, S. Nolte, D. N. Christodoulides, and A. Szameit, On-chip generation of high-order single-photon W-states, Nat Photon **8**, 791 (2014).

[230] C. Kupchak, T. Mittiga, B. Jordaan, M. Namazi, C. Nölleke, and E. Figueroa, Room-Temperature Single-photon level Memory for Polarization States, Scientific Reports **5**, 7658 EP (2015).

[231] C. J. Chunnilall, I. P. Degiovanni, S. Kück, I. Müller, and A. G. Sinclair, Metrology of single-photon sources and detectors: a review, Optical Engineering **53**, 081910 (2014).

[232] K. R. Motes, J. P. Olson, E. J. Rabeaux, J. P. Dowling, S. J. Olson, and P. P. Rohde, Linear Optical Quantum Metrology with Single Photons: Exploiting Spontaneously Generated Entanglement to Beat the Shot-Noise Limit, Phys. Rev. Lett. **114**, 170802 (2015).

[233] M. Napolitano, M. Koschorreck, B. Dubost, N. Behbood, R. J. Sewell, and M. W. Mitchell, Interaction-based quantum metrology showing scaling beyond the Heisenberg limit, Nature **471**, 486 (2011).

[234] S. Haroche, Nobel Lecture: Controlling photons in a box and exploring the quantum to classical boundary, Rev. Mod. Phys. **85**, 1083 (2013).

[235] B. Dayan, A. S. Parkins, T. Aoki, E. P. Ostby, K. J. Vahala, and H. J. Kimble, A Photon Turnstile Dynamically Regulated by One Atom, Science **319**, 1062 (2008), http://www.sciencemag.org/content/319/5866/1062.full.pdf .

[236] A. Reinhard, T. Volz, M. Winger, A. Badolato, K. J. Hennessy, E. L. Hu, and A. Imamoğlu, Strongly correlated photons on a chip, Nat Photon **6**, 93 (2012).

[237] A. Goban, C.-L. Hung, J. D. Hood, S.-P. Yu, J. A. Muniz, O. Painter, and H. J. Kimble, Superradiance for Atoms Trapped along a Photonic Crystal Waveguide, Phys. Rev. Lett. **115**, 063601 (2015).

[238] C. Sayrin, C. Clausen, B. Albrecht, P. Schneeweiss, and A. Rauschenbeutel, Storage of fiber-guided light in a nanofiber-trapped ensemble of cold atoms, Optica **2**, 353 (2015).

[239] F. Le Kien and A. Rauschenbeutel, Electromagnetically induced transparency for guided light in an atomic array outside an optical nanofiber, Phys. Rev. A **91**, 053847 (2015).

[240] R. Mitsch, C. Sayrin, B. Albrecht, P. Schneeweiss, and A. Rauschenbeutel, Quantum state-controlled directional spontaneous emission of photons into a nanophotonic waveguide, Nat Commun **5** (2014).

[241] D. Reitz, C. Sayrin, B. Albrecht, I. Mazets, R. Mitsch, P. Schneeweiss, and A. Rauschenbeutel, Backscattering properties of a waveguide-coupled array of atoms in the strongly nonparaxial regime, Phys. Rev. A **89**, 031804 (2014).

[242] M. Bajcsy, S. Hofferberth, T. Peyronel, V. Balic, Q. Liang, A. S. Zibrov, V. Vuletic, and M. D. Lukin, Laser-cooled atoms inside a hollow-core photonic-crystal fiber, Phys. Rev. A **83**, 063830 (2011).

[243] V. Venkataraman, K. Saha, and A. L. Gaeta, Phase modulation at the few-photon level for weak-nonlinearity-based quantum computing, Nat Photon **7**, 138 (2013).

[244] F. Blatt, T. Halfmann, and T. Peters, One-dimensional ultracold medium of extreme optical depth, Opt. Lett. **39**, 446 (2014).

[245] C. A. Christensen, S. Will, M. Saba, G.-B. Jo, Y.-I. Shin, W. Ketterle, and D. Pritchard, Trapping of ultracold atoms in a hollow-core photonic crystal fiber, Phys. Rev. A **78**, 033429 (2008).

[246] C. Perrella, P. S. Light, J. D. Anstie, F. Benabid, T. M. Stace, A. G. White, and A. N. Luiten, High-efficiency cross-phase modulation in a gas-filled waveguide, Phys. Rev. A **88**, 013819 (2013).

[247] M. Hafezi, D. E. Chang, V. Gritsev, E. Demler, and M. D. Lukin, Quantum transport of strongly interacting photons in a one-dimensional nonlinear waveguide, Phys. Rev. A **85**, 013822 (2012).

[248] M. Hafezi, D. E. Chang, V. Gritsev, E. A. Demler, and M. D. Lukin, Photonic quantum transport in a nonlinear optical fiber, EPL (Europhysics Letters) **94**, 54006 (2011).

[249] M. Pletyukhov and V. Gritsev, Quantum theory of light scattering in a one-dimensional channel: Interaction effect on photon statistics and entanglement entropy, Phys. Rev. A **91**, 063841 (2015).

[250] H. Zoubi, Collective interactions in an array of atoms coupled to a nanophotonic waveguide, Phys. Rev. A **89**, 043831 (2014).

[251] J. S. Douglas, H. Habibian, C. L. Hung, A. V. Gorshkov, H. J. Kimble, and D. E. Chang, Quantum many-body models with cold atoms coupled to photonic crystals, Nat Photon **9**, 326 (2015).

[252] D. E. Chang, J. I. Cirac, and H. J. Kimble, Self-Organization of Atoms along a Nanophotonic Waveguide, Phys. Rev. Lett. **110**, 113606 (2013).

[253] S.-P. Yu, J. D. Hood, J. A. Muniz, M. J. Martin, R. Norte, C.-L. Hung, S. M. Meenehan, J. D. Cohen, O. Painter, and H. J. Kimble, Nanowire photonic crystal waveguides for single-atom trapping and strong light-matter interactions, Applied Physics Letters **104**, 111103 (2014), http://dx.doi.org/10.1063/1.4868975.

[254] I. Aharonovich, A. D. Greentree, and S. Prawer, Diamond photonics, Nat Photon **5**, 397 (2011).

[255] J. Riedrich-Möller, C. Arend, C. Pauly, F. Mücklich, M. Fischer, S. Gsell, M. Schreck, and C. Becher, Deterministic Coupling of a Single Silicon-Vacancy Color Center to a Photonic Crystal Cavity in Diamond, Nano Letters **14**, 5281 (2014), pMID: 25111134, http://dx.doi.org/10.1021/nl502327b .

[256] K. Kakazu and Y. S. Kim, Quantization of electromagnetic fields in a circular cylindrical cavity, (1995), arXiv:quant-ph/9511012 [quant-ph] .

[257] J. Javanainen, O. Odong, and J. C. Sanders, Dimer of two bosons in a one-dimensional optical lattice, Phys. Rev. A **81**, 043609 (2010).

[258] O. Dubovskii, Gap kinematic Frenkel biexciton, Physics of the Solid State **42**, 450 (2000).

[259] A. Goban, K. S. Choi, D. J. Alton, D. Ding, C. Lacroûte, M. Pototschnig, T. Thiele, N. P. Stern, and H. J. Kimble, Demonstration of a State-Insensitive, Compensated Nanofiber Trap, Phys. Rev. Lett. **109**, 033603 (2012).

[260] F. Le Kien and A. Rauschenbeutel, Anisotropy in scattering of light from an atom into the guided modes of a nanofiber, Phys. Rev. A **90**, 023805 (2014).

[261] K. Winkler, G. Thalhammer, F. Lang, R. Grimm, J. Hecker Denschlag, A. J. Daley, A. Kantian, H. P. Büchler, and P. Zoller, Repulsively bound atom pairs in an optical lattice, Nature **441**, 853 (2006).

[262] R. T. Piil, N. Nygaard, and K. Mølmer, Scattering and binding of different atomic species in a one-dimensional optical lattice, Phys. Rev. A **78**, 033611 (2008).

[263] M. T. C. Wong and C. K. Law, Two-polariton bound states in the Jaynes-Cummings-Hubbard model, Phys. Rev. A **83**, 055802 (2011).

[264] T. F. Gallagher, *Rydberg Atoms* (Cambridge University Press, 1994) cambridge Books Online.

[265] A. M. Hankin, Y.-Y. Jau, L. P. Parazzoli, C. W. Chou, D. J. Armstrong, A. J. Landahl, and G. W. Biedermann, Two-atom Rydberg blockade using direct 6*S* to *nP* excitation, Phys. Rev. A **89**, 033416 (2014).

[266] D. Tong, S. M. Farooqi, J. Stanojevic, S. Krishnan, Y. P. Zhang, R. Côté, E. E. Eyler, and P. L. Gould, Local Blockade of Rydberg Excitation in an Ultracold Gas, Phys. Rev. Lett. **93**, 063001 (2004).

[267] H. Saßmannshausen, F. Merkt, and J. Deiglmayr, High-resolution spectroscopy of Rydberg states in an ultracold cesium gas, Phys. Rev. A **87**, 032519 (2013).

[268] T. Manthey, T. M. Weber, T. Niederprüm, P. Langer, V. Guarrera, G. Barontini, and H. Ott, Scanning electron microscopy of Rydberg-excited Bose–Einstein condensates, New Journal of Physics **16**, 083034 (2014).

[269] A. W. Glaetzle, M. Dalmonte, R. Nath, C. Gross, I. Bloch, and P. Zoller, Designing Frustrated Quantum Magnets with Laser-Dressed Rydberg Atoms, Phys. Rev. Lett. **114**, 173002 (2015).

[270] R. M. W. van Bijnen and T. Pohl, Quantum Magnetism and Topological Ordering via Rydberg Dressing near Förster Resonances, Phys. Rev. Lett. **114**, 243002 (2015).

[271] K. W. Madison, Y. Wang, A. M. Rey, and K. Bongs, *Annual Review of Cold Atoms and Molecules: Volume 1*, Annual Review of Cold Atoms and Molecules, Vol. 1 (World Scientific, 2013).

[272] M. Saffman and T. G. Walker, Creating single-atom and single-photon sources from entangled atomic ensembles, Phys. Rev. A **66**, 065403 (2002).

[273] Y. Kosmann-Schwarzbach, *The Noether Theorems: Invariance and Conservation Laws in the Twentieth Century* (Springer-Verlag New York, 2011).

[274] V. Agranovich, O. Dubovsky, D. Basko, G. L. Rocca, and F. Bassani, Kinematic Frenkel biexcitons, Journal of Luminescence **85**, 221 (2000).

[275] T. Kazimierczuk, D. Frohlich, S. Scheel, H. Stolz, and M. Bayer, Giant Rydberg excitons in the copper oxide Cu2O, Nature **514**, 343 (2014).

[276] E. Tignone, G. Pupillo, and C. Genes, Transmissive optomechanical platforms with engineered spatial defects, Phys. Rev. A **90**, 053831 (2014).

[277] J. Schachenmayer, C. Genes, E. Tignone, and G. Pupillo, Cavity-Enhanced Transport of Excitons, Phys. Rev. Lett. **114**, 196403 (2015).

[278] M. O. Scully and M. S. Zubairy, *Quantum Optics* (Cambridge University Press, 1997).

[279] M. Litinskaya, E. Tignone, and G. Pupillo, Broadband photon-photon interactions mediated by cold atoms in a photonic crystal fiber, ArXiv e-prints (2015), arXiv:1512.02312 [quant-ph] .

Edoardo TIGNONE

Cavity quantum electrodynamics: From photonic crystals to Rydberg atoms

Résumé

Dans le premier chapitre de la thèse, nous étudions la possibilité d'améliorer le couplage optomechanique photon-phonon entre le mode de résonance d'une cavité Fabry-Pérot de haute finesse et les vibrations mécaniques des éléments diélectriques (membranes) à l'intérieur de la cavité. En introduisant un défaut quadratique dans la disposition des membranes, nous montrons que le deux couplages (linéaire et quadratique) augmentent. Enfin, nous proposons un modèle très simple avec lequel on cherche à simuler un cristal photonique quasipériodique.
Dans le deuxième chapitre de cette thèse, nous présentons nos résultats de recherche sur le transport d'excitons à travers une cavité visant à augmenter l'efficacité du transport. Le modèle que l'on étudie est une chaîne unidimensionnelle d'atomes froids comprenant chacun deux niveaux énergétiques. Grâce au couplage entre exciton et photon, ces deux quanta s'hybrident et forment deux branches de polariton à l'intérieur de la cavité. Nous avons observé qu'à résonance avec un des deux modes de polariton, on peut transmettre l'exciton via le mode polaritonique dans un temps très court. En outre, le désordre n'affecte la propagation excitonique que de façon algébrique.
Dans le troisième chapitre de cette thèse, nous présentons nos résultats de recherche sur la réalisation d'interactions entre photons grâce à la médiation d'atomes ultrafroids piégés dans un réseaux optique unidimensionnelle et placés à l'intérieur d'une fibre à cristaux photoniques. Nous avons détecté un régime dans lequel on peut réaliser le "bunching" photon-photon.
Dans le quatrième et dernière chapitre de cette thèse, nous étendons les résultats du chapitre précédent aux atomes de Rydberg.

Mots clés: optique non linéaire, cavité, cristal photonique, couplage optoméchanique, transport d'exciton, polaritons, atomes froids, corrélations entre photons, bunching, atomes de Rydberg.

Abstract

In the first chapter of this thesis, we study a quasiperiodic array of dielectric membranes inside a high-finesse Fabry-Pérot cavity. We work within the framework of the transfer matrix formalism. We show that, in a transmissive regime, the introduction of a quadratic spatial defect in the membrane positions enhances both the linear and quadratic optomechanical couplings between optical and mechanical degrees of freedom. Finally, we propose a theoretical model to simulate a one-dimensional quasiperiodic photonic crystal.
In the second chapter of this thesis, we consider the problem of the transport of an exciton through a one-dimensional chain of two-level systems. We embed the chain of emitters in a transverse optical cavity and we show that, in the strong coupling regime, a ultrafast ballistic transport of the exciton is possible via the polaritonic modes rather than ordinary hopping. Due to the hybrid nature of polaritons, the transport efficiency is particularly robust against disorder and imperfections in the system.
In the third chapter of this thesis, we consider an ordered array of cold atoms trapped in an optical lattice inside a hollow-core photonic crystal fiber. We study photon-photon interactions mediated by hard-core repulsion between excitons. We show that, in spite of underlying repulsive interaction, photons in the scattering states demonstrate bunching, which can be controlled by tuning the interatomic separation. We interpret this bunching as the result of scattering due to the mismatch of the quantization volumes for excitons and photons, and discuss the dependence of the effect on experimentally relevant parameters.
In the fourth chapter of the thesis, we extend the results of the previous chapter to the case of Rydberg atoms.

Keywords: Nonlinear optics, cavity, photonic crystal, optomechanical coupling, exciton transport, polaritons, cold atoms, photon-photon correlations, bunching, Rydberg atoms.